SUBSONIC INTAKE DUCT FLOWS

BY

SIDNEY SHIU HIN HO

THESIS SUBMITTED FOR THE DEGREE OF DOCTOR OF PHILOSOPHY

DEPARTMENT OF AERONAUTICAL AND MECHANICAL ENGINEERING
THE UNIVERSITY OF SALFORD

JANUARY 1990

TO THE UNIVERSITY OF SALFORD,
FROM WHERE I HAVE LEARNED SO MUCH.

CONTENTS

Figures

Chapter 4 Results and discussions

Figures

Chapter 5 Numerical computations

Chapter 6 Conclusions and recommendations for further work

Appendices

ACKNOWLEDGEMENTS

The work was carried out in the Department of Aeronautical and Mechanical Engineering at the University of Salford under the guidance of Dr. D. F. Myring and Prof. J. L. Livesey. The author wishes to express his deepest gratitude for their expert advice and continuous encouragement.

The author wishes to thank the Hatfield Division of the British Aerospace plc for providing the intake ducts for investigation and the Science and Engineering Research Council for the financial support.

The experimental work was carried out at the aerodynamics laboratory of the Department. The author wishes to express his gratitude to Mr. A. Fowler for his assistance in establishing the experimental facilities. Many thanks are also due to the staff of the aerodynamics and the thermofluid mechanics laboratories, the instrumentation, the engineering work-shop and the Department's data processing bureau.

The author also gratefully acknowledges Mr. S. E. Konarski for his continuous advice in using the viscous/inviscid code. The computations were carried out at the University of Salford Computing Centre. The author wishes to thank the staff for their excellent advisory service.

Finally, the author is indebted to his parents and family for their moral support and encouragement.

SUMMARY

Here both S-shaped and singly curved (here classified as S-shaped) duct diffusers for intakes in aeronautical propulsion systems are studied. The results are applicable in other situations where similar ducts occur; for example on V/STOL aircraft employing re-direction of thrust, intercomponent ducting in high bypass ratio engines, etc.

An open circuit static test rig, capable of mass flow rates of 5 kg/s, and three-dimensional instrumentation were established. Flow measurements were made in S-shaped intake duct diffusers for rear mounted gas turbine engines in both aircraft and air-breathing missiles. These designs are intended for ventral type inlet installation. These ducts possess cross-sectional shape transitions, from oblate to circular, with area increase and annular ducts at the engine face. The work was aimed at both fundamental understanding of the flows and at establishing test data for the prediction methods. Tests were performed at throat Mach numbers of nominally 0.15 and 0.6 and in the unit Reynolds number range of 3×10^6/m - 2×10^7/m for three different ducts each having different upstream bends but common downstream bends. Detailed boundary layer surveys were made to establish plane of symmetry growth of the viscous region and the extent of three-dimensionality away from the plane of symmetry. Data are presented in the form of velocity profiles, streamwise and cross-flow, integral thicknesses and surface pressure fields. Engine face distortion is assessed from full outlet flow surveys. Flow visualization was recorded using surface oil flow techniques. Evidence is presented of a trend towards three-dimensional separation as the upstream bend increases in severity. For the most extreme case large regions of complex three-dimensional separated flow occur and topological analysis of the recorded surface oil flow pattern allows reconstruction of the separating flow. Clear correlations are established between flow visualization results and flow measurements yielding better understanding. Finally, results were compared with a three-dimensional compressible prediction method.

NOMENCLATURE

A	i) variable defined by $A = \exp(-S/c_v)$ ii) boundary layer crossflow parameter
C	speed of sound
cf_1, cf_2	skin friction coefficients in s and n directions
c_v	specific heat at constant volume
F	entrainment coefficient
$\sqrt{g}$	Jacobian of transformation in three dimensions
g_{ij}, g^{ij}	metric and conjugate metric tensor
H	compressible shape factor
$\overline{H}$	incompressible shape factor
H_o	total enthalpy
h_1, h_2	metric elements in curvilinear coordinates
k_s, k_n	curvature coefficients
M	Mach number
P_o, p	total and static pressures
p1, p2, p3	Conrad probe pressures
pn	Conrad probe pressures normalizing term defined by $pn = p2 - \frac{1}{2}(p1+p3)$
q	Jacobian of transformation on duct surface
R	specific gas constant
Re_θ	momentum thickness Reynolds number
S	entropy
s, n, ζ	streamline coordinates

T_o, T	total and static temperatures
U	resultant or freestream velocity
U_e	streamline velocity at boundary layer edge
U_s, U_n, U_ζ	velocity gradients in the s, n and ζ directions
u, v, w	velocities in s, n and ζ directions
u_e, v_e	velocities at the boundary edge in the ξ and η coordinate directions
u_*, v_*	velocities on the δ^* surface in ξ and η coordinate directions
u_i	velocities in curvilinear coordinates (x^i)
u_τ	frictional velocity $(=\surd(\tau_w/\rho_w))$
V, V^η, V^ζ	throughflow velocities
$\bar{V}^\eta$, $\bar{V}^\zeta$	contravariant mass flow rates
X, Y, Z, B, C, Θ	duct profile coordinates
y	normal distance from the wall $(=\zeta)$
y^+	yu_τ/ν_w
z_δ, z	transformed distance in the ζ direction
$\bar{\ }$, $'$	mean and turbulent quantities

Greek symbols

α	duct bend or freestream turning angle
β, β_o	skew and limiting streamline angles
γ	ratio of specific heats, C_p/C_v
δ	boundary layer thickness

δ^*	displacement surface thickness
δ_1, δ_2	displacement thicknesses
ξ, η, ζ or x^i	curvilinear coordinates
Θ_{11}, Θ_{12}, Θ_{21}, Θ_{22}	momentum thicknesses
ω	vorticity
μ	dynamic viscosity
ν	kinematic viscosity
ρ	density
τ_w	wall shear stress

Suffices

e	boundary layer edge
in	inlet
isen	isentropic
max	maximum
m	intermediate
n	transverse
ref	reference
s	streamwise
w	wall
ζ	normal
*	on displacement surface

N.B. Symbols not shown are defined locally.

CHAPTER 1

INTRODUCTION

CHAPTER 1 INTRODUCTION

Flows in curved ducts are found in a wide range of practical configurations. The most frequently used are S-shaped ducts and passages which occur in a multitude of applications, where a combination of bends is employed to re-direct the flow. In this thesis both S-shaped and singly curved (also classified as S-shaped in this work) duct diffusers for air intake portions of aeronautical propulsion systems are studied. The results are equally applicable in other situations with similar duct geometries and entry flow conditions; for example on V/STOL aircraft which employ considerable re-direction of the engine's thrust, intercomponent ducting in high bypass ratio fan engines, internal combustion engine passages and air conditioning systems.

When a jet engine has to be carried in an aircraft fuselage and the intake is located in an offset position, this necessitates a double bend or S-shaped duct. An exception is when the intake is of the submerged type on for example a stealth aircraft where only a singly curved duct is necessary. S-shaped ducts are found in aircraft with dorsal, wing-root or ventral intakes (Fig. 1-1) and the latter arrangement is frequently adopted in military aircraft design because this type of inlet airframe integration is more tolerant of high angles of incidence.

In recent years, design changes have led to increases in demand for space by modern radar and other guidance equipment which needs to be located at the nose of the aircraft or guided missile for maximum efficiency. This together with a new generation of fighter aircraft cockpit and canopy design for high-g manoeuvre and visibility has made S-shaped intake ducts a necessity. Hence, S-shaped intake ducts have been recognized as an essential component of modern military aircraft and guided air-breathing missiles.

However, attention was only drawn recently to a need for a more thorough understanding of flow in S-shaped intake duct diffusers as it was realized that previous ad hoc tests and prediction methods were simply not adequate (e.g. see Neumann et al 1980).

Perhaps the most distinguishing characteristic of flows in curved ducts is the generation of streamwise vorticity or secondary motion. This alters the character of the flow and is a source of loss. The generation of one class of secondary flow in a bend may be interpreted as the result of a transverse or centrifugal pressure gradient, proportional to $\rho U^2/R$, being created as flow of mainstream velocity U passes round a bend of mean radius R: the secondary flow is formed because the fluid near the flow axis, establishes the radial pressure field and the lower velocity in the boundary layer at the side walls is continually forced round toward the inner wall, and in doing so is continually retarded. This type of secondary flow is classed as pressure driven secondary flow.

Flow in S-shaped ducts is further complicated by the fact that the secondary motion generation at the first bend is not automatically cancelled out at the second bend; the re-direction of pressure gradients because of the second bend not only makes the overall flow very complex but also causes additional increase in growth of the viscous region and hence increase in total pressure loss.

Squire, Winter and Hawthorne (1950-51) described the generation of secondary flow in flow through curved passages as an inviscid process given an initial boundary layer of thickness δ (i.e. an initial cross-stream vorticity). Consider a duct bend of circular cross section and the associated coordinate systems shown in Fig. 1-2. The production of streamwise vorticity ω_s from the cross-stream vorticity ω in the approaching flow can be approximated by the formula :

$$\omega_s = -2 \alpha \omega$$

The equation relates the magnitude and direction of the streamwise vorticity to the existing cross-stream vorticity when the flow is turned through an angle α.

It is however obvious that Hawthorne's analysis is not able to describe the flow process adjacent to the wall where viscous effects dominate and contemporary crossflow models for pressure driven secondary flows of for example Mager (1952), Johnston (1960) and Pilatis (1986) are more suitable.

Streamwise vorticities of the second kind (Prandtl 1952), such as the formation of secondary currents inside a developing turbulent boundary layer and a corner turbulent boundary layer are caused by the non-uniformities in wall turbulence. Such flows are better described by the analysis of Perkins (1970).

Aircraft intakes operating efficiently at low incidence have thin turbulent boundary layers at entry. Hence there is a large core flow region which could be considered to be inviscid. Therefore, work on bends in fully developed pipe flows, by for example Ward Smith (1963) and Rowe (1970), is not quantitatively relevant but nevertheless gives insight into some features of flow in S-shaped intake ducts.

Previous work on S-shaped intake ducts consists largely of unpublished work at aerospace firms. Their work mainly centres on engine face total pressure recovery measurements while little attention is paid to the study of the development of the boundary layer inside the duct which is a prime feature in determining the intake duct performance.

The first published work on experimental studies of flow in S-shaped intake ducts is by Bansod & Bradshaw (1972). They presented measurements of total pressure, static pressure, surface shear and yaw angle in the flow through several 22.5-22.5 degree circular S-shaped ducts (dorsal type) of constant area, each with a thin turbulent boundary layer and a Mach number of around 0.13 at entry. Their tests were performed with the duct at the outlet of a blow-down rig. They discussed the generation of secondary flow at the bends and were able to explain that the region of low total pressure at the lower half of the S-duct outlet (engine face) is due to the expulsion of boundary layer fluid by a pair of contra-rotating vortices in the boundary layer. This is influenced by the interaction between the streamwise vorticity generated in the first bend and the local favourable streamwise pressure gradient in the second bend region.

Taylor et al (1982-84) carried out measurements on two constant area 22.5-22.5 degree S-shaped ducts, one of circular and the other of square shape, each with a thin turbulent boundary layer at entry. Their experiments were conducted using a water tunnel and with the test duct as part of the circuit. Laser-Doppler velocimetry was used to obtain the data. In addition to mean flow data, turbulence data were also presented. Their findings for both ducts are in general similar to that of Bansod & Bradshaw but the secondary flow everywhere in the duct and the total pressure distortion at the outlet are less prominent because of the relatively mild bend curvature and small offset of their ducts; the difference in the results between the two ducts could however be used to highlight the effect of different cross-sectional shape on flow in S-ducts. Perhaps an additional feature in the square section duct is the generation of secondary flow of the second kind in the corner regions which are supported by the anistropy of the turbulent direct stresses. Although the measured data of Taylor do not have enough resolution for the details to be elucidated, their presence is noticeable from the unusual high turbulence and thicker boundary layer in these regions. This was also reported by the following researchers.

Guo & Seddon (1982-83) carried out investigations of flow through a rectangular S-shaped duct and an S-shaped duct with cross-sectional transition from square to circular. Their tests were carried out with the duct mounted in a low speed wind tunnel and the main objective was to investigate the effect of incidence (both pitch and yaw) on secondary flow in the duct and their work suggested that with a good intake lip design the flow structure at low incidence (up to ±10°) remains very similar to the static test cases.

The shortcomings of the aforementioned work on S-shaped ducts are that the experimental studies were mostly carried out on ducts with constant cross-sectional shape as well as constant area and the test conditions were confined to incompressible flow. Hence effects such as diffusion, and compressibility have not been studied.

A more recent experimental study has been carried out by Vakili et al (1984-85) on 30-30 degree circular S-shaped ducts of constant area and of diffusing area distributions at a higher inlet Mach number of 0.6. Measurement of flow direction, total and static pressure was by means of a five-port cone probe. It is however doubtful whether such a probe would produce reliable measurements near the wall when it was under the influence of high shear gradient. Nevertheless, results presented on the constant area duct show similar trends as in incompressible cases reported by other researchers but the data available are not useful for detailed comparison. Also reported is flow separation occurring in the circular S-duct diffuser of area ratio 1.5. The effect of separation on the pressure recovery and flow distortion at the duct outlet are discussed, but no attempt is made to identify the type of separation encountered.

Although all the previous work surveyed above presented measurements within the viscous region, there have been no serious attempts on near wall measurement inside the boundary layer. The general crossflow profile within the boundary layer produced by the transverse pressure gradient in this type of internal flow has never been clear. Therefore, experimental studies on this basis form the major theme of the present work.

Work presented in this thesis is of flow measurements made in S-shaped intake duct diffusers designed for rear mounted gas turbine engines in both missiles and aircraft applications. These designs are intended for ventral type inlet installation. The ducts possess internal features more fully representative of a typical aircraft installation namely with cross-sectional shape transition, from oblate to circular, with area increase and annular rather than circular entry at the engine face. Details of the duct geometries are given in Chapter 2. The present investigation was made contemporaneously with the early stages of an experimental programme of research on S-shaped intakes being made by British Aerospace (Hatfield) in association with the Royal Aerospace Establishment (Bedford). The work was aimed at both fundamental understanding of the flows and at establishing test data for the prediction methods. Tests were performed at throat Mach numbers of nominally 0.15 and 0.60 and in the unit Reynolds number range of $3x10^6/m$ - $2x10^7/m$ for three different ducts each having different upstream bends but common downstream bend geometries. Detailed boundary layer surveys were made using a shear layer probe and a three-port Conrad probe to establish plane of symmetry growth of the viscous region and the extent of three-dimensionality away from the

plane of symmetry, respectively. Data are presented both in the form of velocity profiles - streamwise and crossflow - and integral thicknesses. In addition, surface pressure fields are presented. Engine face distortion may be assessed from outlet flow surveys made by traversing the boundary layer and core region. Flow visualization was recorded using surface oil flow techniques. Detailed evidence is presented indicating a firm trend towards three-dimensional separation as the upstream bend is increased in severity. For the most extreme case considered large regions of separated flow occur, embodying complex three-dimensional features, and topological analysis was carried out on the recorded surface oil flow pattern to construct the separating flow structure. Clear correlations are also established between flow visualization results and flow measurements leading to better understanding of the effects of duct geometry on flow quality. Finally, experimental data for two of the ducts were used to evaluate the prediction method developed by successive workers at the University of Salford. It is considered that the work described in this thesis forms a significant contribution to the design of efficient subsonic diffusers for air-breathing propulsion systems.

DORSAL

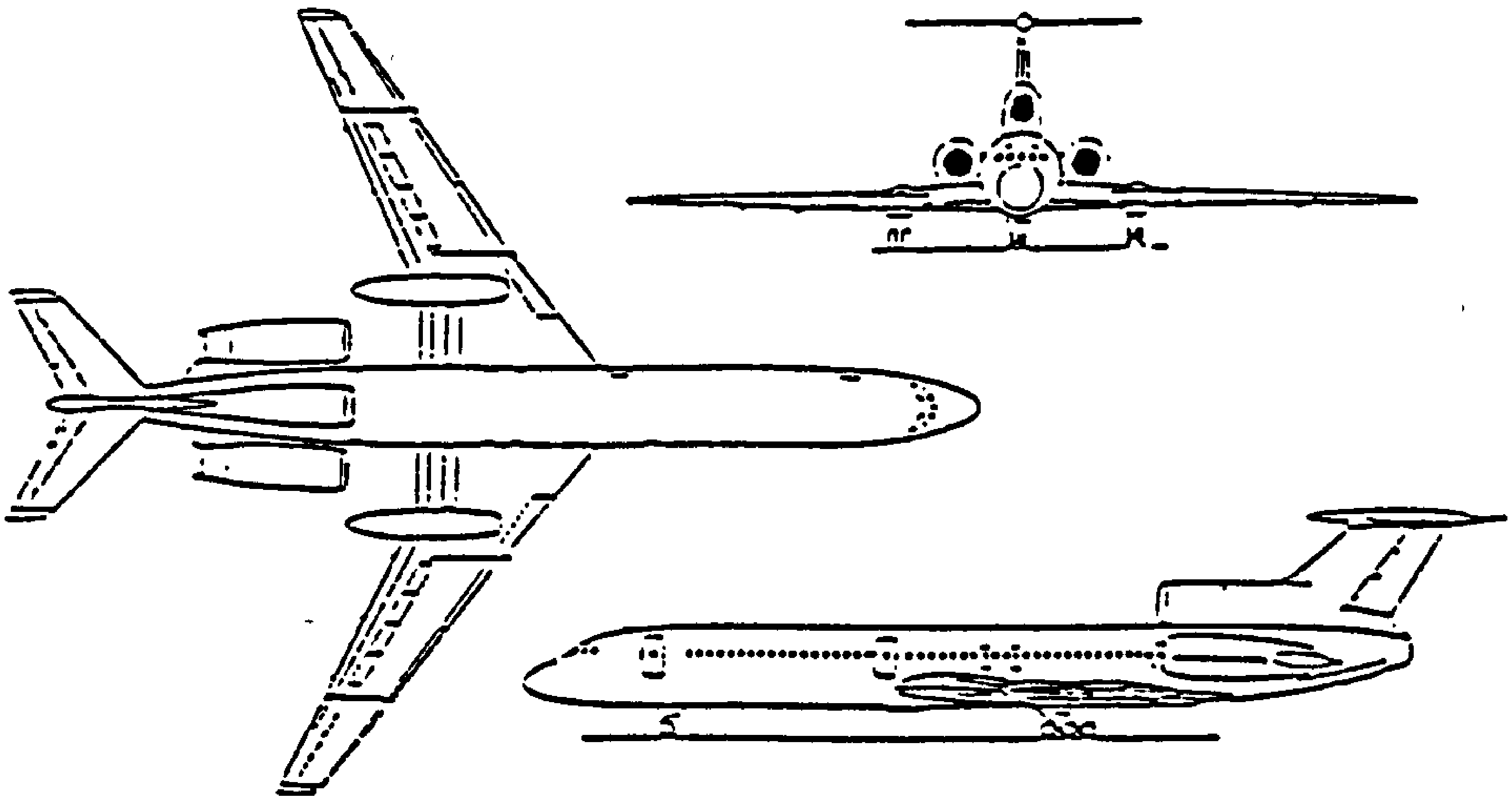

Tupolev Tu-154M medium range three-turbofan transport aircraft (*Pilot Press*)

WING-ROOT

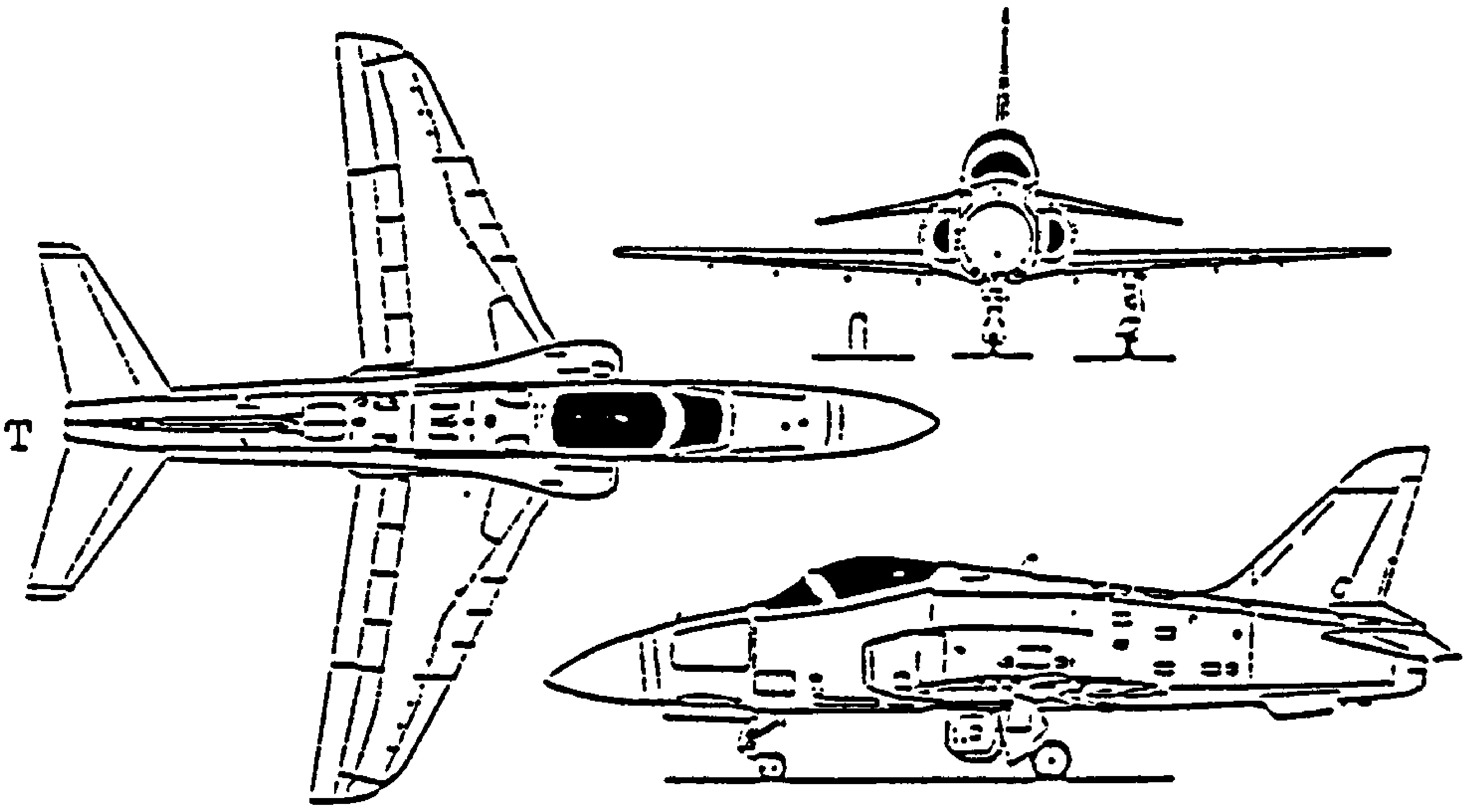

Three-view drawing of the single-seat Hawk 200 Series (*Pilot Press*)

VENTRAL

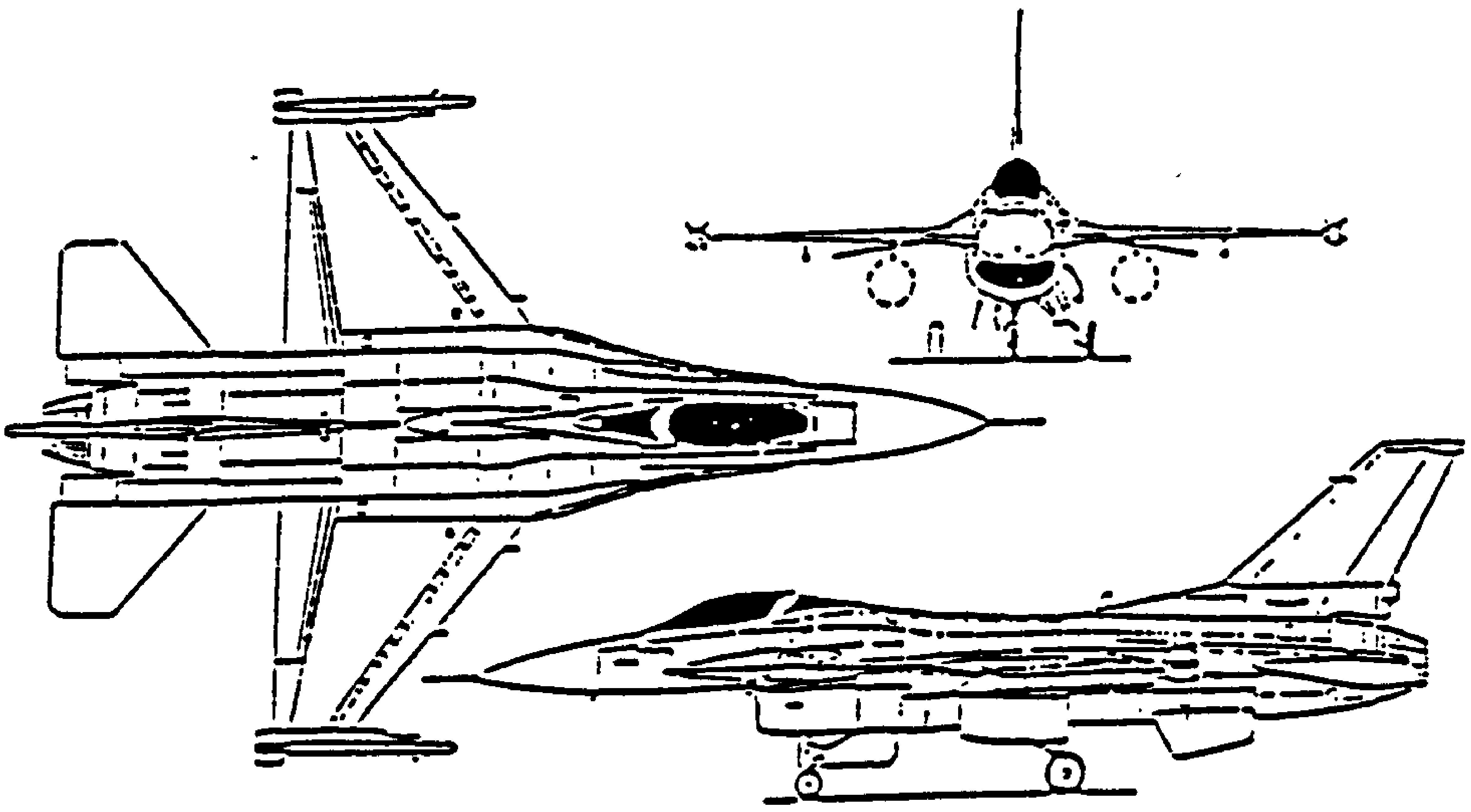

Three-view drawing of General Dynamics F-16C Fighting Falcon (*Pilot Press*)

FIG. 1-1 TYPES OF S-SHAPED INTAKE AND AIRFRAME INTEGRATIONS

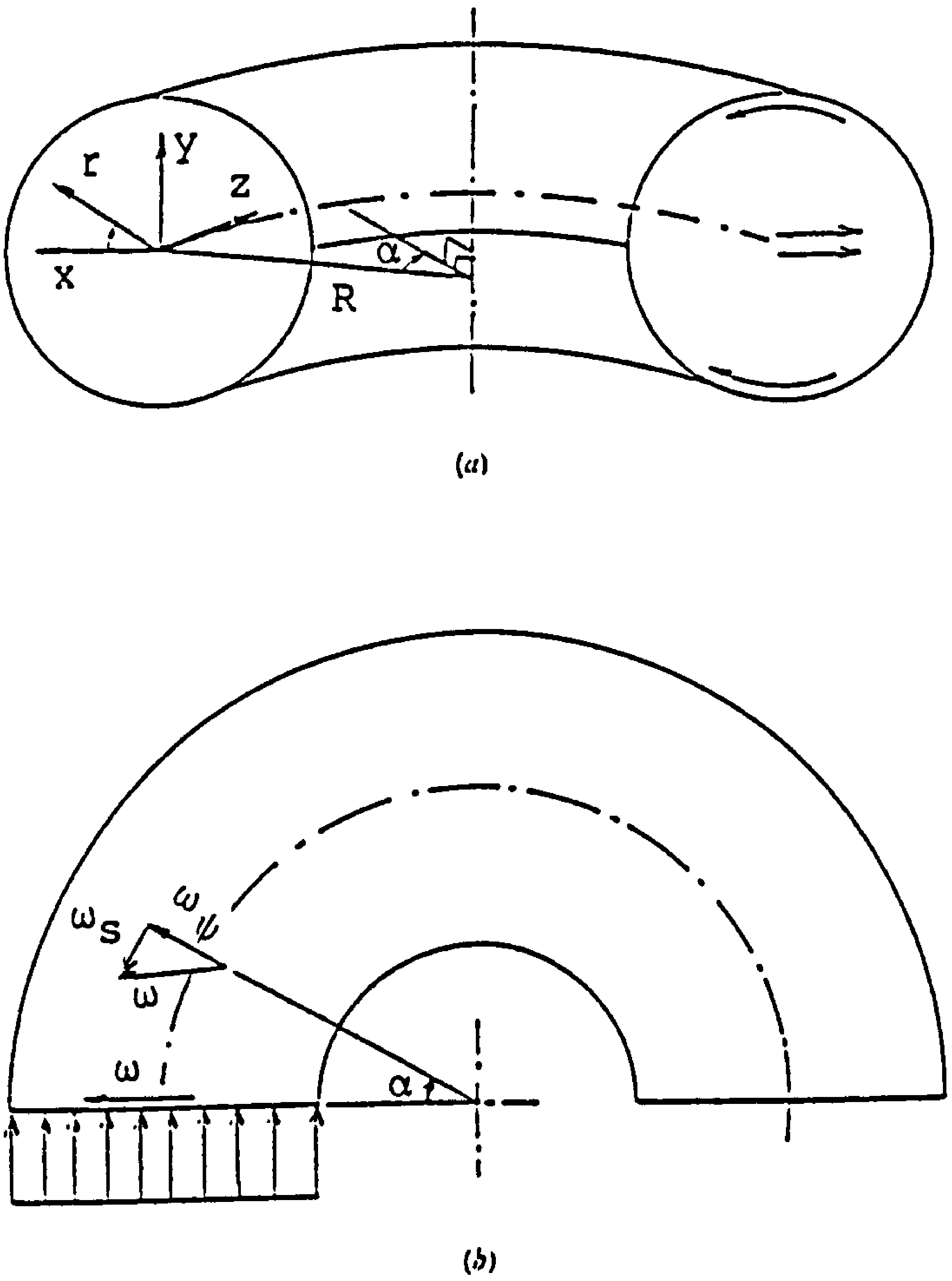

FIG. 1-2

(a) CO-ORDINATE SYSTEMS.

(b) TRANSPORT OF A VORTEX LINE
IN THE LOWER HALF OF THE DUCT.

CHAPTER 2

EXPERIMENTAL APPARATUS

CHAPTER 2 EXPERIMENTAL APPARATUS

2.1 S-shaped intake ducts

2.1.1 Historical background

The three S-shaped intake ducts investigated in the this work were supplied by the Dynamics Group of the Hatfield Division of the British Aerospace plc.

The three ducts were of designations J, M and N. They belonged to a family of six. This family of ducts was evolved during the Project Definition phases of a contemporary air breathing missile project [B22]. The initial aim of the project was to gain experience and attempt to obtain better performance (i.e. reduced engine face distortion and increased engine face pressure recovery) from the intake than from those S-shaped intakes currently employed in some aircraft and missiles.

Ducts J, M and N possess geometrical features that highlight the evolution of the family during the project and hence were selected for further detailed investigations.

2.1.2 Ducts general features and geometries

The ducts were moulded from glass reinforced epoxy resin, with black high-gloss finish inside bore and wall thicknesses of nominally 8mm; the tolerance on bore dimensions was ±0.25mm.

Figures 2-1 to 2-3 show the duct geometries for J, M and N and their area distributions. The duct profile coordinates are shown in the corresponding tables.

The three ducts have the following common features. The length of each duct is 555.0mm, the throat is defined as X=0mm and the engine face is located at X=555.0mm. The throat has an oblate shape of 93.16mm high and 164.94 wide. The engine face has a circular cross section of 206.63mm in diameter. The engine face centre bullet starts at X=412.0mm and has a diameter of 114.0mm. The overall area ratio between the throat and engine face is 1.73; however the diffusion up to the engine bullet has an effective area ratio of 2. The mean radius of curvature of the downstream bend is 323.0mm.

Each duct differs by having different maximum centre line angles, different lengths of taper between bends and a different upstream bend geometry. These geometrical parameters are summarized in the following table.

Duct	J	M	N
Max. centre line angle (deg.)	29.40	26.76	28.10
Length of taper (mm)	288.0	435.0	327.5
Upstream bend mean radius of curvature (mm)	191.0	∞	240.0

Each duct was fully instrumented. There were originally 61 static tappings distributed around and along the duct; 24 extra static tappings were created mainly in the region of the downstream bend (i.e. the bend located just upstream of the engine face) for circumferential wall pressure measurements; the static tappings were made from 1mm bore x 0.4mm hypodermic tubes mounted normal to the duct bore. For boundary layer traversing, 19 boundary layer probe guides were mounted along the upper and lower walls of the duct; the probe guides were made from standard brass adapters and were mounted in such a way that the probe traversed normal to the surface at the measuring points. Locations of the static tappings and boundary layer traversing stations on each duct are indicated in Chapter 4.

A bellmouth (Fig. 2-4) was supplied to be installed at the duct inlet to ensure good entry flow conditions such that an aircraft intake could be simulated.

A circular duct of length 275.0mm and containing a centre body (Fig. 2-5) was supplied to be installed at the duct outlet; the centre body was used to simulate the engine face centre bullet.

Further additions (see later sections) included a transition duct at the duct inlet for turbulent boundary layer development and the engine face traversing ring for a detailed boundary layer survey at the engine face, which supplement the eight arm 40 probe total pressure rake supplied.

2.2 Test rig

2.2.1 Design and construction

Design and construction of the test rig for S-shaped intake duct research took place in the Aeronautical and Mechanical Engineering Department's aerodynamics laboratory. The design of the test rig was largely pre-determined by the intake ducts being tested and by making use of standard equipment available in the laboratory.

Figure 2-6 shows the lay-out of the test rig. It is based on a sucking arrangement which consists of a fan, driven by a 22.5kw electric motor, and a conical diffuser which links the intake duct to the fan. In addition to the use of the bellmouth to ensure good entry flow conditions, a mobile filter box which covers the entrance region was used to eliminate any inlet disturbance.

2.2.2 Fan characteristic and diffuser design

The fan used was of centrifugal type and was housed inside a volute casing driven by a 22.5kW electric motor. It was capable of producing a maximum pressure head of 550mm of water and a volume flow rate well in excess of 5 m^3/s. Control of the air flow was by means of a valve located at the fan inlet. Air was exhausted to atmosphere through a 90° bend into a square duct with a circular final section surrounded by silencing material. The rotational speed of the fan was checked by an optical revolution counter, and did not vary by more than 0.4% of the design speed throughout the test operations. The fan characteristic is shown in Fig. 2-7.

A conical diffuser of 8.27° degree included angle, length to inlet diameter ratio of 7.55 and an area ratio of 4.38 was designed to fit between the fan and the intake duct; it was capable of a static pressure recovery above 70% throughout the test speeds range (Fig. 2-8). The diffuser was made out of sheet metal and was manufactured by the Departmental workshop.

2.2.3 Problem with ground vortex

Owing to the problem of severe flow unsteadiness, initial attempts at duct flow measurement using the test rig were not successful. It was later discovered, by means of smoke visualization, that the problem was mainly caused by the inhalation of a ground vortex. This phenomenon is illustrated in Fig. 2-9a; when air is sucked into the duct, on the ground a moment of momentum is exerted on a point sink flow by a lateral disturbance or wind, resulting in the formation of an eddy stream known as a ground vortex. Motycka et al (1975) pointed out that there exists a critical height ($(H/D)_{cr}$), called the ground vortex living height, between the duct inlet and the ground, well beyond which the duct inlet must have to be positioned in order that the ground vortex ceases to be 'harmful'. The living height is a function of inlet Mach number, lateral wind speed, ambient pressure and temperature. Fig. 2-9b shows typical variations of $(H/D)_{cr}$ with inlet Mach number.

The lateral disturbance on the test rig was most likely to be the rig exhaust back into the laboratory, and it was believed that the distance between the duct inlet and the ground was below the living height of the ground vortex. Since it was not feasible to increase the distance of the rig from the ground, the problem was finally solved by the use of a mobile filter box, which covered the entrance region of the duct during test. The filter box is of size $1m^3$ and is covered with foam sheet 6mm thick as filtering material; the foam sheet has a resistance coefficient of nominally 2.8, which is adequate to eliminate any inlet disturbance [A11]. The use of the filter box was seen to have drastically reduced the flow unsteadiness and considerably improved the quality of flow delivered by the test rig.

2.2.4 Calibration duct

A calibration duct was designed and built in the laboratory for calibration of the multi-tube probe for three-dimensional boundary layer measurement (Fig. 2-10). The duct was designed to be used with the test rig described earlier and hence gave a calibration Mach number range of up to 0.65. The duct was also designed to allow the traversing device for probe calibration to be mounted on both walls of the channel and hence enable the zero error of the probe to be determined.

Figure 2-11 shows the traversing device used for probe calibration, which is the standard equipment available in the laboratory. The device incorporated an anti-backlash gearing system which offers an angular resolution of 0.25° and hence allowed high precison angular positioning of the probe.

2.3 Instrumentation

A Qinling CYG03 differential pressure transducer was used to convert pressure difference into an electrical signal. It had a range of $\pm 35 kN/m^2$, hysteresis of 0.07%FS, non-linearity of ±0.05%FS and repeatability of 0.05%FS. Both sensitivity and zero shift due to temperature were negligible under laboratory conditions. The transducer required an excitation current of

6.2mA and gave a maximum output of 86mV; the excitation current was supplied by a constant current source unit and the output voltage was further amplified by the amplifier of a signal conditioner. Linearity and repeatability of the transducer were checked prior to use and periodically whilst in use.

Two 50cm manometers, one mercury and one paraffin, were used to check and calibrate the pressure transducer; the paraffin manometer was used for the lower end of the range and the mercury manometer was used for the middle to upper end of the range of the transducer. The transducer calibration graphs are shown in Fig. 2-12.

Paraffin and mercury multi-manometers were used to monitor the surface pressures at the duct throat at low and high inlet Mach numbers respectively.

The laboratory's mercury barometer and thermometer were used to measure the laboratory pressure and temperature.

For duct plane of symmetry boundary layer measurements, a single tube probe of 0.55mm diameter with an inner to outer diameter ratio of 0.6 was used. An offset design (Fig. 2-13) had to be adopted in order to avoid the existing tubings from the static tappings, which were embedded in the wall along the duct plane of symmetry.

For three-dimensional boundary layer measurements, a three tube Conrad probe with the two side tubes at 45° tip angle was used (Fig. 2-14); each tube in the probe had identical dimensions to the single tube probe. The probe was calibrated in the calibration duct described earlier. The method of calibration is described in Chapter 3.

Both boundary layer probes and supports were made from 0.33mm bore x 0.11mm and 2.2mm bore x 0.4mm hypodermic tubes respectively. The probe tips were at distances greater than 5 times the probe support diameter (3mm) from the supports; hence interference due to the probe supports was negligible.

A manual traversing device was designed and manufactured for boundary layer traversing. Fig. 2-15 shows a photograph of this device. It employed a hollow screwed rod (M12x1.25) 400mm long and a dial gauge of resolution 0.01mm for probe positioning; the movable parts were spring loaded such that error due to backlash was eliminated. The traversing device was used for both duct symmetry plane and three-dimensional boundary layer measurements. An electronic circuit using a light emitting diode was incorporated with the traversing device to indicate probe contact with the duct wall; the circuit was designed with an operation amplifier (IC741) to ensure high contact sensitivity.

For engine face three-dimensional boundary layer measurements, a ring was designed and manufactured to be rotatable between two specially made flanges installed at the engine face plane (Fig. 2-16). The ring was marked with graduations at 5° intervals and built with a probe guide adapter for the traversing device described above. With this design, a rotate and traverse measurement technique was adopted with only one Conrad probe hence eliminating the cost and time for calibrating a multi-yaw probe rake. This technique offers flexibility in measurement location and avoids blockage to the flow passage as is found with a multi-probe rake.

2.4 Data acquisition system

The data acquisition system (Fig. 2-17) consisted of the following units:

1. An automatic 'Scanivalve' unit which housed the pressure transducer and was controlled by a scanning controller capable of scanning pressures up to 48 channels per run at selectable time intervals from 1ms to 1000ms.

2. A signal conditioning unit providing the excitation current for the pressure transducer, low pass filtering and amplification to the transducer output signals. The amplifier provided 12 different gain settings for optimal sensitivities for low and high test speeds; the output was interfaced with a 12 bit analogue to digital (A/D) converter in the data logger.

3. A micro-processor unit which was pre-programmed to control processes such as analogue to digital conversion of the amplified transducer signals, data logging and data transfer to the computer.

The overall instrumentation error of the data acquisition system was less than 1.2%FS and the source of errors are stated as follow:

1. Pressure transducer hysteresis, non-linearity and repeatability	< 0.170%FS
2. Quantization error of the A/D converter	< 0.025%FS
3. Amplifier non-linearity	< 1.000%FS

The system was supported by the PDP11/44 computer of the Department's data processing bureau. The entire data acquisition process was monitored by a vdu console. The vdu console was equipped with a graphics facility enabling raw data to be plotted on-line for checking.

2.5 Flow visualization

A pyrotechnic smoke generator was used to generate a large quantity of smoke around the duct inlet region, this was used to visualize the ground vortex and random vortices originating from near by obstacles, which were discovered to be the cause of flow unsteadiness in the ducts.

Surface oil flow visualizations were carried out on the three ducts being tested. Mixtures of yellow fluorescent powder and clear paraffin were used; the optimum concentration was obtained after a few runs. Using a 100 watt flood lamp to illuminate the duct inside surfaces, photographs of the oil flow patterns were taken at various positions. The surface oil flow visualization provides a complete time-mean wall shear stress topology which enables flow conditions near the duct wall to be studied.

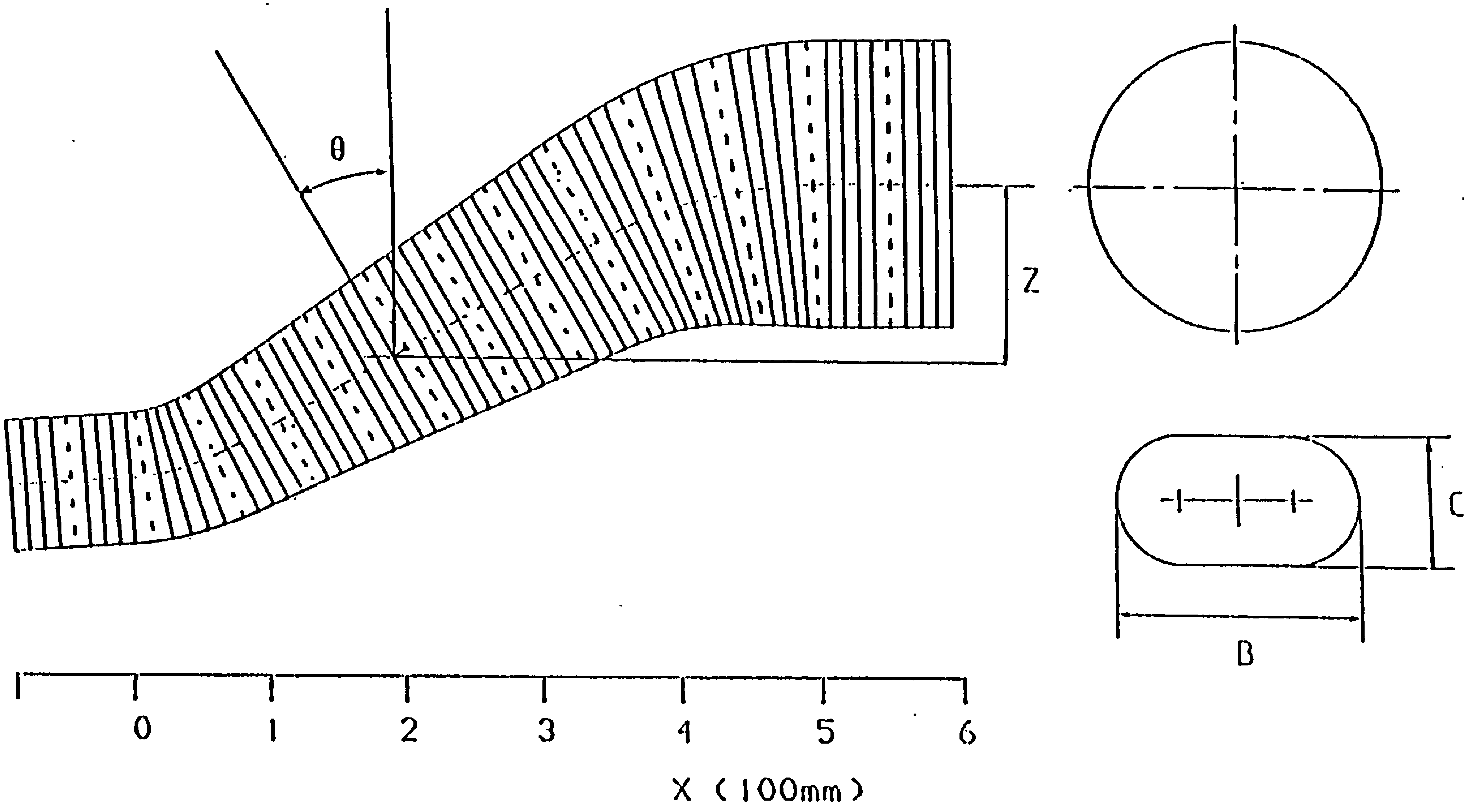

FIG. 2-1a DUCT J PROFILE

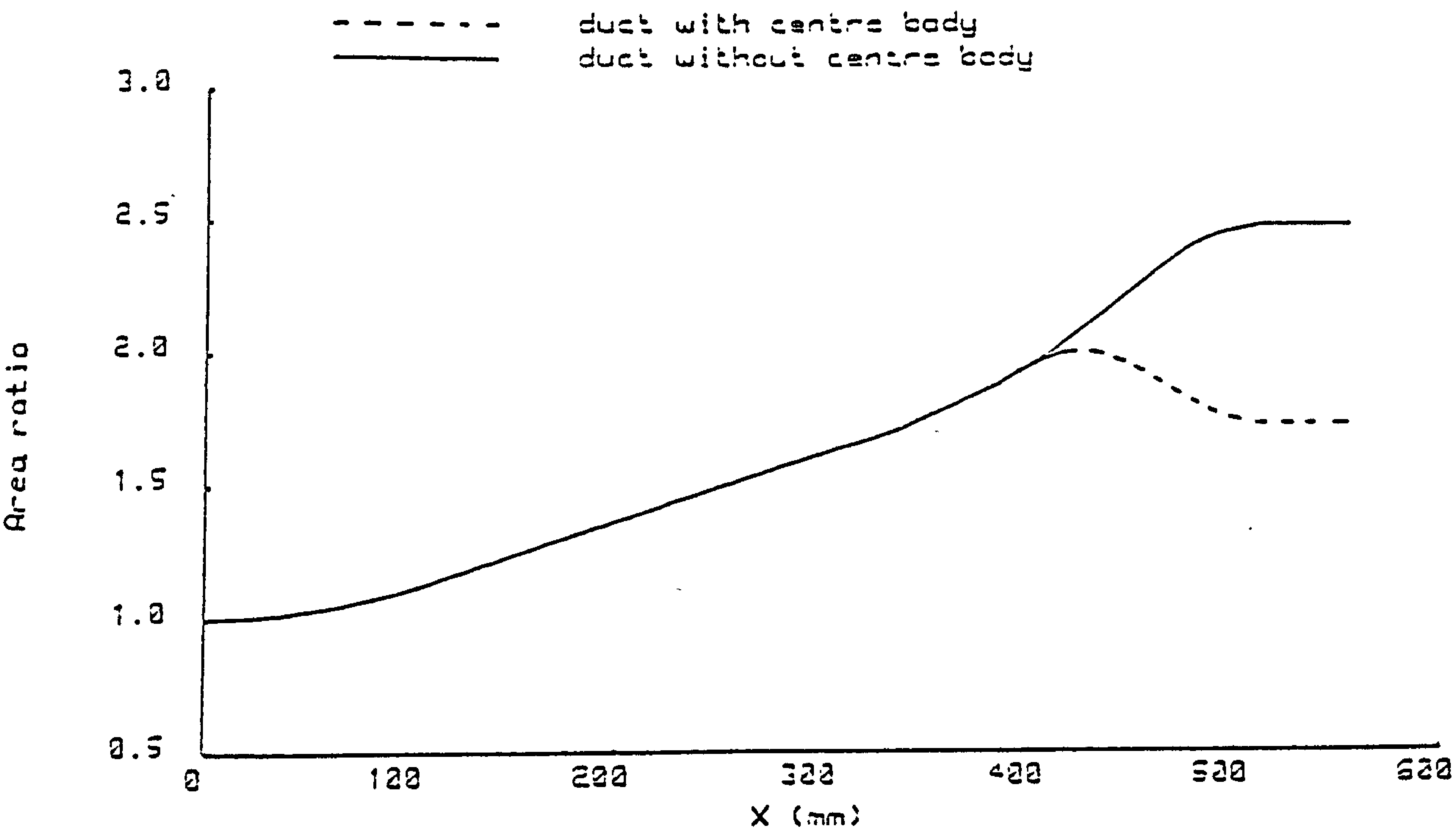

FIG. 2-1b DUCT J AREA DISTRIBUTION

X(mm)	Z(mm)	θ(deg.)	B(mm)	C(mm)
0	215.4	3.5	164.94	93.16
14.5	213.9	9.0	165.5	93.28
43.5	206.5	19.0	166.4	94.59
72.5	194.2	26.2	167.5	97.97
101.5	178.5	29.4	168.93	102.95
130.5	162.16	29.4	170.43	109.66
159.5	145.83	29.4	171.93	116.36
188.5	129.49	29.4	173.42	123.07
217.5	113.15	29.4	174.92	129.78
246.5	96.81	29.4	176.42	136.48
275.5	80.48	29.4	177.92	143.19
304.5	64.14	29.4	179.41	149.89
333.5	47.8	29.4	180.91	156.6
362.5	32.63	25.8	183.13	165.3
391.5	20.3	20.4	185.6	175.45
420.5	11.24	14.7	189.69	187.05
449.5	5.08	9.1	196.48	196.48
478.5	1.45	5.0	203.75	203.75
507.5	0	0	206.63	206.63
536.5	0	0	206.63	206.63
555.0	0	0	206.63	206.63

TABLE 2-1 DUCT J PROFILE COORDINATES

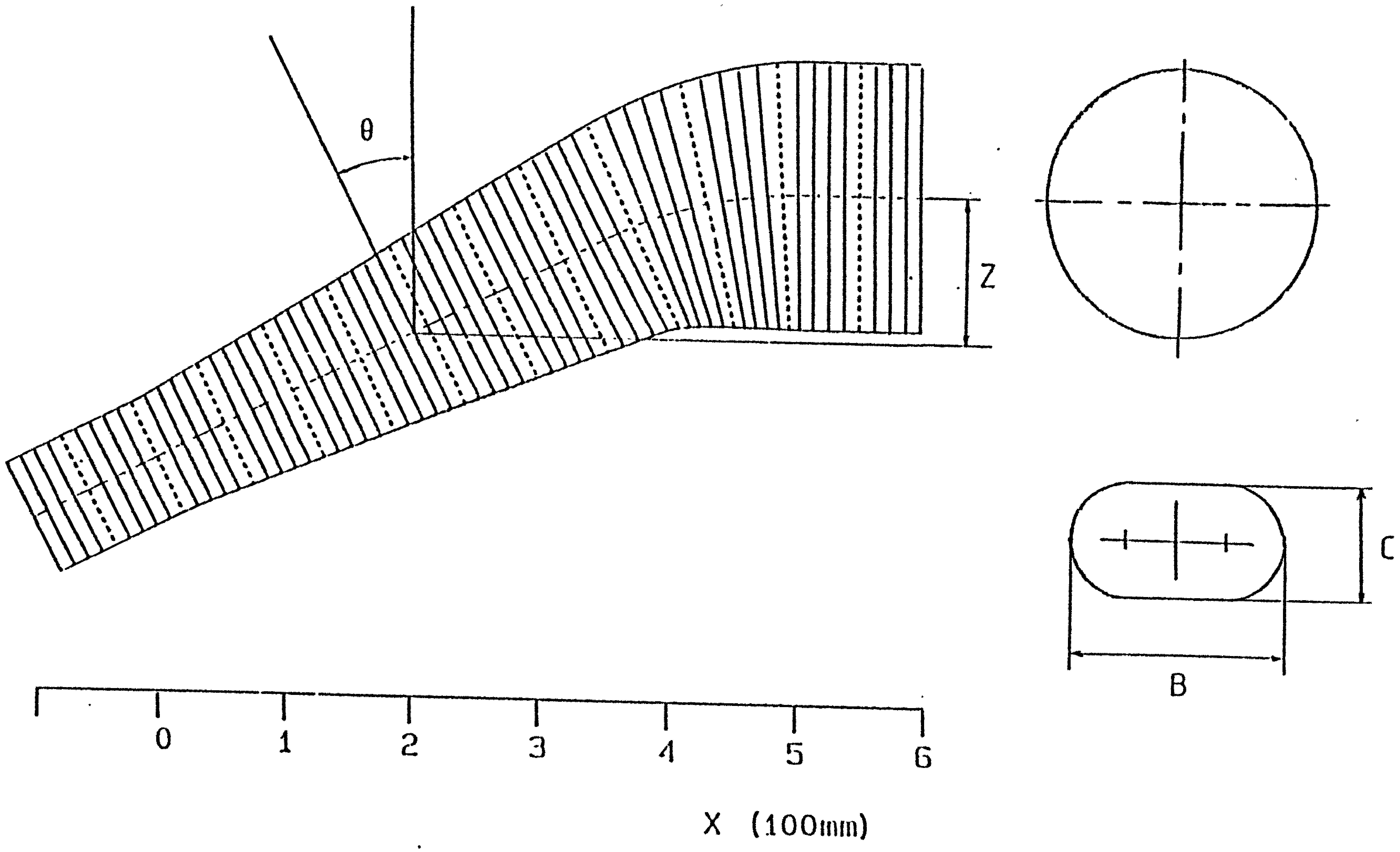

FIG. 2-2a DUCT M PROFILE

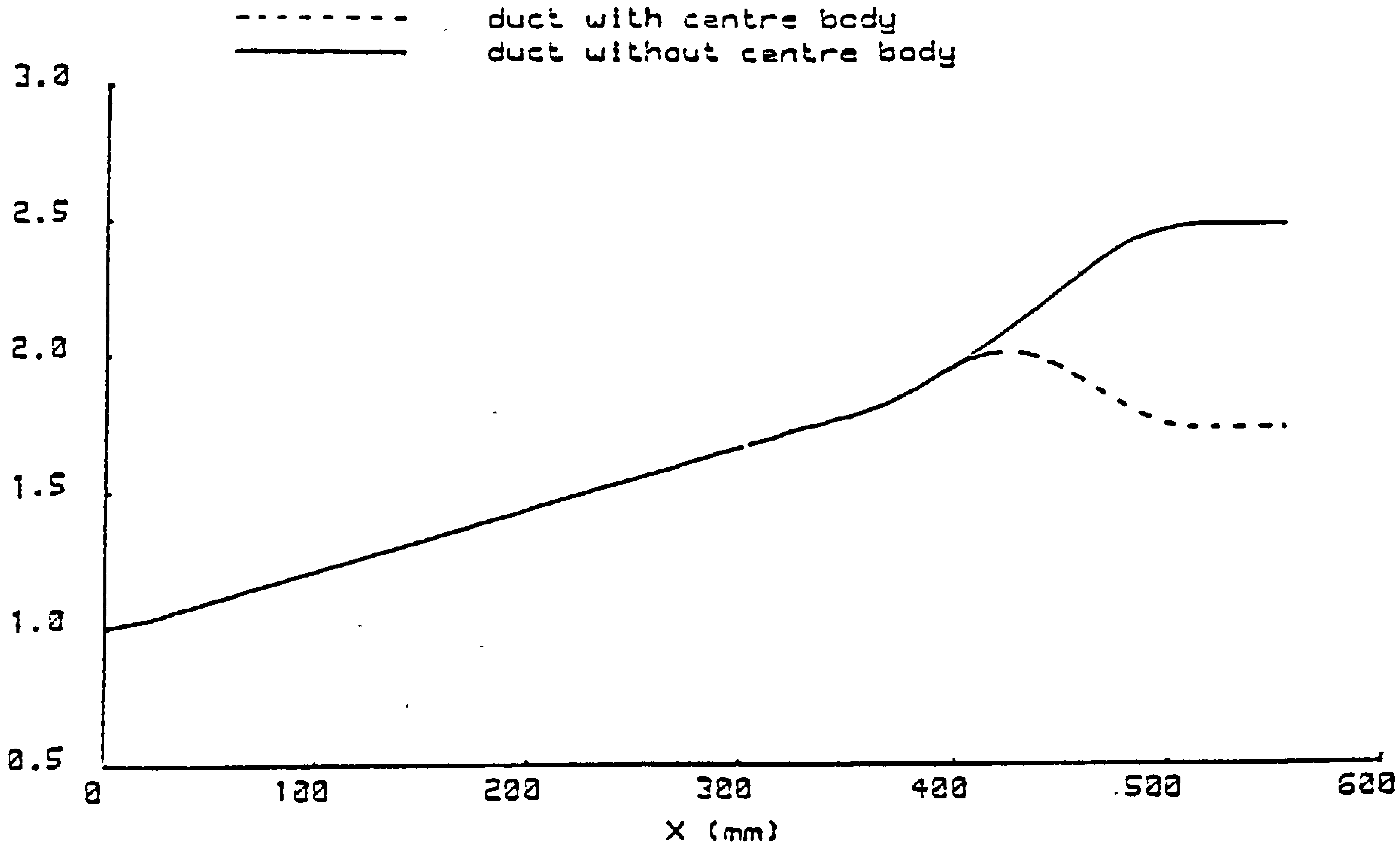

FIG. 2-2b DUCT M AREA DISTRIBUTION

X(mm)	Z(mm)	θ(deg.)	B(mm)	C(mm)
0	215. 4	26.76	164.94	93.16
14.5	208. 9	26.76	164.95	95.07
43.5	193.47	26.76	166.49	100.92
72.5	178.85	26.76	168.03	106.77
101.5	164.22	26.76	169.57	112.63
130.5	149. 6	26.76	171.11	118.48
159.5	134.98	26.76	172.65	124.33
188.5	120.36	26.76	174.19	130.18
217.5	105.74	26.76	175.73	136.04
246.5	91.12	26.76	177.27	141.89
275.5	76.49	26.76	178.81	147.74
304.5	61.87	26.76	180.35	153.59
333.5	47.25	26.76	181.89	159.45
362.5	32.63	26.76	183.13	165. 3
391.5	20. 3	20. 4	185. 6	175.45
420.5	11.24	14. 7	189.69	187.05
449.5	5.08	9. 1	196.48	196.48
478.5	1.45	5. 0	203.75	203.75
507.5	0	0	206.63	206.63
536.5	0	0	206.63	206.63
555.0	0	0	206.63	206.63

TABLE 2-2 DUCT M PROFILE COORDINATES

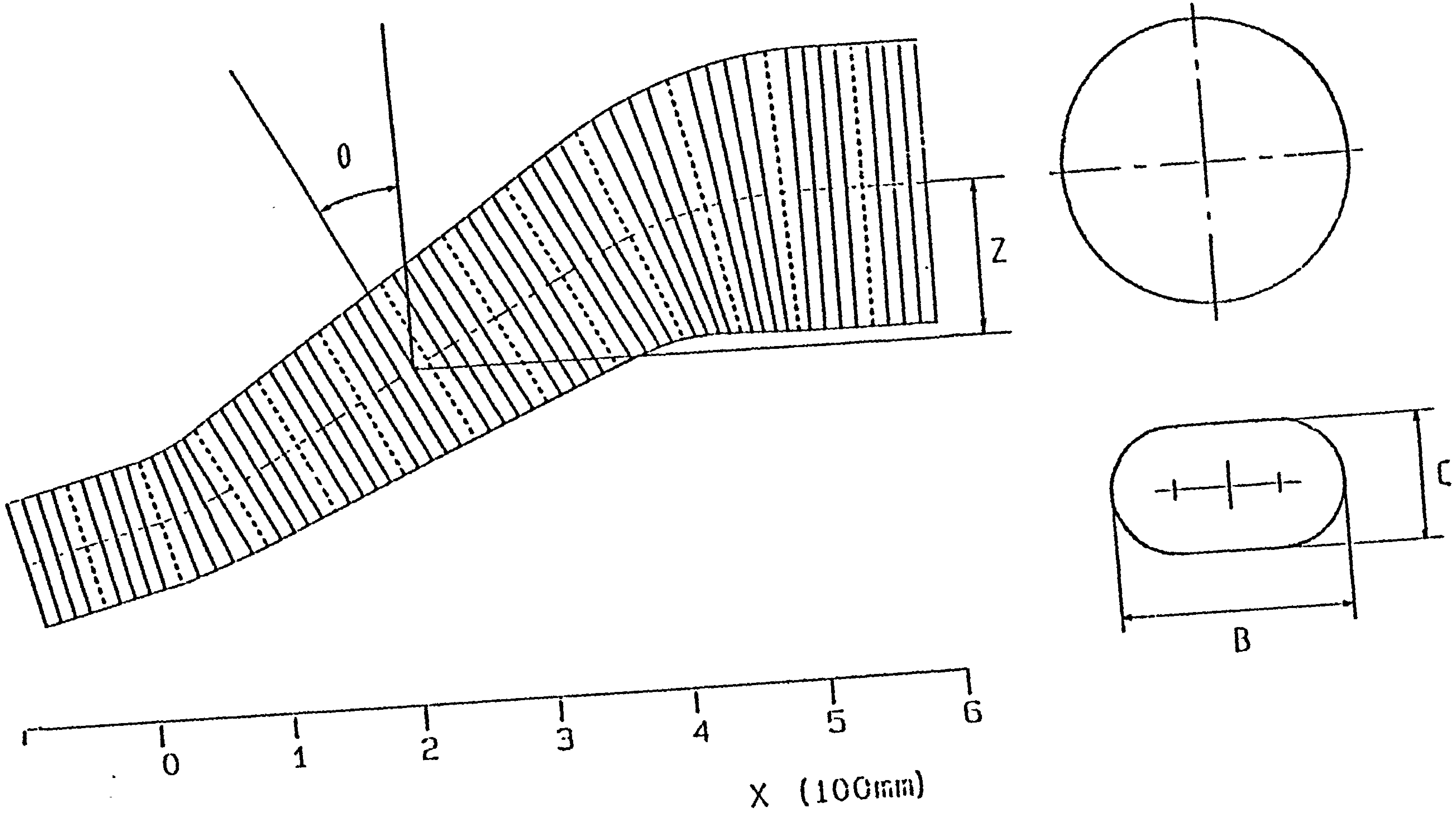

FIG. 2-3a DUCT N PROFILE

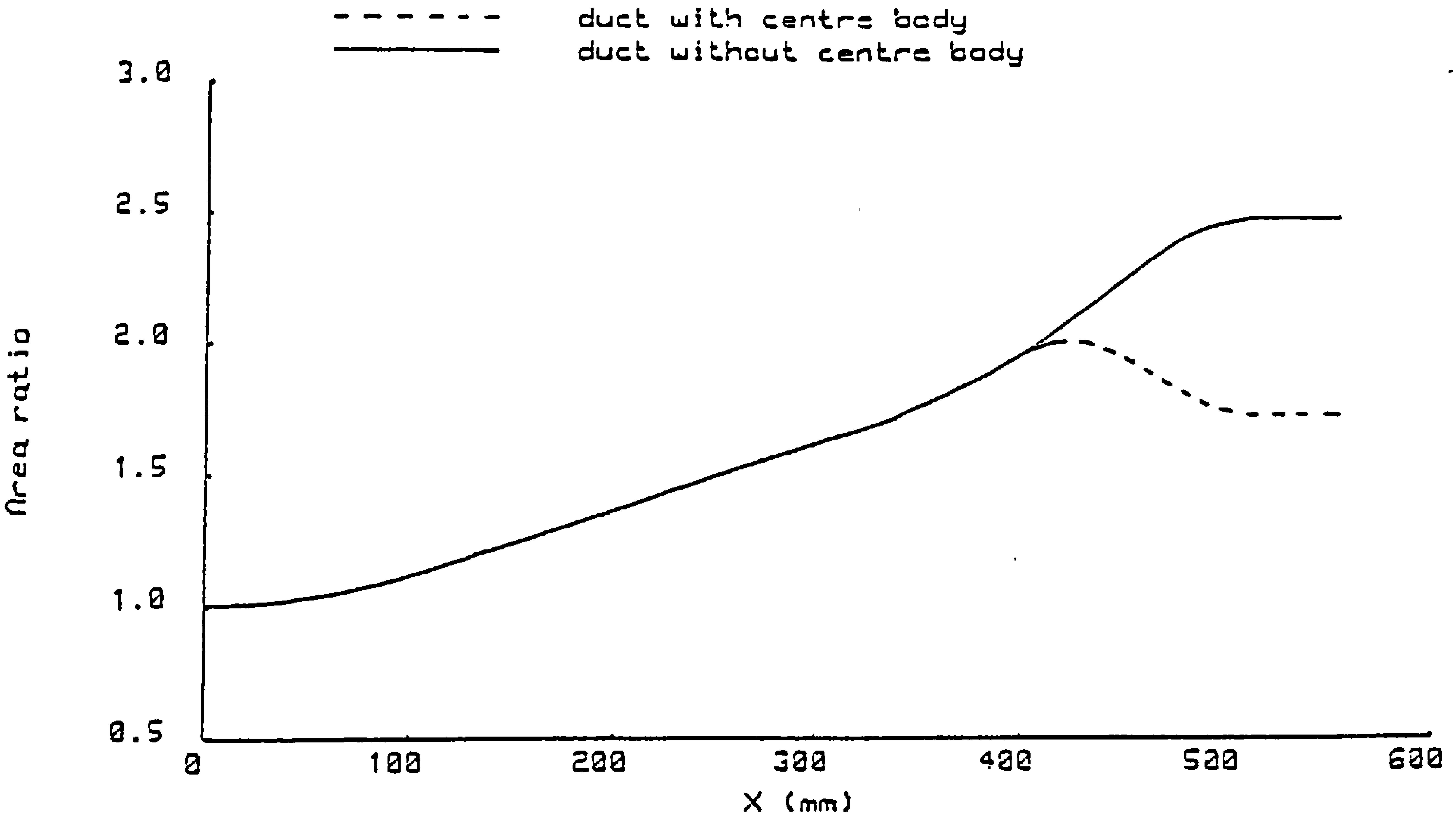

FIG. 2-3b   DUCT N AREA DISTRIBUTION

X(mm)	Z(mm)	θ(deg.)	B(mm)	C(mm)
0	216. 8	13. 0	164.94	93.16
14. 5	212. 9	16. 0	164.95	95.07
43. 5	202. 7	22. 0	166.49	100.92
72. 5	188. 3	28. 1	168.03	106.77
101. 5	173. 0	28. 1	169.57	112.63
130. 5	157. 0	28. 1	171.11	118.48
159. 5	141. 2	28. 1	172.65	124.33
188. 5	126. 0	28. 1	174.19	130.18
217. 5	110. 0	28. 1	175.73	136.04
246. 5	94. 4	28. 1	177.27	141.39
275. 5	79. 1	28. 1	178.81	147.74
304. 5	63. 5	28. 1	180.35	153.59
333. 5	47. 8	28. 1	181.89	159.45
362. 5	32.63	26.76	183.13	165. 3
391. 5	20. 3	20. 4	185. 6	175.45
420. 5	11.24	14. 7	186.69	187.05
449. 5	5.08	9. 1	196.48	196.48
478. 5	1.45	5. 0	203.75	203.75
507. 5	0	0	206.63	206.63
536. 5	0	0	206.63	206.63
555. 0	0	0	206.63	206.63

TABLE 2-3   DUCT N PROFILE COORDINATES

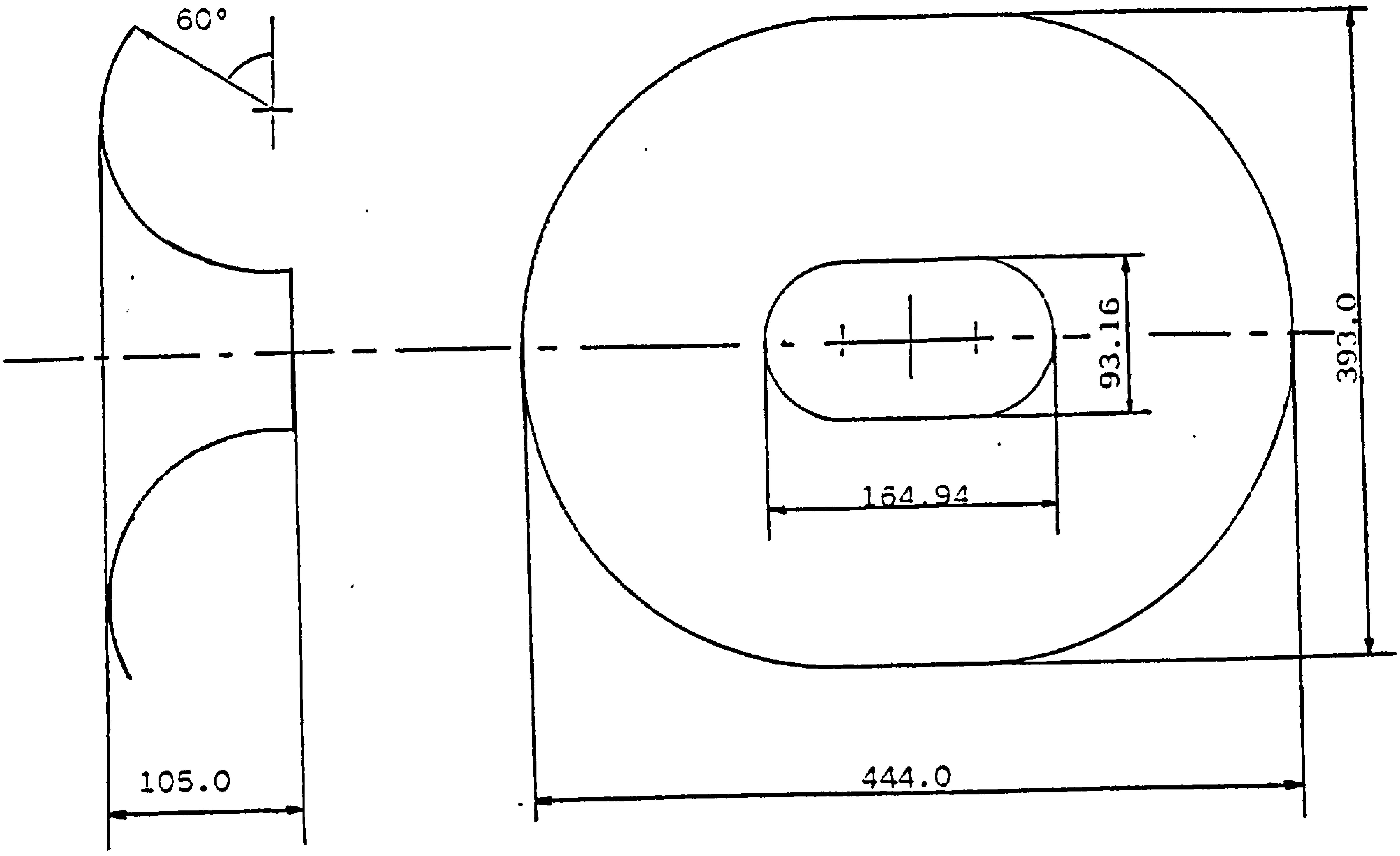

FIG. 2-4 BELLMOUTH PROFILE

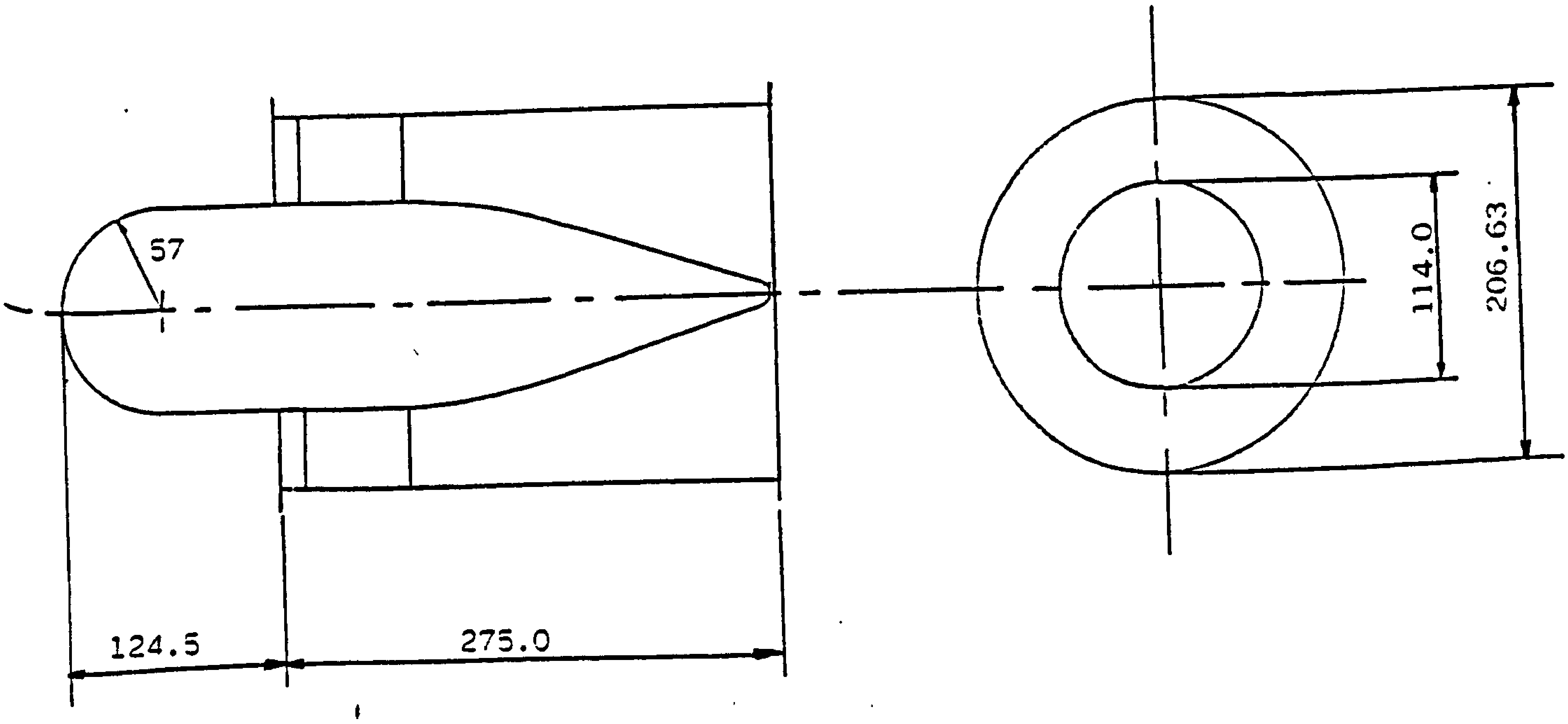

FIG. 2-5 CENTRE BODY PROFILE

ALL DIMENSIONS ARE IN mm

FIG. 2-6a TEST RIG ARRANGEMENT

SCALE 1:8

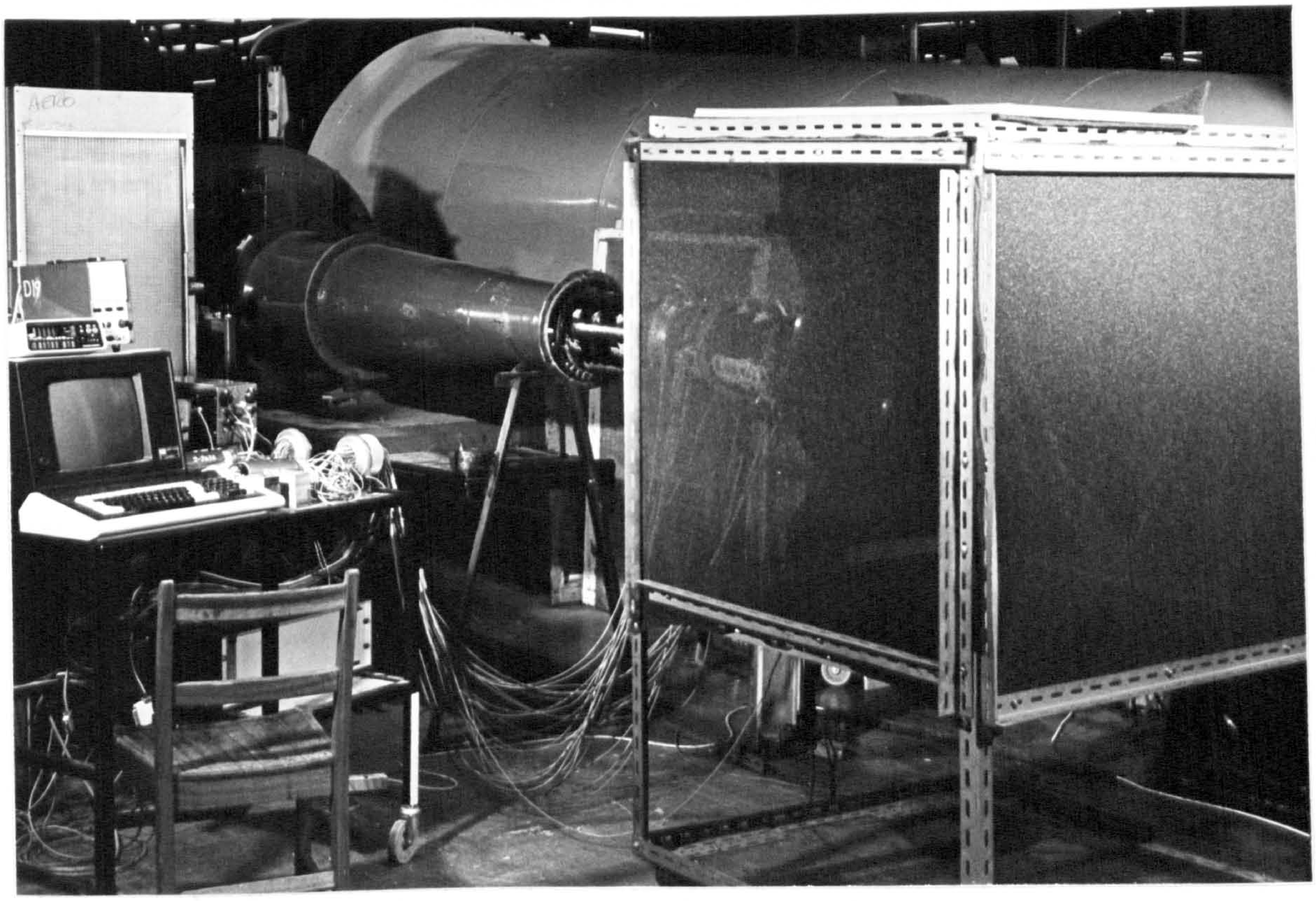

FIG. 2-6b TEST RIG WITH FILTER BOX

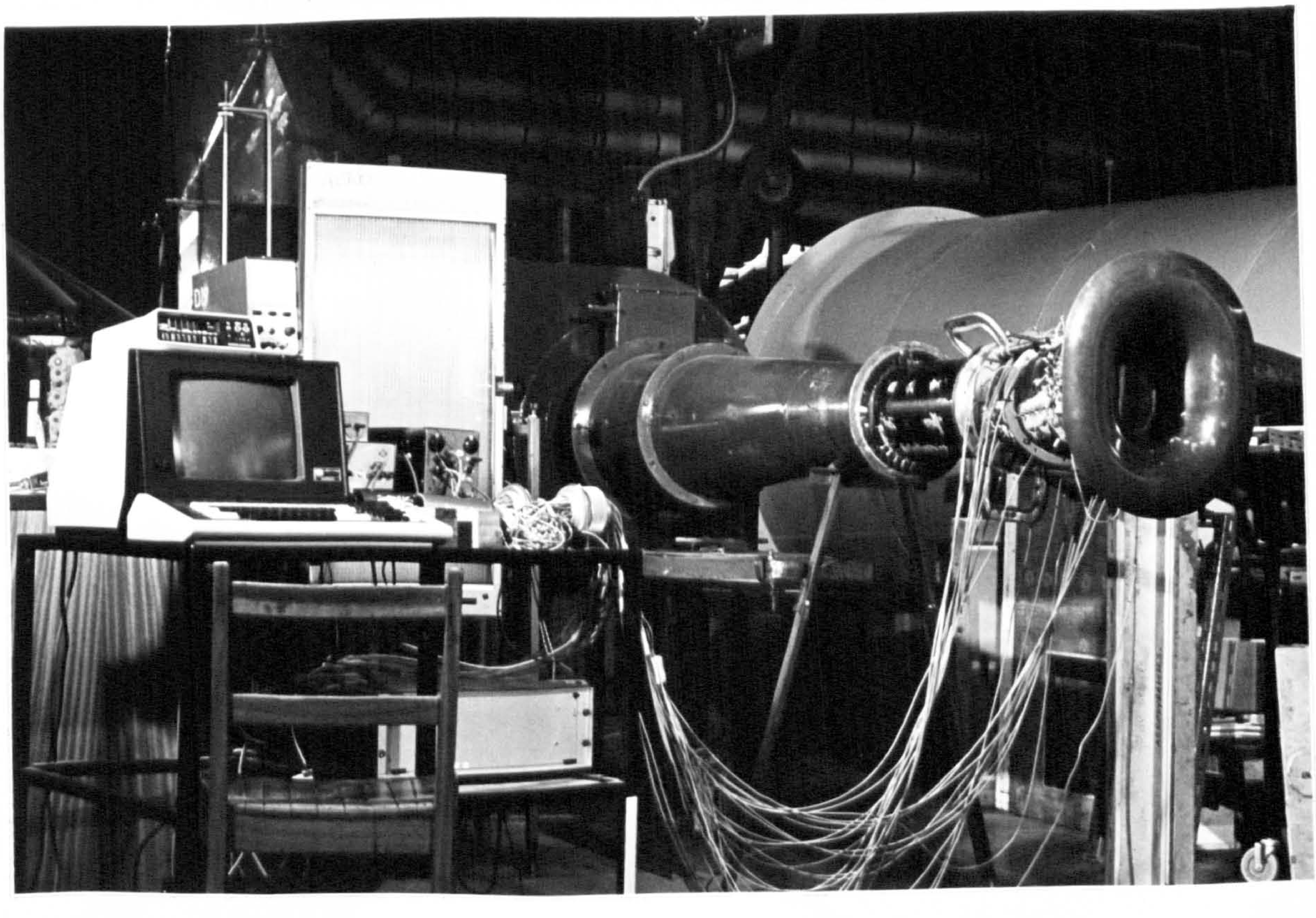

FIG. 2-6c TEST RIG WITHOUT FILTER BOX

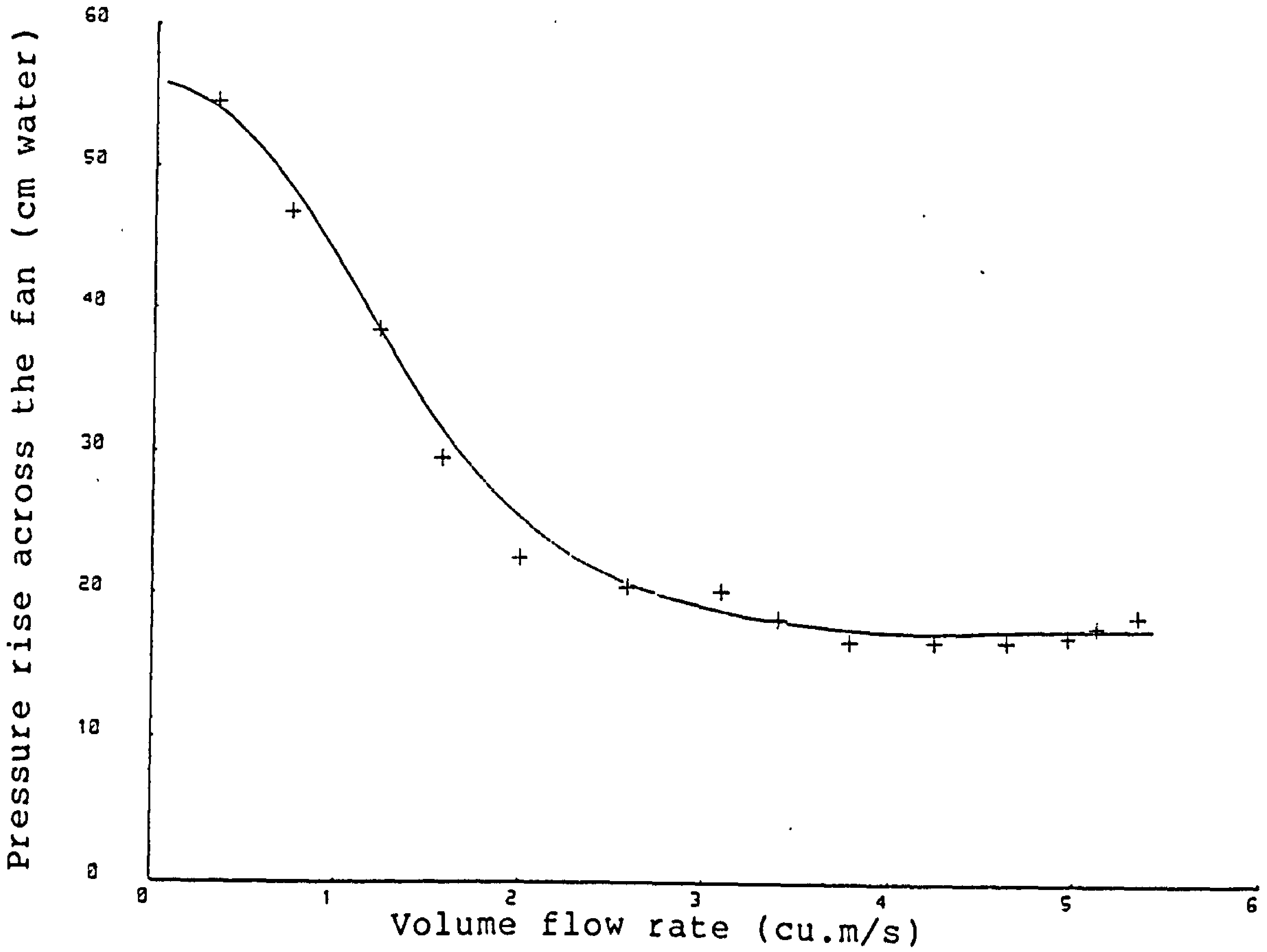

FIG. 2-7 FAN CHARACTERISTIC

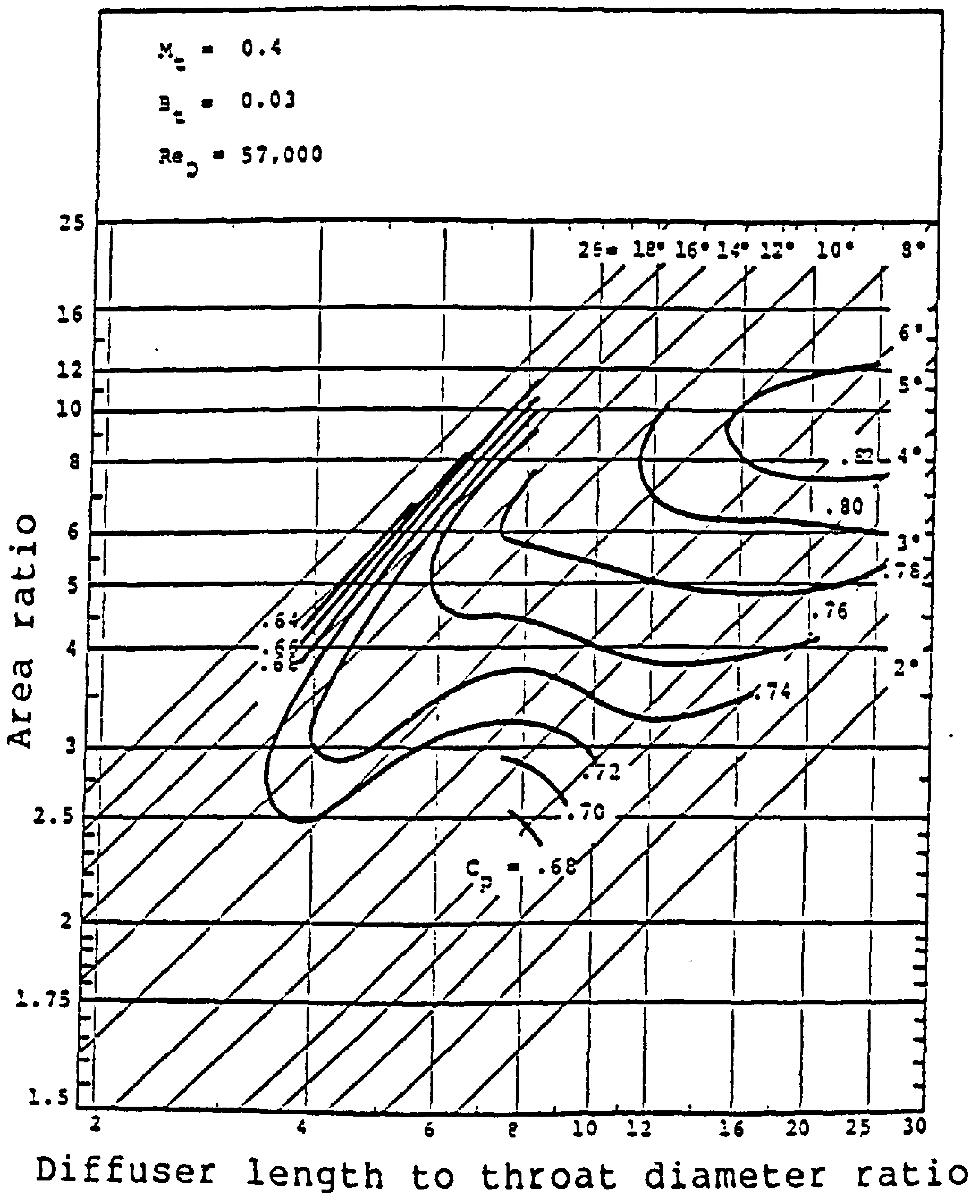

FIG. 2-8 CONICAL DIFFUSER PERFORMANCE MAP [ref.A3]
(Cp - static pressure recovery coeff.)

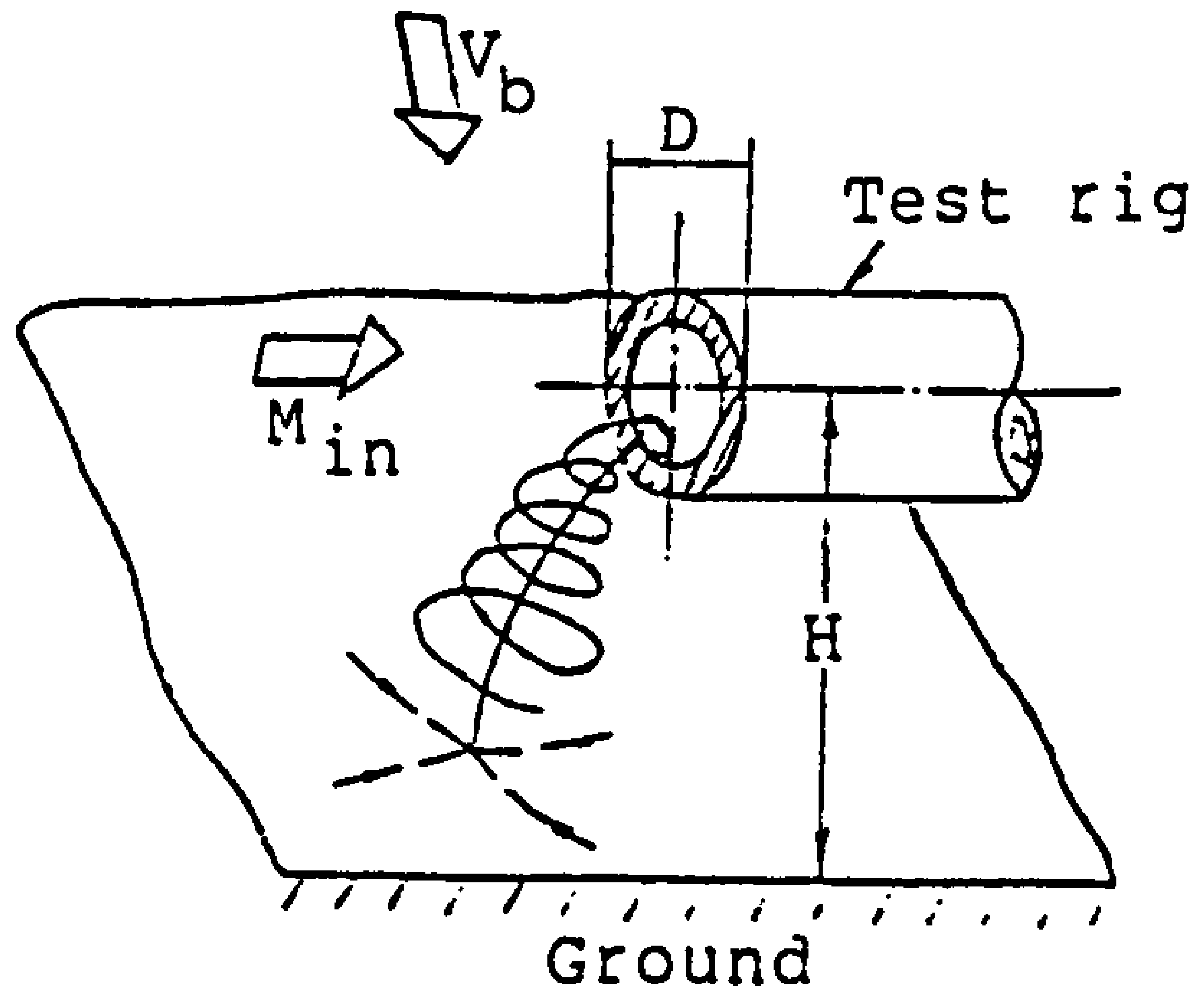

FIG. 2-9a GROUND VORTEX FORMATION

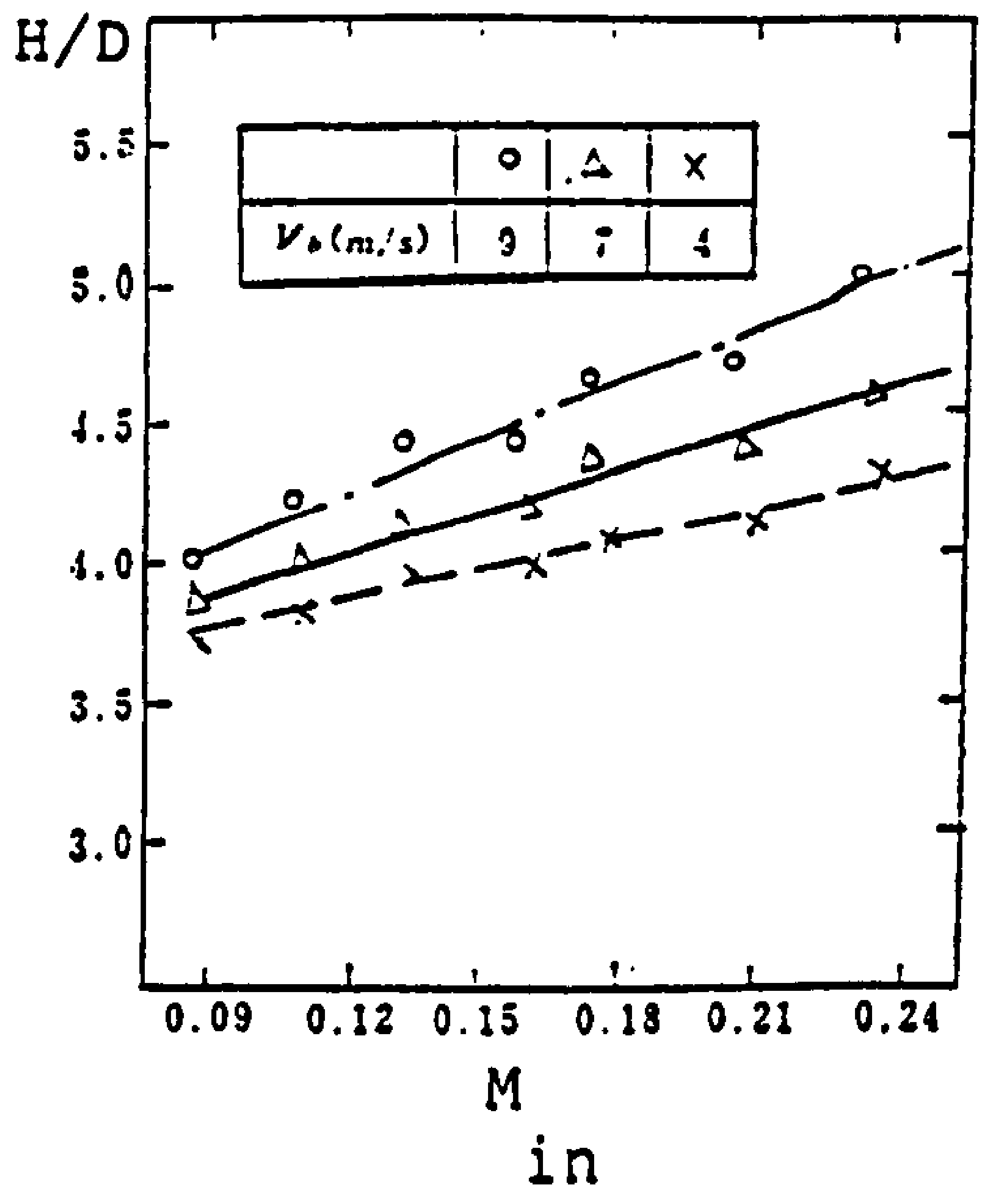

FIG. 2-9b, TYPICAL VARIATIONS OF H/D_{cr} WITH INLET MACH NO. [ref.A12]

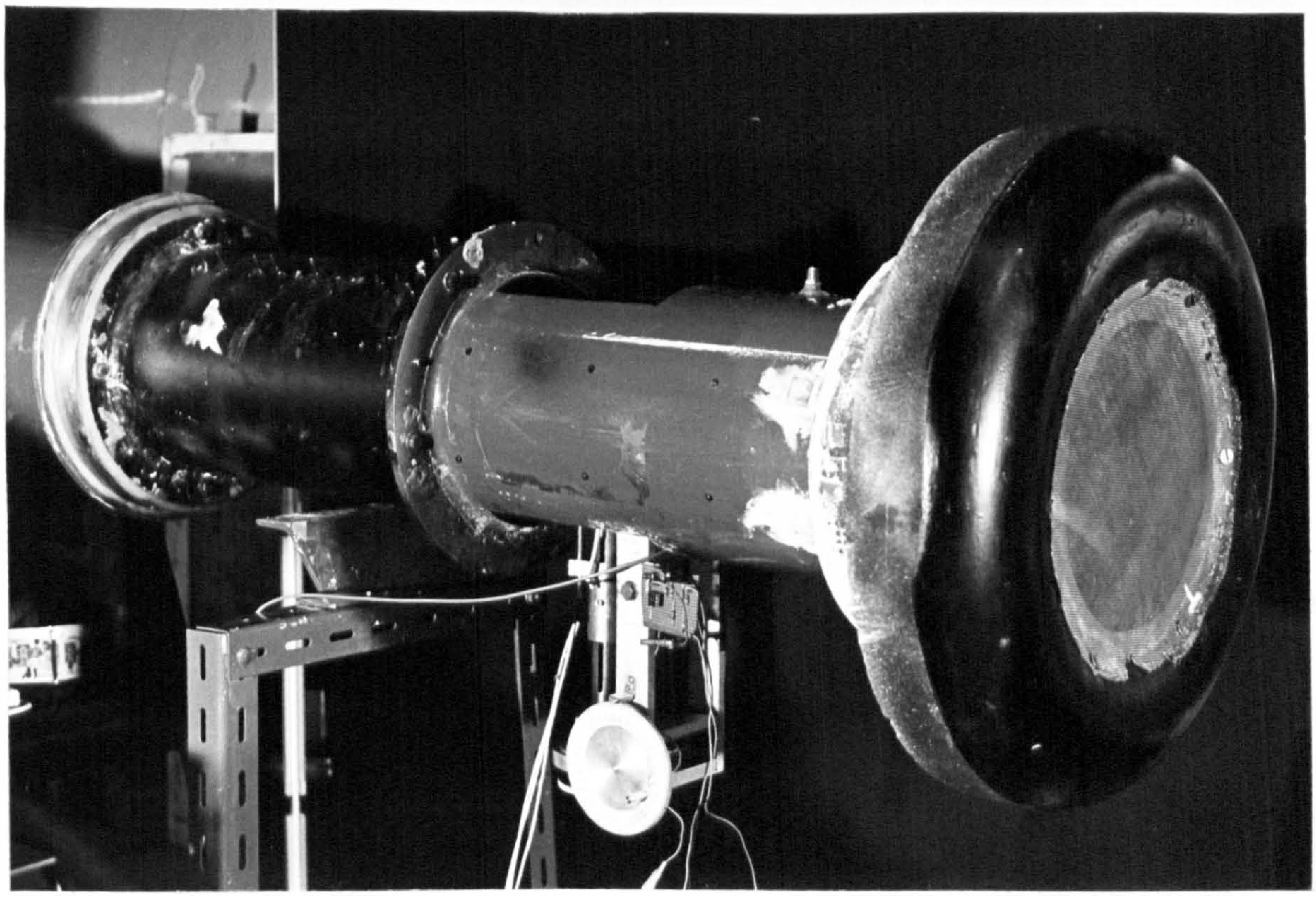

FIG. 2-10a

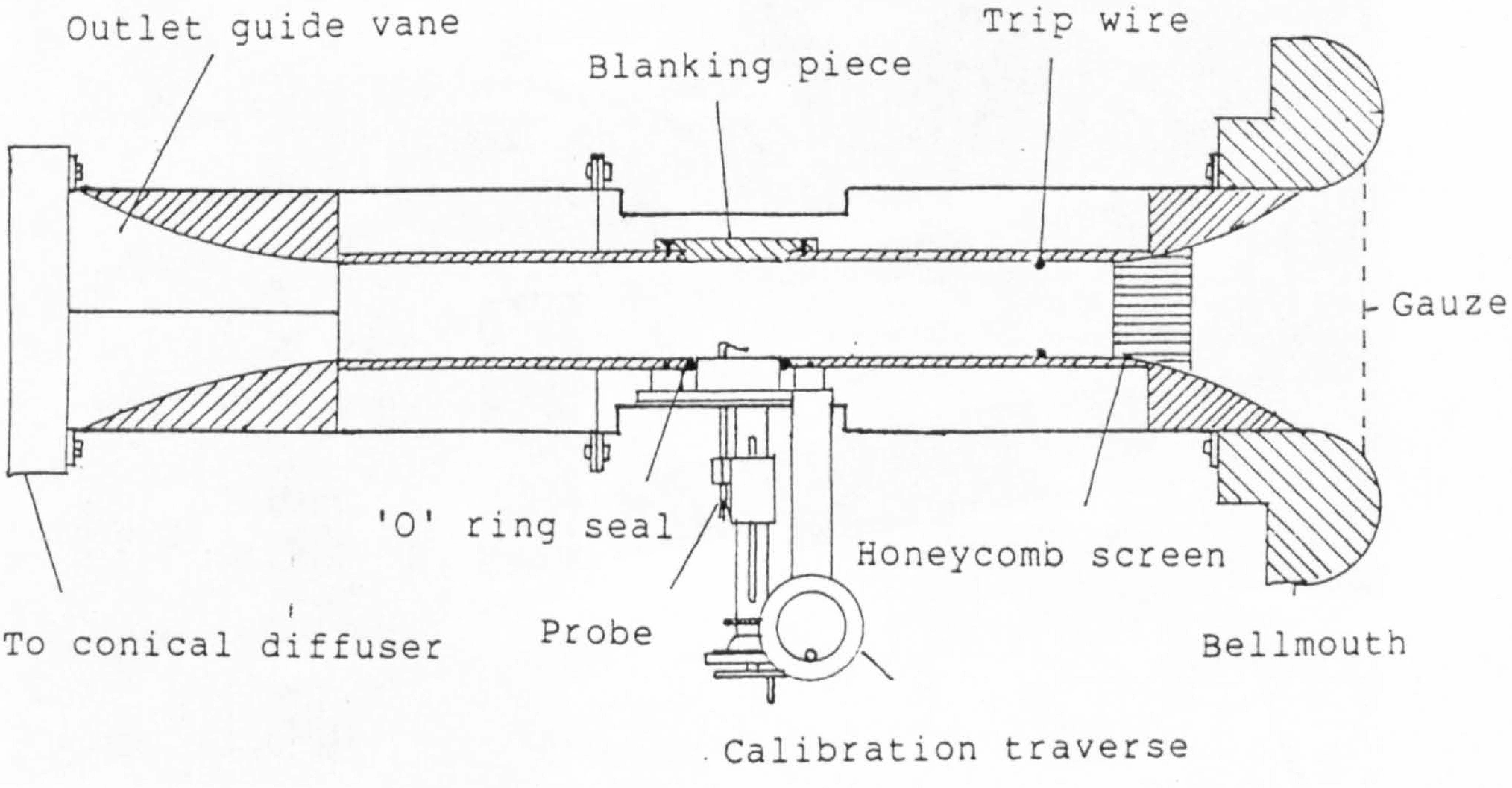

FIG. 2-10b CALIBRATION DUCT

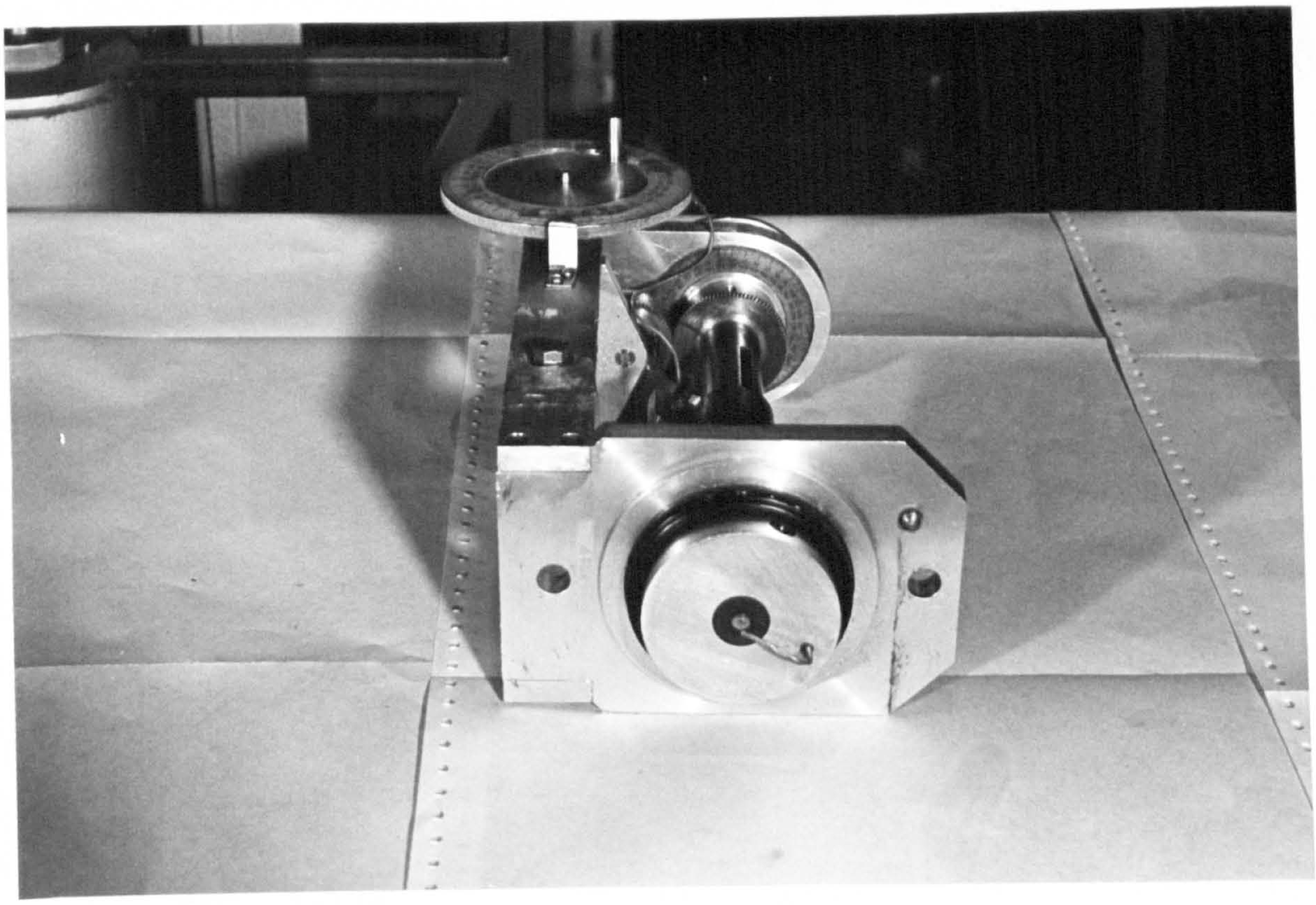

FIG. 2-11a

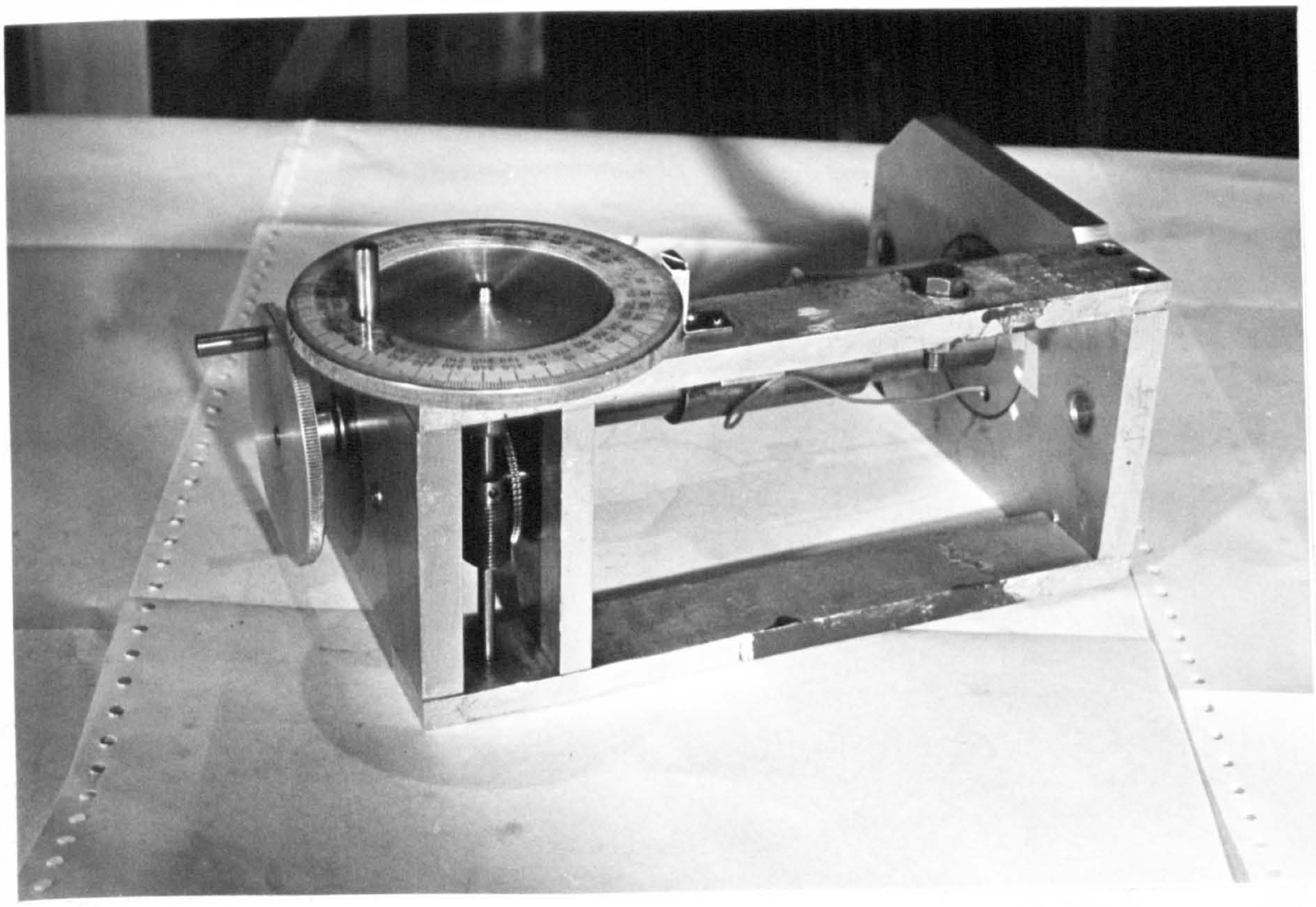

FIG. 2-11b CALIBRATION TRAVERSING DEVICE

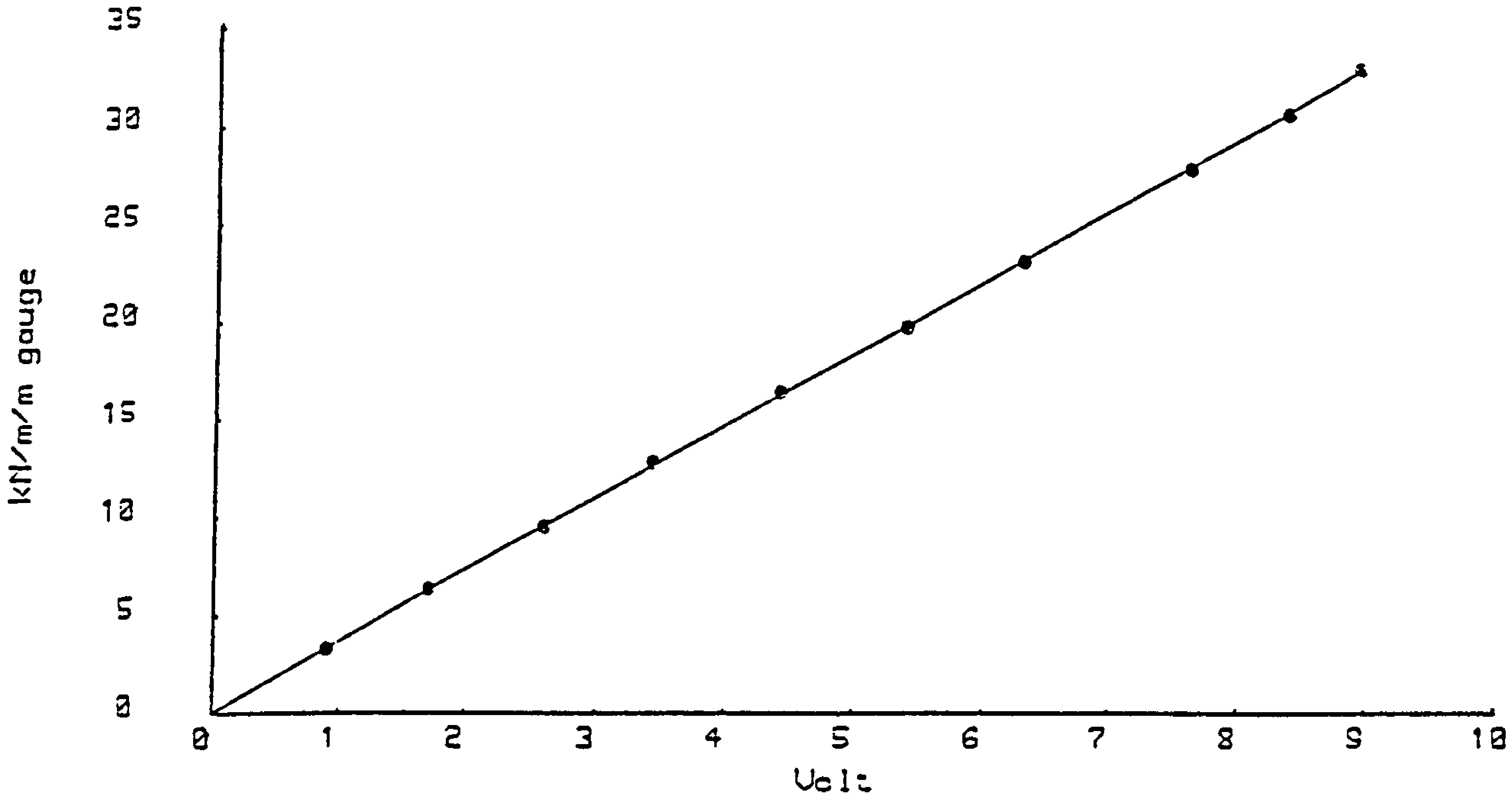

FIG. 2-12a

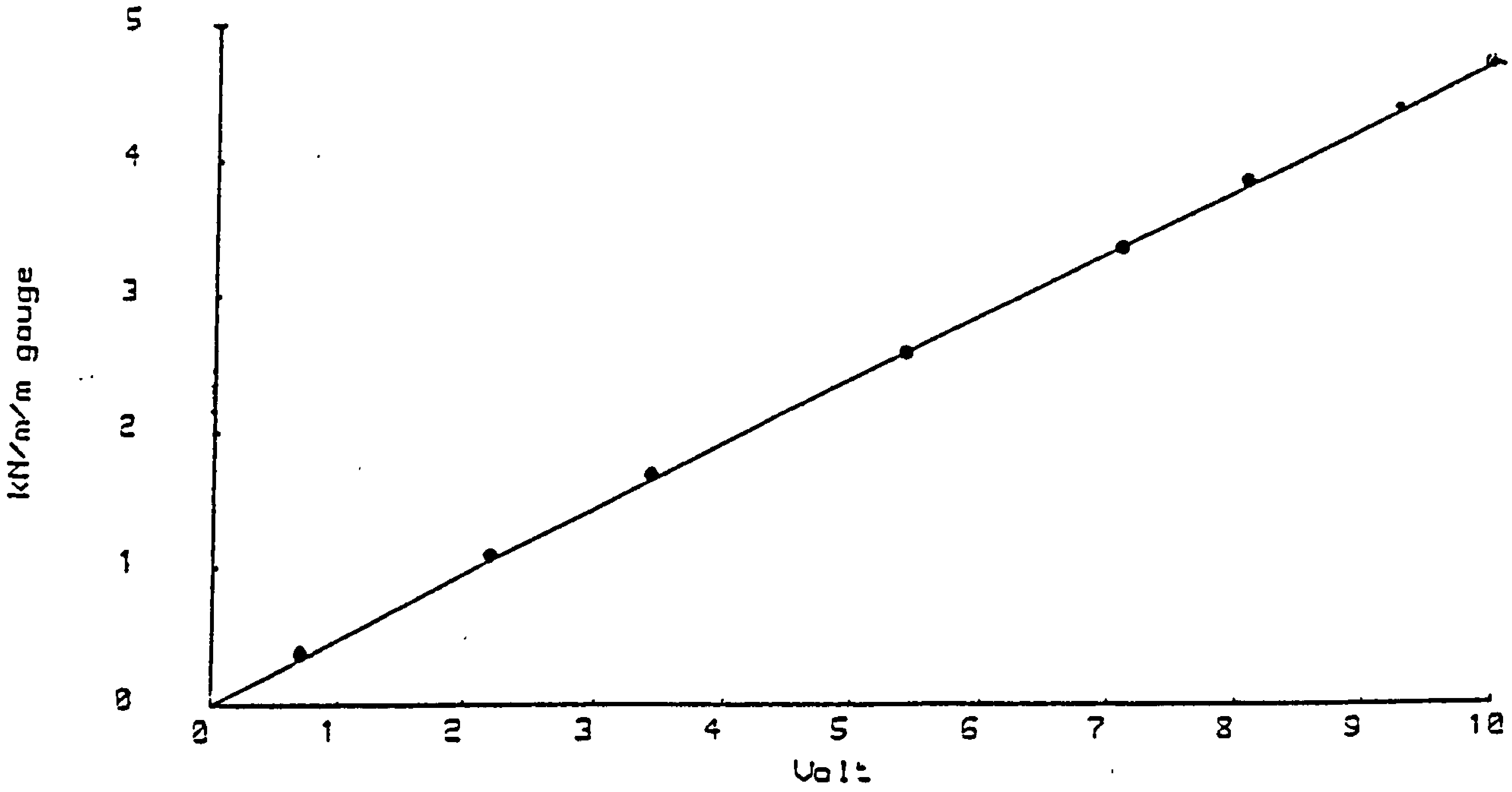

FIG. 2-12b PRESSURE TRANSDUCER CALIBRATIONS

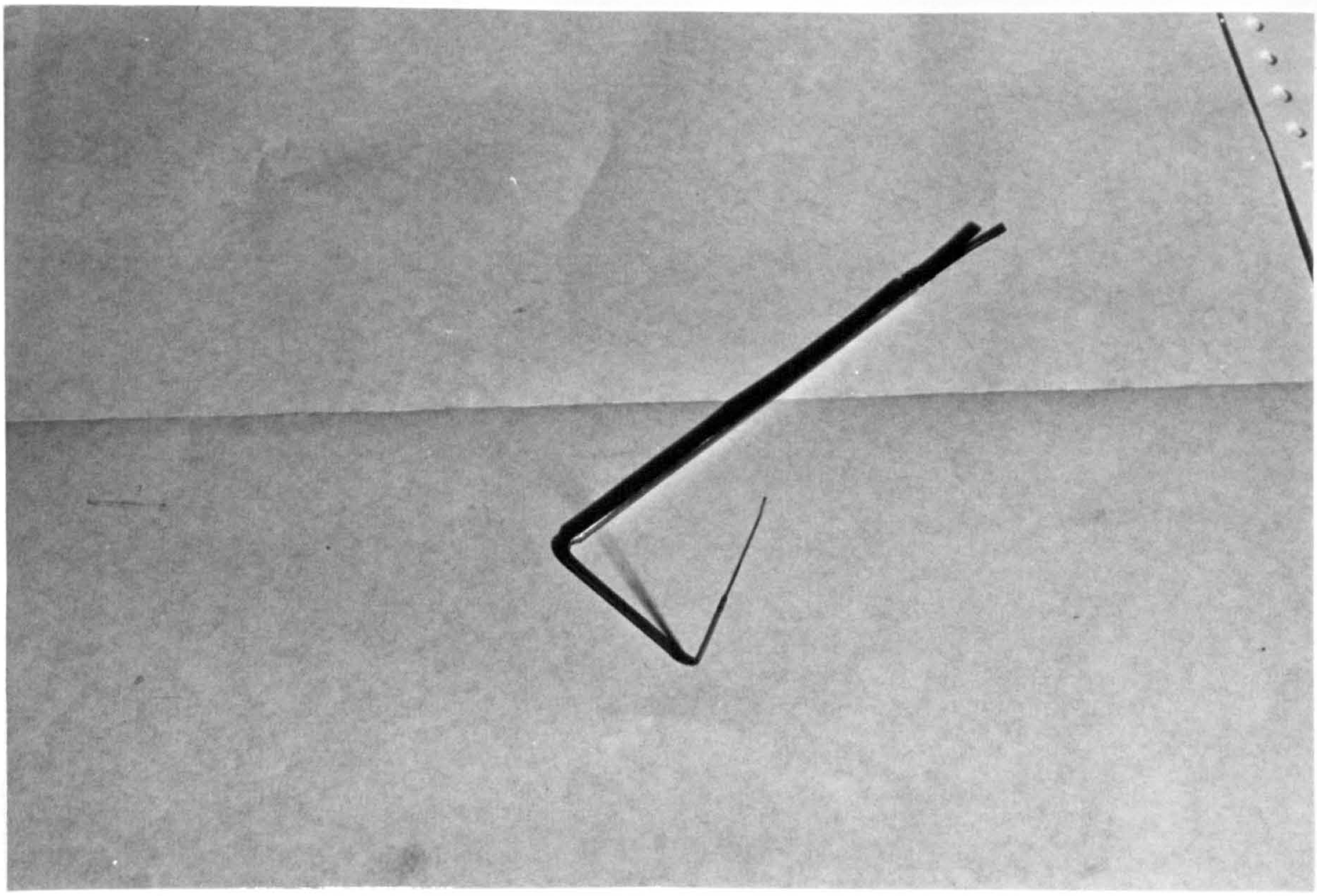

FIG. 2-13 PROBE FOR PLANE OF SYMMETRY BOUNDARY LAYER MEASUREMENT

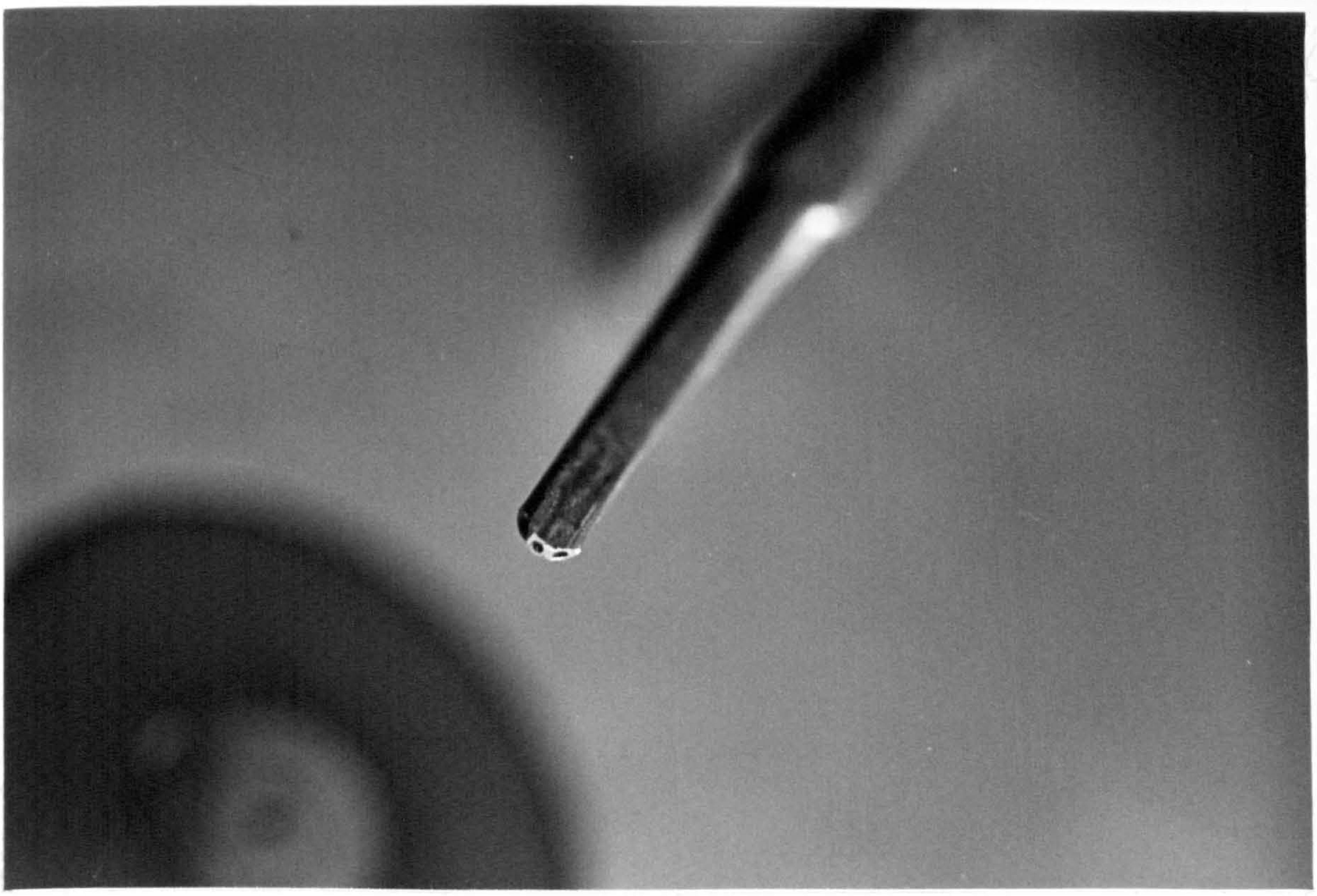

FIG. 2-14 PROBE FOR THREE-DIMENSIONAL BOUNDARY LAYER MEASUREMENT

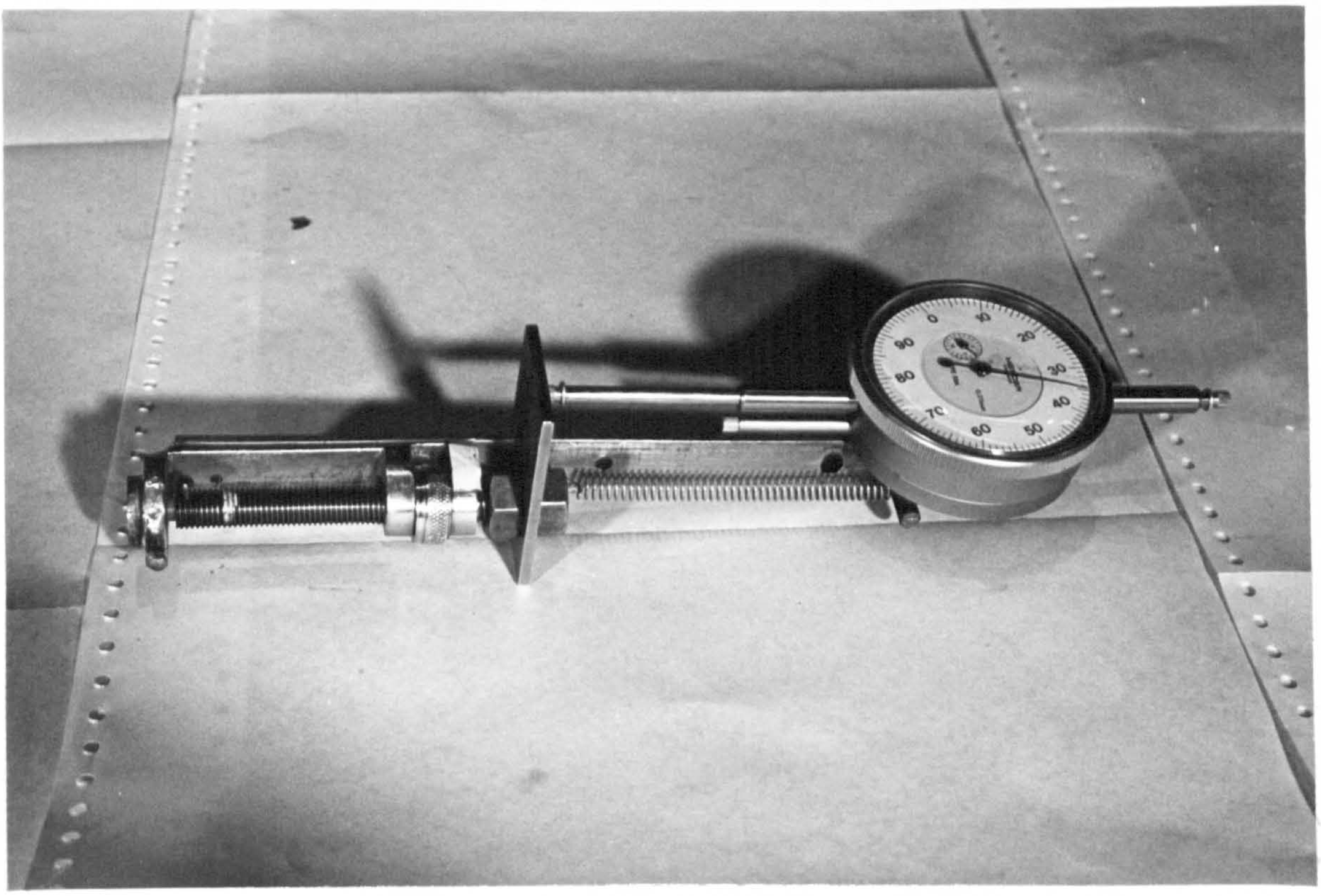

FIG. 2-15 BOUNDARY LAYER TRAVERSING DEVICE

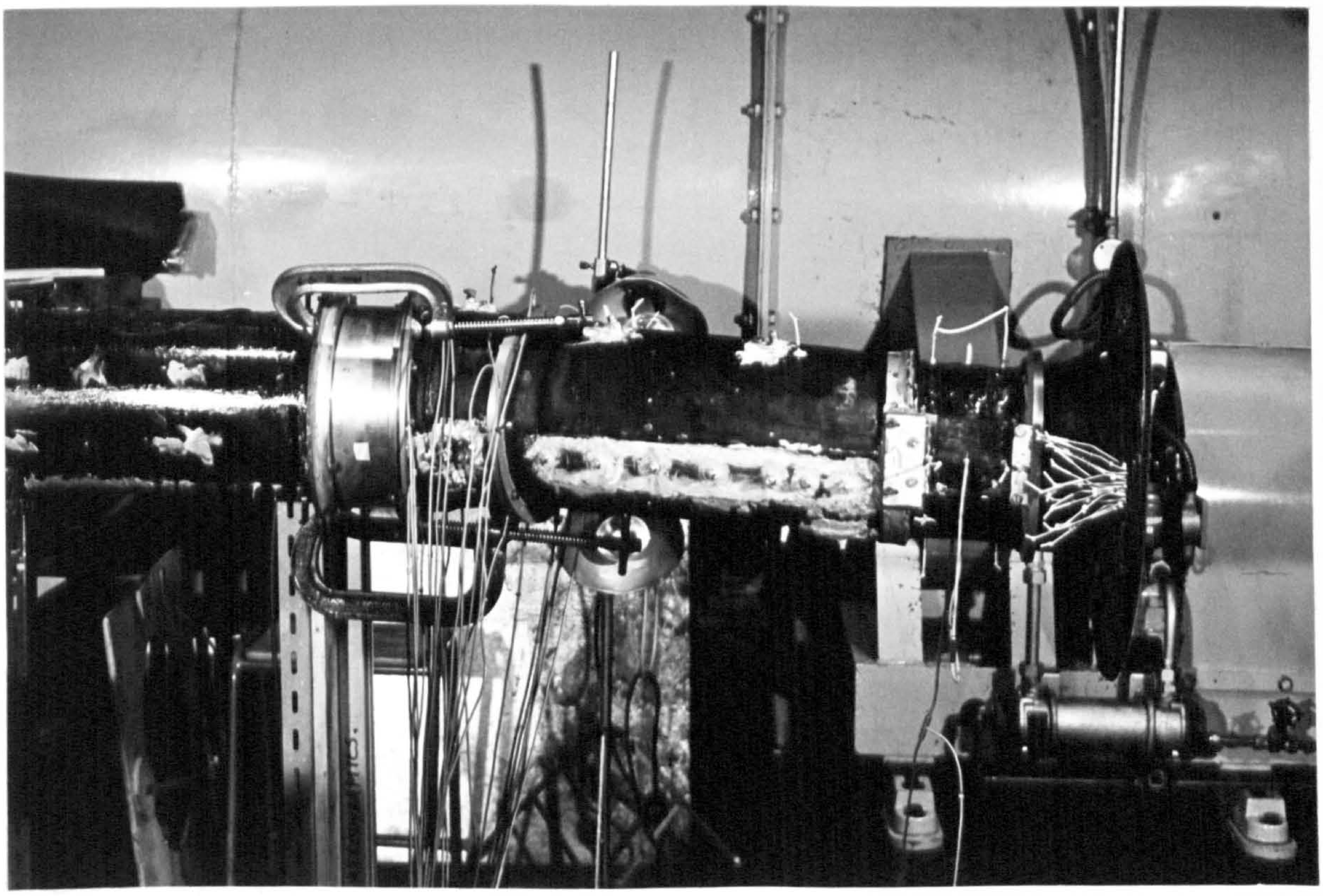

FIG. 2-16 ENGINE FACE BOUNDARY LAYER TRAVERSING RING

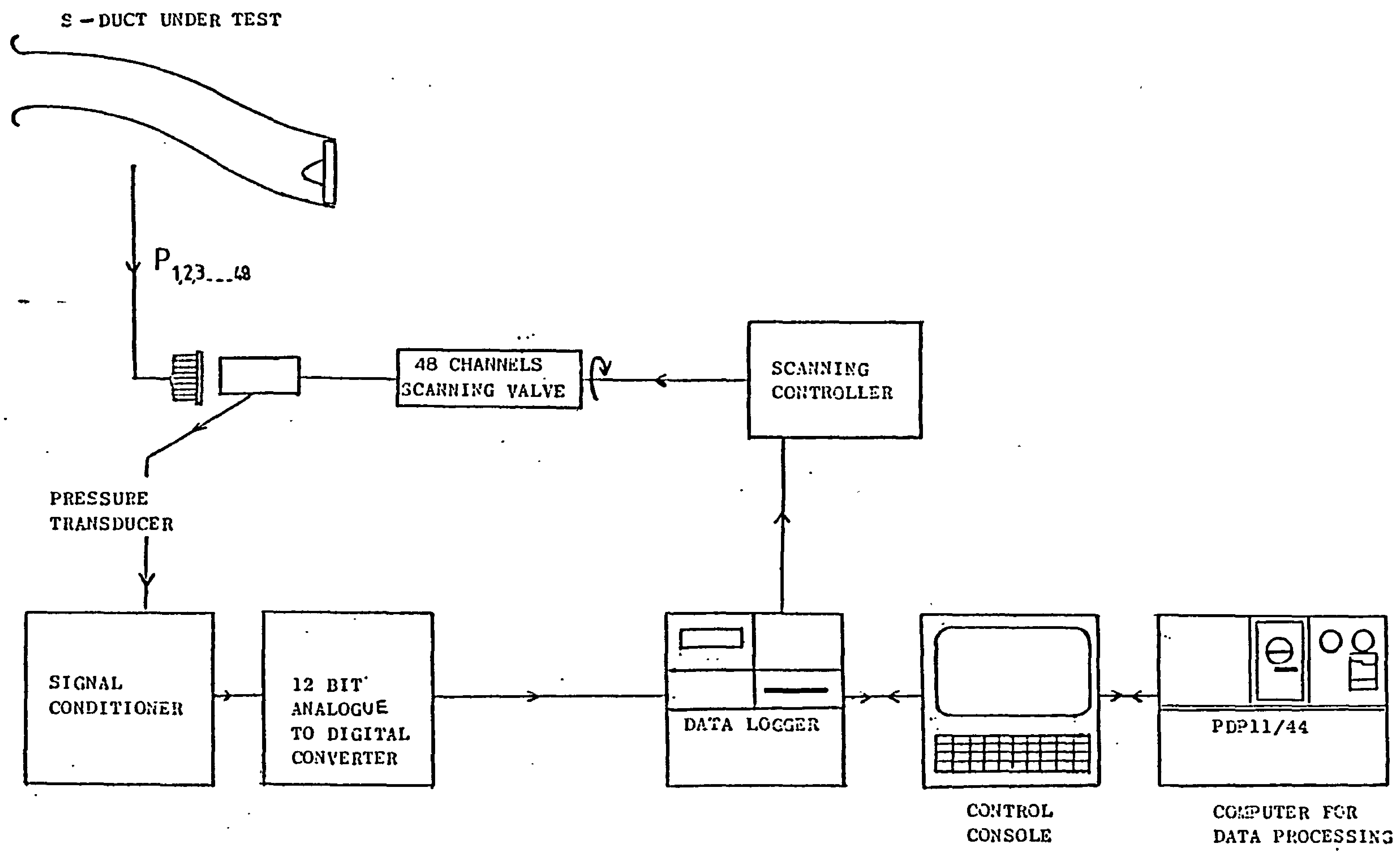

FIG. 2-17 SUBSONIC INTAKE TEST RIG INSTRUMENTATION SYSTEM

CHAPTER 3

MEASUREMENTS

CHAPTER 3 MEASUREMENTS

3.1 S-shaped duct inlet conditions

In order to ensure that turbulent boundary layer development preceded the S-shaped duct inlet, a transition duct (having the same cross section at the inlet, and of length 130mm equal to the equivalent duct inlet diameter) was installed between the bellmouth and the duct to be tested.

It was decided to use a trip wire to provoke boundary layer transition, and Kraemer's method [A21] was used to determine the diameter d of the wire for an effective transition to turbulent boundary layer flow; the condition used is $Re_d\ (=U_e d/\nu) \geq 900$.

For the flow conditions under investigation, a trip wire of 0.75mm diameter was found to adequately provoke transition. The trip wire was fixed by Araldite to the bore of the transition duct, 30mm downstream from the bellmouth joint. The reason for this distance was to avoid the influence of the favourable pressure gradient produced by the bellmouth, which would result in laminar reattachment after the trip wire; this distance was determined by examining the surface pressure distributions along the surfaces of the bellmouth and the transition duct.

In using Kraemer's method, the distance between the point of transition X_{tr} and the position of the trip wire X_k is given by:

$$U_e (X_{tr} - X_k)/\nu = 2\times10^4$$

In this investigation, the transition distances were of the order 6mm and 3mm for low and high inlet Mach numbers respectively. Therefore, the total distance required for the complete transition process was within the transition duct. The trip wire was confirmed to be effective throughout the test speed range by surface oil flow visualization, and transition distances of a similar order as predicted by Kraemer's relation were also observed.

Comparing the boundary layer data measured at the transition duct exit and a modified version (by Gibbings et al 1986) of Coles's relation for the boundary layer after turbulent reattactment,

$$\mathrm{Ln}(H/(H-1)) = 0.094\mathrm{Ln}(Re_{\Theta}) + 0.56$$

Fig. 3-1 shows that undistorted boundary layer profiles were nearly recovered after the 'trip wire' disturbance.

The addition of the transition section resulted in a boundary layer displacement thickness of order 1mm at the S-shaped duct inlet; this was equivalent to a blockage, B_t of 2.7% in diffuser terminology, where B_t is defined as:

$$B_t = 1 - \dot{m}(\mathrm{actual})/\dot{m}(\mathrm{ideal})$$

where $\dot{m}$ is the mass flow rate; the level of blockage was considered to be small and therefore acceptable. The Reynolds numbers based on the boundary layer momentum thickness were the order of 10^3 and 10^4 for low and high inlet Mach numbers respectively. Therefore, the viscous effects in the external core flow could be assumed to be negligible.

3.2 Multi-tube probe calibration

Owing to the space limitation and surface complexity inside the duct, a fixed probe measurement method was used. The flow direction and velocity were determined from correlations based on the relationship between probe pressures and flow direction. Based on the assumption that the velocity component normal to the wall was small in comparison to the streamwise and crosswise velocity components, measurements were then confined to surfaces parallel to the wall; hence a three tube Conrad probe was used.

Calibration of the probe was carried out in the calibration duct using the calibration traversing device described in Chapter 2. The probe was positioned on the tunnel centre line, and the probe pressures p1, p2 and p3 (see Fig. 3-2) were obtained at different probe yaw angles ranging from -45° to 45° at two different Mach numbers of 0.15 and 0.6. The stream total pressure P_o (=p2) was obtained when the probe was at zero yaw angle to the flow, that is when p1=p3, and the static pressure p was measured by the wall static tap. In order that the zero error of the probe could be determined, calibration was repeated with the probe inverted by installing the traversing device on the opposite wall of the tunnel.

Calibration data were reduced to the forms suggested by Dudzinski & Krause (1969), namely yaw angle, normalized total pressure difference $(p2-P_o)/pn$ and normalized static pressure difference $(\frac{1}{2}(p1+p3)-p)/pn$ which are functions of a normalized yaw pressure difference $(p1-p3)/pn$; pn is defined as $p2-\frac{1}{2}(p1+p3)$. These correlations are shown in Figs. 3-2 to 3-4.

It can be seen that the yaw angle and the normalized total pressure difference are unique functions of the normalized yaw pressure difference throughout the calibration flow conditions. However, the dependence of the normalized static pressure difference function on Mach number casts doubt on the ability of the probe to determine static pressure, hence measurement of the static pressure should be carried out by an independent means. Fig. 3-2 also indicated that the probe zero error is negligible within the experimental accuracy.

Finally, the calibration was checked by comparing the measurements of the turbulent boundary layer developed on the tunnel wall behind the trip wire; this was carried out at probe yaw angles of 0° and 30° (Fig. 3-5).

3.3 Measurements in S-shaped ducts

Tests were performed at nominal inlet Mach numbers of 0.15 and 0.60 for the three S-shaped intake duct diffusers described earlier. The test Mach numbers covered both the incompressible and subsonic compressible flow regimes. Detailed boundary layer and surface pressure measurements were made to establish duct plane of symmetry growth of the viscous region and the extent of the three-dimensionality away from the plane of symmetry. Extensive traversing of the boundary layer and the core region at the duct outlet (engine face) were also carried out to enable engine face distortion to be assessed.

3.3.1 Wall pressure measurements

Wall pressure measurements were carried out on each duct along the upper and lower walls in the duct plane of symmetry and circumferentially in two cross-sectional planes at locations before and after the second bend.

Before measurement the following procedures were carried out:

1. The power supply to the electronic equipment was turned on to allow adequate 'warming-up' time (approx. 30mins); this was particularly essential for the pressure transducer.
2. Each static tapping was connected via plastic tubes to the numbered ports on the Scanivalve.
3. Leak tests were carried out on all pneumatic connections by blocking each static tapping after feeding in a pressure greater than the atmospheric pressure, the pressure transducer output was then observed via a digital voltmeter for any variation.

The following procedures were carried out for each run:

1. The laboratory pressure and temperature were recorded before and after the test; the averages were used as stagnation values in the calculations. A minor correction was used to account for total pressure loss across the inlet filter box.
2. Flow in the duct was allowed to settle after starting the rig (approx. 3 mins.).
3. The mean inlet wall pressure was set by adjusting the mass flow rate to give the desired inlet Mach number.

4. The gain of the pressure transducer signal amplifier was selected such that the maximum pressure difference signal was within the range of the A/D converter input (0-10V).

5. The pressure transducer was calibrated against a known reference pressure using a manometer at the selected amplifier gain and the transducer output at zero pressure difference was recorded.

6. Data sampling and logging was completed.

Normally several sets of data for the same duct flow condition were collected for statistical analysis, repeatability and consistency checks. Data collected on the data logger were transferred to the Department's PDP11 computer for reduction and analysis.

The pressure data were finally reduced to the form of the pressure coefficient,

$$Cp = (p-p_{in})/Q_{in}$$

where Q_{in} is the mean inlet dynamic head

and p_{in} is the mean inlet static pressure

and the Mach number,

$$M_{isen} = \sqrt{(2\ ((P_{o(core)}/p)^{(\gamma-1)/\gamma} - 1)/(\gamma-1))}$$

In using the above relation, isentropic core flow conditions were assumed.

3.3.2 Boundary layer measurements

A) Duct plane of symmetry boundary layer

Boundary layer measurements were first carried out on the upper and lower walls along the plane of symmetry of each duct. Although the boundary layer development was not two-dimensional, owing to flow field convergence or divergence, negligible or zero crossflow at the plane of symmetry enabled conventional two-dimensional measurement techniques to be used; for the reason mentioned in Chapter 2, an offset design probe was used.

Because of the difficulties involved in producing and calibrating an offset multi-tube probe, flow symmetry checks had to rely on surface flow visualization and crossflow data obtained at the duct outlet.

A.1 Measurement procedure

At each traverse station, the probe was aligned with the line formed by the wall static taps located along the plane of symmetry; since total-pressure probes are insenitive to yaw, errors were less than 1% of the dynamic pressure, as long as the misalignments were less than 15°. Other pre-measurement procedures and the setting of the duct flow conditions were similar to that of the wall pressure measurement described previously. Boundary layer traversing was commenced once the flow in the duct reached a steady state. The point at which the probe left the wall was determined by the breaking of an electronic circuit. Mean-total pressure, the wall static pressure and the probe position were recorded by the data logger at each traverse station once a steady probe pressure signal was observed via the digital voltmeter. The traversing was completed when no significant change in probe pressure signal was observed. The above measurement procedure was repeated at a different inlet Mach number.

A.2 Reduction of data

Macmillan's wall proximity correction [A13], Fig. 3-6 and the displacement correction of 0.15D (D=probe external diameter) [A2] to account for the total pressure gradient effects were applied to all near wall measurements (y<2D). No attempt was made to correct error due to the effects of turbulence because of the unreliable information in literature. However, for most boundary layer flows the turbulence intensity is less than 10%. Consider the following:

$$u = \overline{u}\sqrt{(1+\overline{u'^2}/\overline{u^2})} \simeq \overline{u}(1+\tfrac{1}{2}\overline{u'^2}/\overline{u^2})$$

It can be seen that for a streamwise turbulence intensity of 10%, $u \simeq \overline{u}(1+0.005)$; hence the effect on the average differential pressure is negligible.

Mean-velocity profiles were obtained from the mean-total pressure profiles by using the following relations:

$$P_o/p = (1+\tfrac{1}{2}(\gamma-1)M^2)^{\gamma/(\gamma-1)} \qquad (3\text{-}1)$$

$$T_o/T = (1+\tfrac{1}{2}(\gamma-1)M^2) \qquad (3\text{-}2)$$

$$u = M\sqrt{(\gamma RT)} \tag{3-3}$$

The specific heat ratio γ and the specific gas constant R of the air were taken to be 1.403 and 287.4J/kg K respectively. The total temperature T_o was the ambient laboratory temperature at the time of the test and its variation across the boundary layer based on a recovery factor of 0.89 for turbulent boundary layer was estimated to be less than 1% throughout the test Mach number range.

The boundary layer thickness δ is defined as the distance from the surface at which $u(=U_e) = 0.995U_{max}$.

For boundary layer traversing carried out on flat surfaces, the static pressure p was assumed to be constant throughout the boundary layer and the local wall static pressure was used. In regions where longitudinal curvature was significant, p was corrected at each traverse station by assuming that pressure varied according to $dp/dy=\rho u^2/(y\pm r)$, where r is the local surface radius of curvature, and the + & - represent convex and concave surfaces respectively. The correction was applied by numerical means described as follows:

The normal pressure gradient was approximated by the backward difference formula,

$$(p_i - p_{i-1})/dy = (\rho u^2)_i/(y\pm r) \tag{3-4}$$

where $dy=y_i-y_{i-1}$; subscripts i & i-1 refer to the current and previous traverse stations respectively. Equation (3-4) was iterated with Equations (3-1) to (3-3) to obtain the correct p_i. The first uncorrected values of ρ (=p/RT) and u obtained via measurement were used at the start of the iteration. p_{i-1} at the first traverse station was provided by the wall static pressure. Convergence was normally achieved within 10 iterations for an error criterion of 0.01%.

To estimate the local skin friction coefficient cf, the frictional velocity u_τ $(=\sqrt{(\tau_w/\rho_w)})$ was first obtained through the best agreement between the near wall experimental data and the log law of the wall,

$$u/u_\tau = 2.44\mathrm{Ln}(y^+) + 4.9 \qquad (3\text{-}5)$$

where $y^+ = yu_\tau/\nu_w$.

The kinematic viscosity at the wall ν_w was determined by using the Sutherland viscosity law,

$$\mu_w/\mu_{ref} = \frac{T_{ref} + 110}{T_w + 110}\left(\frac{T_w}{T_{ref}}\right)^{1.5}$$

where $\mu=\nu*\rho$. The reference values were obtained from the International Standard Atmosphere Table [A9] and the wall temperature T_w was determined by using the Crocco's relation for adiabatic flow using a recovery factor of 0.89,

$$T_w = T_e(1+\tfrac{1}{2}0.89(\gamma-1)M_e^2)$$

where T_e is the temperature at the edge of the boundary layer which can be calculated using Equation (3-3) by putting $M = M_e$. Finally, cf was calculated using:

$$cf = 2(T_e/T_w)/(U_e/u_\tau)^2$$

Before applying Simpson's numerical integration technique to determine the boundary layer integral parameters, Equation (3-5) was used with the u_τ obtained to describe the velocity profile between $y/\delta=0.01$ (approx. end of viscous sub-layer region) from the wall and the first traverse station. As the majority of the velocity profiles obtained possessed substantial law of the wall regions, this method was considered to be satisfactory in determining the integral parameters. The following streamwise integral parameters were calculated:

$$\Theta_{11} = \int_0^{\delta} \frac{\rho u}{\rho_e U_e^2} (U_e - u)\, dy$$

$$\delta_1 = \int_0^{\delta} \left(1 - \frac{\rho u}{\rho_e U_e}\right) dy$$

$$H = \delta_1 / \Theta_{11}$$

$$H_1 = (\delta - \delta_1)/\Theta_{11}$$

where $\rho/\rho_e = \left[(1+\frac{1}{2}(\gamma-1)M^2)/(1+\frac{1}{2}(\gamma-1)M_e^2) \right] p/p_e$

B) Three-dimensional boundary layer measurement

Three-dimensional boundary layer measurements were carried out at the engine face compressor plane and at various locations on the side wall of each duct. Because of the uncertainty in determining the static pressure using the Conrad probe (see Fig. 3-4), static pressure measurement had to rely on the wall static tap; since all the measurements were carried out on surfaces of zero or small streamwise curvature the variation in static pressure can confidently be assumed to be negligible throughout the boundary layer.

B.1 Measurement procedure

The measurement procedure was identical to that of the plane of symmetry measurement. Boundary layer traversing was commenced after aligning the centre tube of the probe with the wall static tap and the setting of the duct flow conditions. The traversing was completed when no significant changes in the probe pressure signals p1, p2 and p3 were observed.

B.2 Reduction of data

The mean-total pressures and the flow directions throughout the boundary layer were determined from the correlations (Figs. 3-2 to 3-3) obtained during the probe calibration; Lagrange's three-point interpolation formula was used to interpolate values between the calibrated data points.

Once the mean-total pressure profile was determined, the mean-resultant velocity (U) profile was obtained using Equations (3-1) to (3-3) as before. The skew angles (β) across the boundary layer were obtained by resolving the flow directions with respect to the streamwise velocity vector at the edge of the boundary layer. The streamwise (u) and crosswise (v) velocity components were given by the trigonometric relations,

$$u = U \cos\beta$$

$$v = U \sin\beta$$

The streamwise skin friction coefficient cf_1 was first determined by the method described in the last section, and the resultant skin friction cf is given by:

$$cf = cf_1/\cos\beta_o$$

where β_o is the limiting streamline angle relative to the freestream streamline.

In addition to the streamwise integral parameters, the following crosswise boundary layer integral thicknesses were also calculated:

$$\Theta_{12} = \int_0^\delta \frac{\rho v}{\rho_e U_e^2} (U_e - u)\, dy$$

$$\Theta_{21} = - \int_0^\delta \frac{\rho u v}{\rho_e U_e^2}\, dy$$

$$\Theta_{22} = - \int_0^\delta \frac{\rho v^2}{\rho_e U_e^2}\, dy$$

$$\delta_2 = - \int_0^\delta \frac{\rho v}{\rho_e U_e}\, dy$$

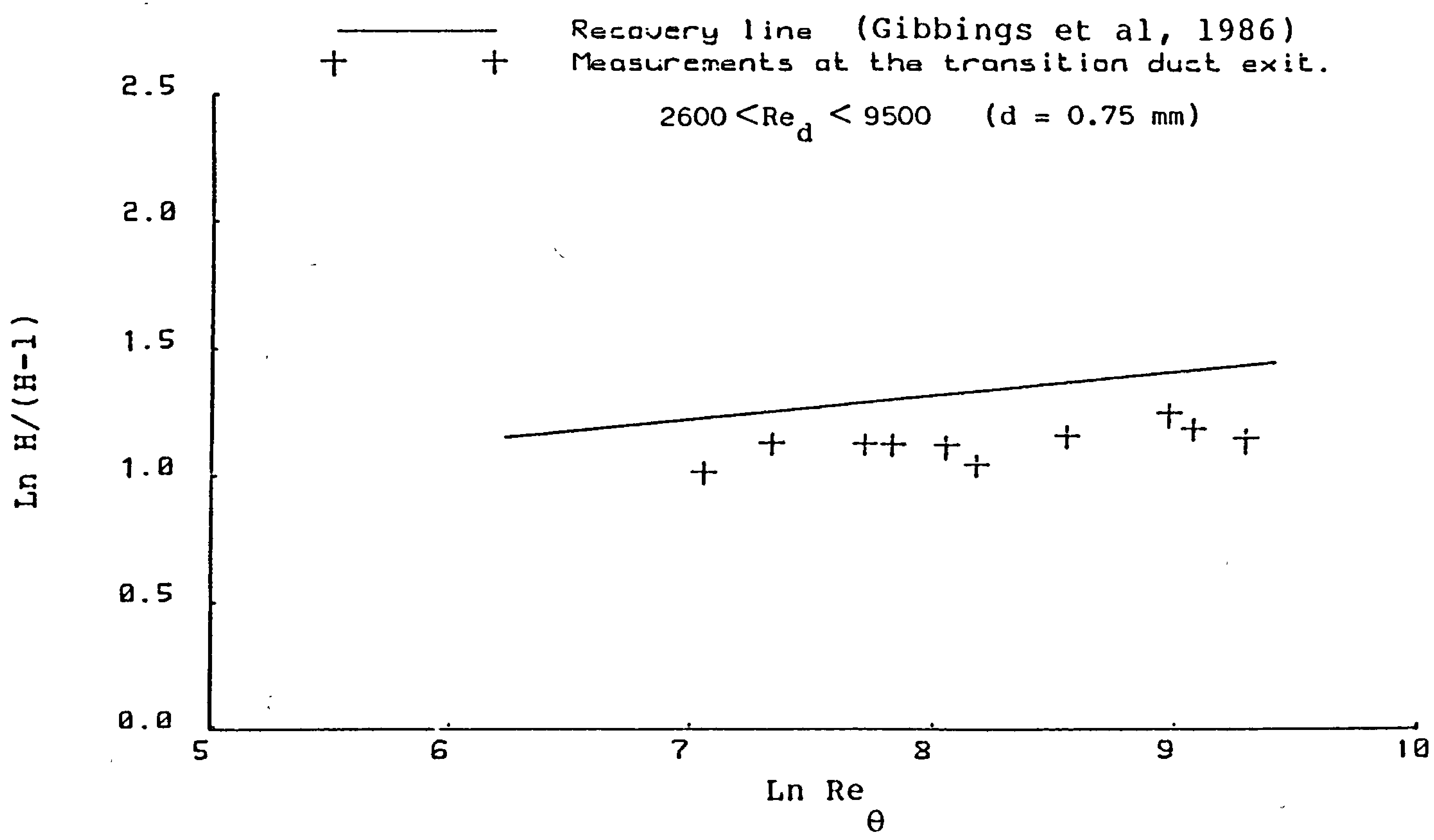

FIG. 3-1 RECOVERY OF BOUNDARY LAYER PROFILES AFTER THE TRIP WIRE
(d = trip wire dia.)

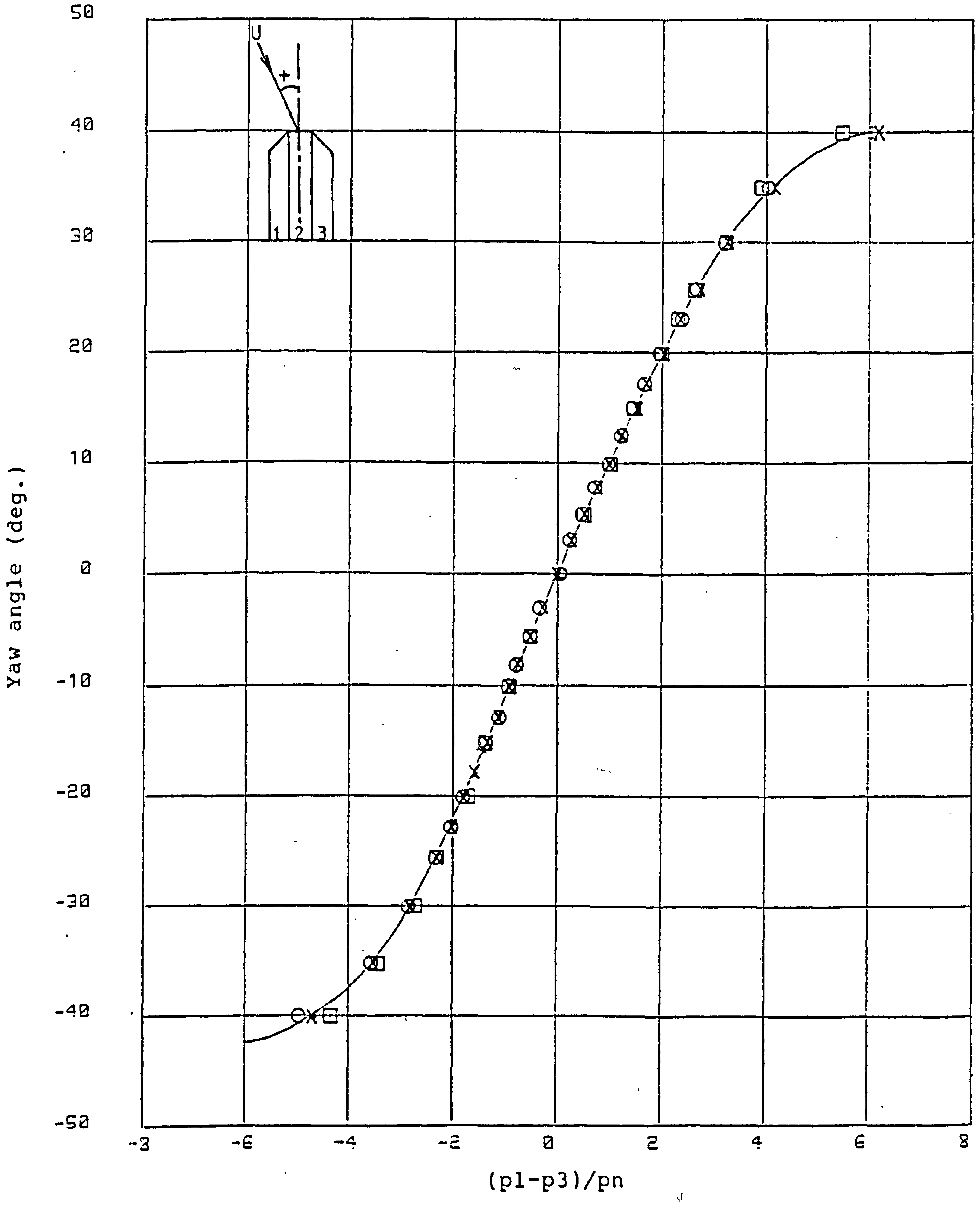

FIG. 3-2 YAW ANGLE VERSUS
NORMALIZED YAW PRESSURE DIFFERENCE
$(pn = p2-\frac{1}{2}(p1+p3))$

MACH NO.	0.15	0.60
	□	x, o(probe inverted)

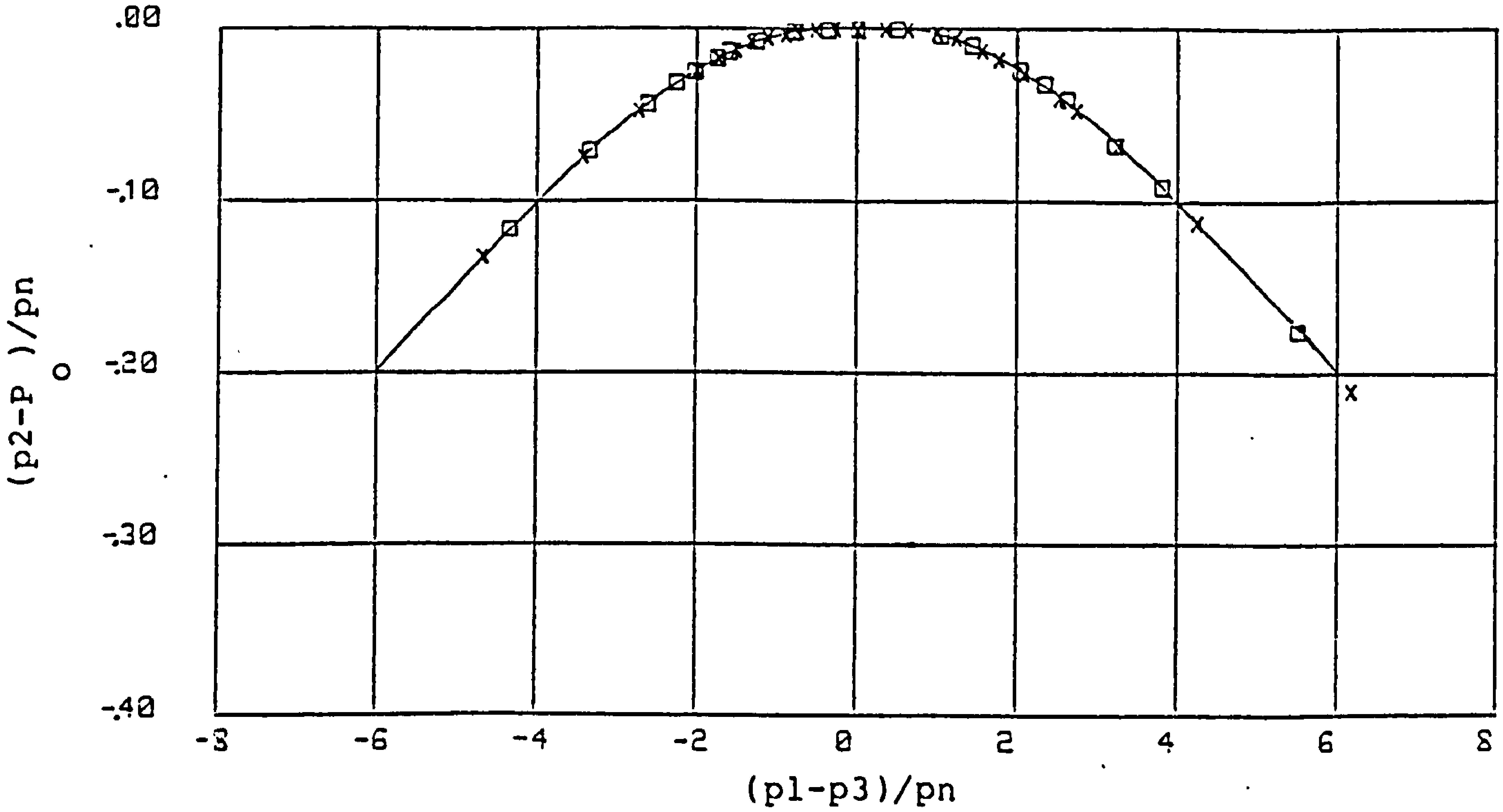

FIG. 3-3 NORMALIZED TOTAL PRESSURE DIFFERENCE VERSUS NORMALIZED YAW PRESSURE DIFFERENCE

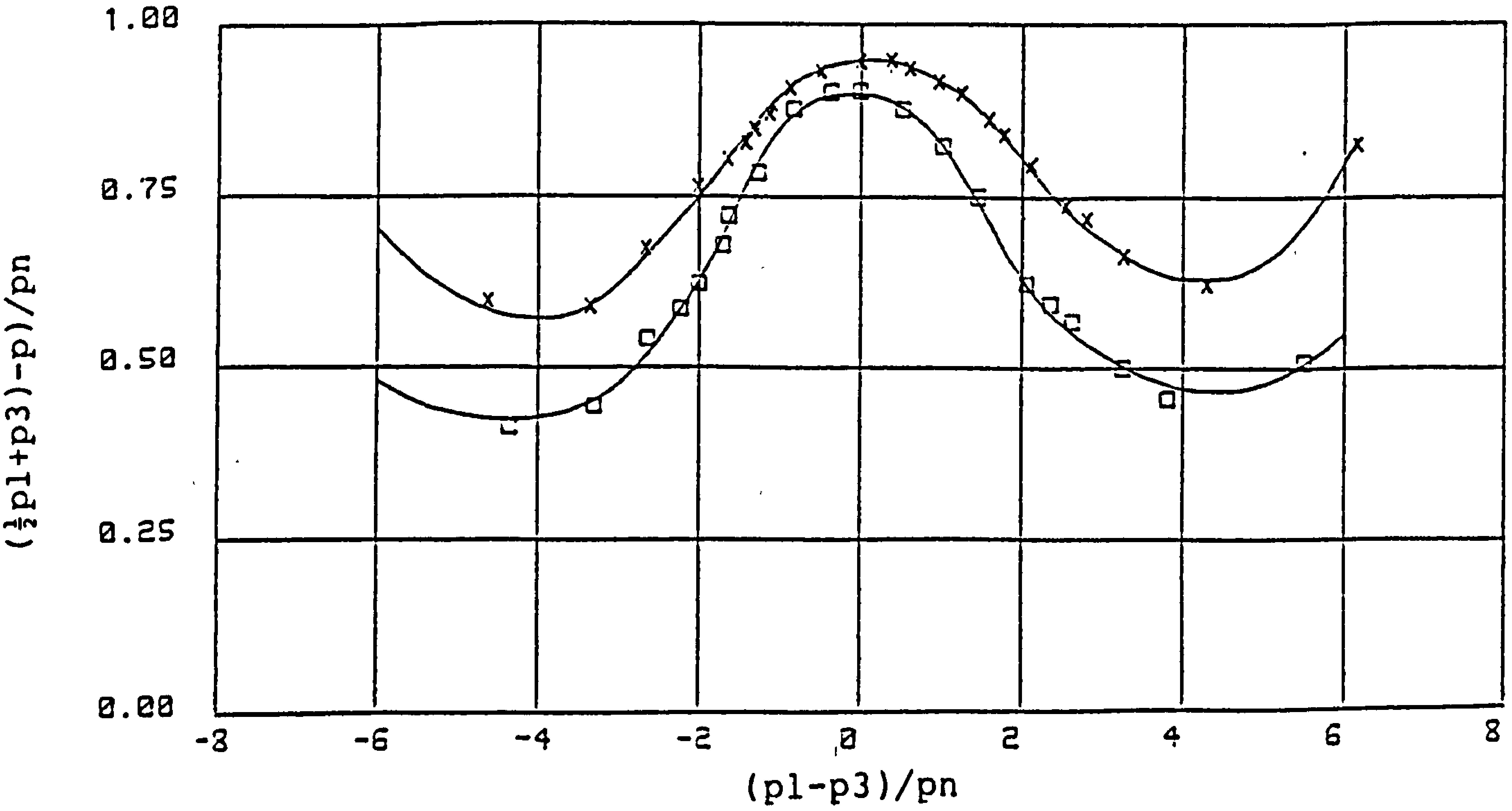

FIG. 3-4 NORMALIZED STATIC PRESSURE DIFFERENCE VERSUS NORMALIZED YAW PRESSURE DIFFERENCE

MACH NO.	0.15	0.60
	□	x

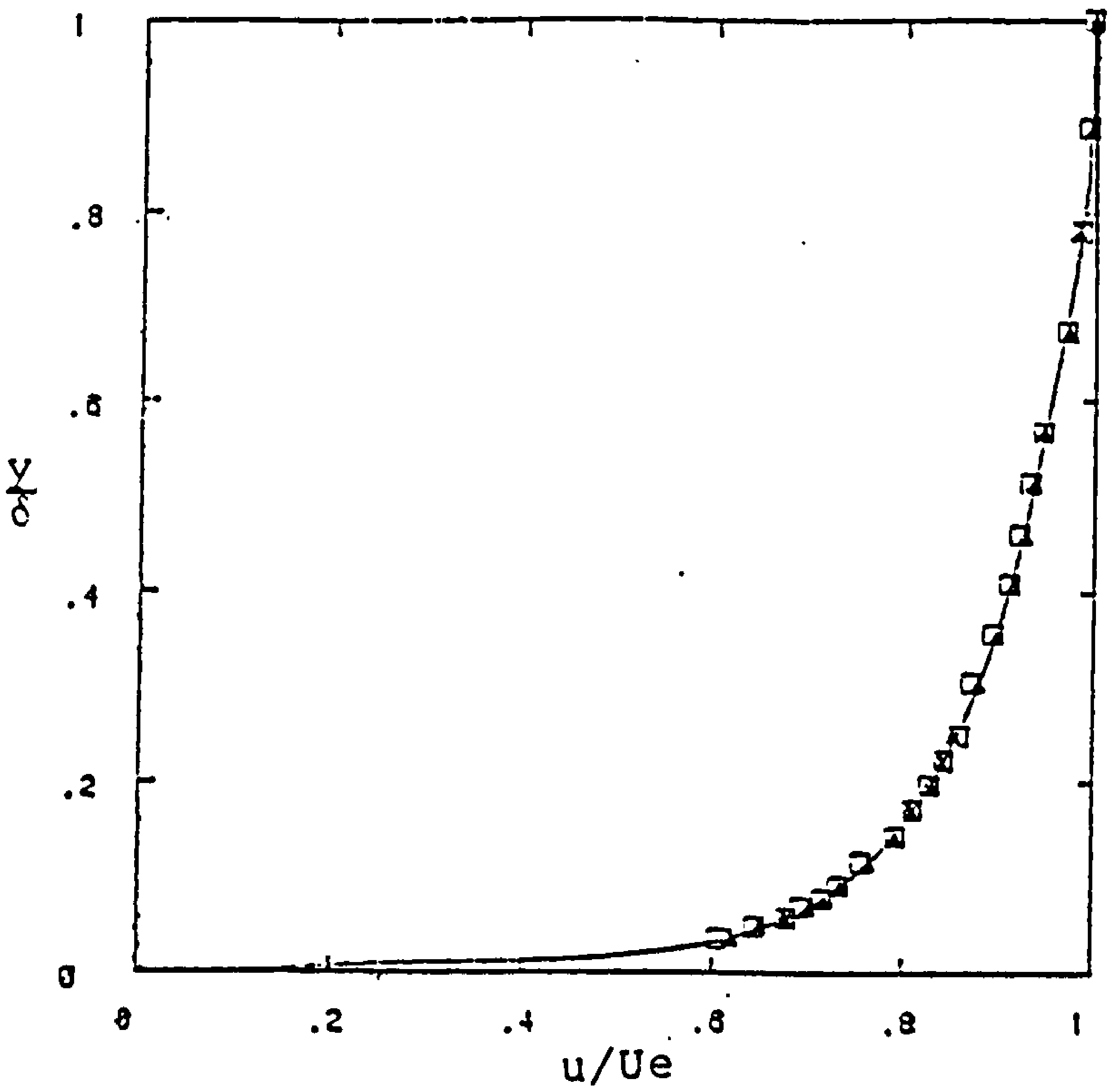

FIG. 3-5 PROBE CALIBRATION CHECK

YAW ANGLE (deg.) 0.0 30.0
▲ □

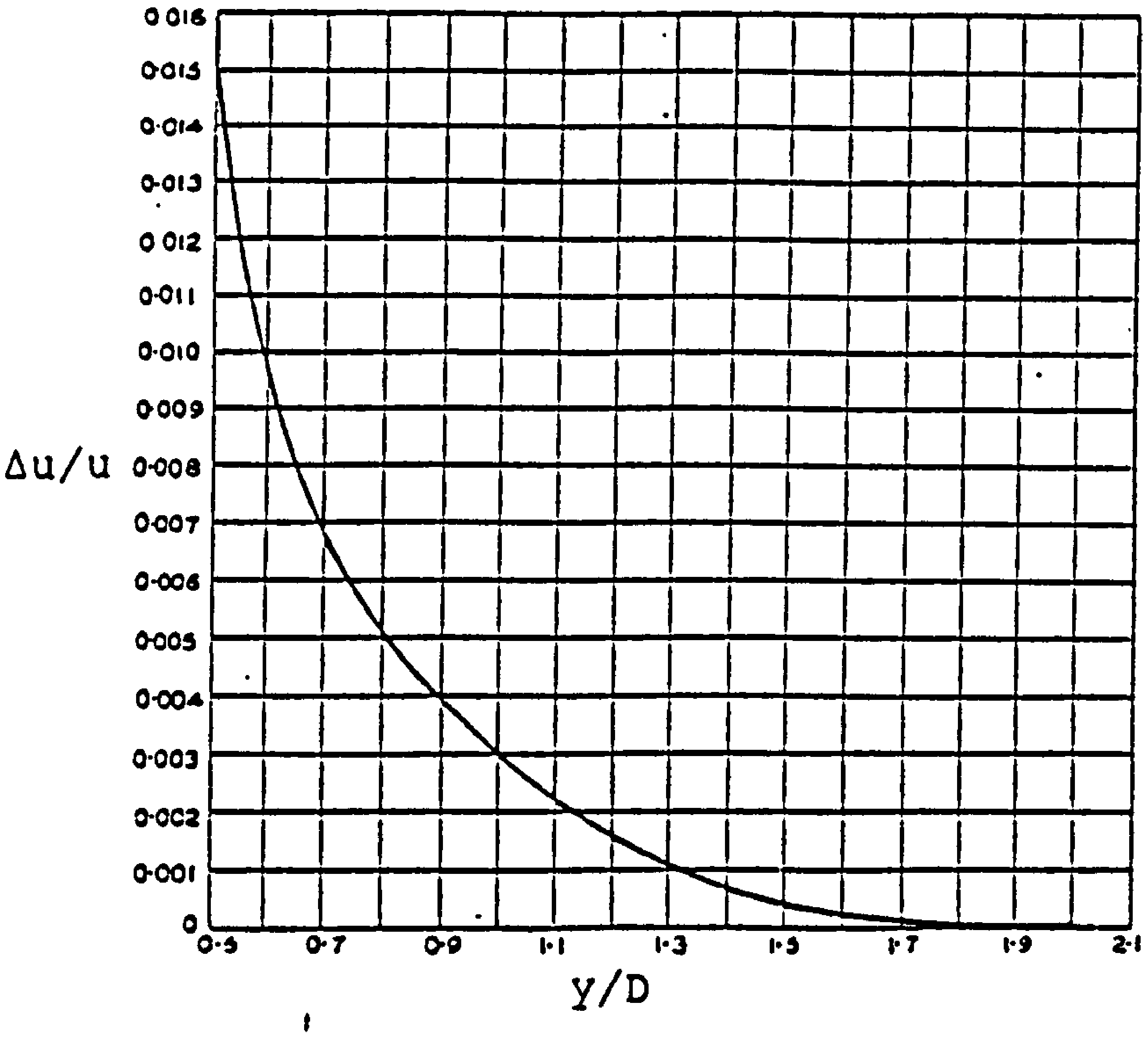

FIG. 3-6 THE WALL EFFECT EXPRESSED AS A FUNCTION OF y/D [ref.A13]
D = probe ex. dia.
Δu correction, to be added to measured velocity u

CHAPTER 4

RESULTS AND DISCUSSIONS

CHAPTER 4 RESULTS AND DISCUSSION

4.1 Introduction

Results of measurements carried out on each duct are presented in this chapter. Data of Duct M are first shown and discussed, followed by Duct N and then Duct J. This sequence corresponds to increasing severity of the upstream bend curvatures of the duct which were found to play crucial roles in setting duct flow quality. Measurements for each duct are further sub-divided into the following groups:

1. Plane of symmetry data.
2. Three-dimensional boundary layer data.
3. Flow visualization and interpretation.

Where possible the incompressible and the subsonic flow data are plotted together to provide ease of comparison such that compressible effects can easily be distinguished.

4.2 Duct M results

4.2.1 Plane of symmetry data

The Duct M configuration is shown again in Fig. 4-1 for ease of reference against measurements. The duct possesses only one bend located near the duct outlet; the bend has a mean radius of curvature of 323.0mm and provides a mean flow turning angle of 26.8°.

Figures 4-2 and 4-3, show the static pressure coefficient Cp and the Mach number distributions along the upper and lower walls. The acceleration of the flow up to the duct throat is due to the displacement effect of the boundary layer in the straight transition section. From the duct throat (X=0mm), the straight diffusing section displays its diffusing effect. Surface pressures on the upper and lower walls remain identical until about X=40mm. Thereafter, the effect of the downstream bend is quite apparent. The pressure difference between the two walls is the highest at the mid-bend position (X=430mm), with high pressure on the upper wall (outside wall) and low pressure on the lower wall (inside wall) as a result of the radial pressure gradient due to the curvature. From the bend exit plane (X=500mm) there is a tendency for the flow to converge; however the flow is still far from uniform when the duct outlet is reached. The trends for low and high inlet Mach numbers are the same, except for an overall increase in Cp level at high inlet Mach number and a small reduction in pressure difference between the upper and lower walls in the bend region due to the increase in boundary layer thickness which is to be explained later.

Figures 4-4 to 4-7 show the streamwise mean-velocity profiles and the corresponding logarithmic profiles developed along the upper and lower walls. From the duct throat, velocity profile development remains similar on the upper and lower walls due to the same order of pressure rise until at around X=300mm where the effects of the outside and the inside walls of the bend become significant.

The outside wall (on the upper wall) produces a continued pressure rise. Consequently, there is a tendency towards boundary layer separation at about X=333.5mm, but this is soon overcome by the accelerating flow around the centre body (starts at X=412mm), which also restricts further pressure rise. The favourable effect provided by the centre body can be seen from the recovering velocity profiles and the corresponding variations of the wake components, illustrated in the logarithmic plots. The profiles at X=443.5 and 478.5mm exhibited a dip below the wall law at the outer edge of the inner layer owing to the destabilising concave curvature effect; this effect increases the turbulent mixing hence reducing the velocity gradient locally [E2].

On the inside wall (on the lower wall), the flow over-expanded after encountering the high curvature convex surface. The diversion of the inner layer from the wall law from X=420.5mm to 478.5mm reflects this effect and exhibits also the slow response of the boundary layer to the suddenly imposed curvature (note that the curved surface starts at X=385mm and finishes at X=420.5mm). However, the fairly rapid recovery thereafter (see profile at X=555mm) could be attributed to the stabilizing convex curvature effect [E1].

The boundary layer profile development appears to be similar at both the low and high inlet Mach numbers except that the destabilising effect on the concave surface seems only apparent at low Mach number.

Figures 4-8 to 4-11 show the boundary layer integral parameters and the skin friction coefficient cf (=cf_1) distributions. Their development is in-line with the surface pressure variation described earlier and the same trends are displayed at low and high inlet Mach numbers.

Steeper pressure rise at high inlet Mach number is the main cause of the extra increase in displacement thickness δ_1 and momentum thickness Θ_{11}. In general, compressibility at subsonic speed has the effect of reducing the density ratio ρ/ρ_e as temperature increases towards the wall (assuming an adiabatic wall), thus contributing further to the increase in δ_1 but reducing Θ_{11}. However, the effect of compressibility is only marginal on the actual δ_1 and Θ_{11} distributions considering the present moderate subsonic Mach number, but it is appreciated readily from the increase in the shape parameter H $(=\delta_1/\Theta_{11})$ and the decrease in cf, which are results of the decrease in density towards the wall and the thickening of the viscous sub-layer; the latter is apparent when comparing the logarithmic velocity profiles of the two different test speeds. Finally, as a result of the increase in boundary layer thickness at high inlet Mach number the pressure difference between the upper and lower walls is reduced. This is especially noticeable in the bend region where the boundary layer growth reached a maximum (see Fig. 4-2).

In order to check the flow convergence and divergence on the plane of symmetry and the differences produced by the three ducts, it is useful to calculate the integral of the momentum equation in the plane of symmetry. The momentum balance principle of Fraser (1986) was adopted; using the boundary layer integral parameters and the cf values obtained, the procedure involves numerical integration, by Simpson's rule, of the boundary layer streamwise momentum equation for plane of symmetry conditions,

$$\frac{\partial\theta_{11}}{\partial s} + \theta_{11} U_s (H+2-M_e^2) - \tfrac{1}{2}cf_1 = -\theta_{11} k_s$$

where U_s and k_s are defined by

$$U_s = \frac{1}{U_e} \frac{\partial U_e}{\partial s} \quad \text{and} \quad k_s = \frac{1}{h_{2s}} \frac{\partial h_{2s}}{\partial s}$$

Here, h_{2s} is the metric element in the n direction of the streamline coordinate system (s,n,ζ) (Fig. A-1).

The results, normalized by θ_{11} at the duct inlet, are shown in Fig. 4-12. Duct M shows the expected trends in $-\int\theta_{11} k_s \partial s$ with different values of this parameter on the upper and lower walls in the bend region, which correspond to the flow divergence ($k_s>0$) and convergence ($k_s<0$) respectively; these flow conditions are confirmed by the surface oil flow shown in Figs. 4-25 and 4-26.

Figures 4-13 and 4-14 show circumferential Cp and Mach number distributions at X=412.5mm and 555mm which are at the entry to the bend and the duct outlet/engine face respectively. The distributions are not far from sinusoidal. The maximum pressure occurs on the outside wall (0°/360°) and the minimum pressure occurs on the inside wall (180°) of the bend as a direct result of the radial pressure gradient which is proportional to $\rho U^2/R$.

4.2.2 Three-dimensional data

A) Duct side wall measurements

Three-dimensional boundary layer measurements were carried out on the starboard-side wall at the mid-bend position (see Fig. 4-1), X=425mm, where crossflow is believed to be most significant. The results are presented in the form of streamwise and crosswise velocity profiles and the skew angle variations across the boundary layer; the crosswise velocity profiles are shown as Johnston type polar plots (Fig. A-2).

Results of the measurements are shown in Fig. 4-15. It can be seen that the effect of the pressure rise throughout the duct has resulted in less full and wake-like streamwise velocity profiles (high H values).

The effect of the circumferential pressure gradient is obvious from the significant skew in the boundary layer. The skew angle shows a monotonic increase towards the wall, which indicates that the interference effect of the measuring probe is negligible; however the flow angle indicated by the first point from the wall is not reliable as the probe was in contact with the wall.

Based on the bend turning angle α at the measurement location, the Hawthorne's linear inviscid theory (App. A) predicts the outer region of the triangular profile well. But the main shortcoming of the Hawthorne's formula is that it neglects viscous effects, which limits the velocity defect in the inner region of the boundary layer, and this is allowed for in Johnston's triangle model (App. A). However, both Hawthorne's prediction and Johnston's model do not appear to be entirely valid as the outer region of the crossflow is not a straight line: here the reduction of the crosswise velocity is greatest in the outermost region and the corresponding change in the vicinity of the apex lags behind. This is believed to be associated with the high H and wake-like streamwise velocity profile. Although Mager adopted a parabolic type of crossflow representation (App. A), it does not fit the outer region of this type of profile well.

The size of the measuring probe prohibited further measurements inside the inner region of the boundary layer. It is however practice to assume flow in this region to be collateral, represented, in the polar plot, by a mean straight line between the origin and the points in the vicinity of the apex; the angle of inclination of the line to the abscissa indicates the limiting streamline angle β_o. On examining the trend of the skew angle variation in the near wall region for the present case the assumption appears to be valid as it is rather unlikely that there is significant change from constant in skew angle within a small distance from the wall; although there is still a possibility that variation within the viscous sub-layer can be non-collateral, β_o indicated by the mean straight line is of important relevance in any correlation for the outer region as pointed out by Prahlad (1973). Fig. 4-15-c2 also shows that the thickening of the viscous sub-layer at high Mach number has increased considerably the range or y^+ ($=u_\tau y/\nu_w$) value of the collateral region.

B) Engine face plane measurements

Because of the flow symmetry condition, measurements were only carried out in the starboard-side half of the engine face plane.

Results of the boundary layer survey are shown in Figs.

4-16 and 4-17. Flow symmetry is implied by plots 1 and 5 which correspond to the upper wall (0°) and the lower wall (180°) respectively (see Fig. 4-1).

The streamwise velocity profiles and the corresponding logarithmic profiles are similar to the conventional two-dimensional profile, and close agreement with the law of the wall is due to the small streamwise pressure gradient; this enables the streamwise skin friction component cf_1 to be obtained by the method described in Chapter 3.

The crossflow profiles match both Johnston's and Mager's models quite well because of overall reduction in circumferential pressure gradient after the bend. The regions in which the crossflow velocity ratio, v/U_e reaches its largest values tend to correspond with the regions of highest circumferential pressure gradient (see Fig. 4-13). The trends at both inlet Mach numbers are the same, except that the increase in boundary layer thickness at high inlet Mach number has resulted in increased curvature in the outer part of the triangular profiles.

Figures 4-18 to 4-21 show the circumferential distributions of the streamwise, and crosswise integral thickness parameters, the streamwise shape parameter H and the resultant skin friction coefficient cf. Due to the near perfect symmetry of the flow, data from 180° to 360° (port-side) are duplications of the starboard-side data such that the overall engine face flow condition could easily be assessed.

The distributions of the streamwise integral parameters, δ_1, Θ_{11} and H displayed the streamwise development of the boundary layer at the engine face plane and also reveal the extreme conditions on the upper (0°) and the low (180°) walls. The cf distributions show consistent trends with the streamwise integral parameters.

The crosswise integral thicknesses show sinusoidal distributions with nominal zero thickness at stations corresponding to the duct plane of symmetry (0° & 180°), and the maxima at the highlight of the side walls (i.e. at stations 90° and 270°) which coincide with the maximum crossflow locations.

The trends at both inlet Mach numbers are the same, except for the usual increase in magnitude of the integral parameters and decrease in skin friction coefficient at high inlet Mach number.

The circumferential distributions of the boundary layer edge flow direction (relative to lines parallel to the duct outlet axis or engine axis) and the limiting streamline angles are shown in Figs. 4-22 and 4-23. The distributions show trends consistent with the crossflow and the crosswise integral parameter distributions. Unlike the other parameters, the flow angles remain identical at both speeds.

Figure 4-24 shows the total pressure ratio contours and the projections of the velocity vectors in the engine face plane. The total pressure contours remain undistorted despite the presence of the secondary flow. However, there is a significant increase in total pressure loss and the growth of the viscous region at high inlet Mach number. The direction of the secondary flow can be observed from the distribution of the projected crossflow vectors.

4.2.3 Flow visualization

The experimental results confirmed that the freestream turning angle, the limiting streamline angle and the boundary layer development remain similar for the low and higher flow speeds. Flow visualization was then carried out at an inlet Mach number of approximately 0.4 which was considered to be adequate to reveal the surface flow phenomena applicable to both flow speeds; this is also a compromise between the choices of test speed and the oil/dye mixture being used in order that a clear surface oil flow pattern could be obtained.

Figures 4-25 and 4-26 show photographs of the surface oil flow pattern taken from the engine face plane. The pattern demonstrates clear consistency with the results described earlier. It can be seen that surface flow divergence on the upper wall and convergence on the lower wall occurred some distance (at approx. X=200mm) downstream of the throat. The oil flow pattern on the upper wall also shows that the near separating boundary layer profile on the upper wall from about X=333.5mm (see also Figs. 4-4 & 4-6) did not have enough shear to drive the oil/dye mixture on the surface hence resulting in an largely undisturbed region until the re-energization of the boundary layer produced by the pressure field of the centre body. The surface oil pattern from the bend region to the duct outlet clearly reveals significant features of the secondary flow.

4.3 Duct N results

4.3.1 Plane of symmetry data

The Duct N configuration is shown in Fig. 4-27. The duct possesses a bend located immediately downstream of the throat. The bend has a mean radius of curvature of 240.0mm and provides a mean flow turning angle of 15.6°. The second bend geometry remains identical to that of Duct M.

Figures 4-28 and 4-29 show the static pressure coefficient Cp and the Mach number distributions measured along the upper and the lower walls. The effect of the first bend on re-directing the inlet flow can be seen from the marked difference in pressures between the upper and lower walls; this effect influences the flow further upstream, well into the transition duct. Soon after the first bend the pressure rises rapidly on both walls owing to the diffusing effect of the straight diffuser section. The pressure gradient reversal effect of the second bend imposes a cross-over point at about X=125mm. The presence of the upstream bend effectively neutralizes the upstream effect of the second bend as described in the discussion of the Duct M results. Consequently, the pressure levels on both walls remain very close along the straight diffusing section, but the pressure difference between the two walls at the second bend still remains quite considerable and there is no sign of convergence at the duct outlet. The trend is similar at both inlet Mach numbers, except that at high inlet Mach number there is a sharper pressure rise after the first bend, especially on the upper wall.

Figures 4-30 to 4-33 show the streamwise mean-velocity profiles and the corresponding logarithmic profiles developing along the upper and lower walls.

The velocity profiles on the upper wall have an initially favourable development owing to the favourable pressure gradient created by the inside wall of the first bend. The velocity profiles in this region exhibit a fuller shape and the favourable effect is easily noticeable from the corresponding logarithmic profiles. Immediately after the first bend, the abrupt change in pressure gradient sign causes the boundary layer to grow rapidly and the velocity profiles deteriorate to a separating profile at about X=188.5mm: at low inlet Mach number, an incipient separation shape is almost maintained throughout the region between X=188.5mm and X=420.5mm. However, at high inlet Mach number, because of the steeper pressure rise after the first bend, the boundary layer eventually separates and reverse flow profiles are formed between X=188.5mm and X=420.5mm. The boundary layer reattaches at about X=449.5mm under the influence of the centre body; the favourable effect provided by the centre body can be seen from the logarithmic profiles in this region.

The boundary layer remains fully attached along the lower wall because of the moderate pressure rise. On approaching the second bend, it can be seen that the flow accelerates on the inside wall of the second bend and is followed by an expansion, which is soon suppressed by the blockage effect of the centre body.

At the second bend, arguments about the effects of the concave and convex surfaces on the boundary layer applied to Duct M are equally valid in the present case. However, there is a much more severe circumferential migration of boundary layer fluid as a result of the separation which is to be discussed later.

Figures 4-34 to 4-37 show the boundary layer integral parameters and the skin friction coefficient distributions. The integral parameter development on the upper wall fully revealed the separation condition in the region between X=188.5mm and X=420.5mm; integration over the separation profile results in a raised value of the displacement thickness parameter δ_1 and a lowered value of the momentum thickness Θ_{11}; this is especially so at high inlet Mach number where reverse flow profiles are presented. The corresponding drastic change in the shape parameter H in the separation region can be seen in Fig. 4-36.

Similar pressure gradients on the lower wall in both test cases produced similar δ_1 and Θ_{11} distributions, compressibility having only a marginal effect on these thickness parameters, but a more distinct effect on the H and cf distributions.

The boundary integral parameters and cf as measured along the plane of symmetry are used in a momentum balance check, as in the Duct M test case. The results are shown in Fig. 4-38. Compared with Duct M (Fig. 4-12), Duct N shows a different behaviour owing to the effect of the upstream bend.

On the upper wall, the effect of the first bend can be seen to have caused the flow to converge initially. However, severe flow divergence occurs subsequently as the second bend effect begins to dominate; results for the high inlet Mach number beyond X=188.5mm should however be interpreted with caution as the validity of the momentum balance is questionable since reverse flow is present. Nevertheless, the results still show trends similar to those of the low speed test case.

Flow development on the lower wall can be seen to have virtually zero convergence or divergence and hence appears to be two-dimensional; this is consistent with the surface oil flow of Fig. 4-52, which shows that flow on the lower wall in the vicinity of the plane of symmetry looks very much like a two-dimensional flow. This flow condition could be explained by the thin boundary layer along the wall and the drastic development of δ_1 on the upper wall which has significantly altered the effective flow geometry of the duct.

Figures 4-39 and 4-40 show the circumferential Cp and Mach number distributions in the cross-sectional planes at X=412.5mm and X=555 which are at entry to the second bend and the engine face respectively. At X=412.5mm, the pressure distribution between the circumferential stations 0°-60° and 300°-360° shows a 'flat' region (i.e. constant pressure), which indicates likely regions of vanishing skin friction and the circumferential extent of the separation region at this cross-sectional plane. Pressure distributions at X=555mm indicates that flow reattachment has taken place, allowing the boundary layer to develop in a region of significant circumferential pressure gradient.

4.3.2 Three-dimensional data

A) Duct side wall measurements

Three-dimensional boundary layer surveys were carried out on the starboard side wall of the duct at three streamwise locations: X=50.0, 130.0 and 425.0mm (see Fig. 4-27), which are at the middle and downstream of the first bend and the middle of the second bend respectively. At the first two measurement positions, the measuring probe was set parallel to the duct centre line in the straight diffusing section after the first bend. At the third position, the probe was set parallel to the duct outlet section centre line.

Results of the measurements are shown in Fig. 4-41. Streamwise velocity and the skew angle variations across the boundary layer are presented. The crossflow variation is shown in the form of a polar plot.

The polar plot at the first position is similar to the normal triangular shape; it also indicates that the freestream turning angle followed closely the bend turning angle as shown by Hawthorne's prediction. Although there exists a large pressure difference between the inside and outside wall of the bend, it does not give rise to significant crossflow because of the thin boundary layer and the small mean curvature of the bend.

Measurements at the second position show that the crossflow dies away fairly rapidly soon after the first bend as the circumferential pressure gradient changes direction, but the crossflow at high inlet Mach number appears to have persisted longer.

At the third position, it can be seen from the streamwise velocity profile that the boundary layer is approaching a separation profile. The circumferential pressure gradient affects the inner part of the boundary layer most because of the low momentum fluid in the inner region; this can also be seen from the magnitudes of the crossflow and the limiting streamline angle. Consequently, the outer region of polar plot becomes highly curved. Crossflow models of Johnston and Mager do not fit this profile.

It can be seen from the side wall measurements that as a result of the incipient flow separation at low speed, and the flow separation and reattachment at high speed on the upper wall, the effective duct flow geometry has been significantly altered; hence the freestream turning path at the second bend no longer follows the bend curvature (cf. Fig. 4-15 of the Duct M results).

B) Engine face plane measurements

Results of the boundary layer survey carried out at the engine face plane are shown in Figs. 4-42 and 4-43. The circumferential variations of the crossflow are shown in the form of polar plots. The corresponding skew angle variations, streamwise and logarithmic velocity profiles are also presented.

Despite the flow separation upstream, flow symmetry about the duct plane of symmetry is still maintained. This can be seen in the measurements at stations 1 and 5 .

Stations 1 and 2 are located downstream of the separation region, hence measurements show re-developing type profiles. The polar plot at station 2 shows a re-developing type crossflow profile, which is similar to the type found behind a separation bubble on a swept wing [D9].

Measurements at station 3 show the further downstream development of the side wall profile at X=425mm described earlier (Fig. 4-41). It can be seen from the polar plot that the curved outer region of the near separation profile is still retained.

The station 4 location is remote from the separation region, and owing to the reduction in circumferential pressure gradient on the lower wall, the polar plot of the crossflow resumes a normal triangular shape.

The overall trend at both inlet test speeds is the same, but the differences highlight the increase in the effect of the separation at higher speeds.

Figures 4-44 to 4-47 show the circumferential distributions of the streamwise, and crosswise integral thickness parameters, the streamwise shape factor and the resultant skin friction coefficient.

The streamwise integral parameters show different trends when compared with those of Duct M. Both δ_1 and θ_{11} distributions show a peak on either side of the upper wall, and decrease fairly rapidly to a minimum towards the lower wall. The type of distribution suggests that concentrated vortices may have formed within the boundary layer as a result of adverse streamwise and cross-wise pressure gradients; these vortices may then cause the eruption of the boundary layer fluid in the vicinity of the upper wall.

The crosswise integral parameters increase significantly owing to the severe crossflow generated as a result of the flow separation and reattachment occurring upstream. The major increase can also be seen to occur in the vicinity of the upper wall. It can be observed that the integral thickness distributions are consistent with the crossflow distribution at the engine face shown in Fig. 4-50.

The circumferential distributions of boundary layer edge flow direction and the limiting stream line angle are shown in Figs. 4-48 and 4-49. The severity of the crossflow is again demonstrated by the large limiting streamline angles shown.

The crossflow distributions and the total pressure contours at the compressor plane are shown in Fig. 4-50. The distortion of the total pressure contours and the increase in the viscous region in the upper half of the plane are the results of the upstream flow separation and possible vortex formation. The conditions at both inlet Mach numbers remain similar, but there is a considerable reduction in total pressure recovery at high inlet Mach number.

4.3.3 Flow visualization

Flow visualization was carried out at an inlet Mach number of 0.4 as it was anticipated that the incipient nature of the separation on the upper wall at low speed would not produce a distinct oil flow pattern sufficient to illustrate the surface flow phenomenon. Figs. 4-51 to 4-52 show photographs of the surface oil flow pattern taken from the engine face plane. Fig. 4-51 shows the complexity of the separation on the upper wall occurred downstream of the first bend.

After detailed examination of the surface oil flow pattern, most of the critical points can be identified; a critical point is the point where the wall shear stress trajectories do not follow uniquely defined directions and where the wall shear stress is zero (App. B). In joining these points together and applying the corresponding characteristic directions associated with each critical point, the separation lines and the attachment lines then become identifiable. Finally the surface topological map of the separation is constructed and depicted on the transparency overlapping Figs. 4-51 to 4-52.

Owing to the weak nature of the surface flow at the beginning of the separation, a clear surface oil flow pattern cannot be obtained; therefore a definite surface shear stress topology in the early part of the flow separation cannot be confirmed. The separation appears to begin on each side of the duct plane of symmetry line with an open (Wang 1972) or local (Tobak & Peake 1985) separation line (OS); that is, the line does not originate from a critical point. Instead only gradual convergence of wall shear stress trajectories indicates that the flow leaves the vicinity of the wall; later findings of Duct J suggested that flow separation in Duct N could merely be a weaker version of the vortex type separation (see Duct J results).

The following discussion refers to the downstream region of the separation: the separation line (OS) can be seen to have terminated at the saddle point S downstream, where it also meets the attachment line A on the edge of the side wall. A reattachment nodal point, N is clearly visible on the plane of symmetry line in the second bend region; the location of this point is in fact directly opposite to the nose of the centre body, which was removed when the photograph was taken. The connection between the nodal point N and saddle point S can be seen to have formed another attachment line. There is uncertainty regarding the upstream connection of the nodal point N owing to the problem with the surface oil flow in the area. However, it can be inferred from the measurements along the plane of symmetry and the general topological features of the surrounding oil flow pattern that a separation type saddle point is likely to be present. Finally, it can be said that the line A-S-N-S-A forms a boundary between the separation region on the upper wall and the well developed flow on the rest of the duct wall.

Three-dimensional flow separation often is a characteristic feature accompanying vortex development. In the present case, flow leaves the surface on either side of the separation line OS and forms a dividing stream-surface, which normally rolls-up to form a vortex system. Since the surface oil flow pattern cannot uniquely define the separated vortex field (Dallmann 1985), it is possible that the vortex system could either terminate at or continue beyond the saddle point S. In either case, streamwise swirling motions are induced, which can be explained by the Biot-Savart law of induced velocity, hence supporting the particular distributions of boundary layer integral parameters at the engine face.

Although flow reattachment has taken place the severity of the crossflow at the second bend and the duct outlet is apparent from surface flow directions as indicated by the surface oil flow pattern.

Figure 4-52 also shows the surface oil flow pattern on the lower wall of the duct. It can be seen that there is negligible crossflow on most of the lower wall, hence confirming the earlier discussion on the results of the momentum balance on the lower wall.

4.4 Duct J results

4.4.1 Plane of symmetry data

The Duct J configuration is shown in Fig. 4-53. The duct geometry is similar to that of Duct N, but with a much tighter first bend: the bend has a mean radius of curvature of 191.0mm and provides a mean flow turning angle of 22.7° to the inlet flow. The second bend geometry remains identical to that of Ducts M and N.

Figures 4-54 and 4-55 show the static pressure coefficient Cp and the Mach number distributions along the upper and the lower walls on the plane of symmetry. The distributions can be observed to be a further development of those of Duct N as the first bend curvature increases. The pressure difference between the upper and lower walls at the bend increased by an average of 37%. The upstream and downstream influence of the first bend intensified with the downstream effect extended further downstream. Hence, much of the upstream influence of the second bend is neutralized until about X=260mm, but there is a considerable increase in pressure difference between the upper and lower walls at the second bend.

The trend for low and high inlet Mach numbers is again the same, but the Cp levels at the two test speeds appear to be much closer than the previous two ducts tested. Similar to Duct N, there is a steeper pressure rise on the upper wall after the first bend at high inlet Mach number.

Figures 4-56 to 4-59 show the streamwise mean-velocity profiles and the corresponding logarithmic profiles developed along the upper and lower walls on the plane of symmetry.

The velocity profiles on the upper wall have an initially favourable development between entry and the first bend due to the accelerating flow on the early part of the inside wall of the bend. After the bend, the profiles have developed into a separating profile at the end of the steep pressure rise at X=130.5mm. Thereafter, severe flow separation occurs, which prevents measurements being carried out until X=449.5mm, where flow reattachment is found to have occurred under the influence of the centre body. The logarithmic velocity profiles at the second bend show a significant destabilising concave curvature effect, which may also be connected with the development of the flow through separation and reattachment. Further downstream of the reattachment, the favourable effect of the centre body has resulted in re-developing profiles with severe overshoot in the near wall region (see profile at X=555mm), especially at high Mach number; almost certainly, the boundary layer will have departed severely from equilibrium. The shear stress profile $-\rho\overline{u'v'}(y)$ cannot therefore be assumed to be directly related to the mean-velocity profile u(y). Unlike the Duct N test case, the separating condition at both test speeds remains similar.

The boundary layer remains fully attached along the lower wall. The velocity profile development resembles closely those of Duct N, except that the pressure gradient change at the first bend is reflected more clearly in the logarithmic profiles as a result of increases in bend curvature and the flow appears to be over expanded at the second bend, which can be seen from the increase in departure of the inner region of the boundary layer from the wall law.

Figures 4-60 to 4-63 show the boundary layer integral parameters and the skin friction coefficient distributions.

On the upper wall, no integral parameters were obtained in the separation region. Although the separating conditions are similar at both the low and high inlet Mach numbers, the integral parameter distributions reveal that the separation increases in severity at high speed, and there appears to be a delay in reattachment. These features could also be observed in the velocity profiles shown.

On the lower wall, distributions of δ_1 and θ_{11} show that the boundary layer growth is further suppressed by the increase in extent of the separation on the upper wall when compared with the Duct N results. The shape factor distribution shows that velocity profiles maintain a constant shape throughout the straight diffusing section. The cf distribution also shows a consistent trend with the wall pressure distribution and velocity profile development. The compressibility effect could again be appreciated by noting the different levels in H and cf distributions at different inlet Mach numbers.

Due to the lack of data on the upper wall, a momentum balance check is carried out only on the lower wall and the results are shown in Fig. 4-64; this indicates that flow convergence or divergence is negligible on the lower wall, which is similar to Duct N with virtually two-dimensional flow. The surface oil flow of Fig. 4-78 confirms this finding.

Figures 4-65 and 4-66 show the circumferential Cp and Mach number distributions in the cross-sectional planes at X=412.5mm and X=555mm, which are at entry to the second bend and the engine face respectively. The distributions are similar to those of Duct N, except that there is an overall reduction in Cp level, and an increase in pressure difference between the upper wall (0/360°) and the lower wall (180°) at X=412.5mm; the constant pressure region on the upper wall indicates the circumferential extent of the separation at this station.

4.4.2 Three-dimensional data

A) Side wall measurements

Three-dimensional boundary layer surveys were carried out on the starboard wall of the duct at three streamwise locations: X=50, 130 and 425mm, which are at the middle and downstream of the first bend and the middle of the second bend respectively (see Fig. 4-53). At the first two measurement positions, the measuring probe was set parallel to the duct centre line in the straight diffusing section after the first bend. At the third position, the probe was set parallel to the duct outlet section centre line. Results of the measurements carried out at these positions are shown in Figs. 4-67

Compared with the Duct N results, the increase in the first bend curvature has resulted in a significant increase in the freestream turning angle. Measurements downstream of the first bend show that the crossflow has reduced considerably, but a significant amount still persists, especially at high inlet Mach number.

The boundary layer at the mid-second bend position behaves quite differently from the Duct N flow. It can be seen from the streamwise velocity profile that although the measurement position is immediately outside of the separation region there is no sign of the boundary layer approaching separation as found in the Duct N results, and the corresponding polar plot of the crossflow, although having a peculiar curved outer region especially at high Mach number, shows a nominally triangular shape. This could be understood by noting the following: Firstly, there is an overall reduction in pressure rise after the first bend. Therefore, flow outside the separation region still remains to be diffused; this can be observed from the fuller shape of the streamwise velocity profile. Secondly, an increase in domination of the first bend occurs as the bend curvature increases, which has the effect of maintaining the crossflow generated at the bend much further downstream; this is evident from the crossflow measurement results described above.

Hawthorne's formula predicts the freestream turning at both bends well, but Mager's model does not fit the crossflow profile at the second bend owing to the large limiting streamline angle and the peculiar skew angle variation.

B) Engine face plane measurements

It was realized in this test case that flow symmetry about the duct plane of symmetry is no longer preserved, therefore, a complete circumferential boundary layer survey was carried out at the engine face. The results are shown in Figs. 4-68 and 4-69.

Measurements at stations 1, 2 and 8 show re-developing type profiles downstream of the separation region. The polar plots of the crossflow at stations 2 and 8 show re-developing profiles with highly curved outer regions, indicating that the effect of the circumferential pressure gradient on re-developing boundary layer is most severe; it is believed that there is a severe displacement between the surface shear-stress vector direction $\tan^{-1}(\overline{w'v'}/\overline{u'w'})$ and the mean-velocity gradient direction $\tan^{-1}(\partial v/\partial u)$ owing to the non-equilibrium flow after reattachment [D11]. However, the profiles at stations 3 and 7, which are immediately outside the separation region, do not appear to be affected by the flow separation and reattachment or the non-equilibrium flow; these results are also consistent with the reasoning put forward earlier in the side wall measurements discussion. From stations 3 to 5 and 7 to 5 the crossflow magnitudes show a corresponding decrease as the circumferential pressure gradient decreases towards the lower wall (180°). The trend is similar for both inlet Mach numbers tested, but flow asymmetry is intensified at high inlet Mach number.

Figures 4-70 to 4-73 show the circumferential distributions of the streamwise, and crosswise integral thickness parameters, the streamwise shape factor and the resultant skin friction coefficient.

The distributions can also be seen to be affected by the flow asymmetry, and the asymmetry effect is especially noticeable from the crosswise thickness parameter distributions. However, the overall trends could still be observed to be similar to those of Duct N: compared with the Duct N results (Figs. 4-44 to 4-47), the maxima and minima on the streamwise and crosswise thickness parameters distributions appear to be more distinctive with increases in amplitudes; these suggest the possible increase in intensity of the concentrated vortices that might have formed within the boundary layer. The streamwise shape factor and the resultant skin friction coefficient distributions, however, show much smoother variations.

The circumferential distributions of boundary edge flow direction and the limiting streamline angle are shown in Figs. 4-74 and 4-75. It can be observed that flow asymmetry occurs mainly within the boundary layer. Unlike the Duct M and N test cases, the peak limiting streamline angles are mainly confined to regions downstream of separation.

The crossflow distributions and the total pressure contours at the compressor plane are shown in Fig. 4-76. Flow in most part of the upper half plane becomes fully viscous as the boundary layer grows to an extent that it merges with the centre body boundary layer. The distortion of the total pressure contours in the upper half of the plane is now worse. The flow asymmetry becomes more pronounced at high inlet Mach number. It can be seen that the aerodynamic plane of symmetry no longer coincides with the geometric plane of symmetry. However, the basic flow features remain largely unaltered.

4.4.3 Flow visualization

Flow visualization was carried out at an inlet Mach number of 0.4. As a result of the severe flow separation in the duct, a clear surface oil flow pattern was obtained, which revealed in detail the separation phenomenon on the upper wall of the duct.

Figures 4-77 to 4-78 show photographs of the surface oil flow pattern. It can be seen that the separation occurs immediately after the first bend following abrupt pressure gradient reversal (see Fig. 4-54) and that the separation begins on each side of the duct symmetry plane line with a three-dimensional vortex type flow separation with spiral focus critical point ensembles (App. B), that is critical point with vortical flow springing from the surface; four such points can be identified in the region. However, the rest of the separation feature remains largely similar to that of Duct N.

In the present test case the separation pattern exhibits slight asymmetry about the duct plane of symmetry, which is likely to be caused by fluctuations as well as imperfections in the inlet flow and boundary conditions. However, the overall separation phenomenon can be said to be nominally symmetrical about the plane of symmetry. It is also noted that general flow asymmetry about the plane of symmetry is related directly to slight flow separation asymmetry.

Topological analysis was carried out on the oil flow pattern in the separation region; three further critical points, saddle points S, are established in the vicinity of the foci (F) to complete a structurally stable surface separated flow. The resulting map of the surface topological structure of the separation is shown in Fig. 4-77.

Based on Fig. 4-77, various possible spatial separation flow structures can be conjectured. Fig. 4-79 show two of such possibilities. The conjectured separation flowfield includes the concatenation of the vortex systems generated as a result of the three-dimensional flow separation; here the plane of symmetry pattern is inferred from experimental observations and Hunt's topological rule (Hunt et al 1978) illustrated in Fig. 4-80, where the resulting pattern can be identified as the plane of symmetry pattern of a U-shaped vortex system (Peake & Tobak 1982) with the spatial critical point N introduced being the core of the vortex.

Figs. 4-79a and 4-79b show, respectively, that the concatenated vortex system could either terminate at or continue beyond the downstream saddle point S. For the latter, the vortex filaments will be stretched and intensified owing to the blockage effect of the centre body (Helmhotz theorem). In either case, streamwise swirling motions are introduced (Biot-Savart law), which are evident from the distributions of the boundary layer integral parameters at the engine face.

Although the type of separation encountered is severe and complex, it can be deduced from the topological map of the surface flow that, since there is no saddle to saddle critical points connection, the separated flow field are structurally stable (Peake & Tobak 1982, Dallmann 1983); that is, changes in parameters such as Mach number and Reynolds number and further increase in upstream bend curvature or duct offset would result in the same topological surface separation flow structure. It is believed that such structural stability is maintained by the bounding duct wall, and especially the centre body.

4.5 Concluding remarks

Tests were performed at inlet Mach numbers of nominally 0.15 and 0.6 for three different S-shaped intakes ducts; namely, ducts J, M and N each having different upstream bends but common downstream bend geometries.

In addition to the surface pressures and Mach number distributions, boundary layer data are presented in the form of mean-velocity profiles - streamwise and crosswise - and integral parameters.

The majority of the streamwise velocity profiles possess substantial linear regions on semi-logarithmic plots which are in good agreement with the law of the wall, thus enabling skin friction coefficients to be calculated.

The linear inviscid theory of Hawthorne predicted some of the freestream turning in the bend region well. Crossflow models of Johnston and Mager seem only to be suitable for boundary layers in region away from separation and re-developing layer regions.

Effects of compressibility can be seen to have increased the rate of pressure rise and the thickness of the boundary layer, hence increasing the rate of deterioration of the diffusing duct flow.

Detailed evidence is presented indicating a firm trend towards three-dimensional vortex type flow separation as the upstream bend increased in severity. Although the centre body which represents the engine compressor face centre bullet forced the separated flow to reattach prior to the engine face, the flow at the engine face is however far from uniform.

Table 4-1 shows the commonly used engine face performance coefficients, for the assessment of intake duct flow quality, calculated for each duct at the typical operating inlet Mach number of nominally 0.6. Effect of flow separation can seen to have significantly increased the distortion coefficients of Duct N and J, thus the engine surge margin will be reduced accordingly; the DC60 value of Duct J is approaching the maximum acceptable value for most large pitch blade row compressor designed for noise reduction [B3]. The associated reduction in total pressure recovery coefficient will directly affect the engine thrust, which is related to the coefficient on a greater than 1:1 basis. Although Duct M appears to be most efficient, it could only be used for submerged type intake owing to its configuration thus losing the benefit, possibly, of pre-diffusion.

DUCT	M_{in}	η(%)	SC60(%)	DC60(%)
M	0.635	97.0	2.2	6.34
N	0.610	96.7	2.9	9.60
J	0.600	95.7	6.2	21.5

Table 4-1 Engine face performance coefficients

M_{in}	inlet Mach number
η	total pressure recovery coefficient = $\bar{P}_f/P_{oin}$
SC60	swirl coefficient = $\bar{V}_{60max}/U_{in}$
DC60	distortion coefficient = $(\bar{P}_f - \bar{P}_{60min})/Q_f$

where

$\bar{P}_f$	area average total pressure at the engine face
$\bar{P}_{60min}$	minimum average total pressure in a 60° sector of the annular section at the engine face
P_{oin}	inlet total pressure
$\bar{V}_{60max}$	maximum average circumferential velocity in a 60° sector of the annular section at the engine face
U_{in}	mean inlet velocity
Q_f	mean dynamic head at the engine face

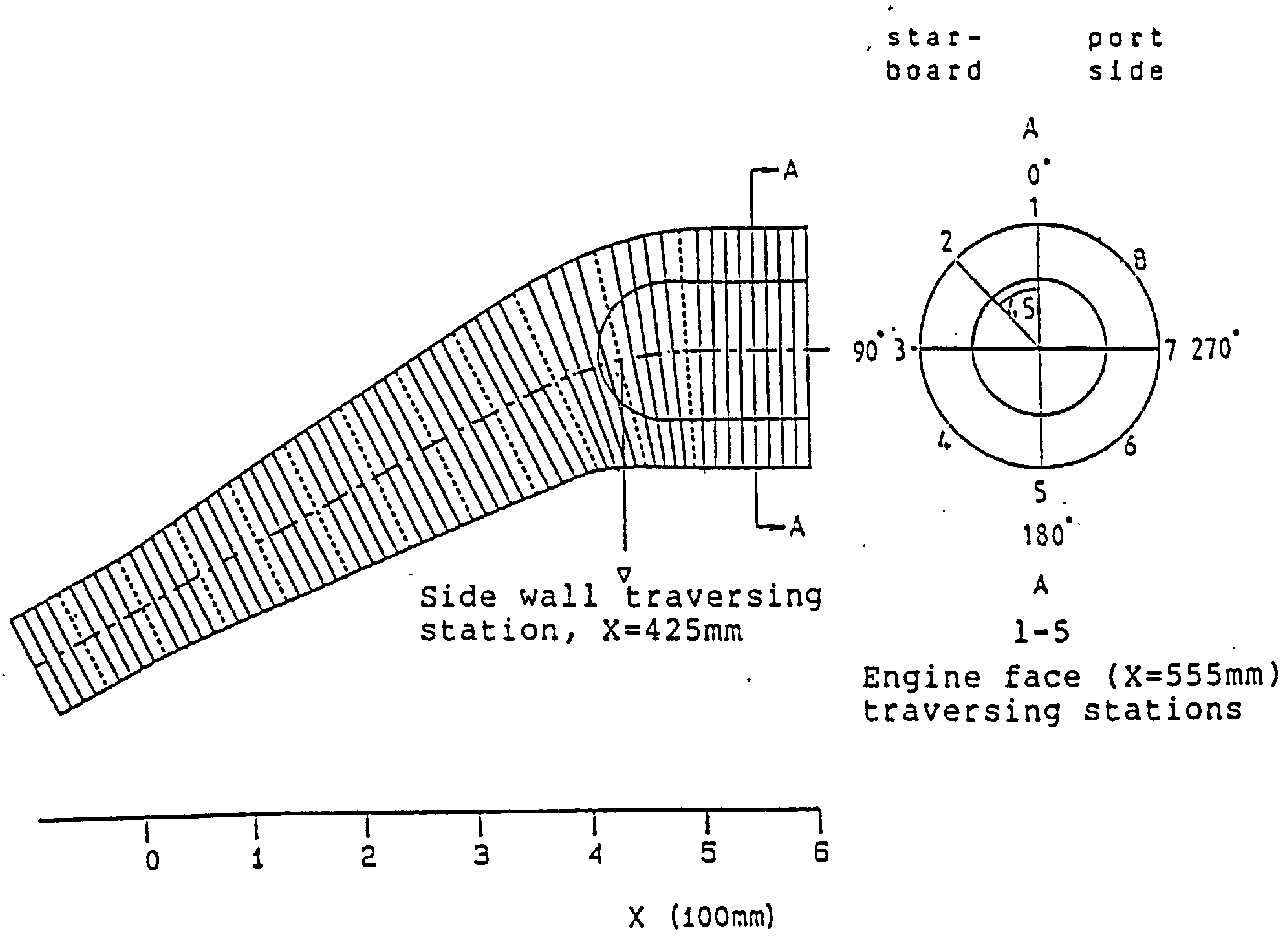

FIG. 4-1 DUCT M PROFILE

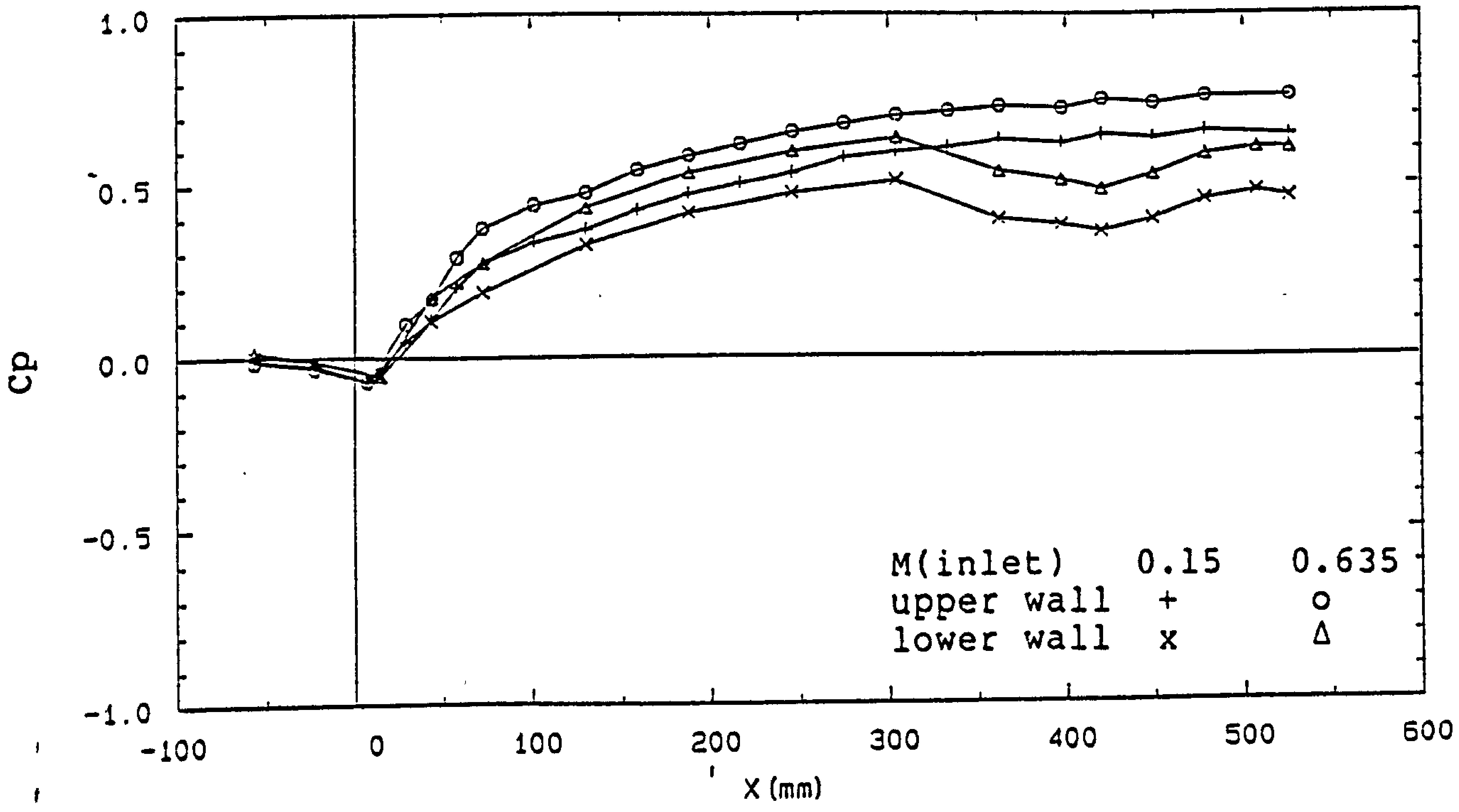

FIG. 4-2 PRESSURE DISTRIBUTIONS (DUCT M)

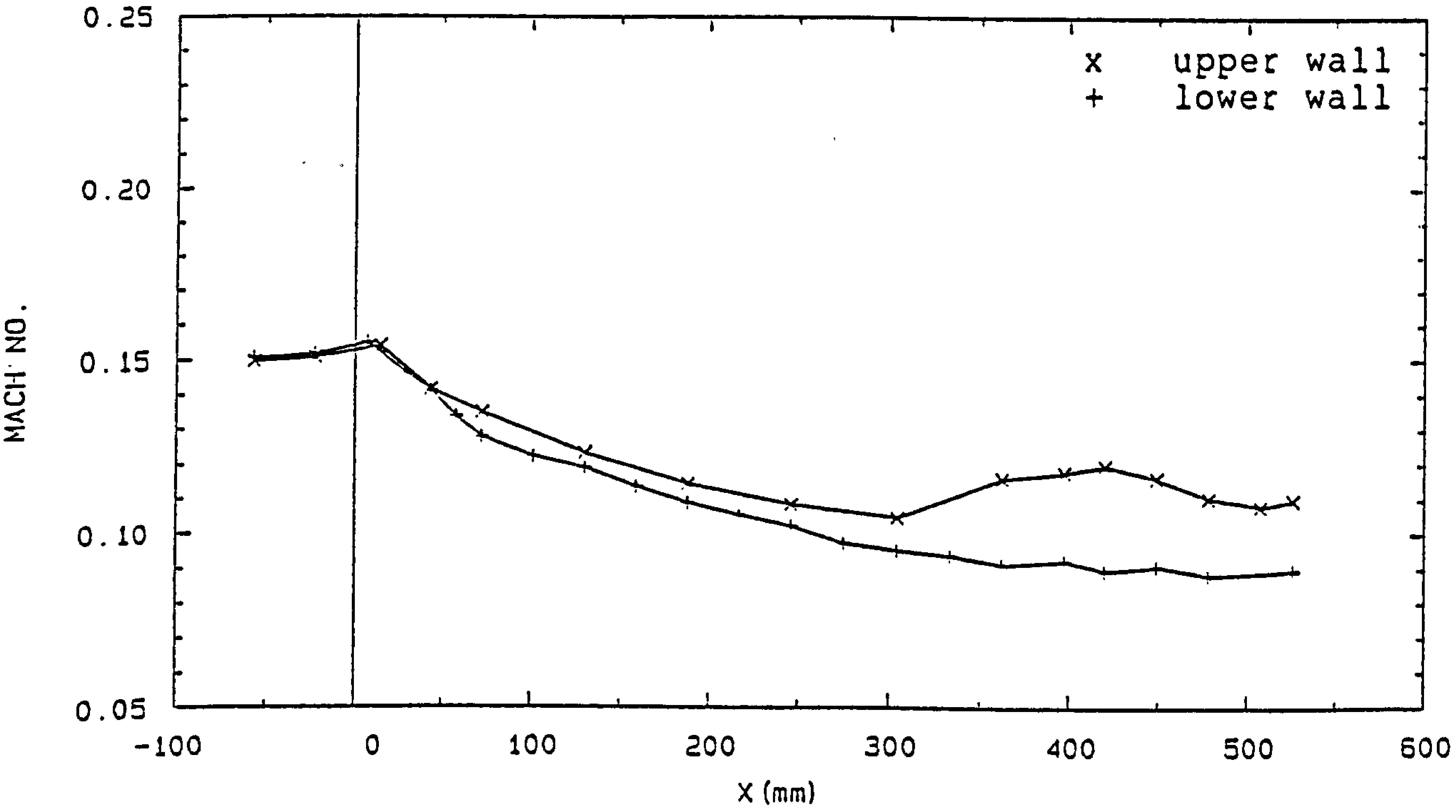

a) $M_{inlet} = 0.15$

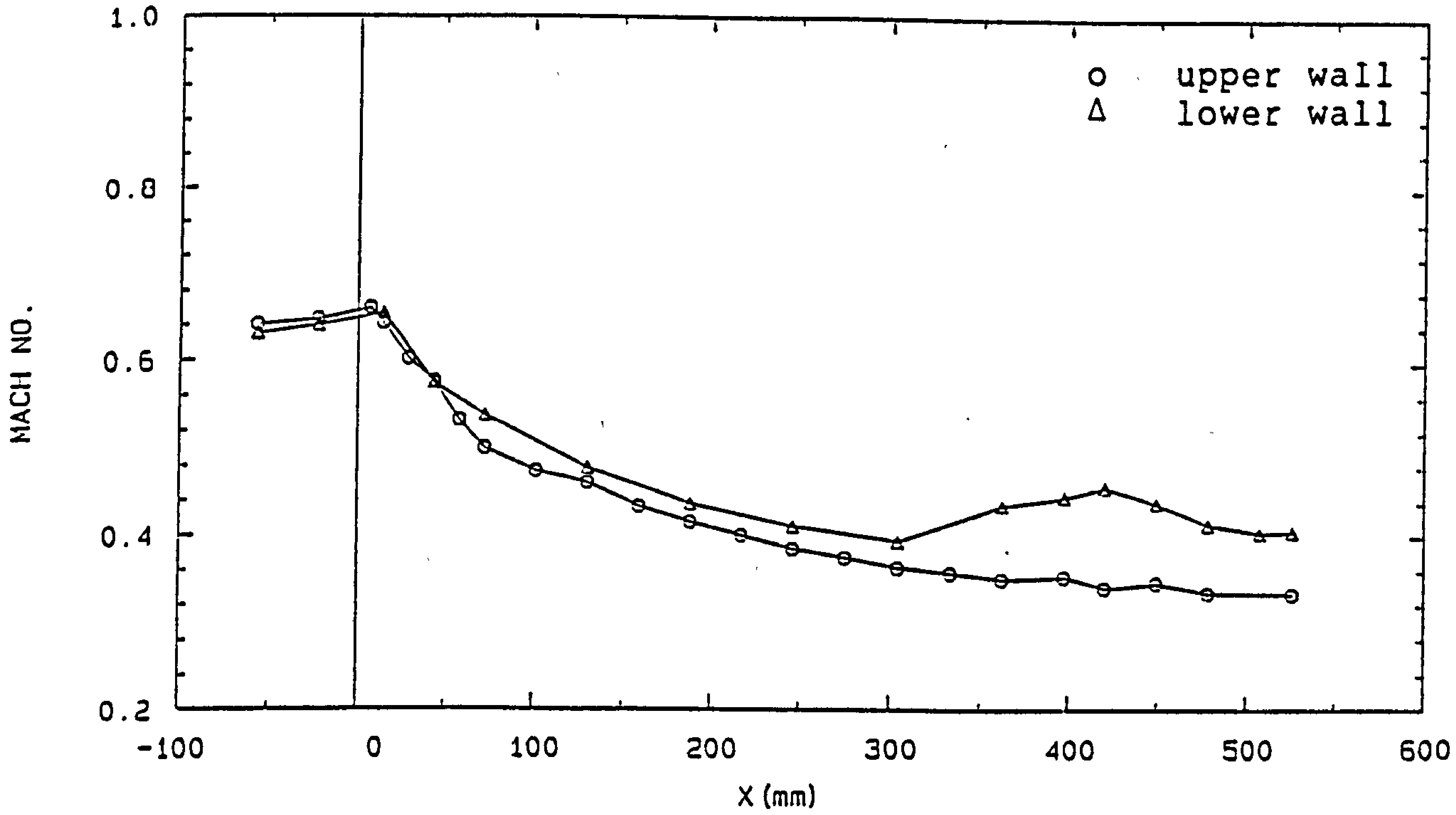

b) $M_{inlet} = 0.635$

FIG. 4-3 MACH NUMBER DISTRIBUTIONS (DUCT M)

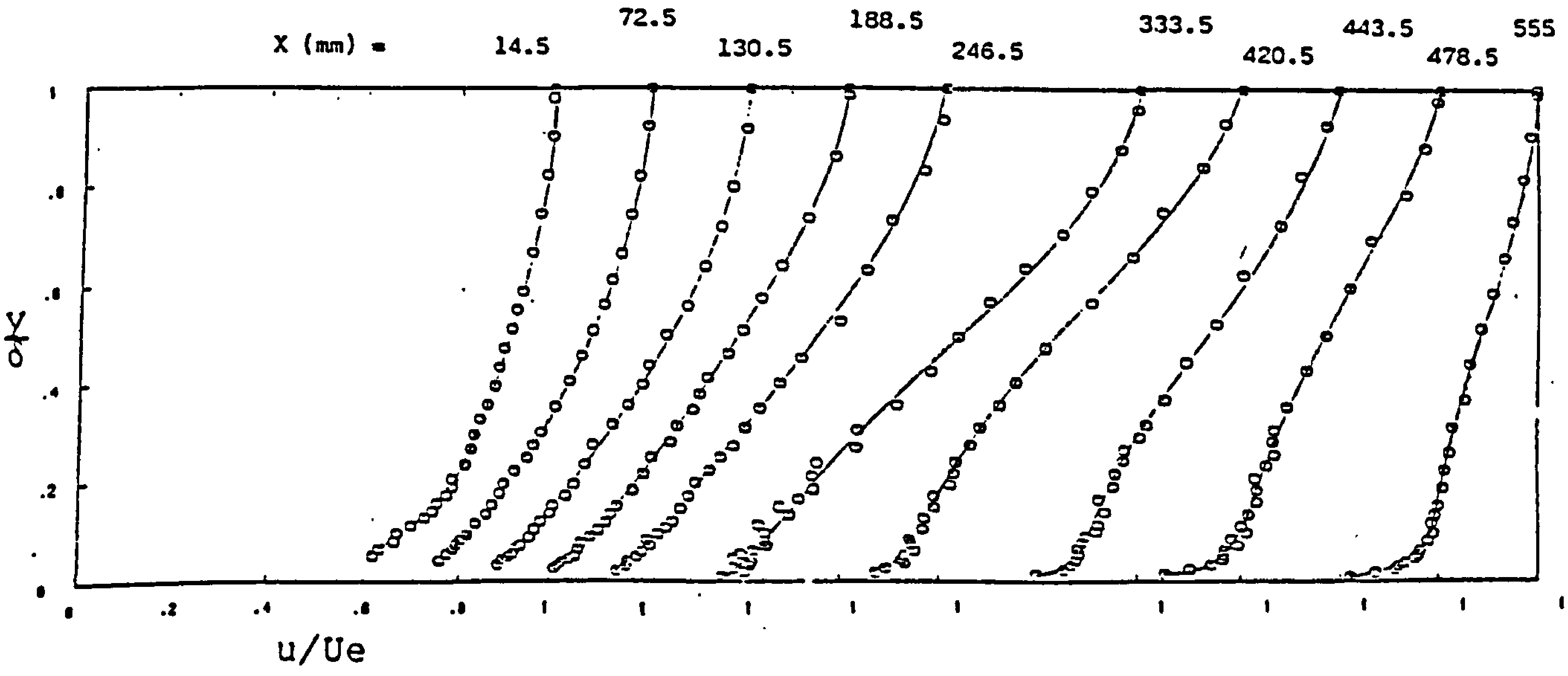

a) Upper wall

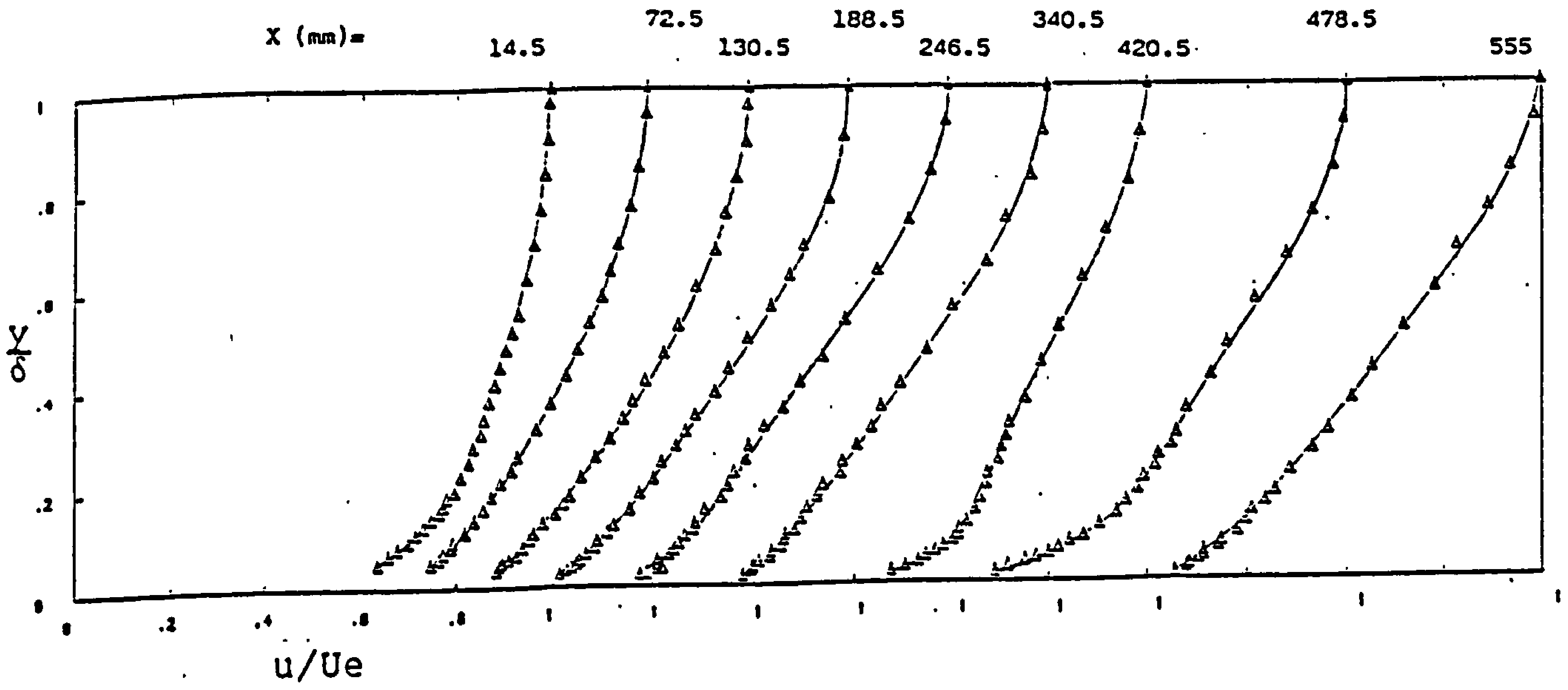

b) Lower wall

$M_{inlet} = 0.15$

FIG. 4-4 VELOCITY PROFILES (DUCT M)

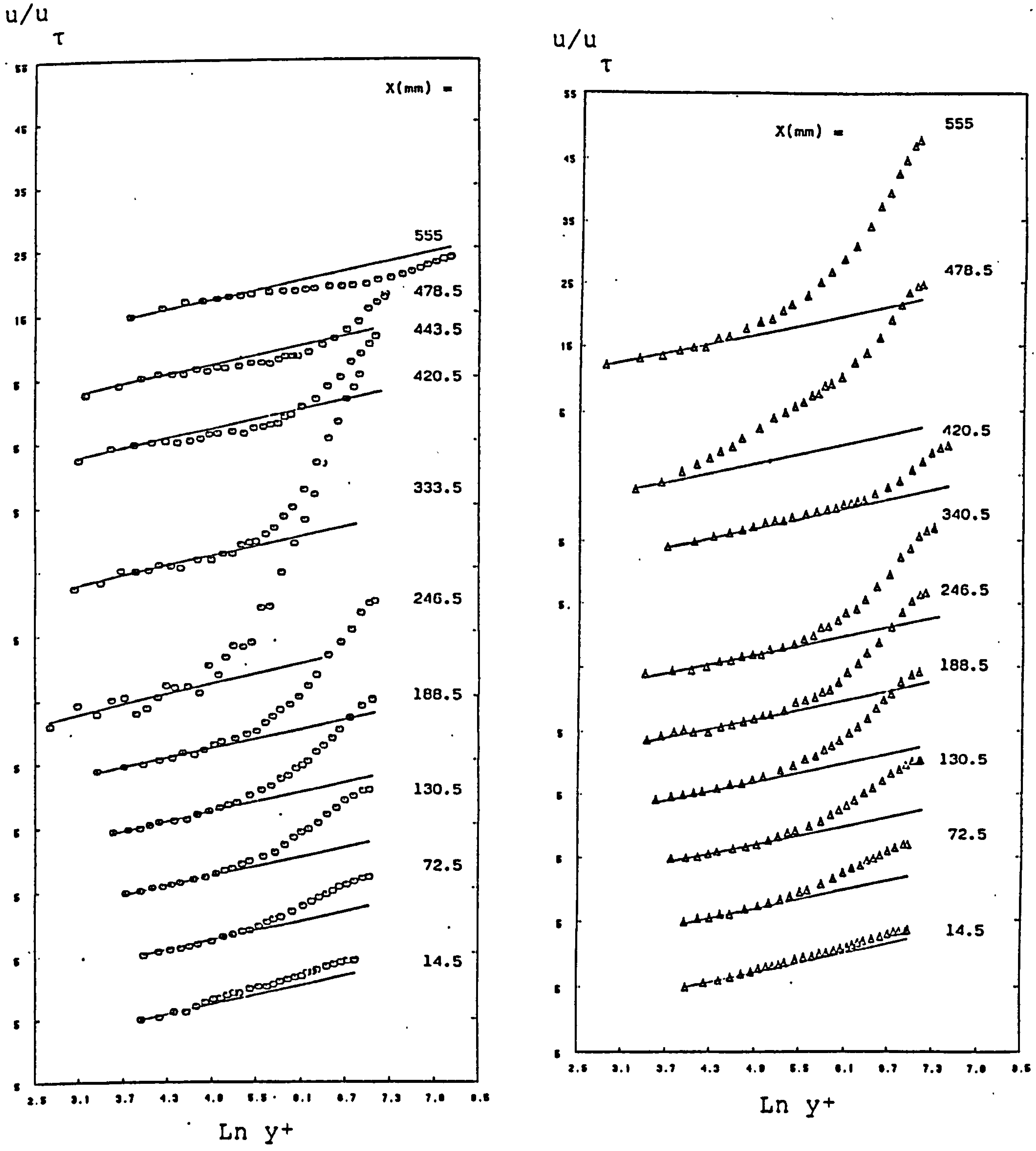

a) Upper wall b) Lower wall

M_{inlet} = 0.15 ——— Law of the wall

FIG. 4-5 LOGARITHMIC VELOCITY PROFILES (DUCT M)

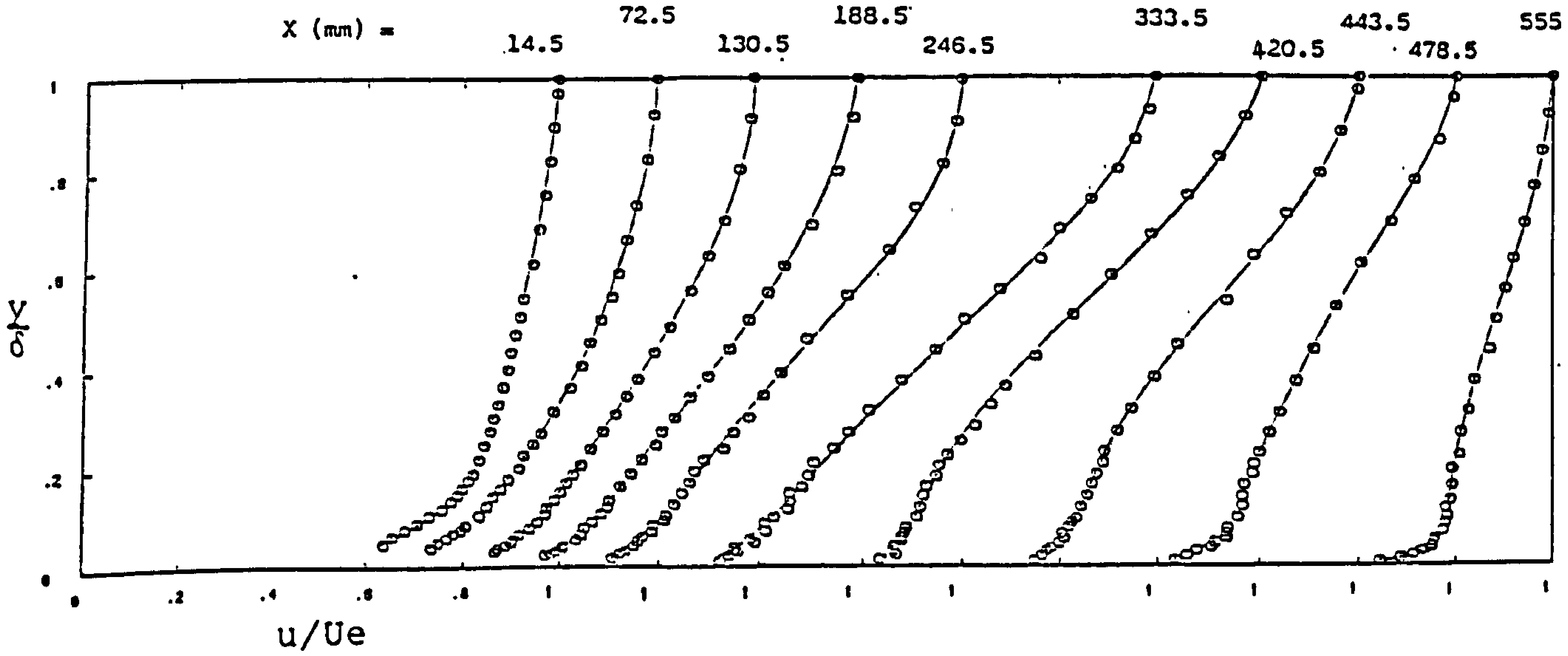

a) Upper wall

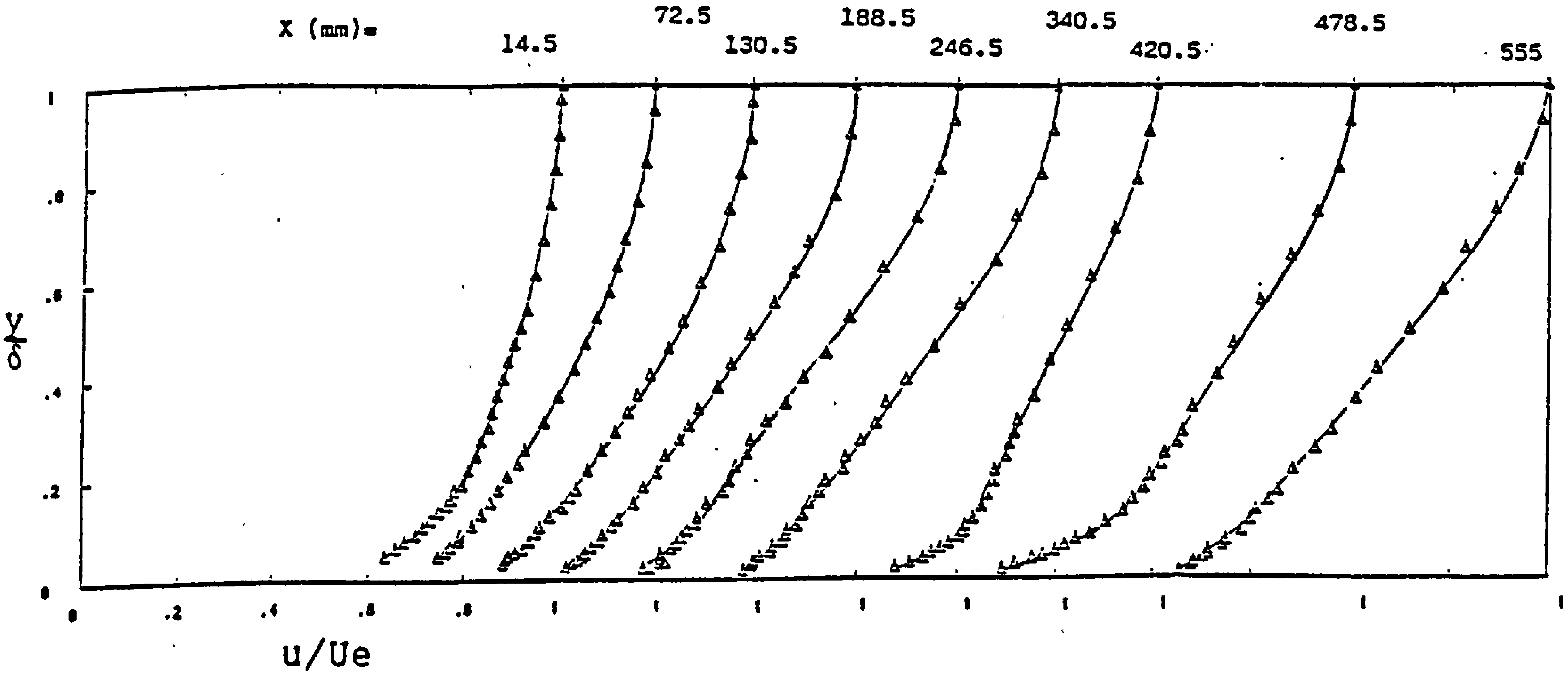

b) Lower wall

$M_{inlet} = 0.635$

FIG. 4-6 VELOCITY PROFILES (DUCT M)

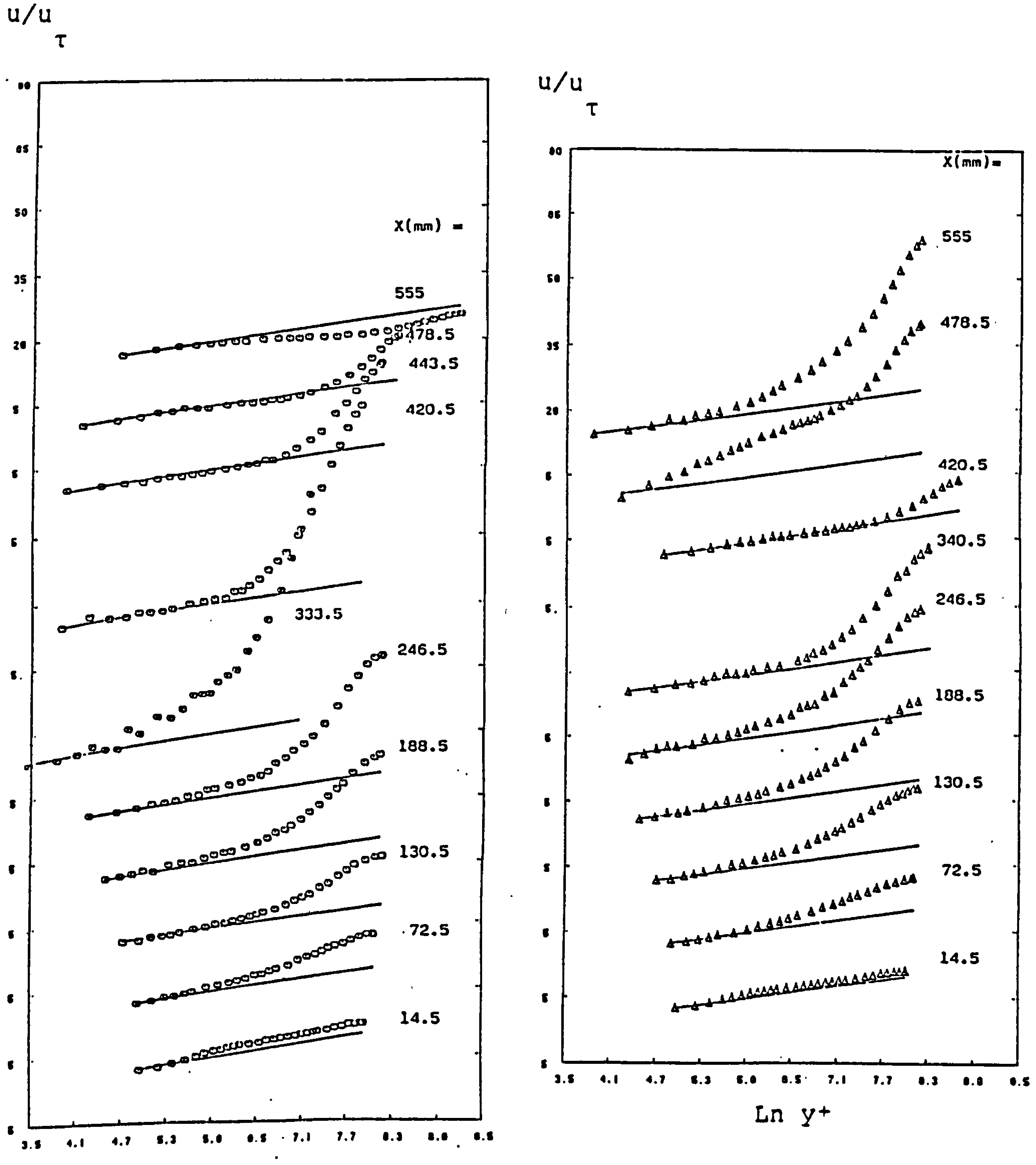

a) Upper wall   b) Lower wall

M_{inlet} = 0.635   ____ Law of the wall

FIG. 4-7 LOGARITHMIC VELOCITY PROFILES (DUCT M)

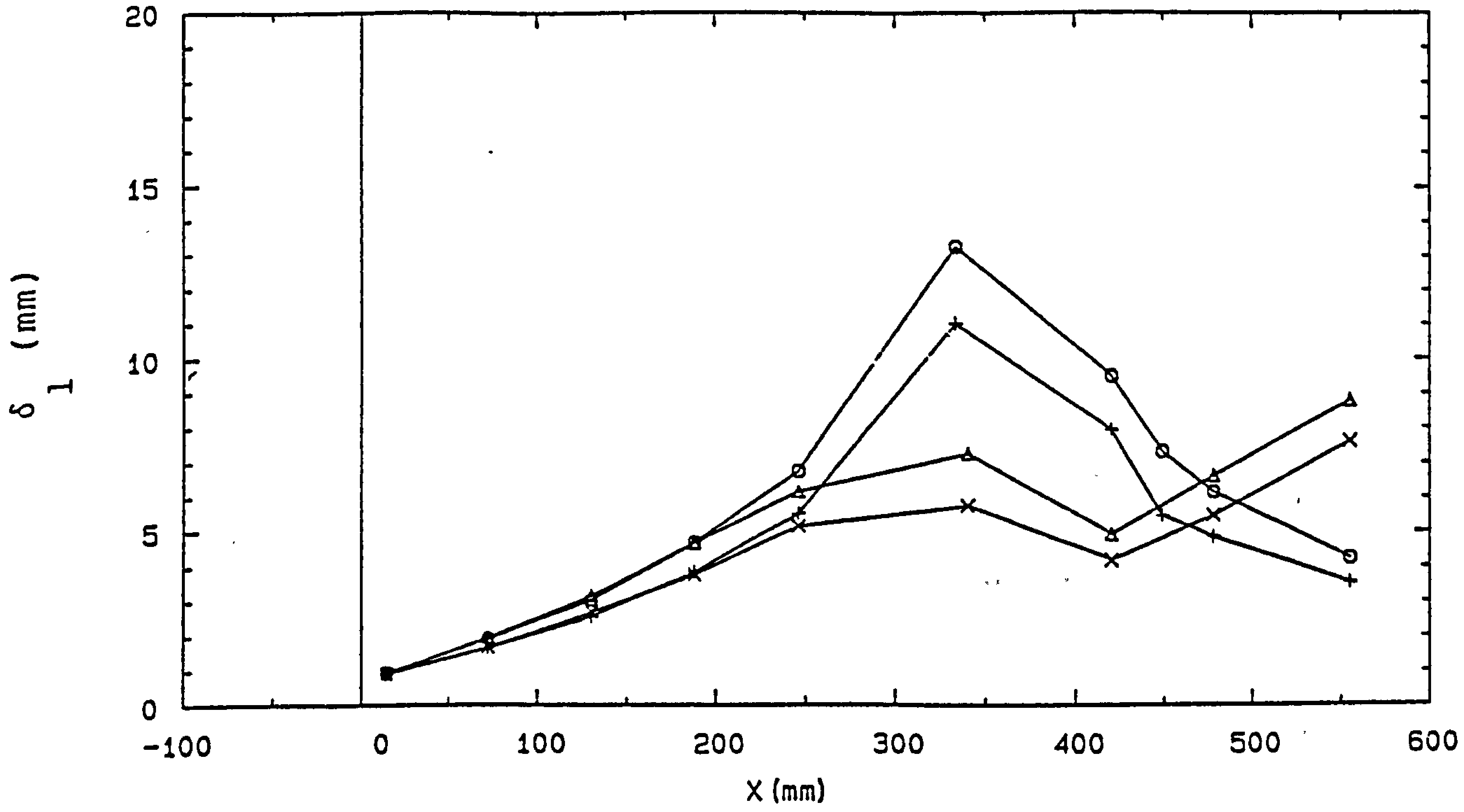

FIG. 4-8 DISPLACEMENT THICKNESSES DISTRIBUTIONS (DUCT M)

M(inlet)	0.15	0.635
upper wall	+	o
lower wall	x	Δ

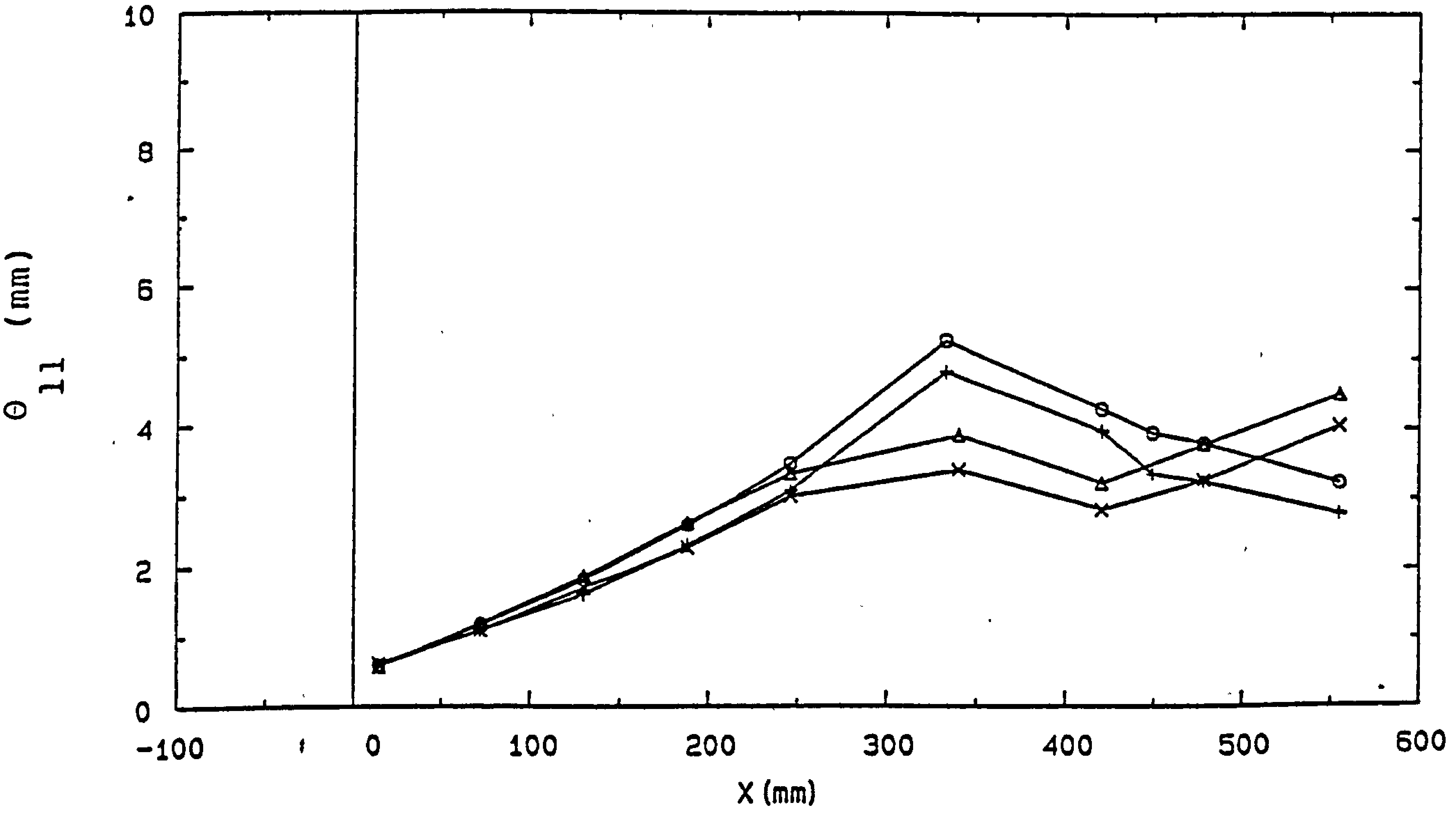

FIG. 4-9 MOMENTUM THICKNESSES DISTRIBUTIONS (DUCT M)

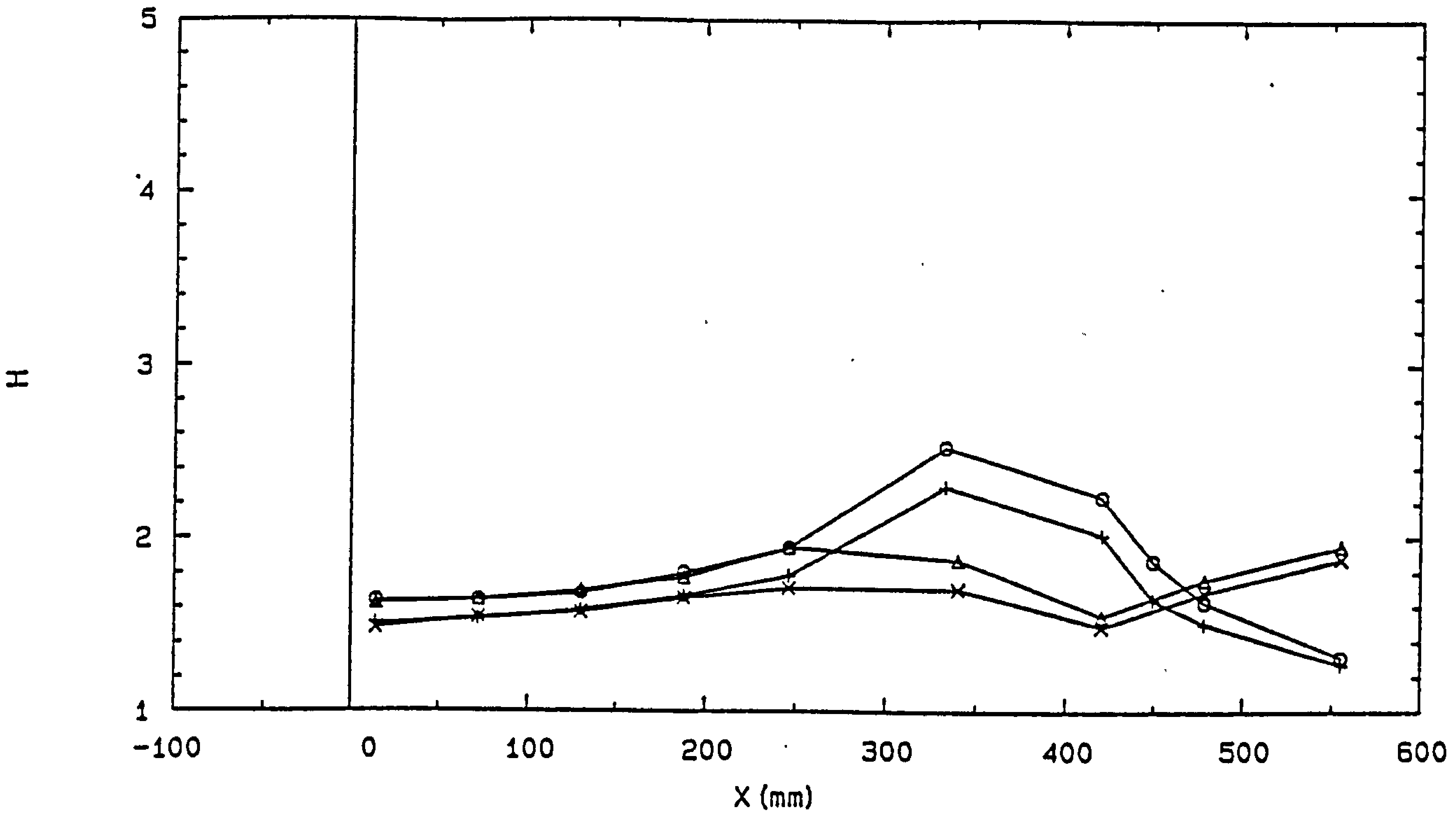

FIG. 4-10 SHAPE PARAMETER DISTRIBUTIONS (DUCT M)

M(inlet)	0.15	0.635
upper wall	+	o
lower wall	x	Δ

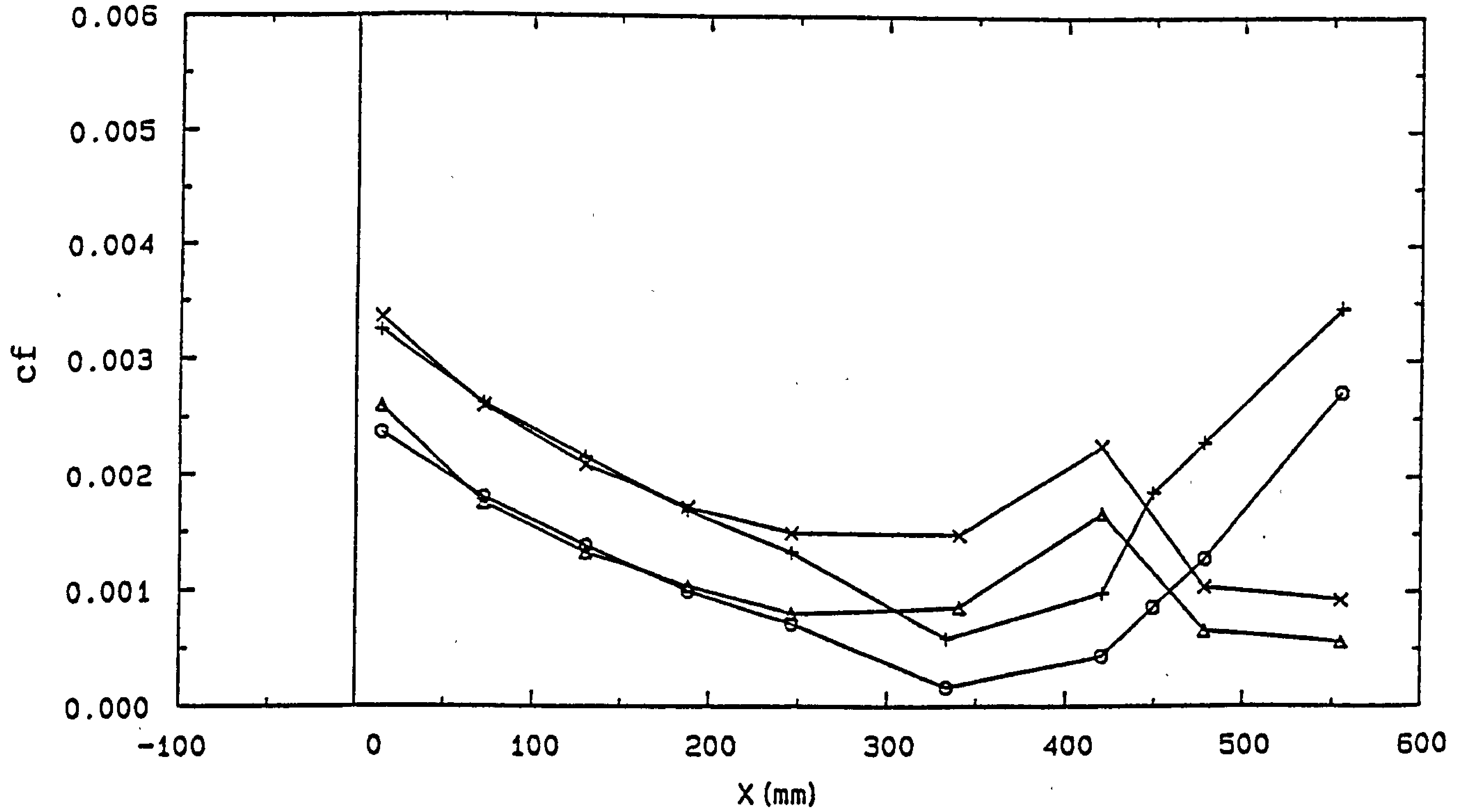

FIG. 4-11 SKIN FRICTION DISTRIBUTIONS (DUCT M)

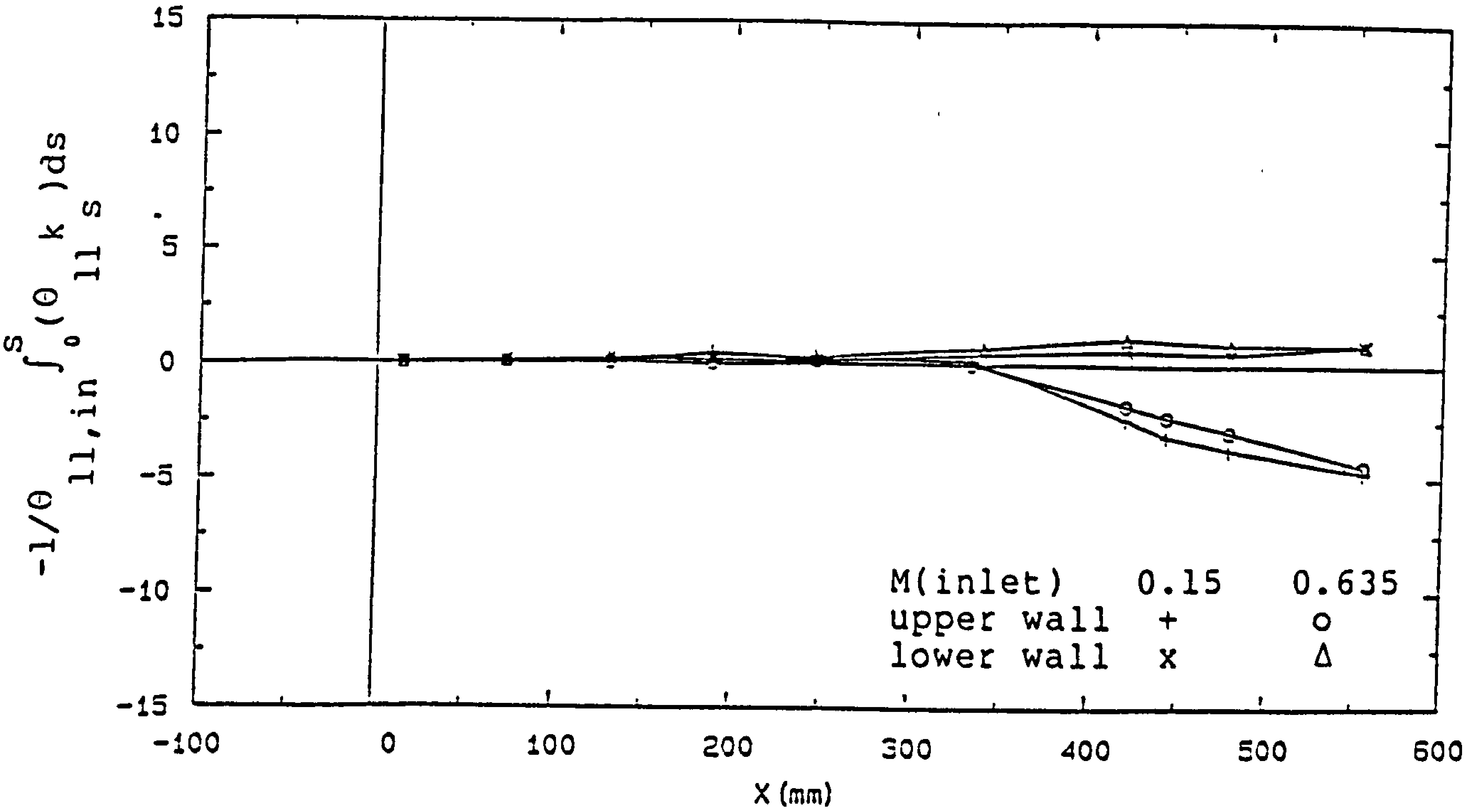

FIG. 4-12 MOMENTUM BALANCE (DUCT M)

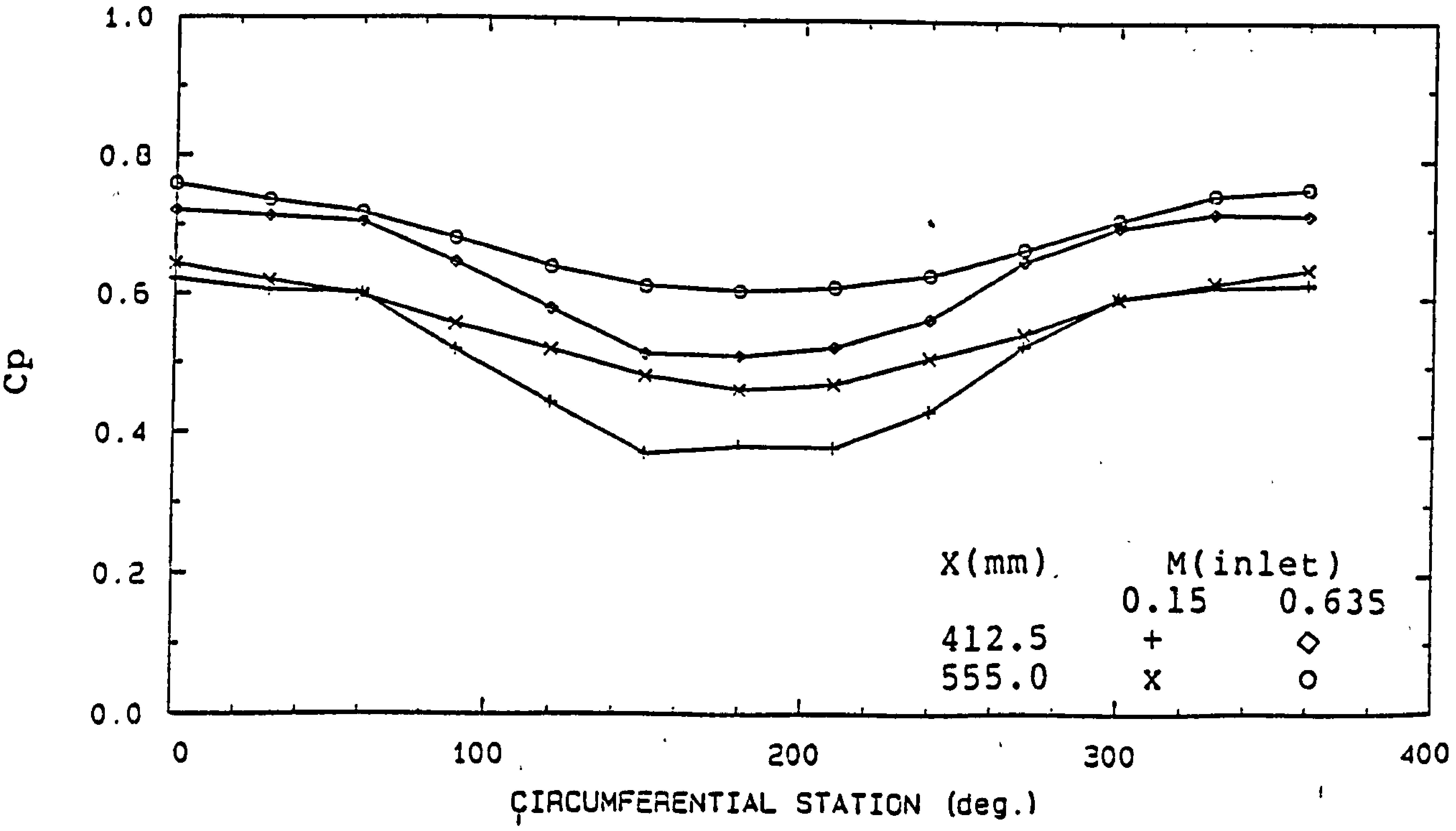

FIG. 4-13 PRESSURE DISTRIBUTIONS (DUCT M)

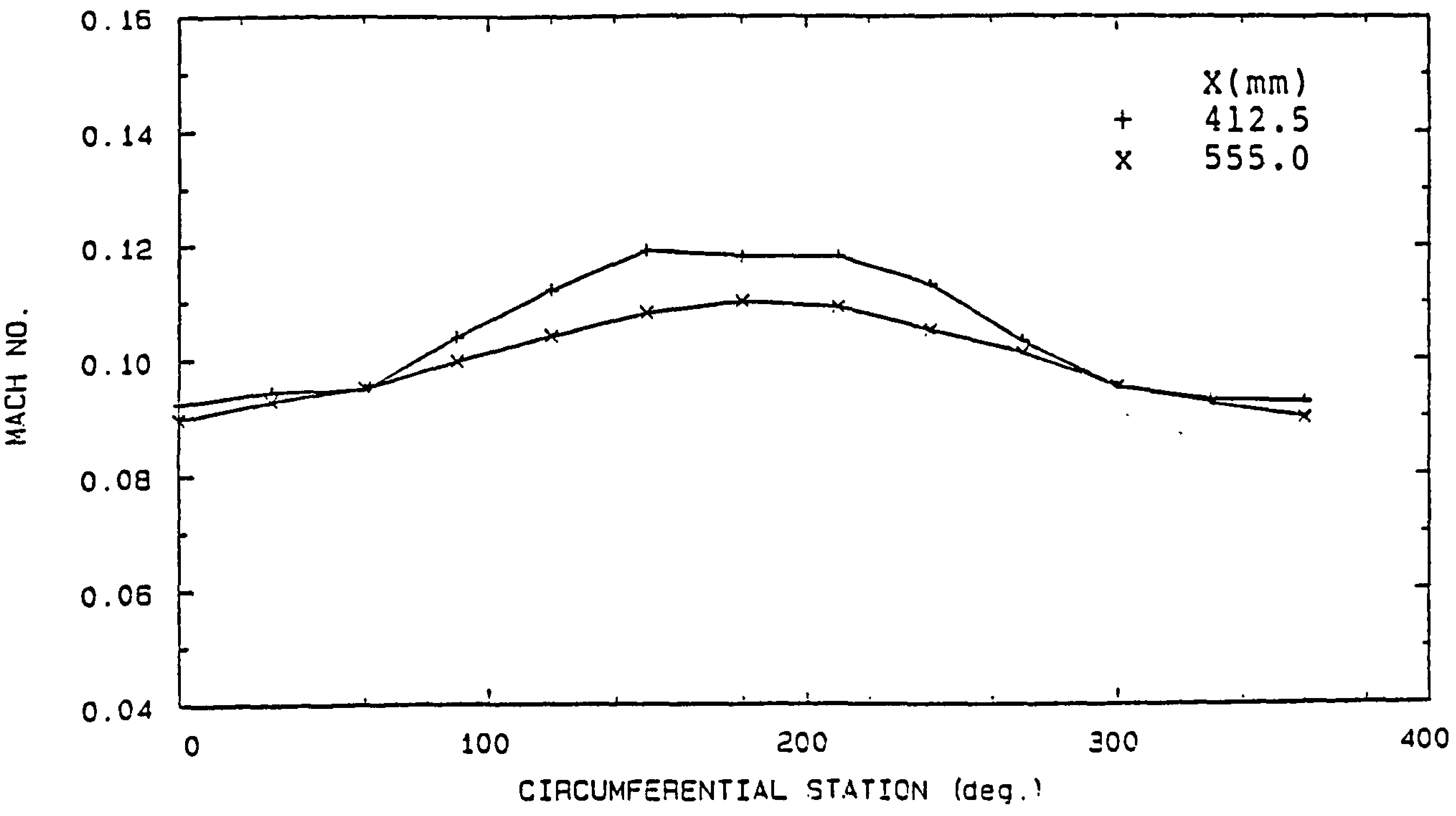

a) $M_{inlet} = 0.15$

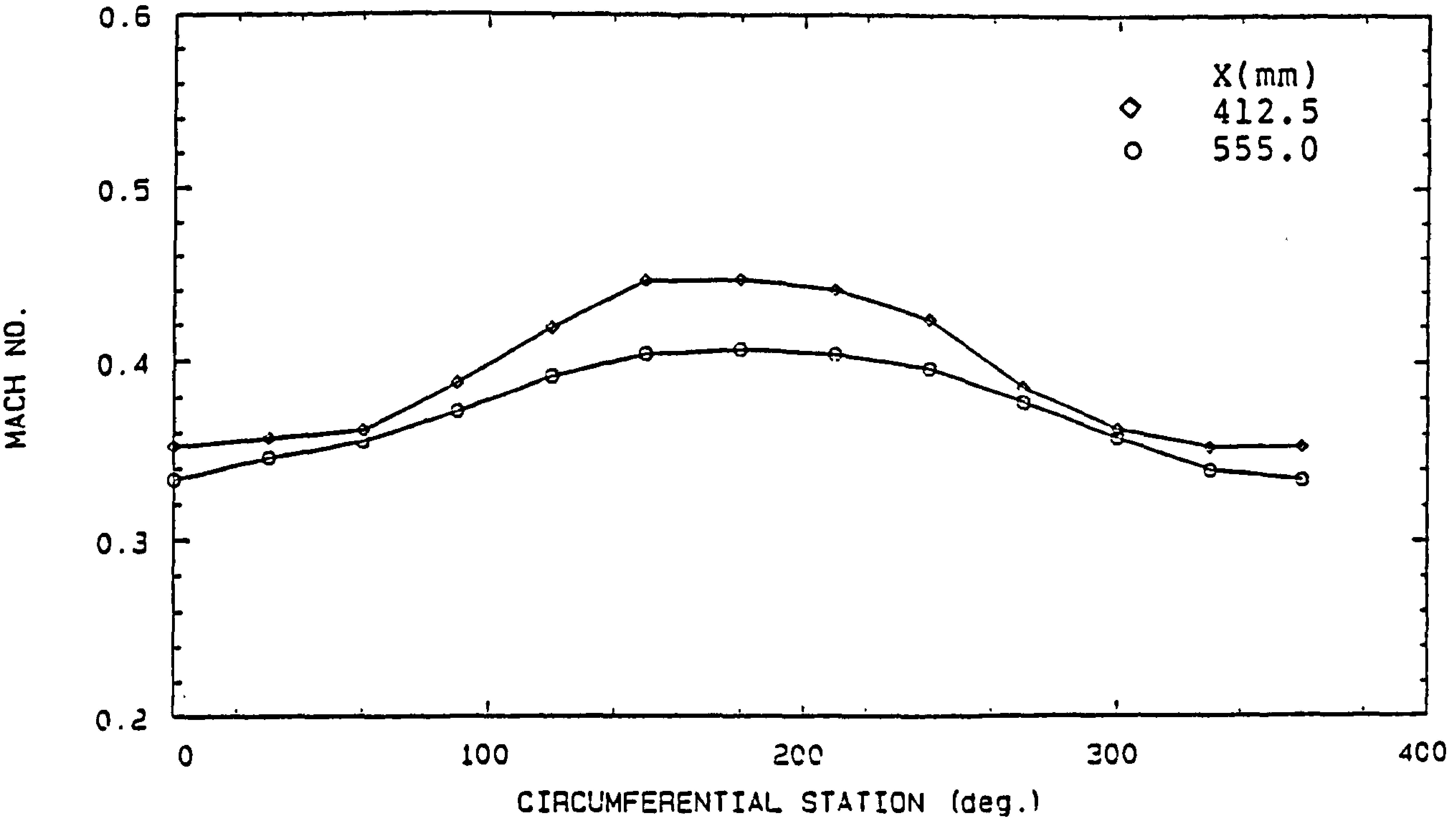

b) $M_{inlet} = 0.635$

FIG. 4-14 MACH NUMBER DISTRIBUTIONS (DUCT M)

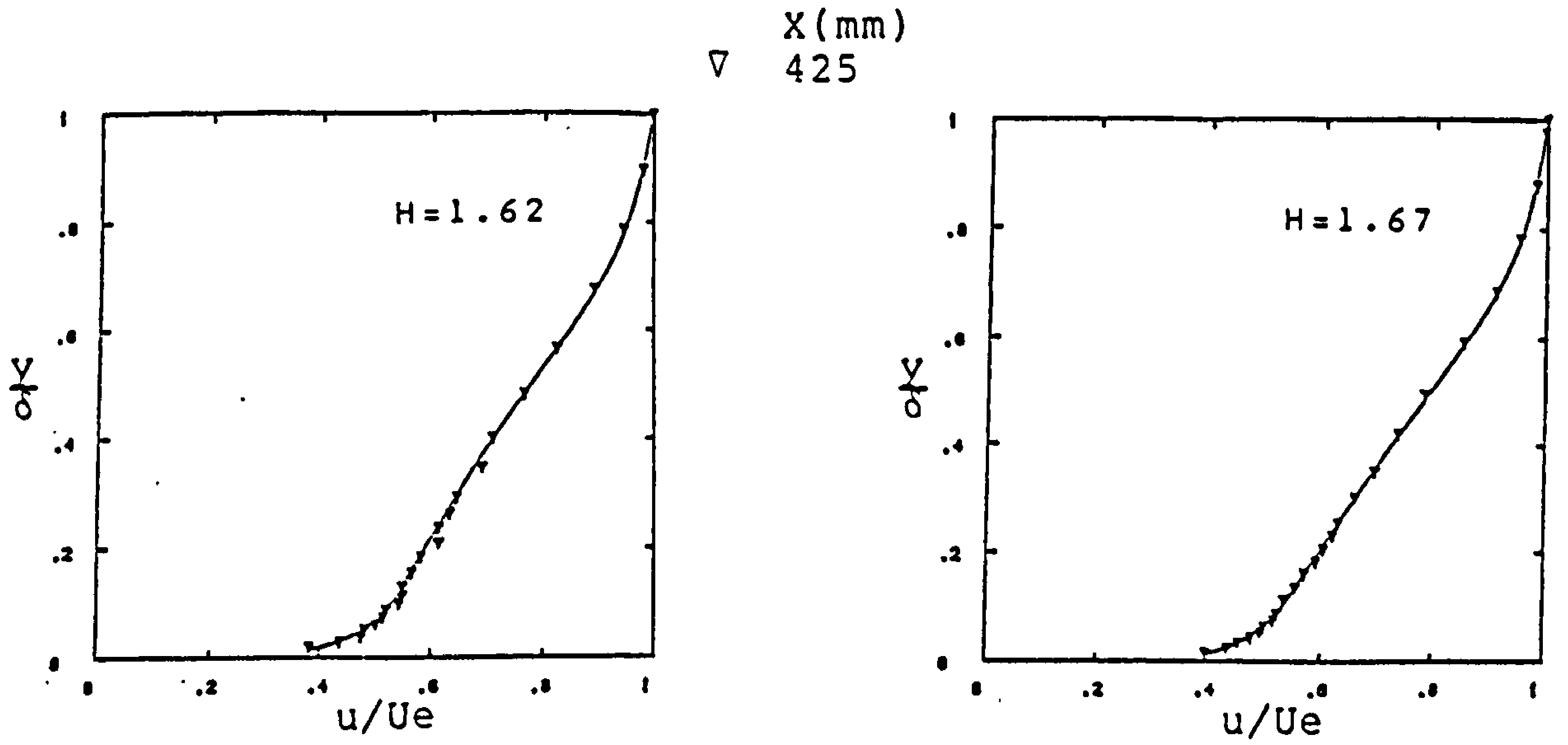

a1, a2) Streamwise velocity profiles

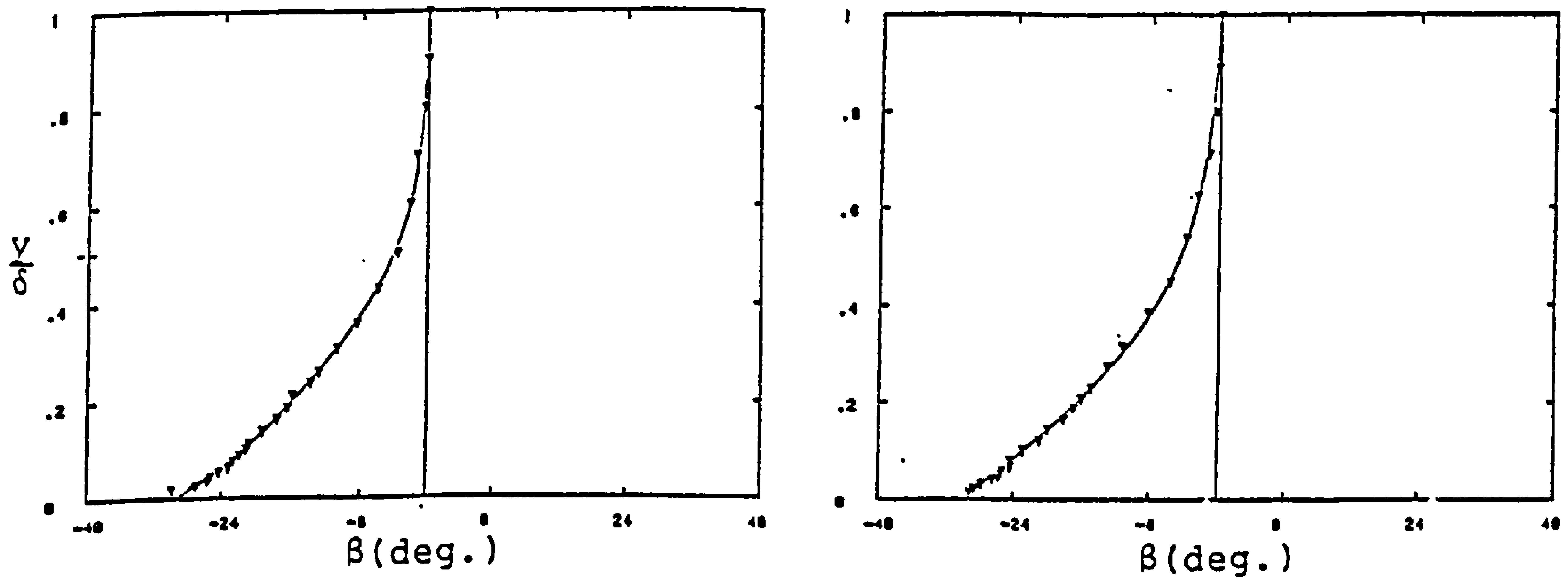

b1, b2) Skew angle profiles

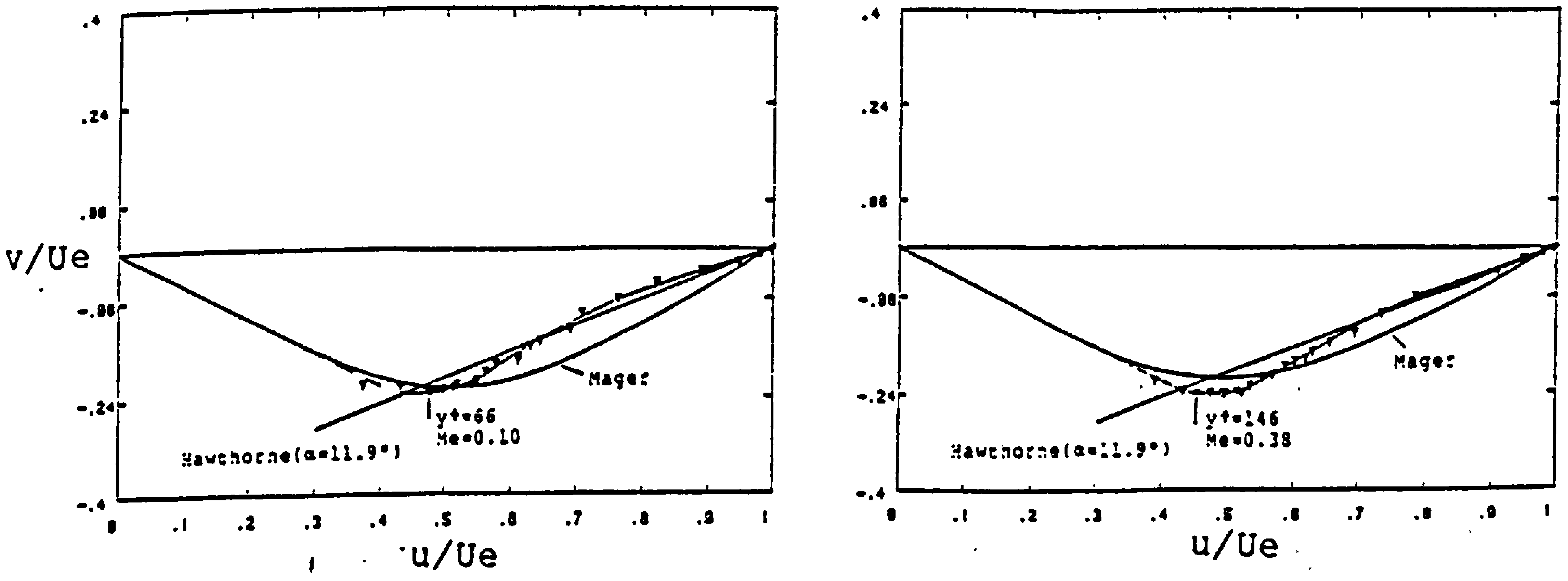

c1, c2) Polar plots

M_{inlet} = 0.15 M_{inlet} = 0.635

FIG. 4-15 SIDE WALL BOUNDARY LAYER (DUCT M)

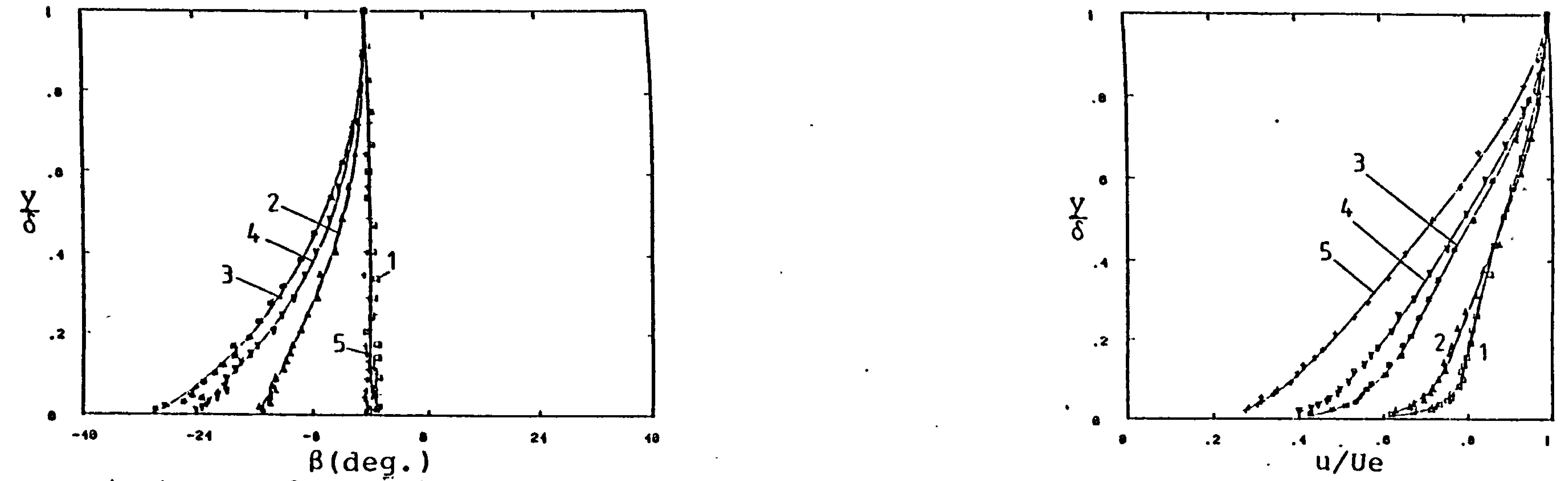

a) Skew angle profiles

b) Streamwise velocity profiles

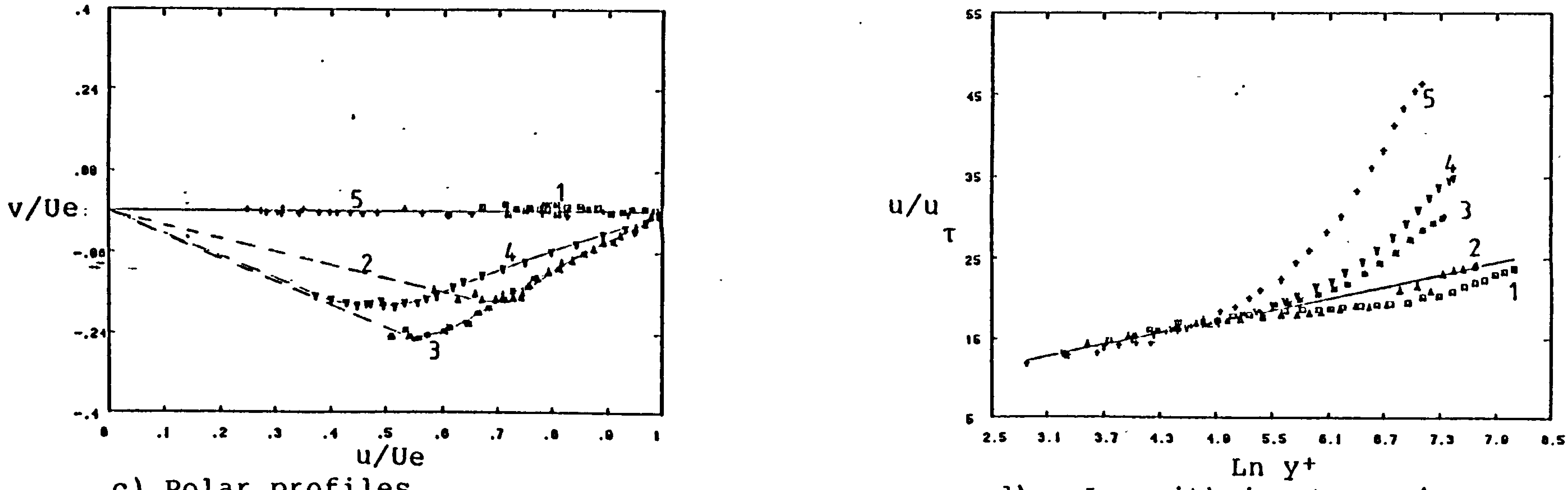

c) Polar profiles

d) Logarithmic streamwise velocity profiles

M_{inlet} =0.15, X=555mm

——— Law of the wall

FIG. 4-16 ENGINE FACE BOUNDARY LAYER (DUCT M)

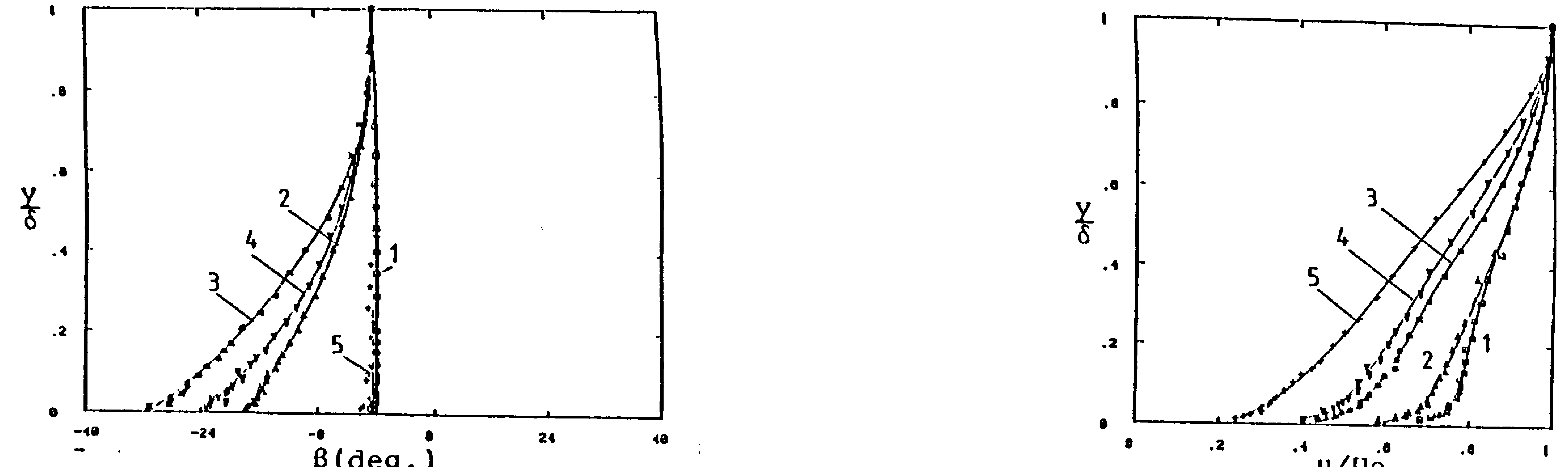

a) Skew angle profiles

b) Streamwise velocity profiles

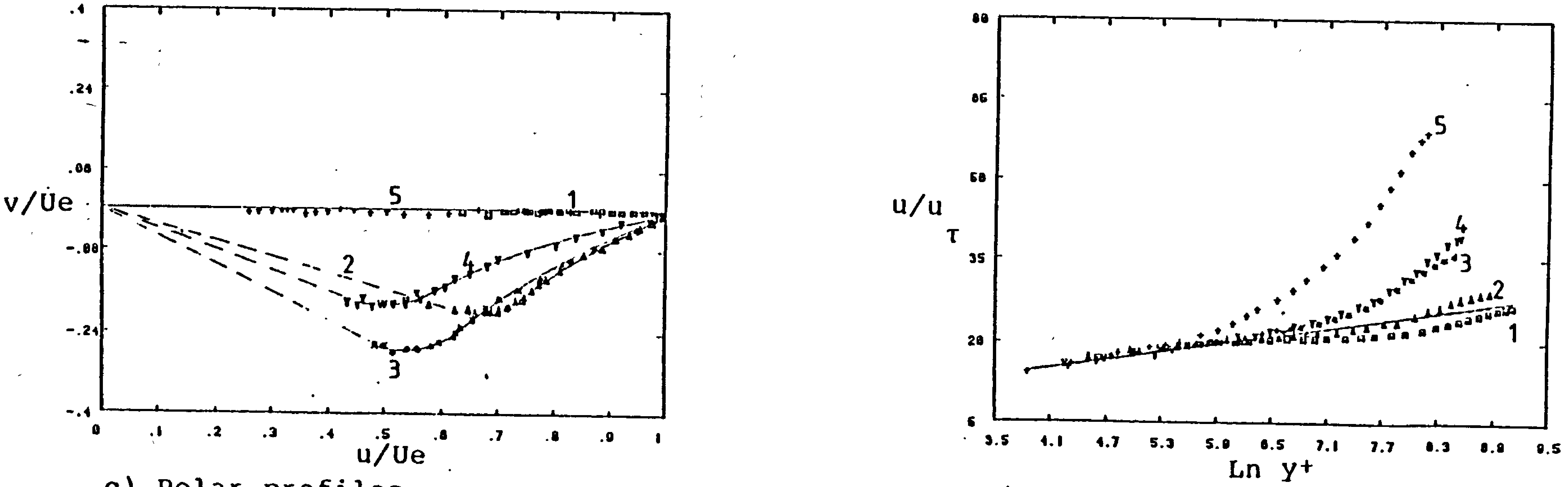

c) Polar profiles

d) Logarithmic streamwise velocity profiles

M_{inlet} =0.635, X=555mm

—— Law of the wall

FIG. 4-17 ENGINE FACE BOUNDARY LAYER (DUCT M)

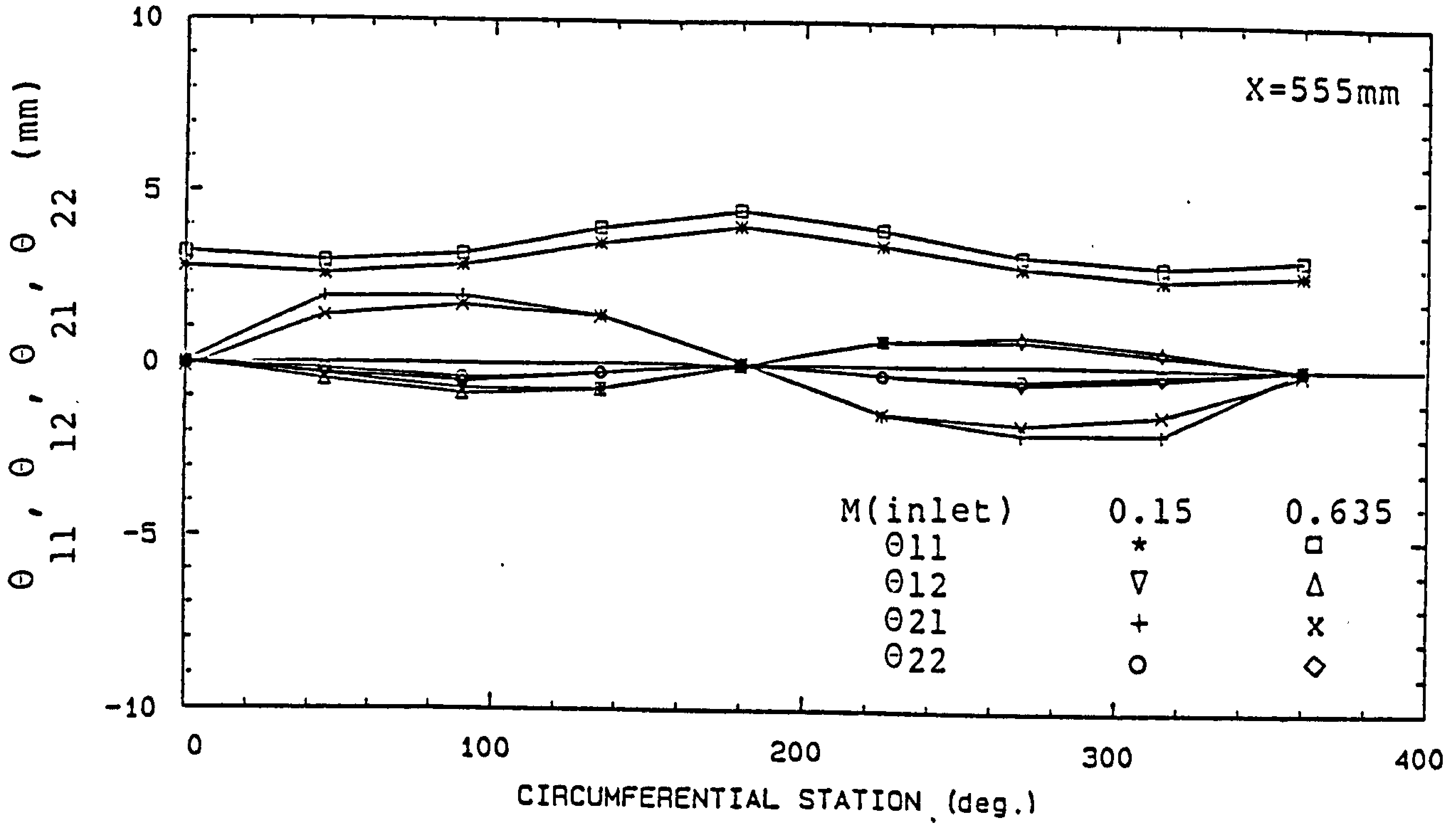

FIG. 4-18 MOMENTUM THICKNESSES DISTRIBUTIONS (DUCT M)

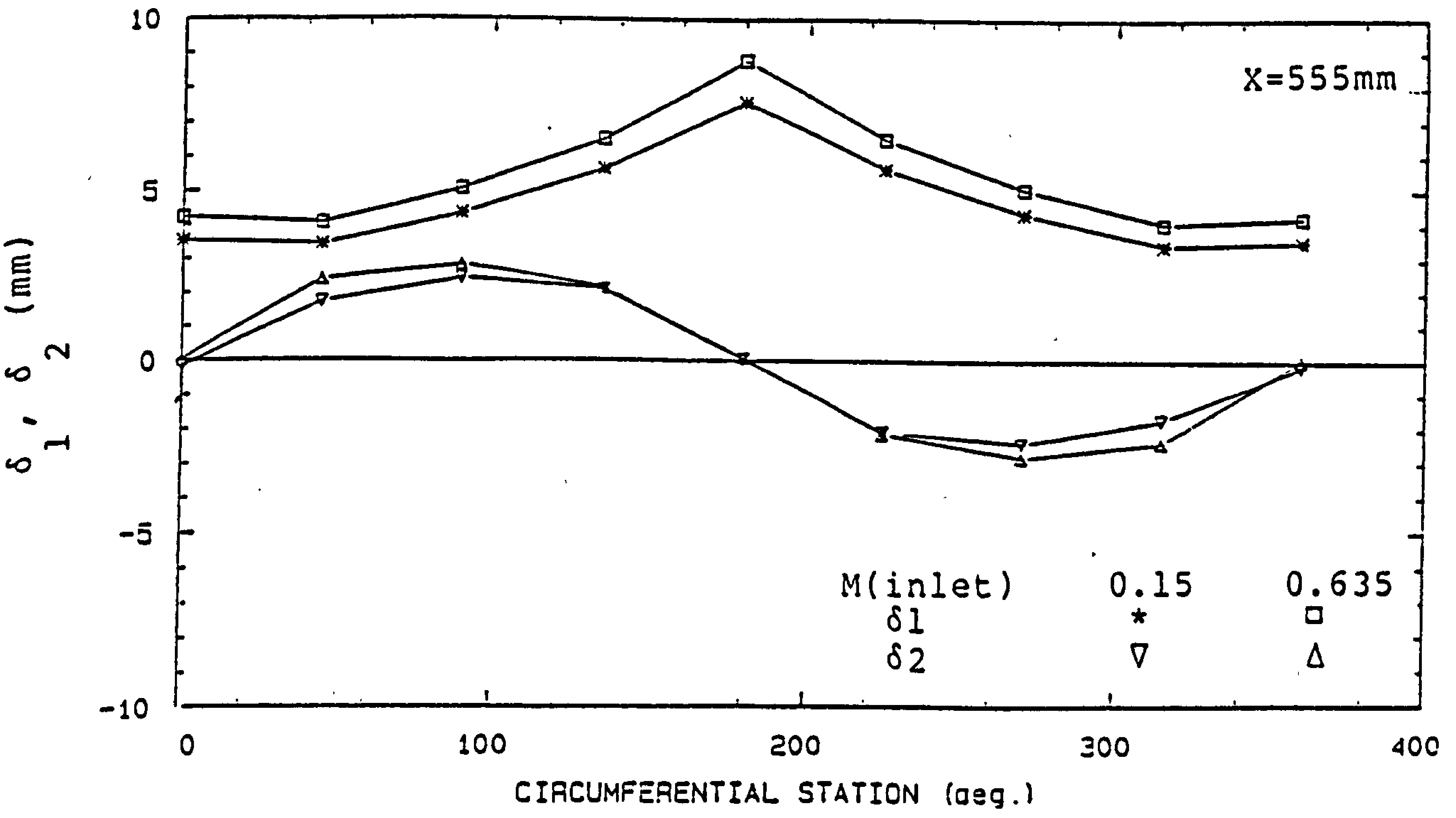

FIG. 4-19 DISPLACEMENT THICKNESSES DISTRIBUTIONS (DUCT M)

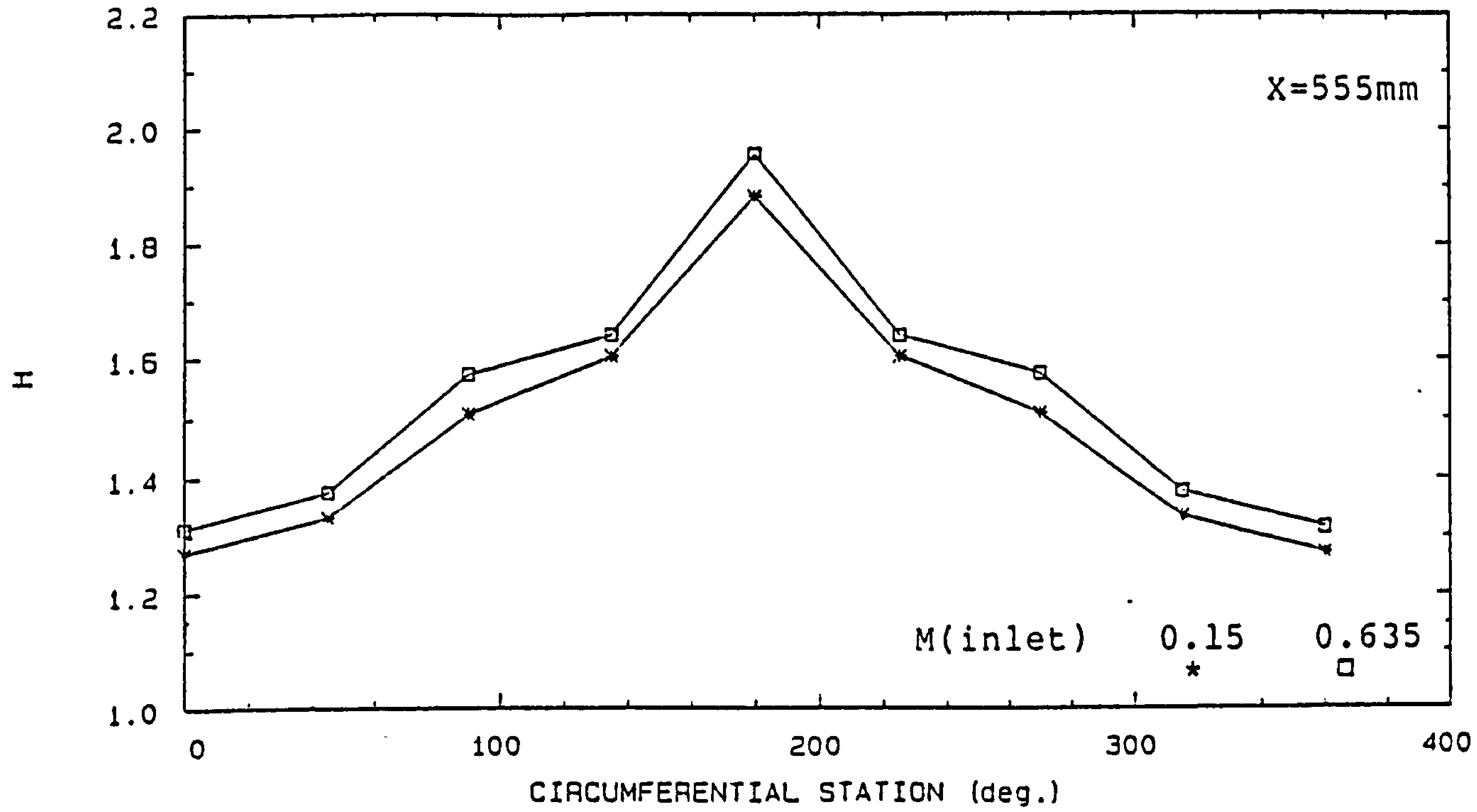

FIG. 4-20 SHAPE PARAMETER DISTRIBUTIONS (DUCT M)

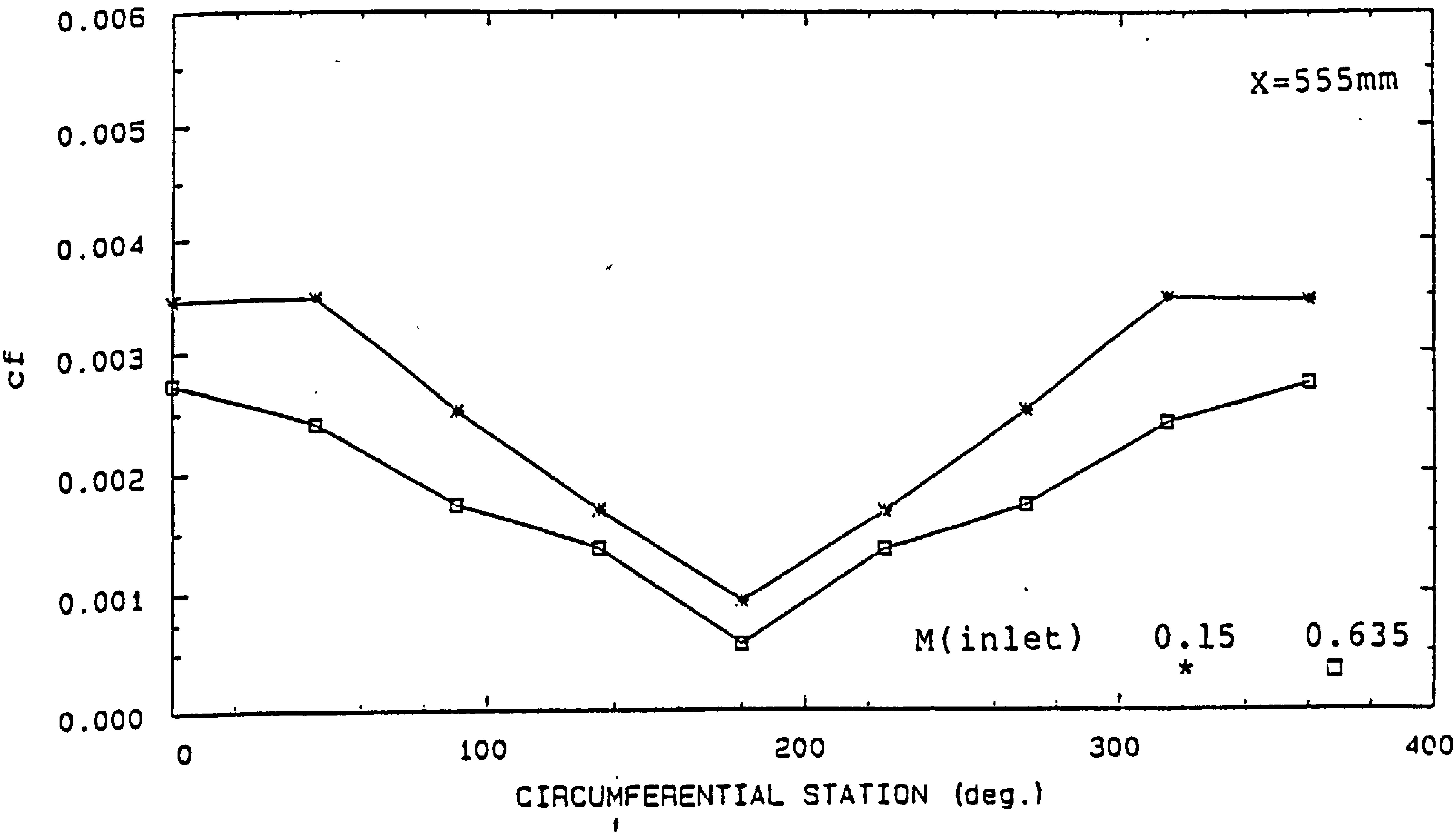

FIG. 4-21 SKIN FRICTION DISTRIBUTIONS (DUCT M)

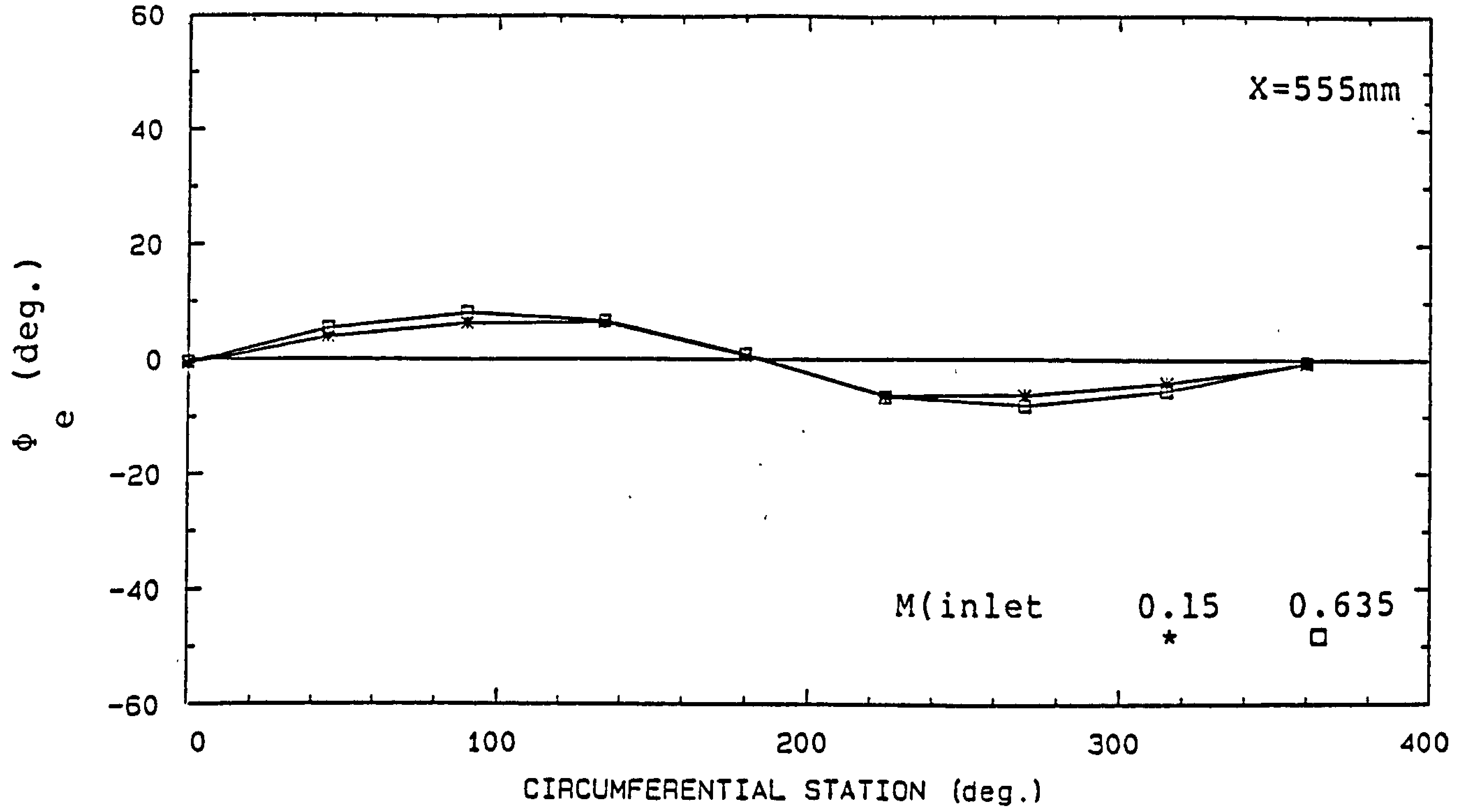

FIG. 4-22 BOUNDARY LAYER EDGE FLOW DIRECTIONS RELATIVE TO DUCT OUTLET AXIS (DUCT M)

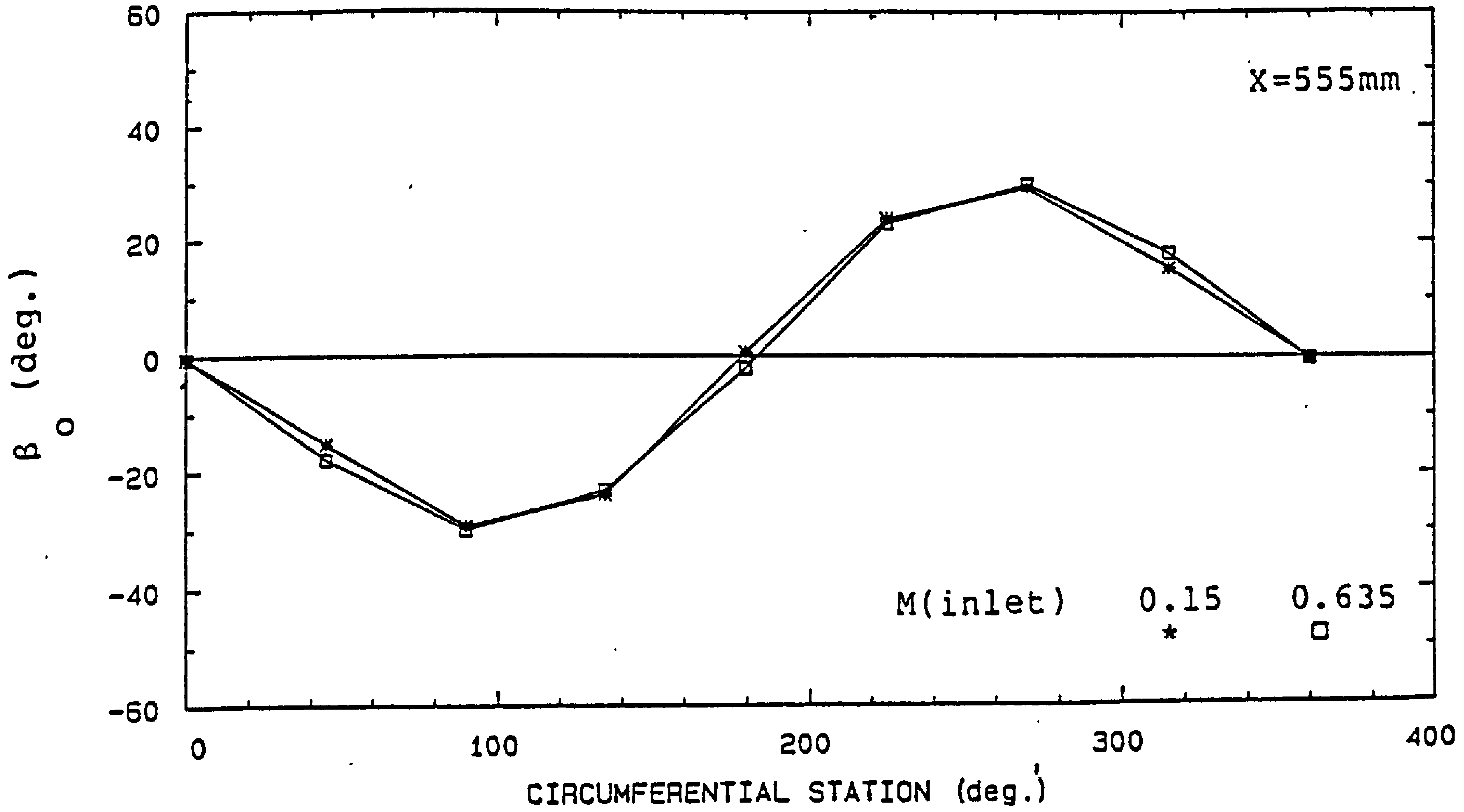

FIG. 4-23 LIMITING STREAMLINE ANGLE DISTRIBUTIONS (DUCT M)

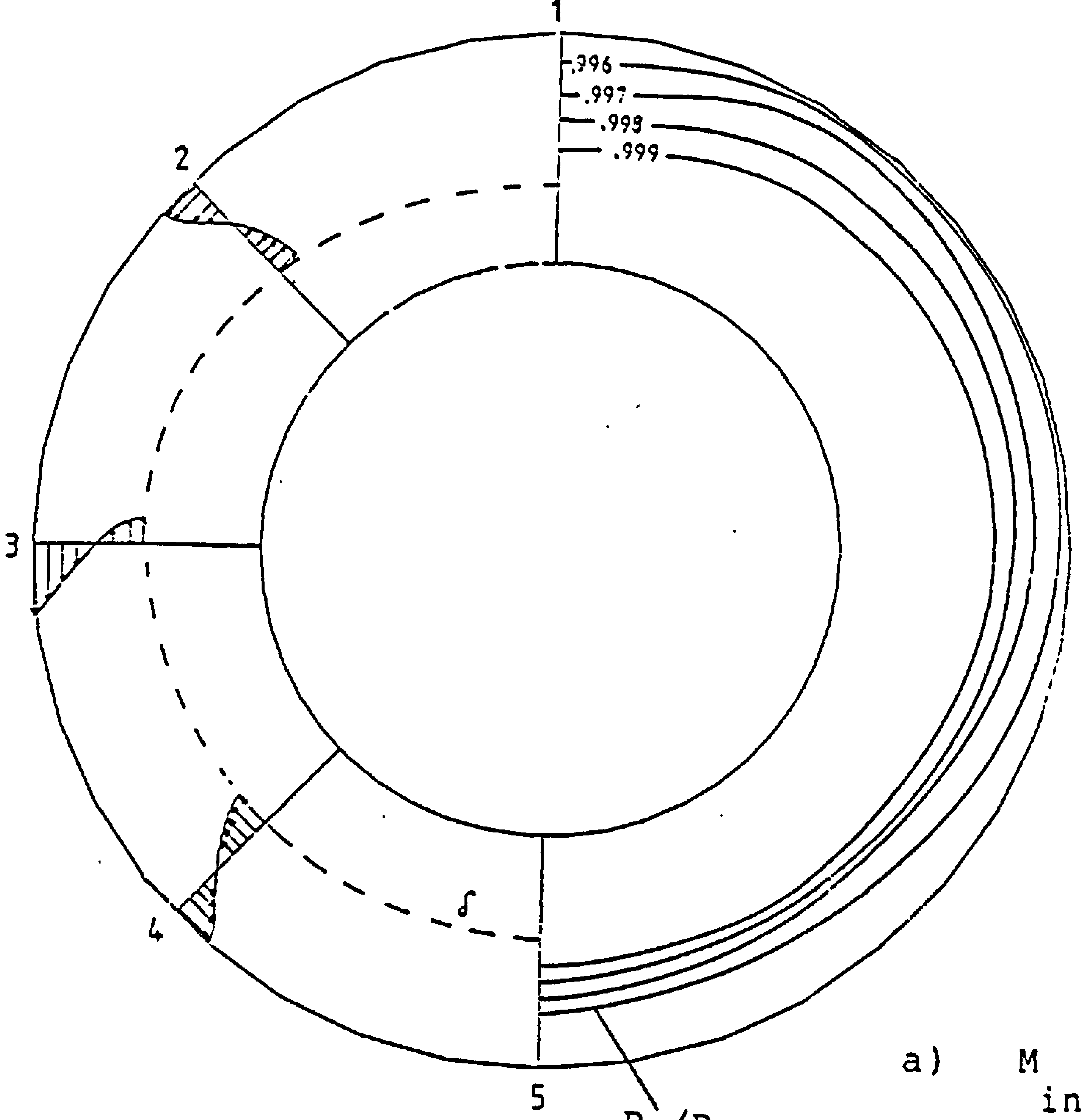

a) $M_{inlet} = 0.15$

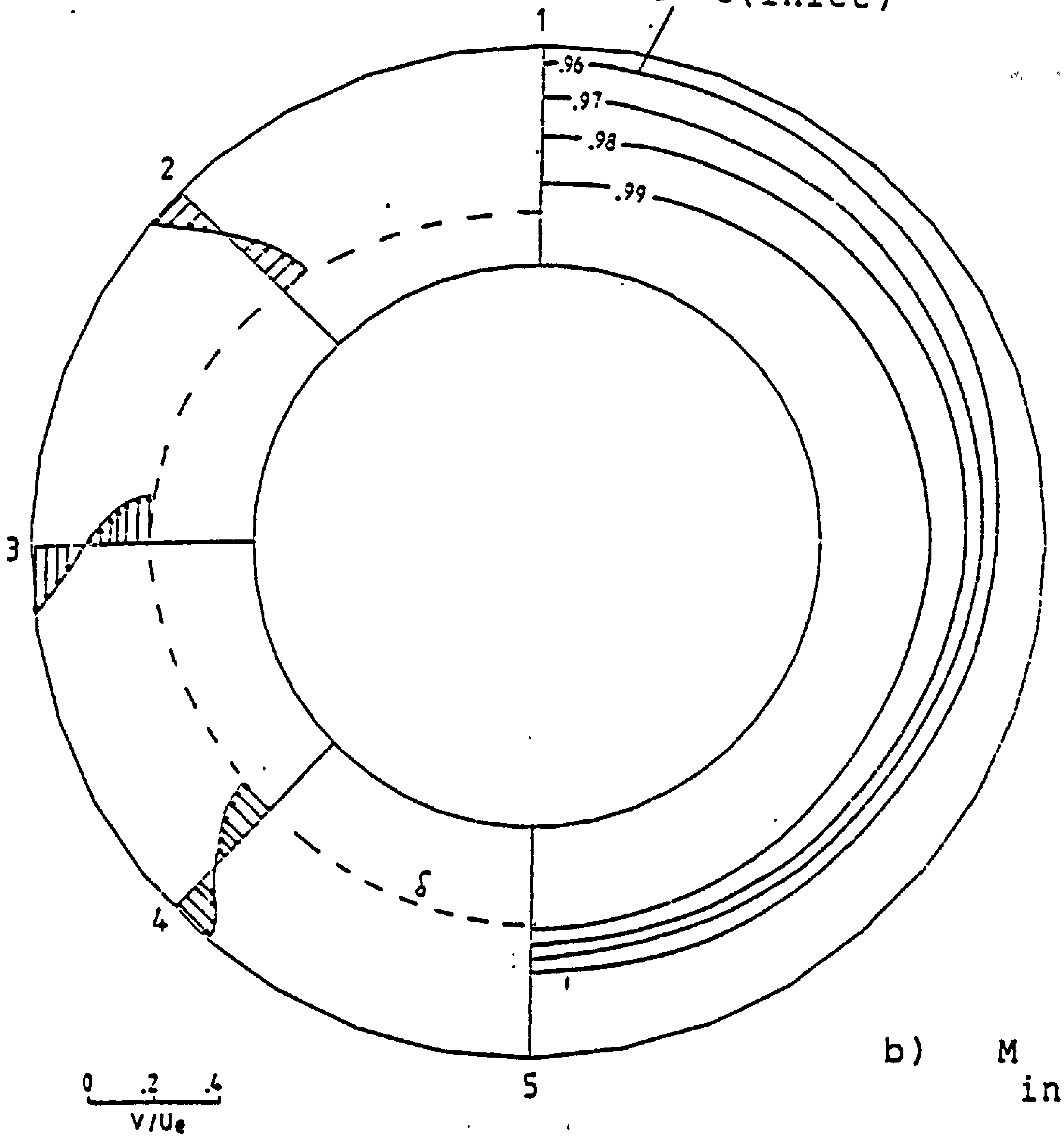

b) $M_{inlet} = 0.635$

FIG. 4-24 ENGINE FACE CROSSFLOW AND TOTAL PRESSURE DISTRIBUTIONS (DUCT M)

Upper wall

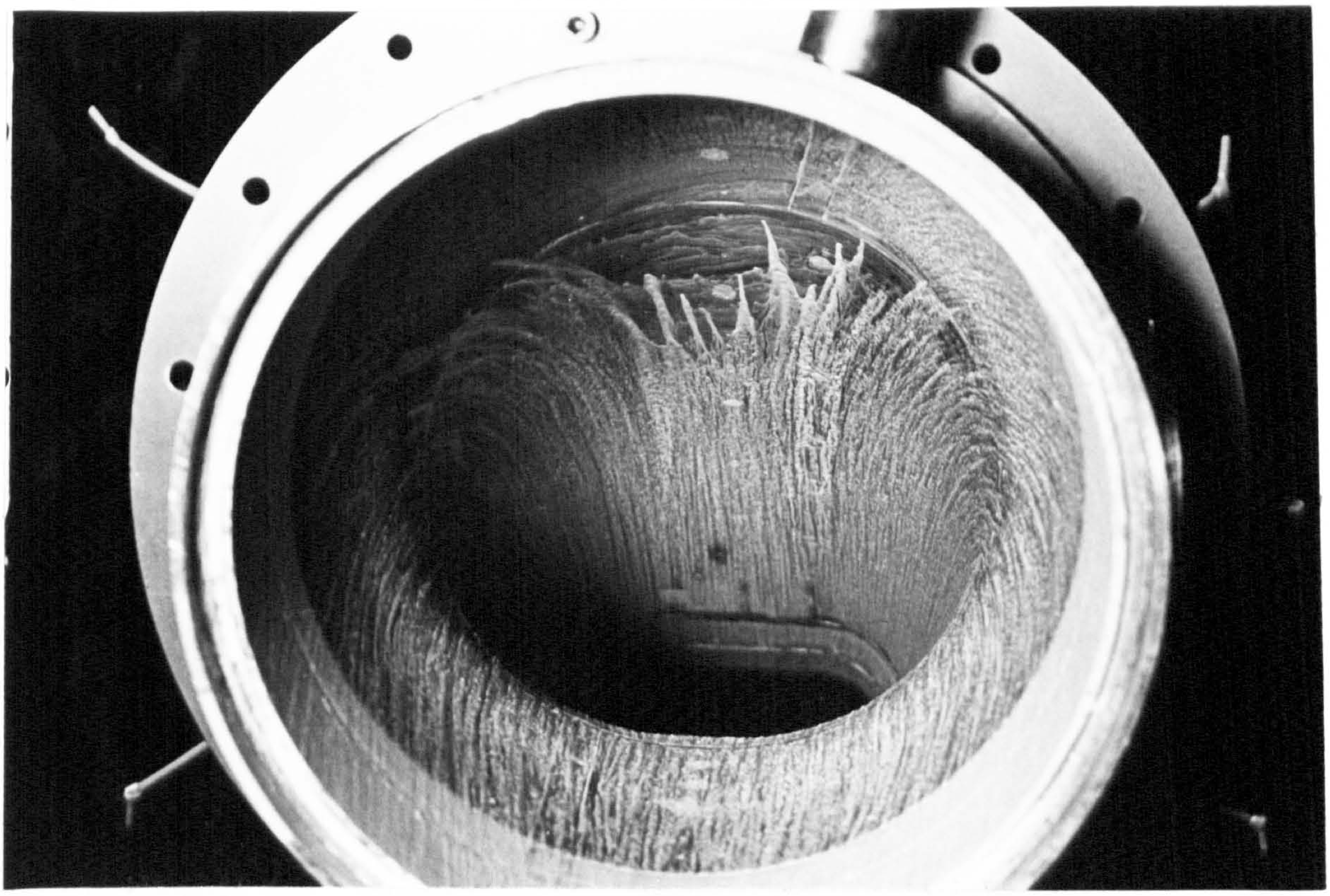

Upper wall

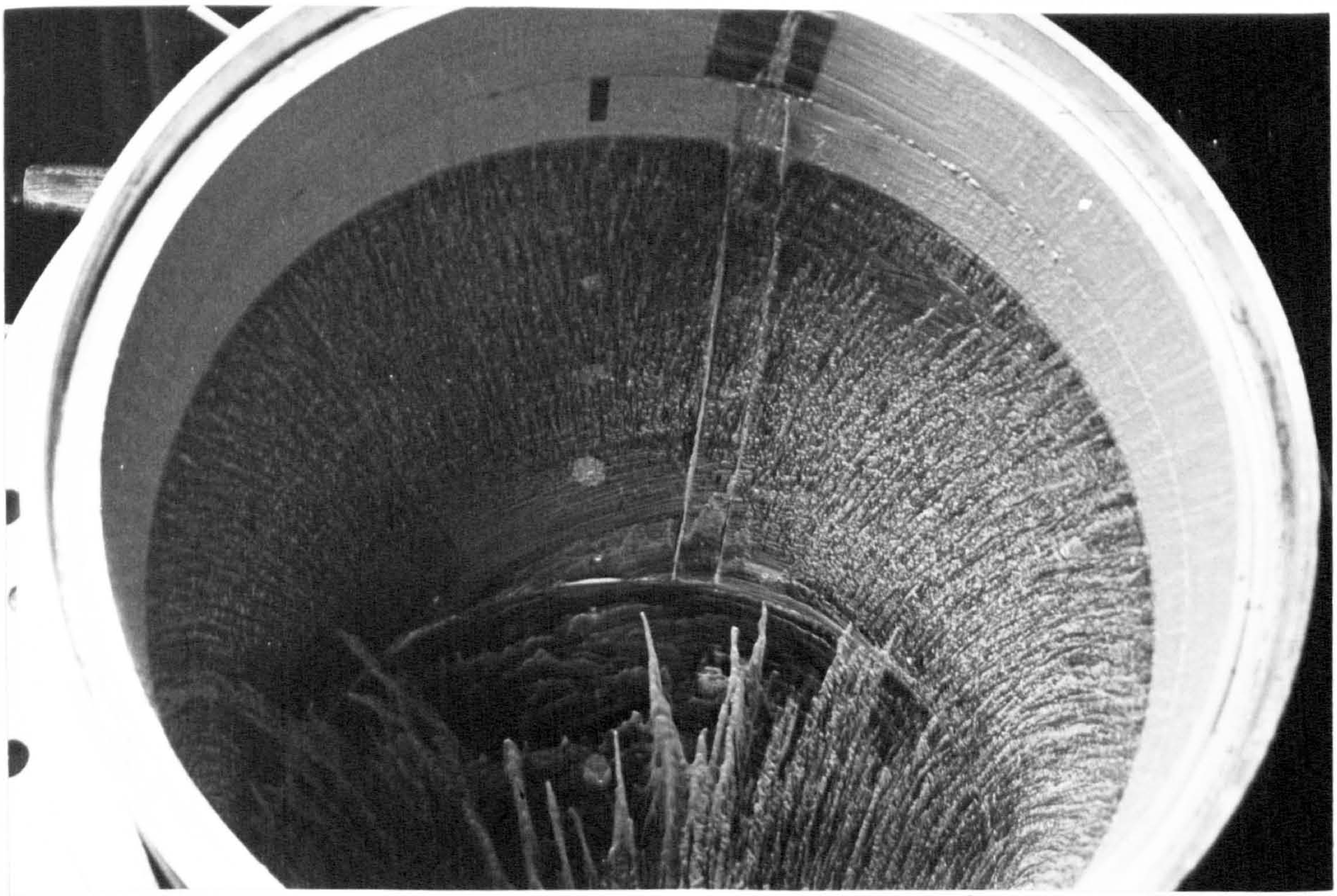

FIG. 4-25 SURFACE OIL FLOW VISUALIZATION (DUCT M)

Upper wall

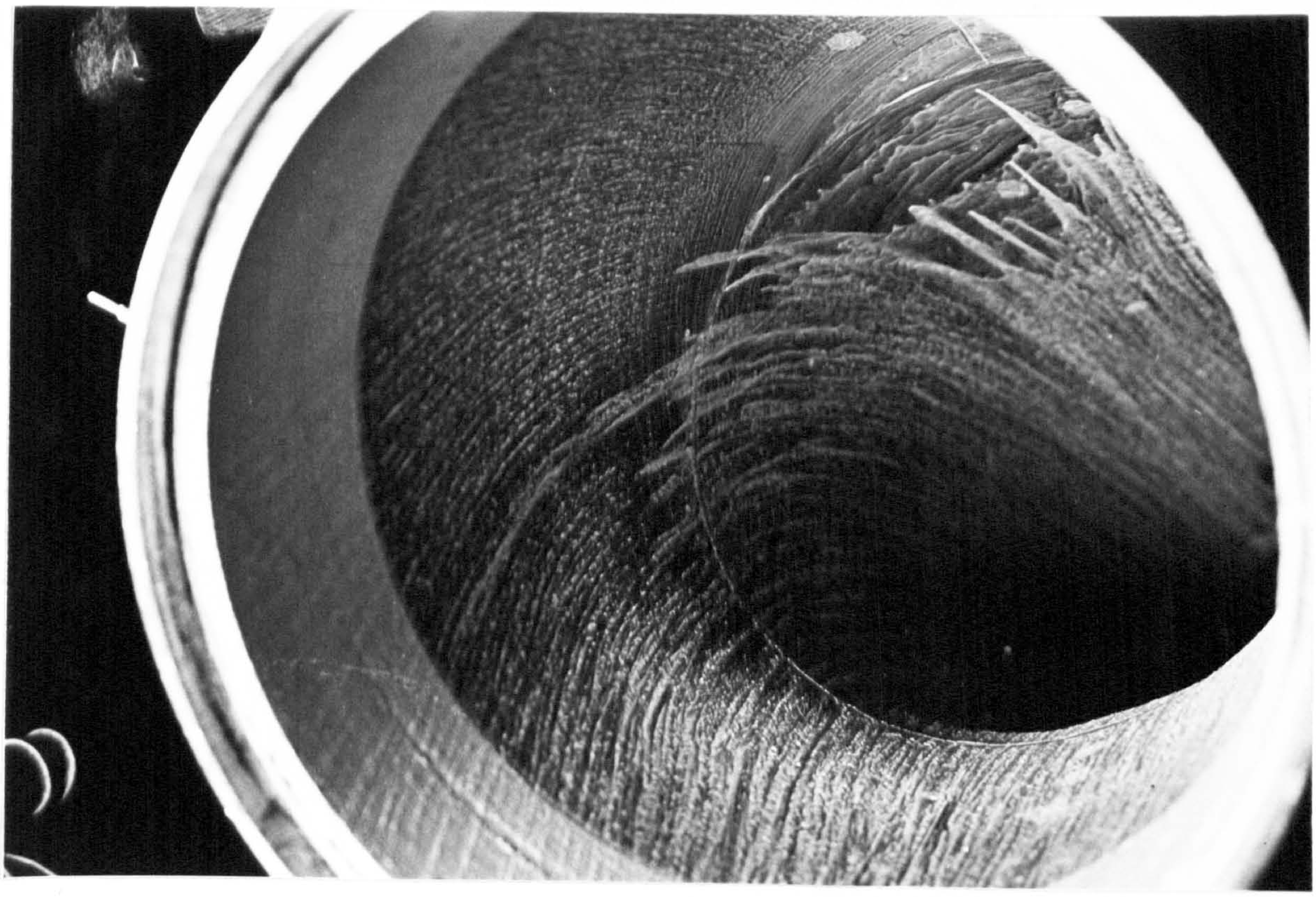

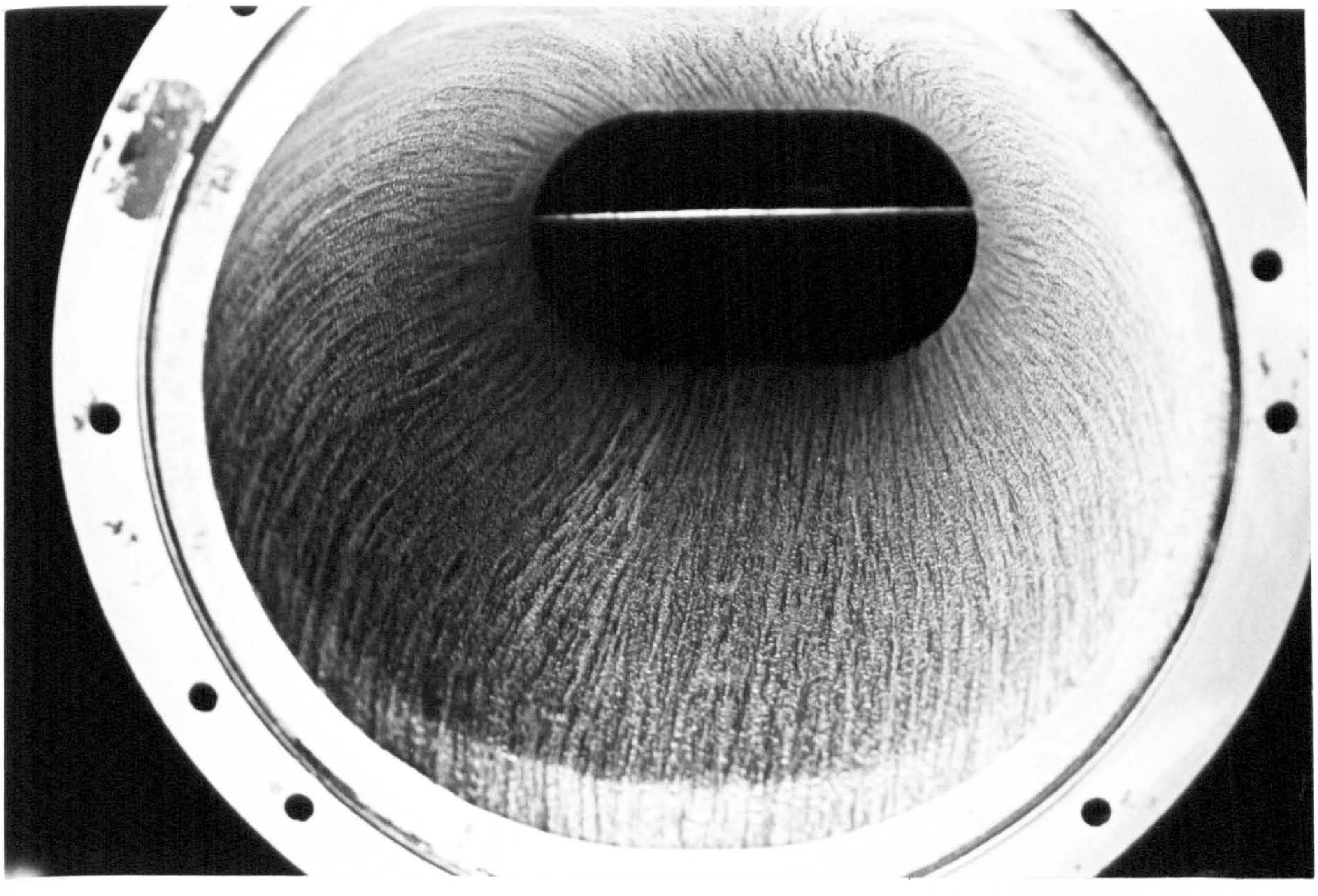

Lower wall (second bend detached)

FIG. 4-26 SURFACE OIL FLOW VISUALIZATION (DUCT M)

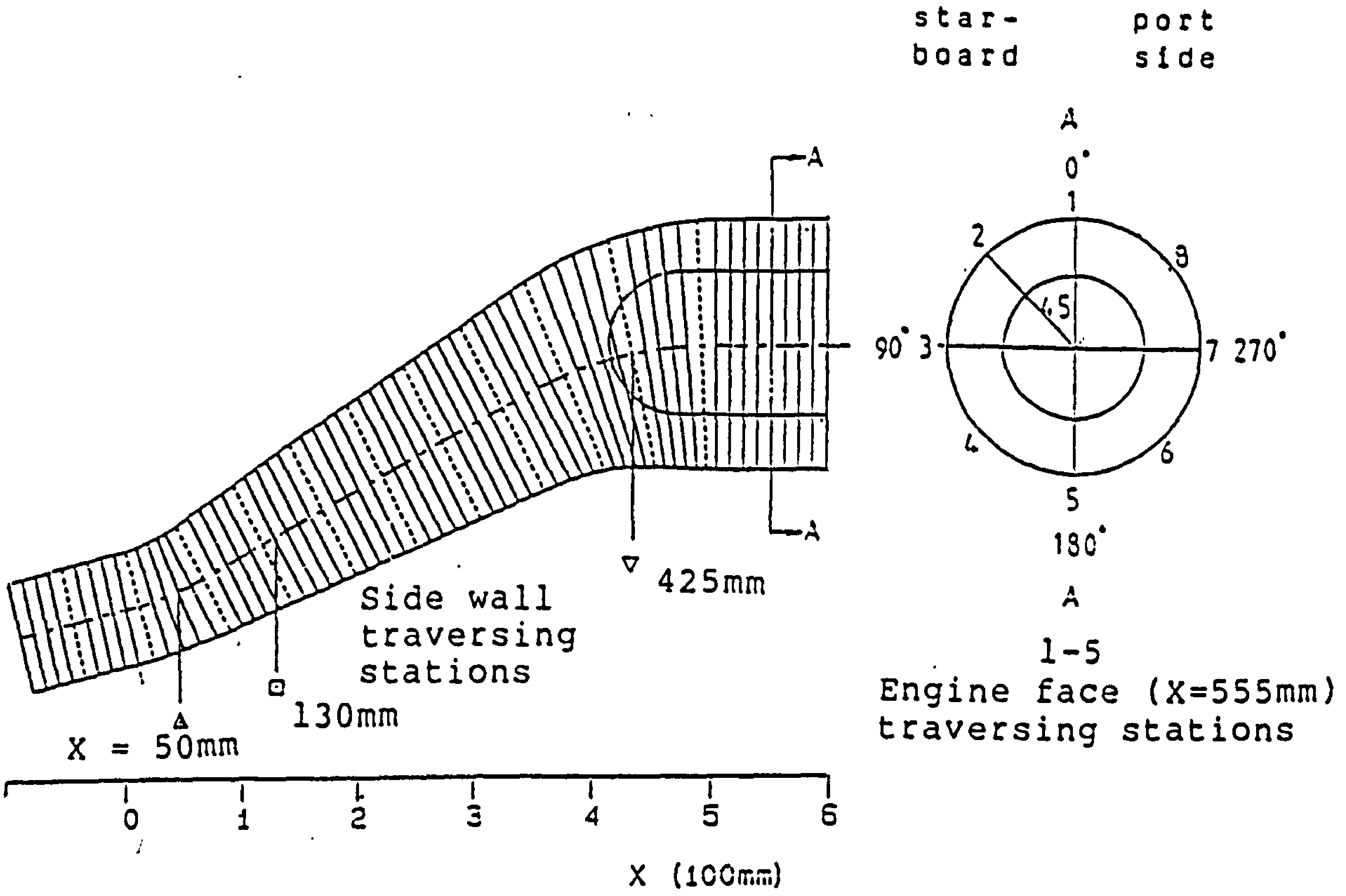

FIG. 4-27 DUCT N PROFILE

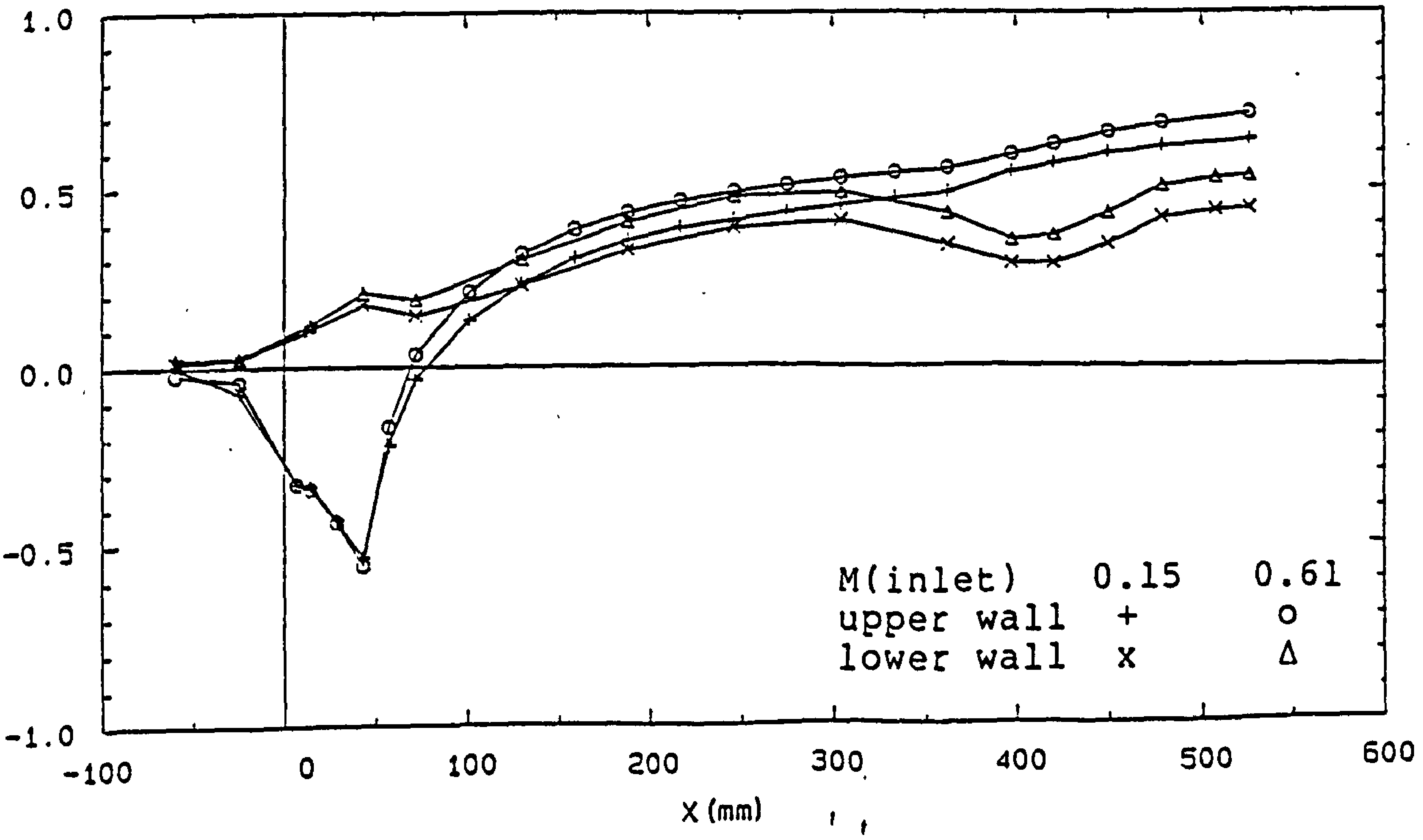

FIG. 4-28 PRESSURE DISTRIBUTIONS (DUCT N)

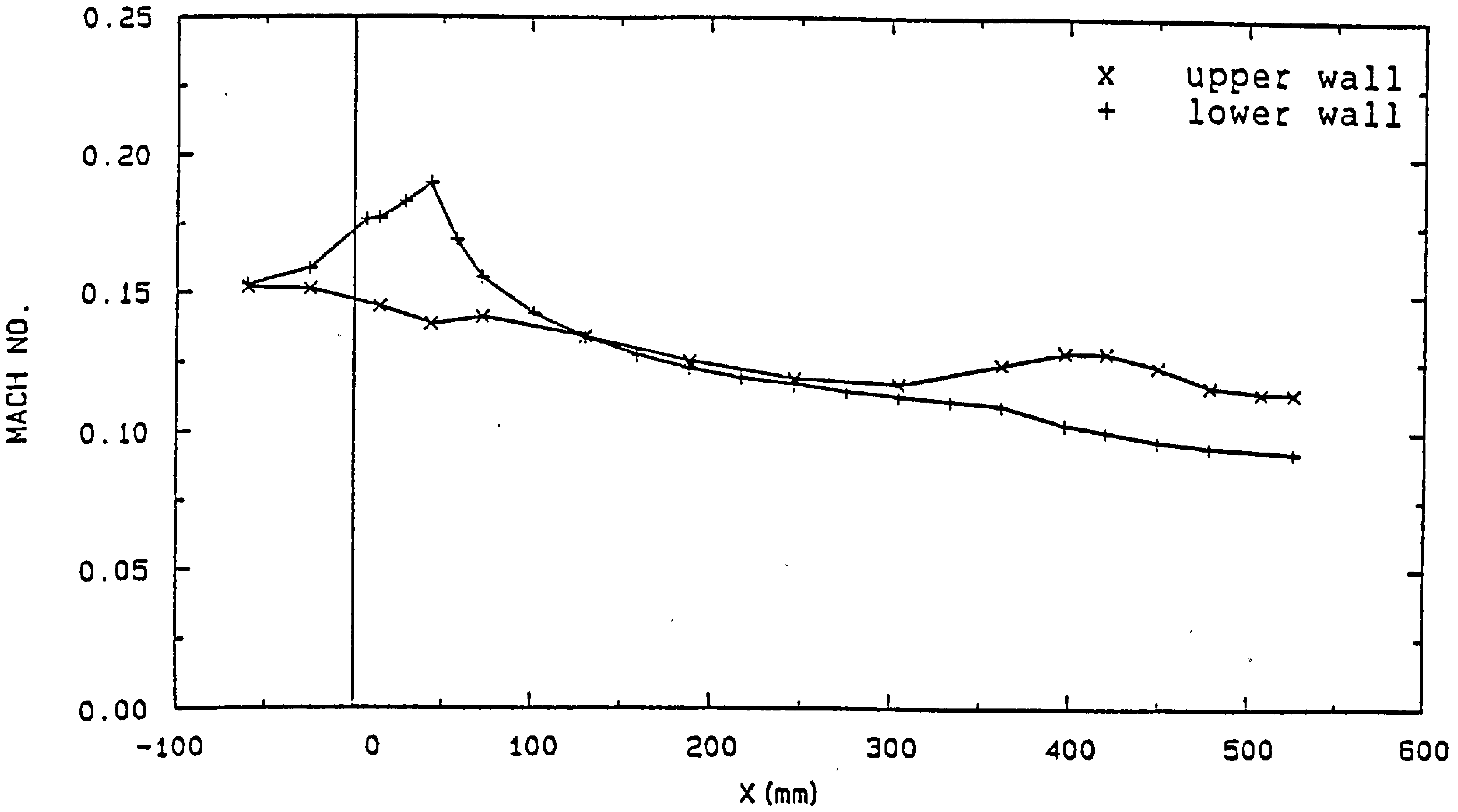

a) $M_{inlet} = 0.15$

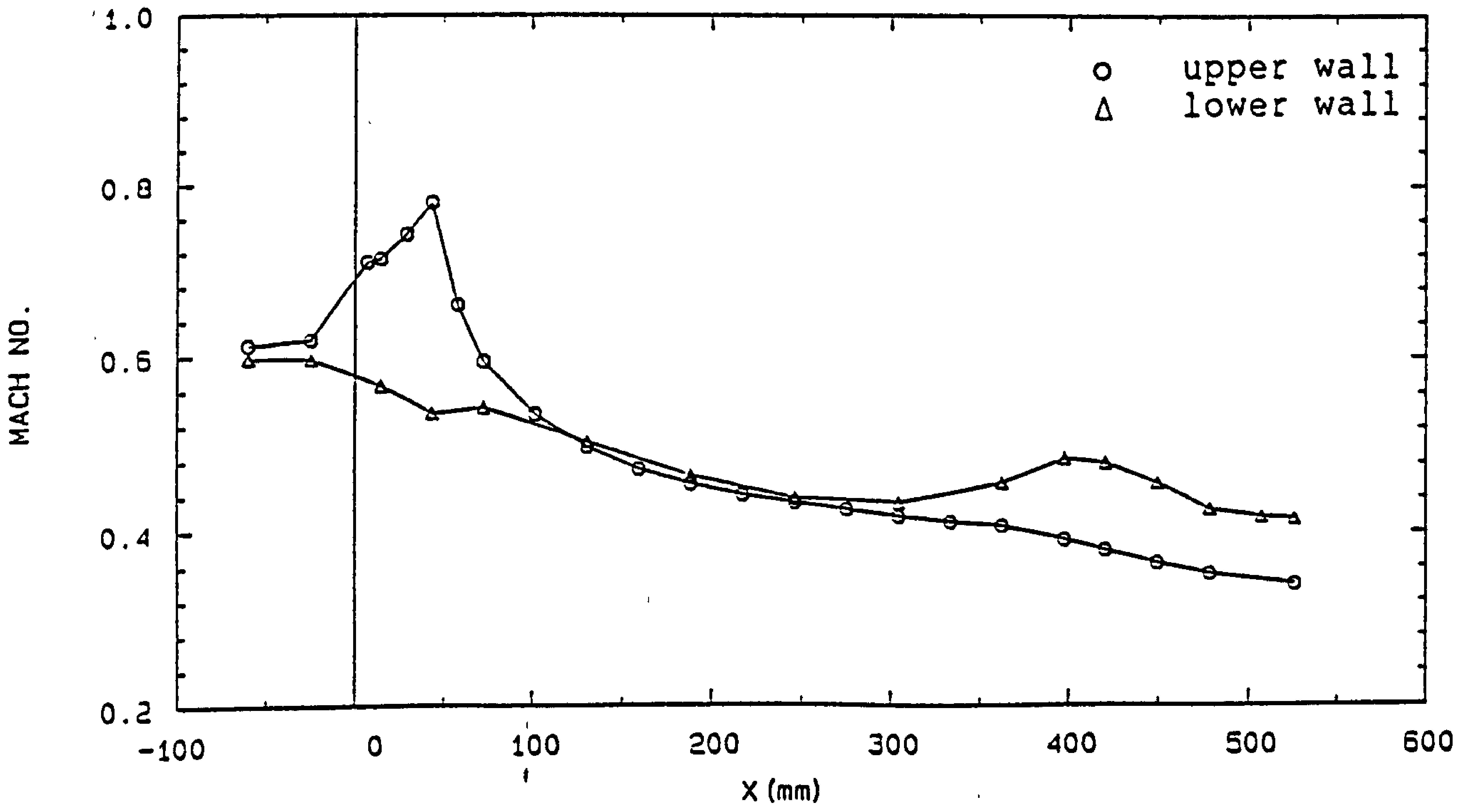

b) $M_{inlet} = 0.61$

FIG. 4-29 MACH NUMBER DISTRIBUTIONS (DUCT N)

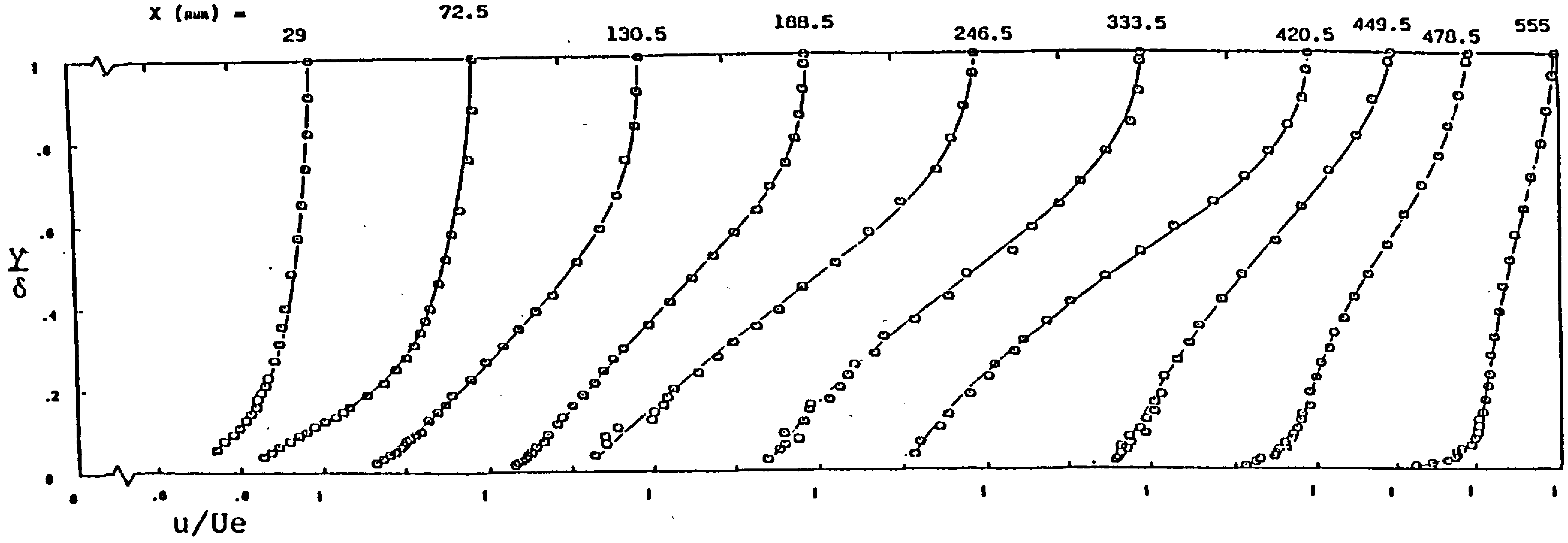

a) Upper wall

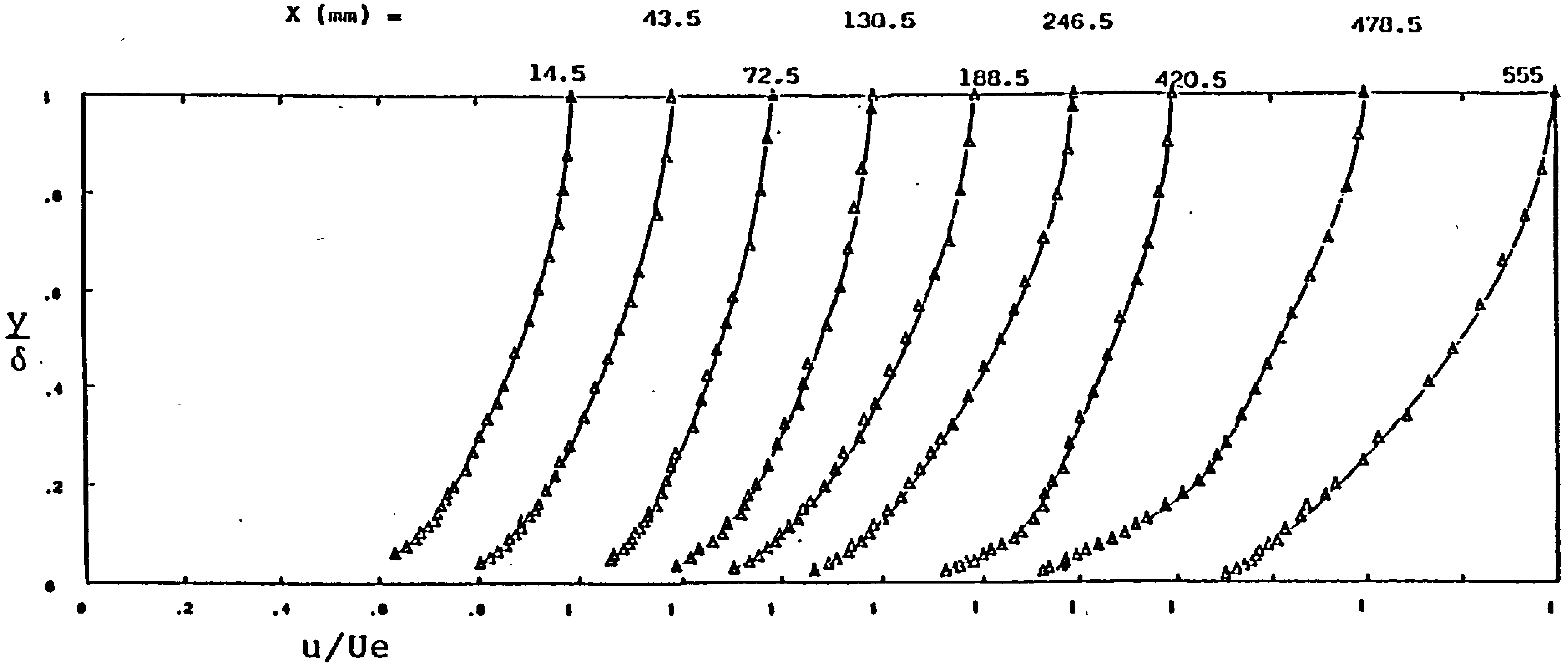

b) Lower wall

$M_{inlet} = 0.15$

FIG. 4-30 VELOCITY PROFILES (DUCT N)

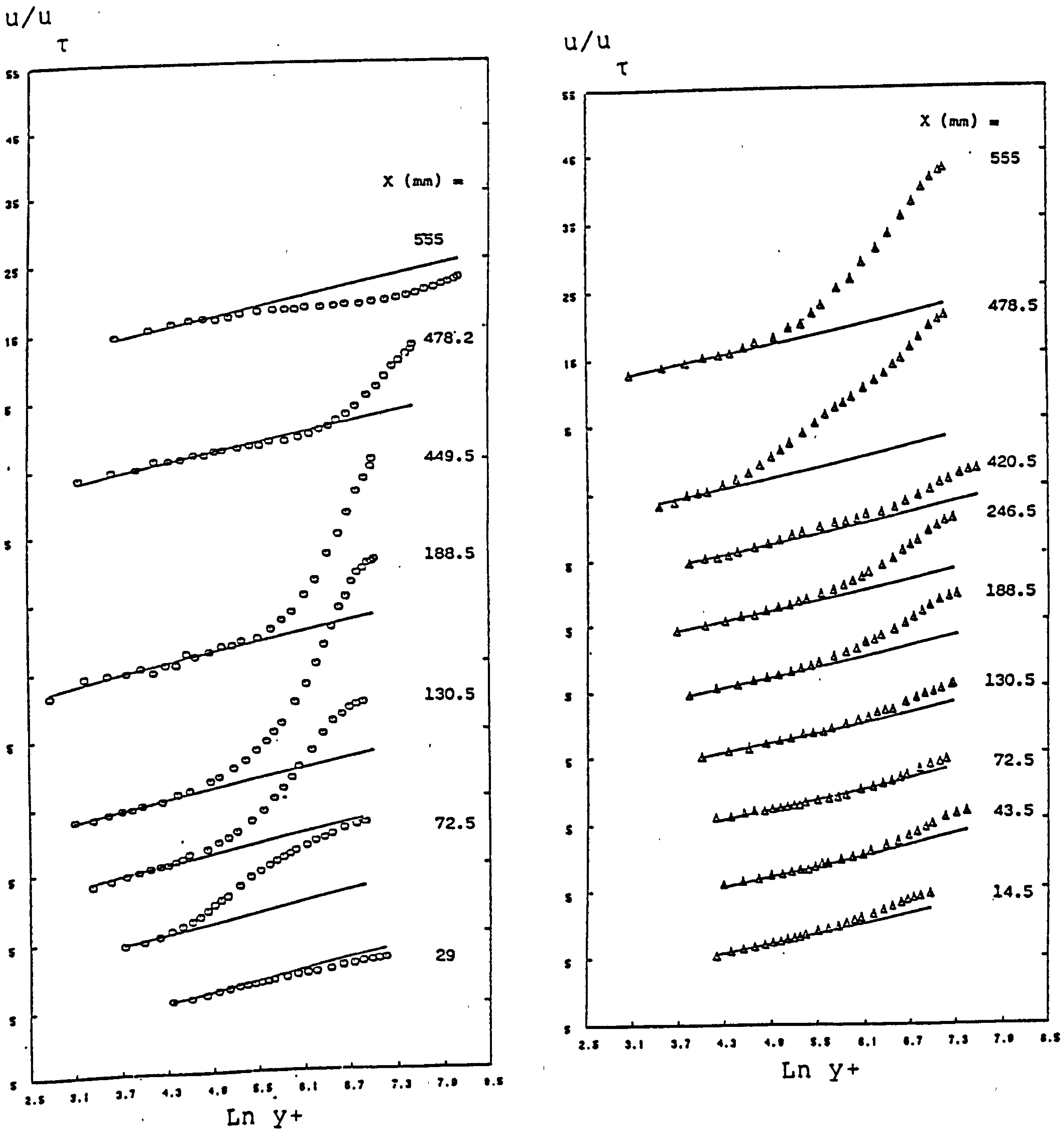

a) Upper wall b) Lower wall

$M_{inlet} = 0.15$ ——— Law of the wall

FIG. 4-31 LOGARITHMIC VELOCITY PROFILES (DUCT N)

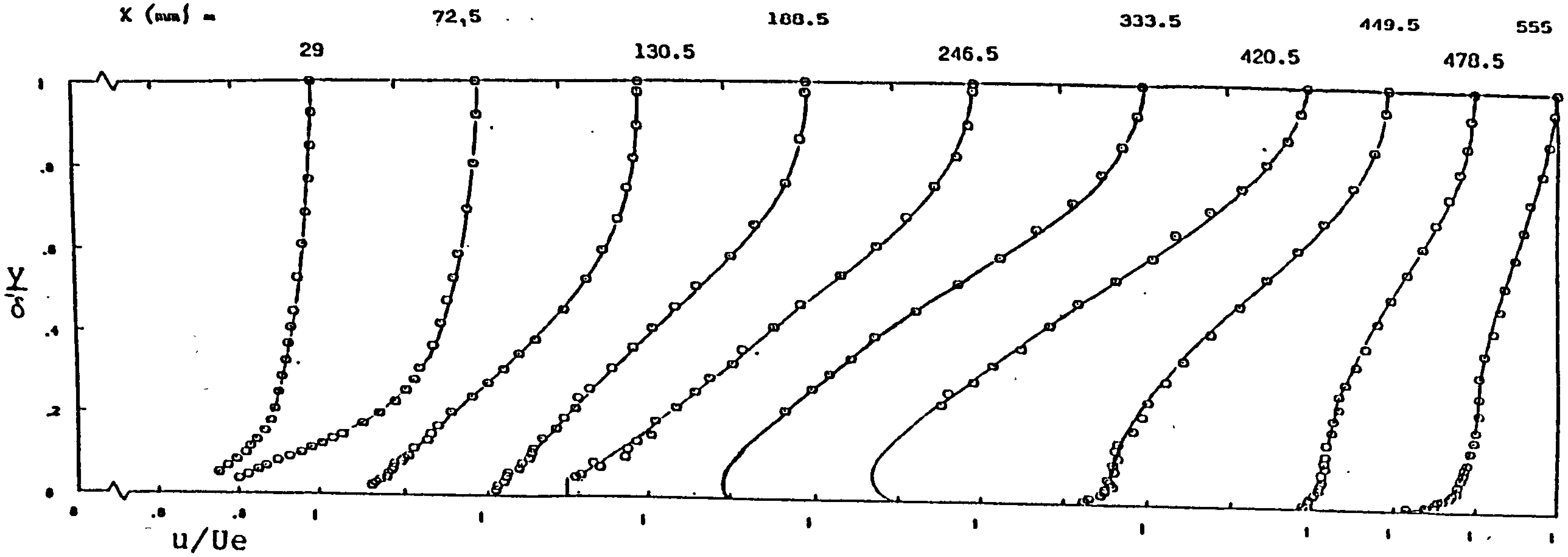

a) Upper wall

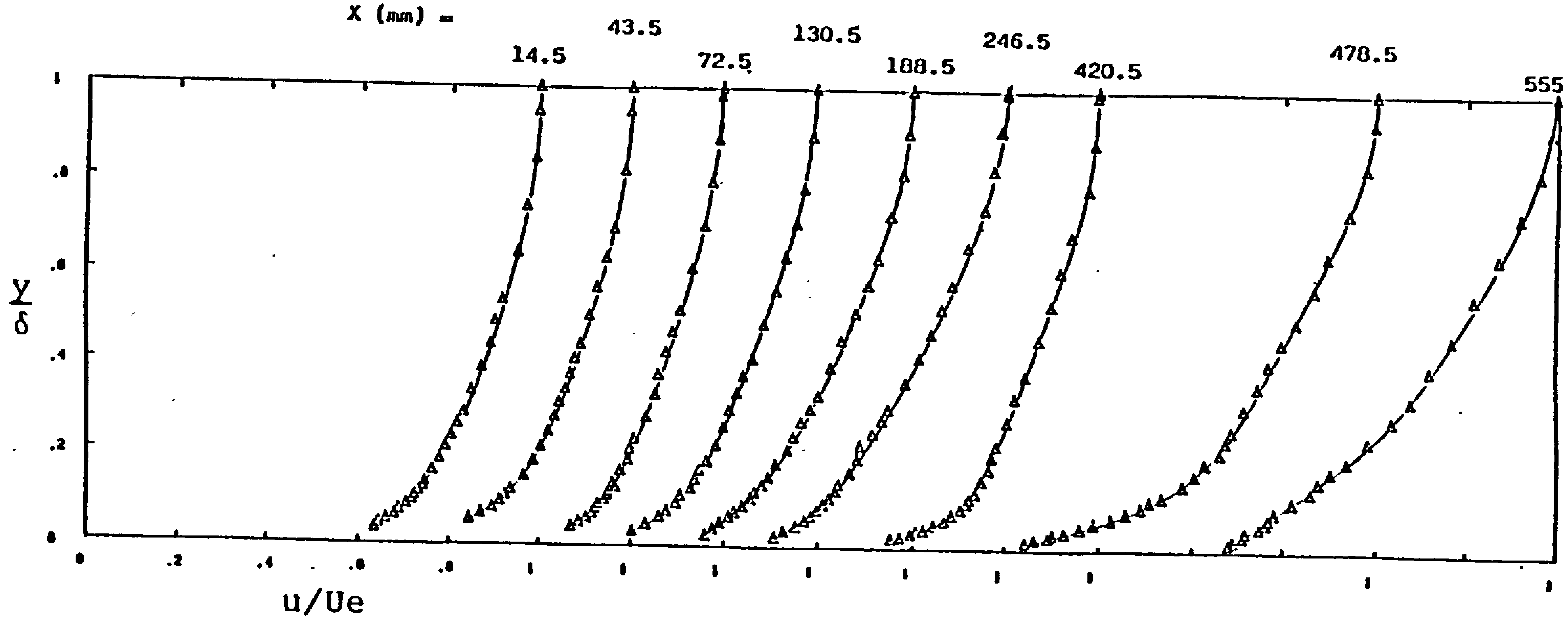

b) Lower wall

$M_{inlet} = 0.61$

FIG. 4-32 VELOCITY PROFILES (DUCT N)

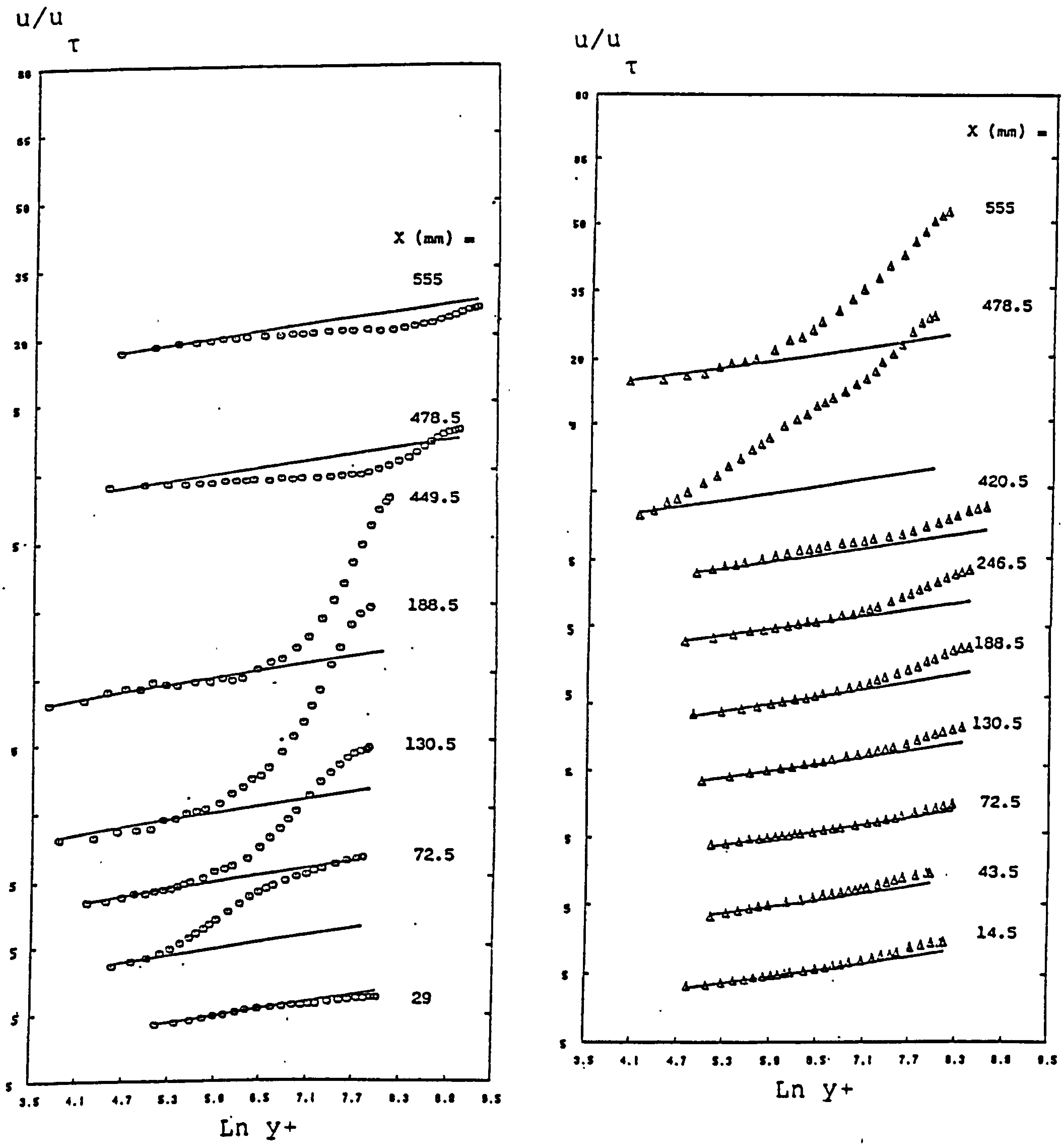

a) Upper wall b) Lower wall

$M_{inlet} = 0.61$ —— Law of the wall

FIG. 4-33 LOGARITHMIC VELOCITY PROFILES (DUCT N)

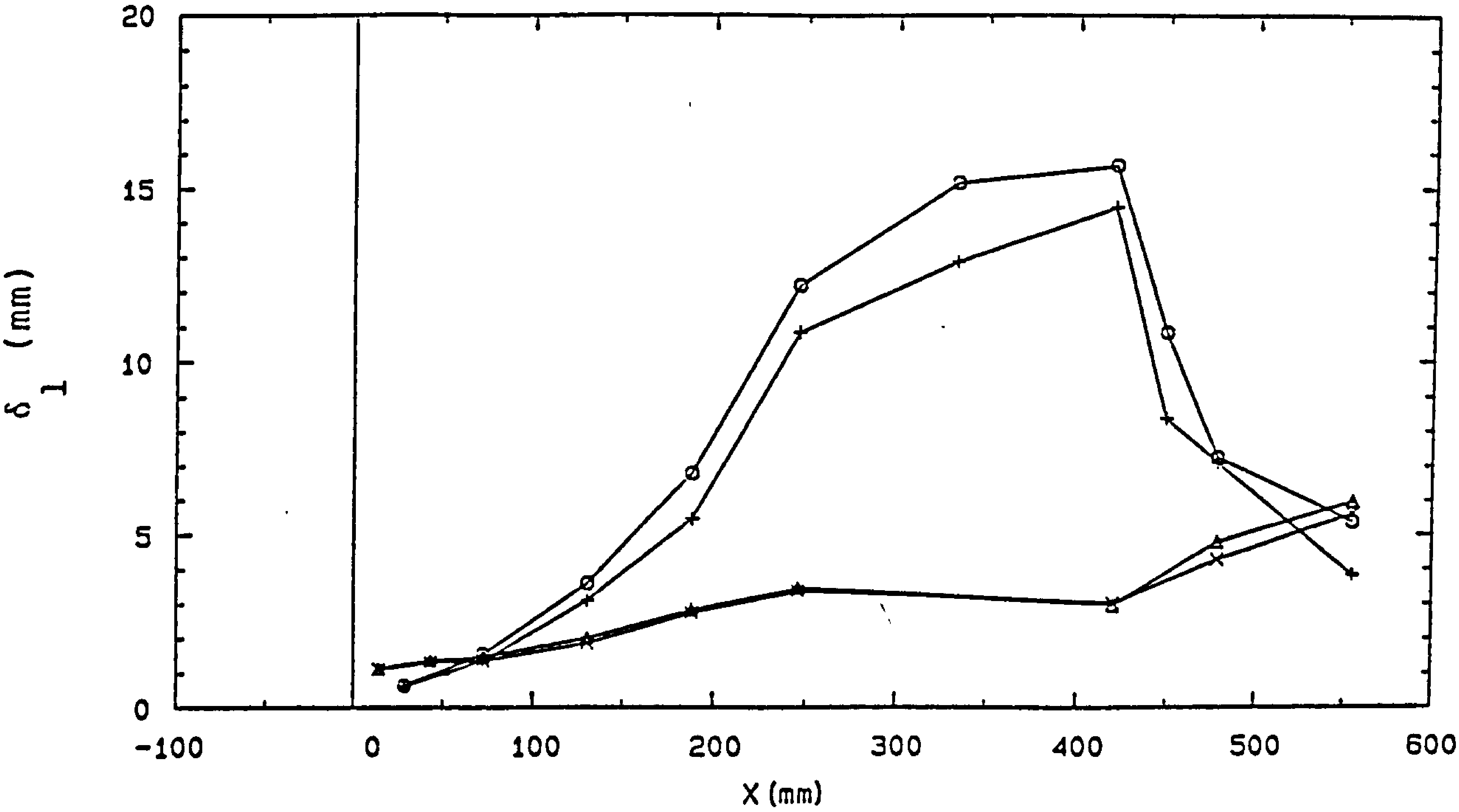

FIG. 4-34 DISPLACEMENT THICKNESSES DISTRIBUTIONS (DUCT N)

M(inlet)	0.15	0.61
upper wall	+	o
lower wall	x	Δ

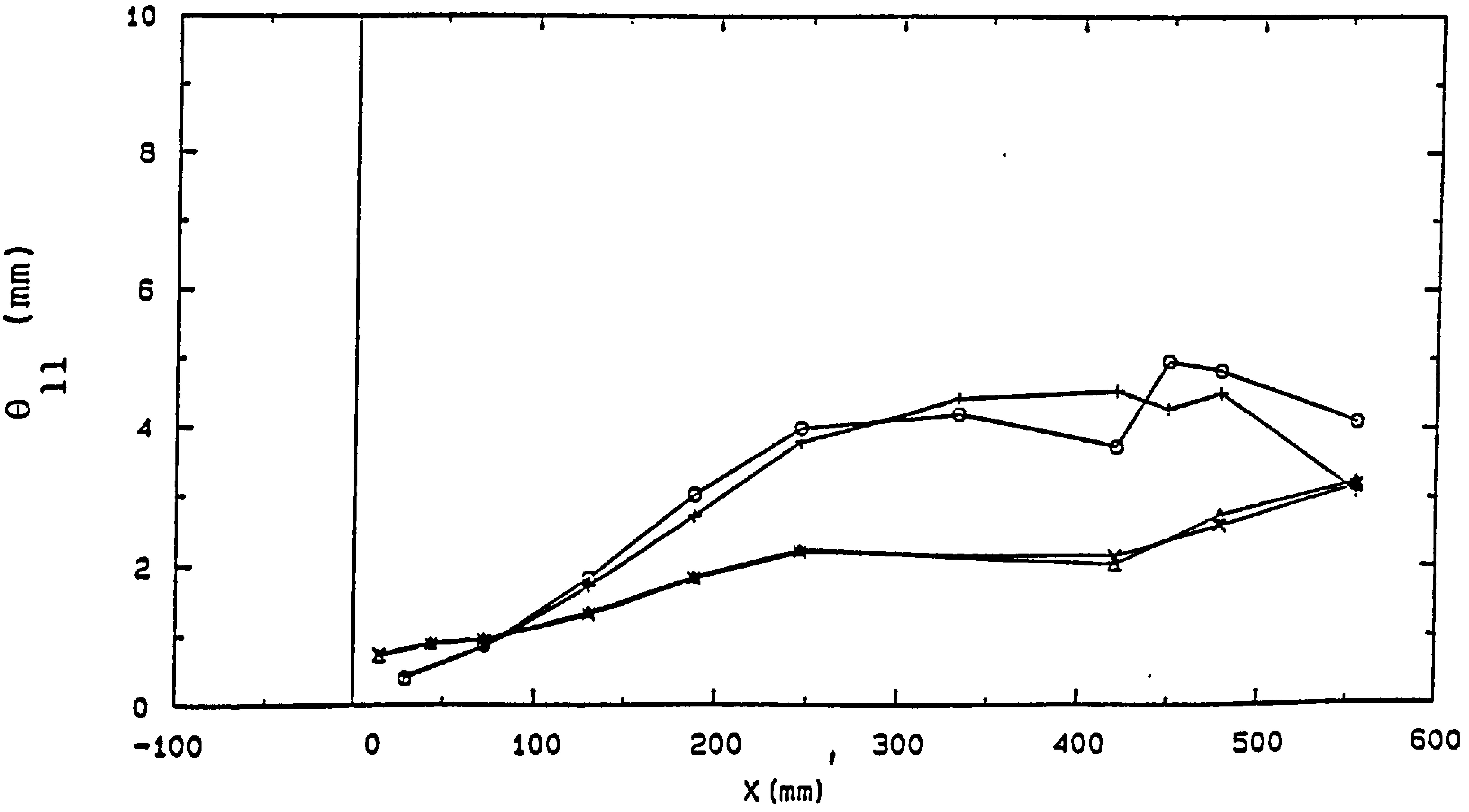

FIG. 4-35 MOMENTUM THICKNESSES DISTRIBUTIONS (DUCT N)

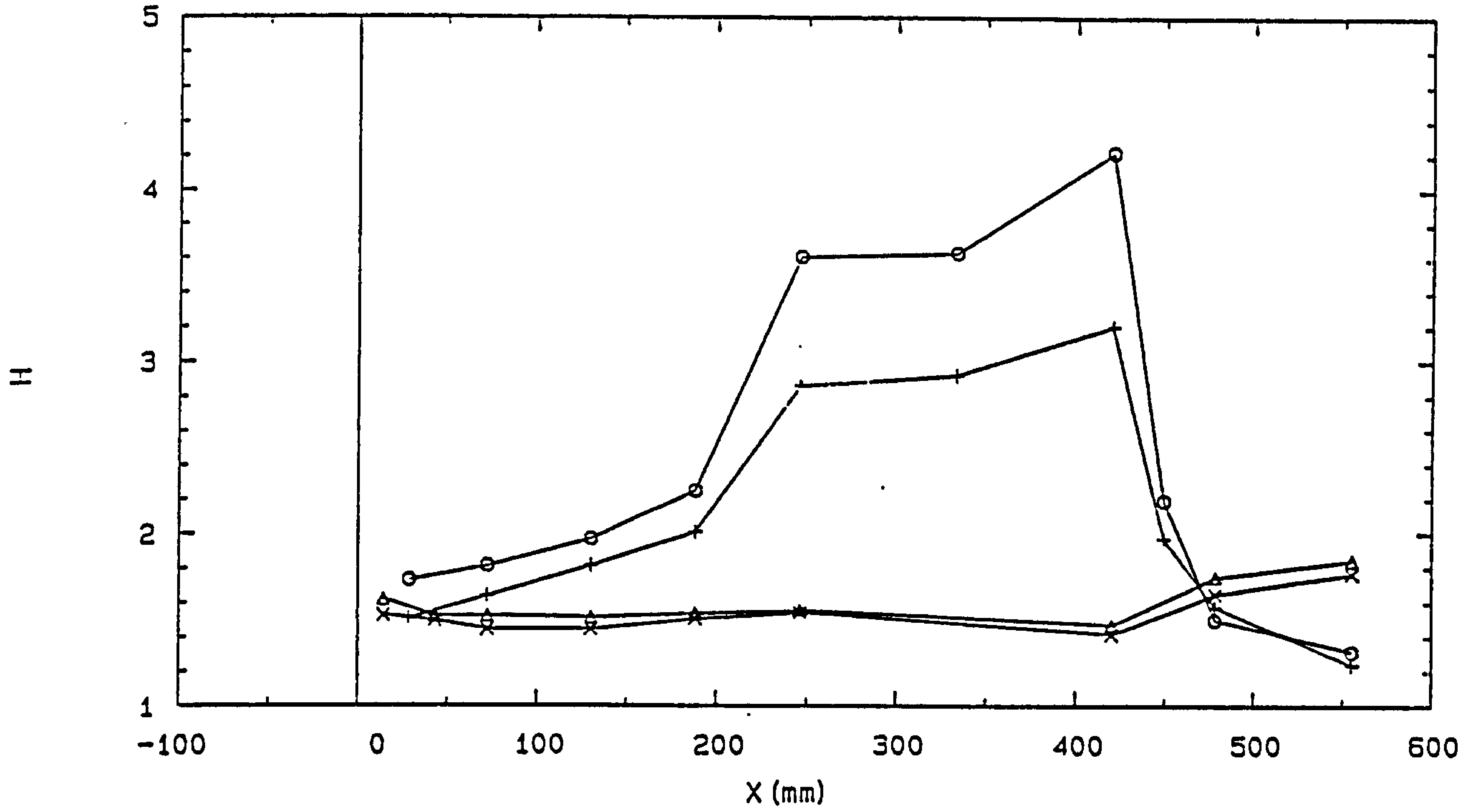

FIG. 4-36 SHAPE PARAMETER DISTRIBUTIONS (DUCT N)

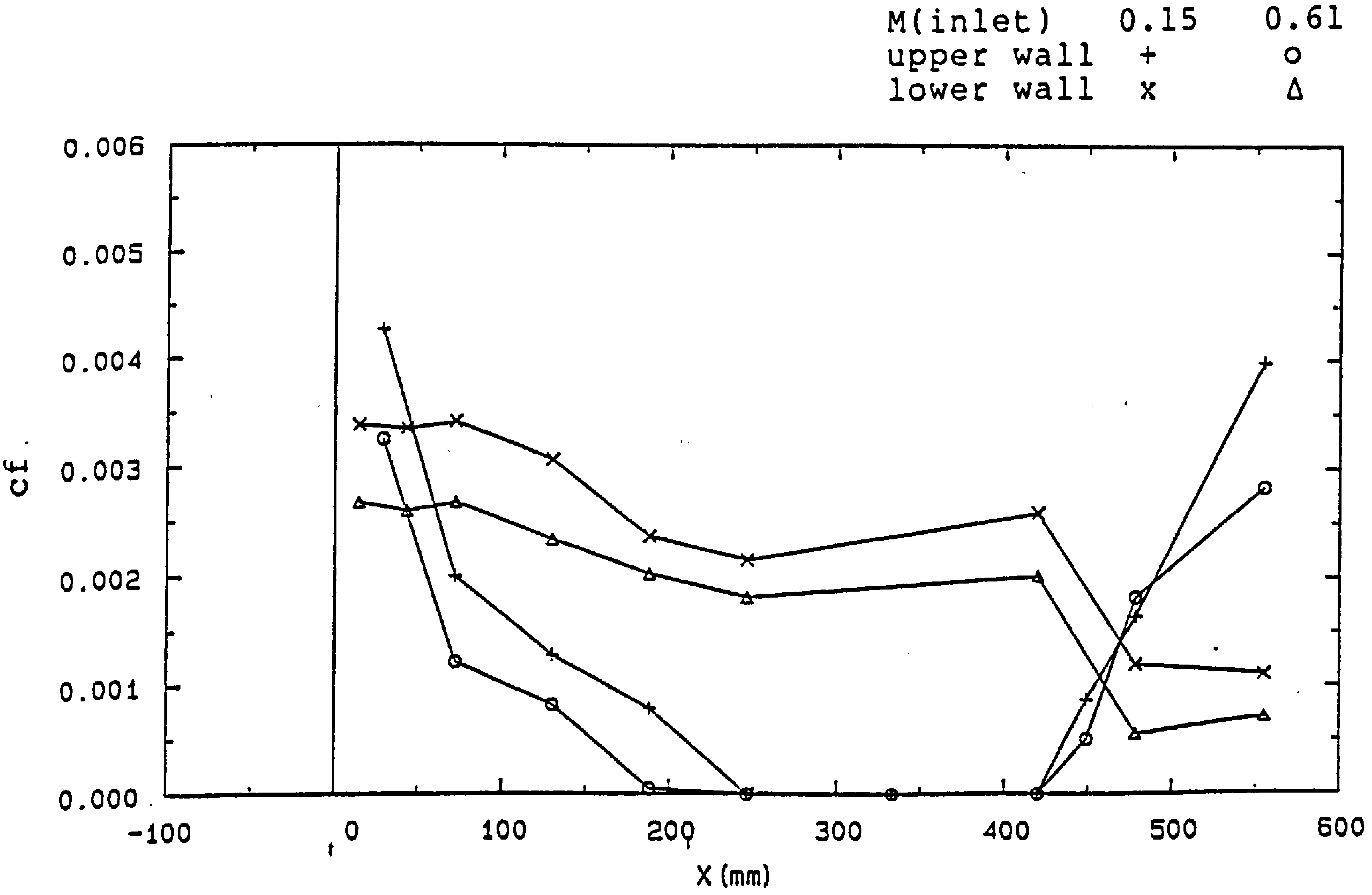

FIG. 4-37 SKIN FRICTION DISTRIBUTIONS (DUCT N)

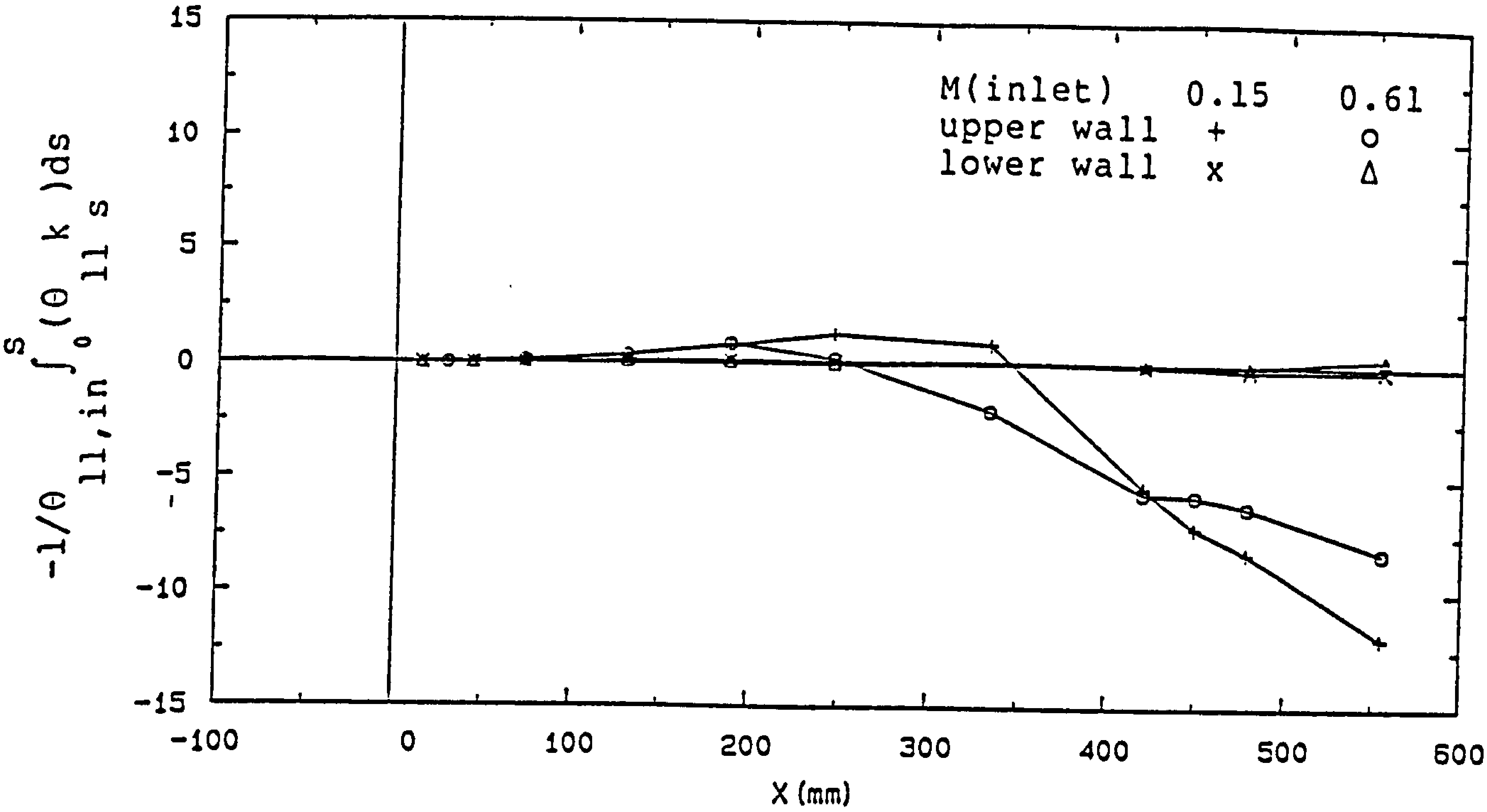

FIG. 4-38 MOMENTUM BALANCE (DUCT N)

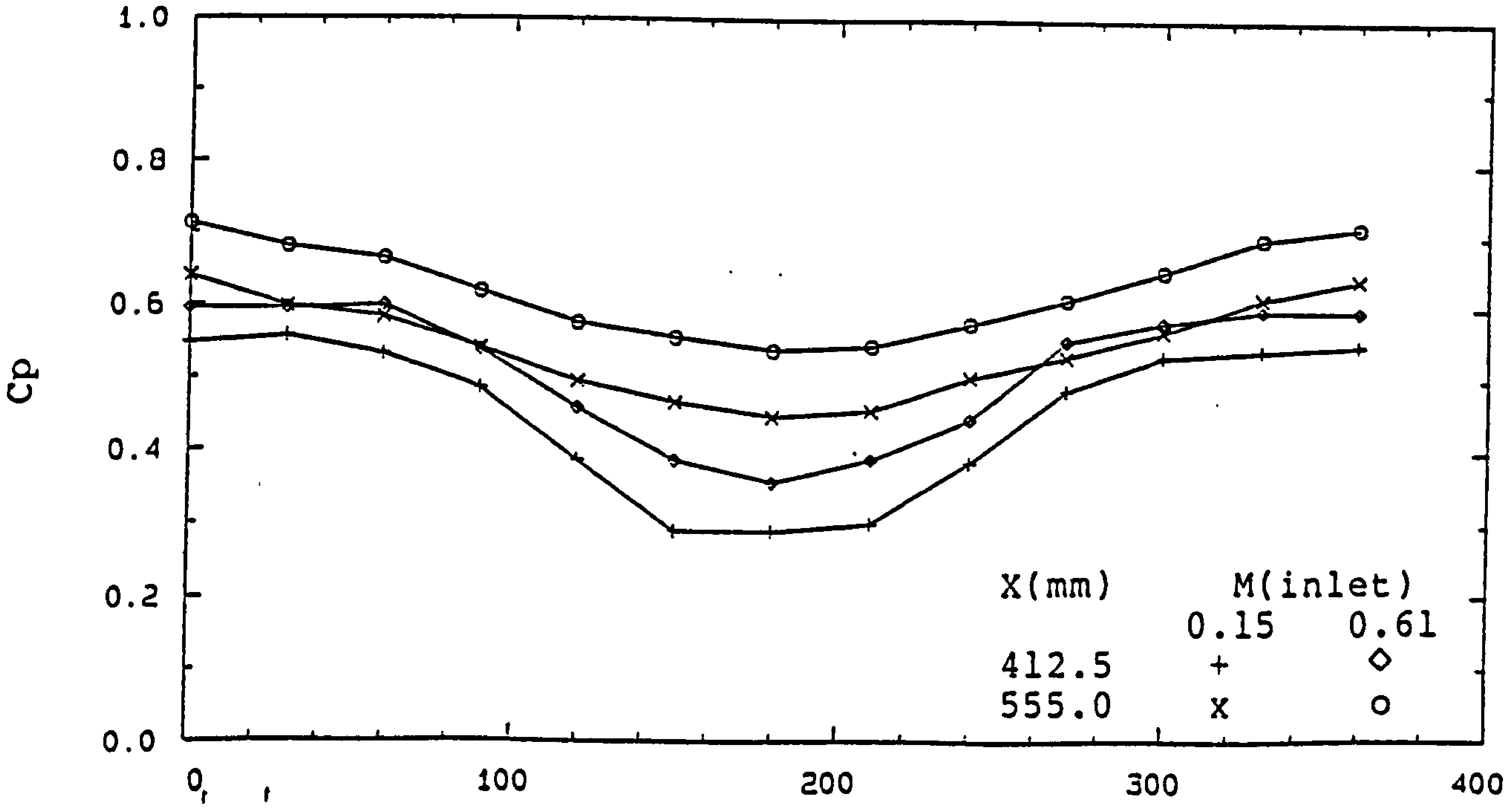

FIG. 4-39 PRESSURE DISTRIBUTIONS (DUCT N)

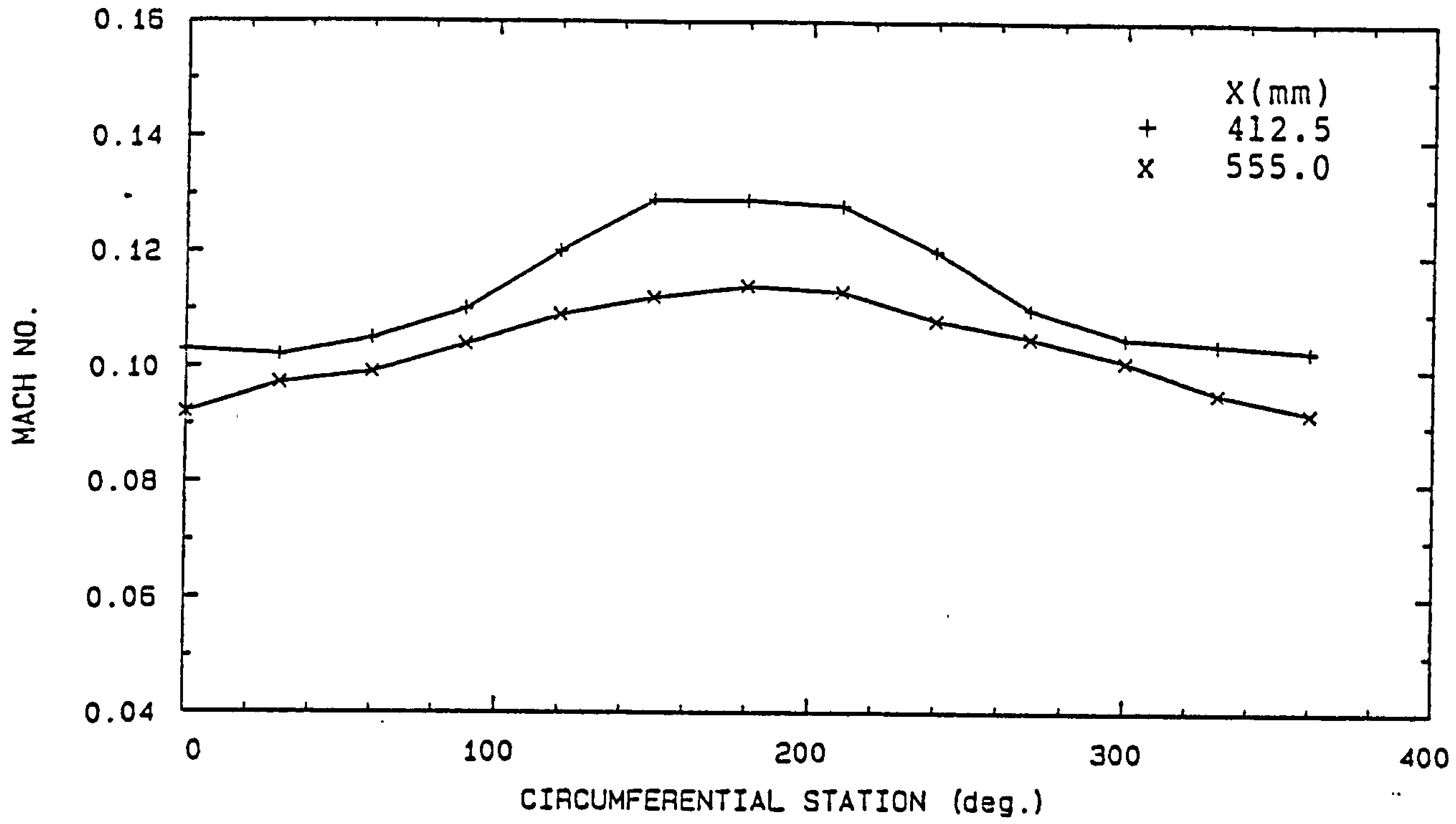

a) $M_{inlet} = 0.15$

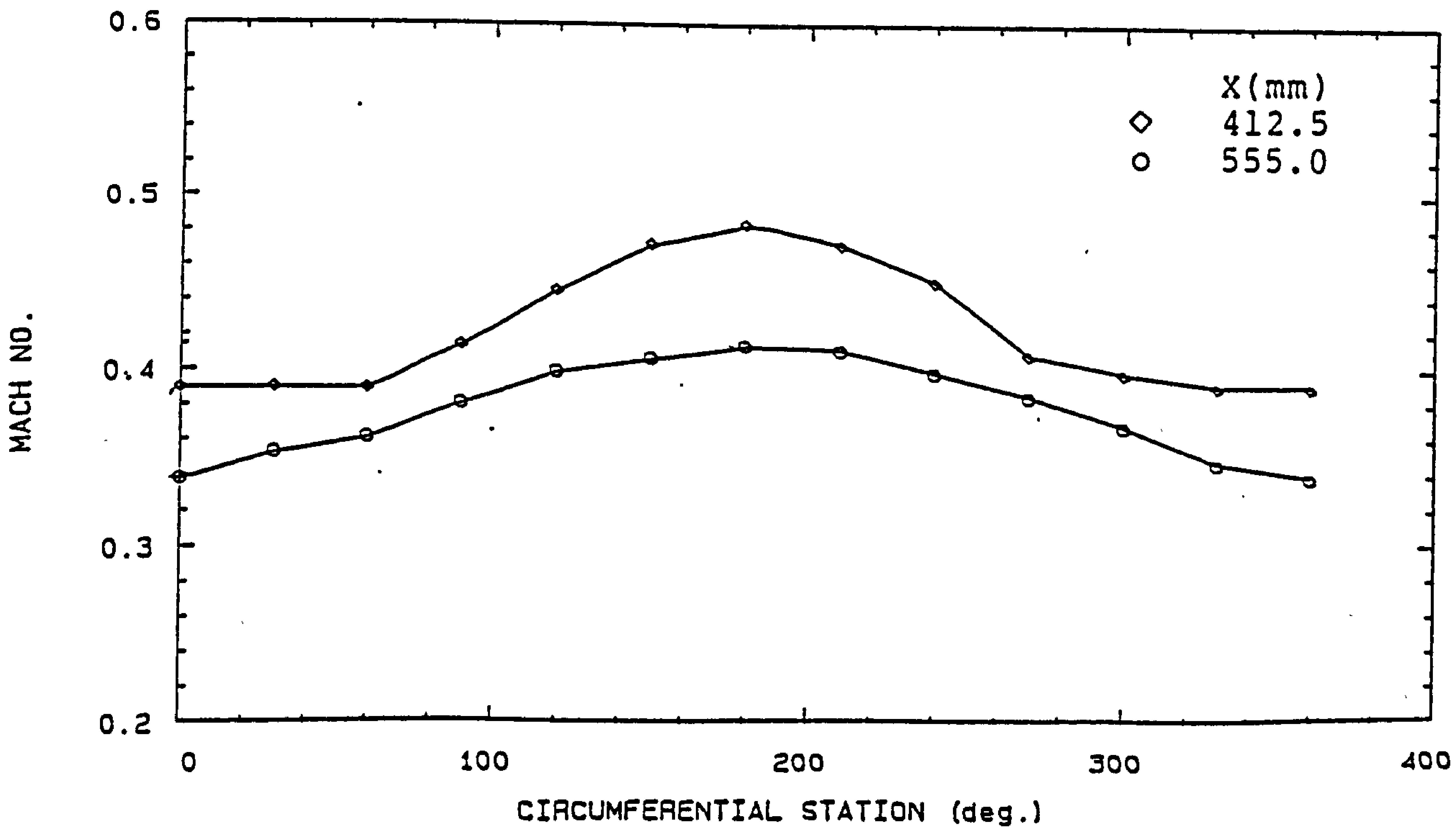

b) $M_{inlet} = 0.61$

FIG. 4-40 MACH NUMBER DISTRIBUTIONS (DUCT N)

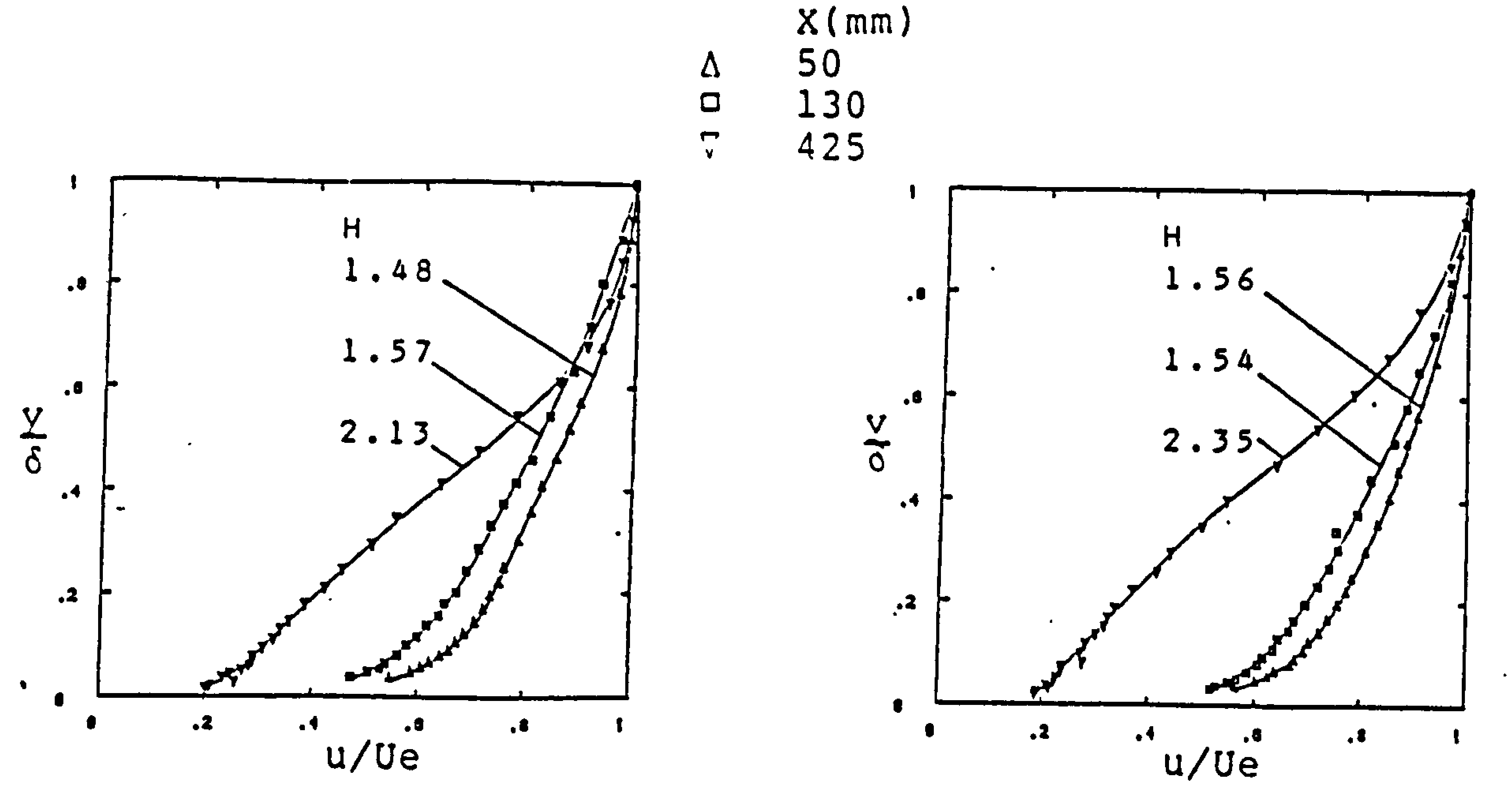

a1, a2) Streamwise velocity profiles

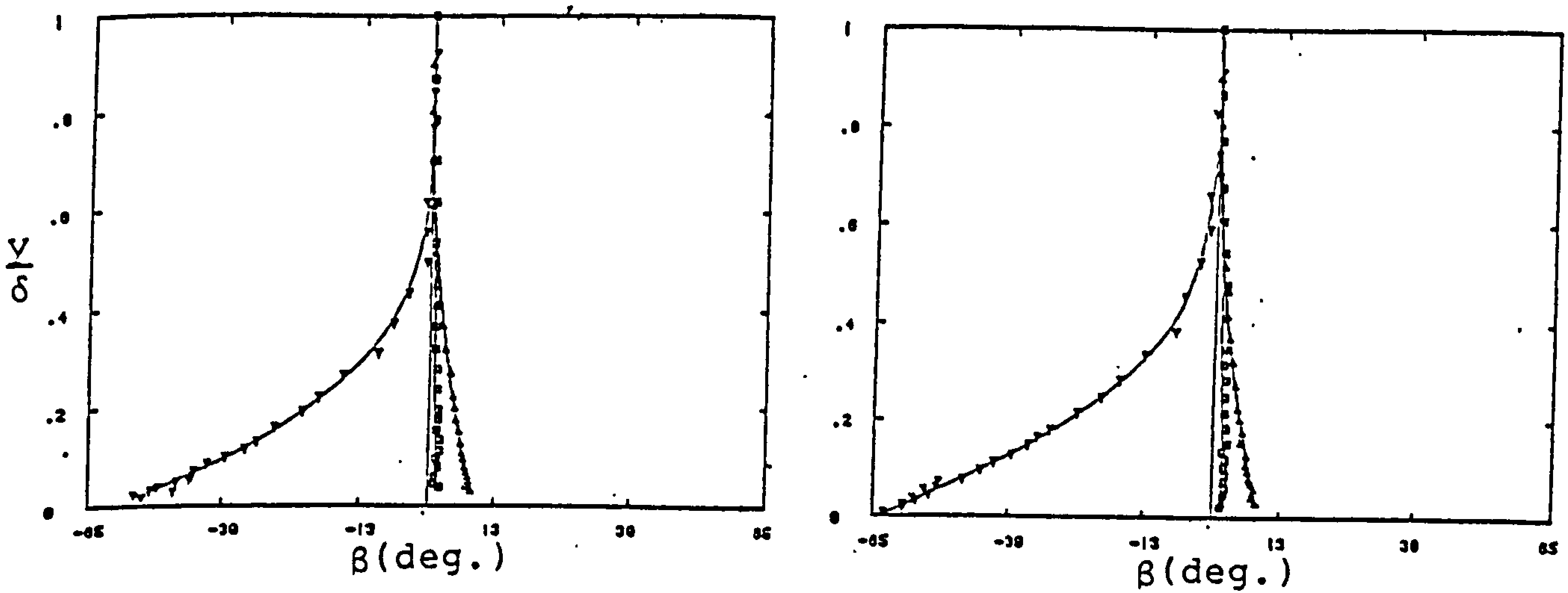

b1, b2) Skew angle profiles

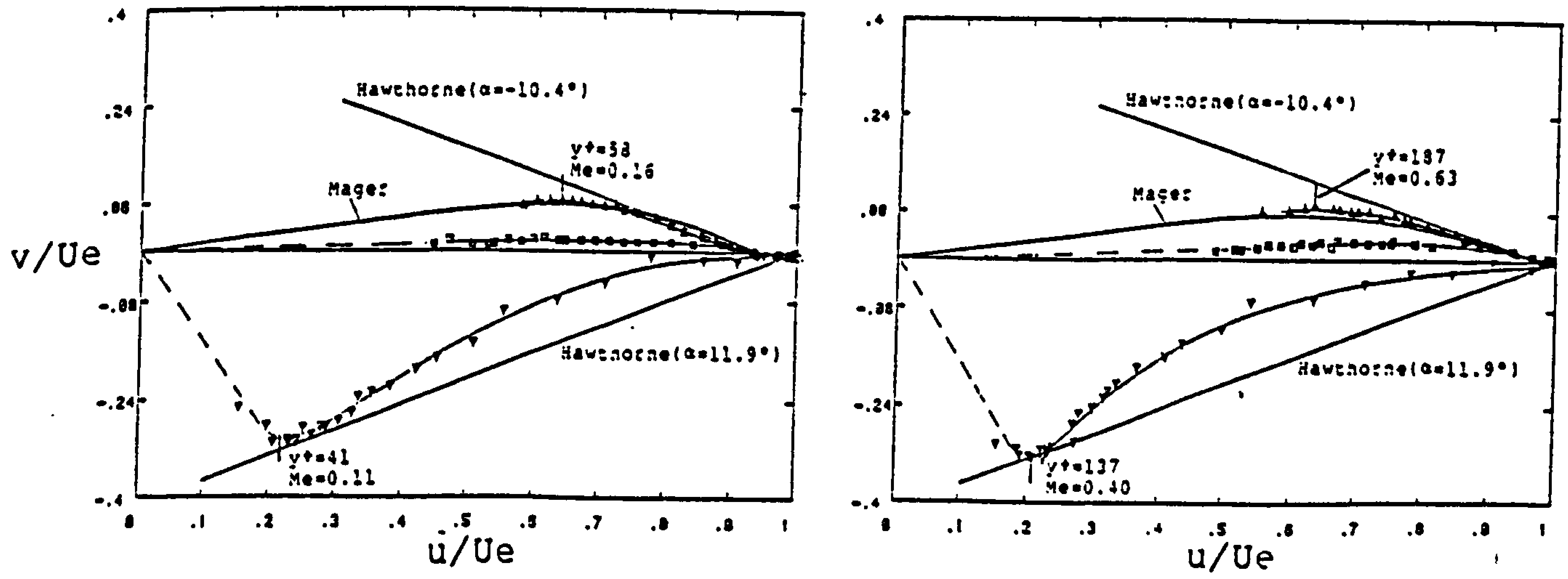

c1, c2) Polar plots

$M_{inlet} = 0.15$ $M_{inlet} = 0.61$

FIG. 4-41 SIDE WALL BOUNDARY LAYER (DUCT N)

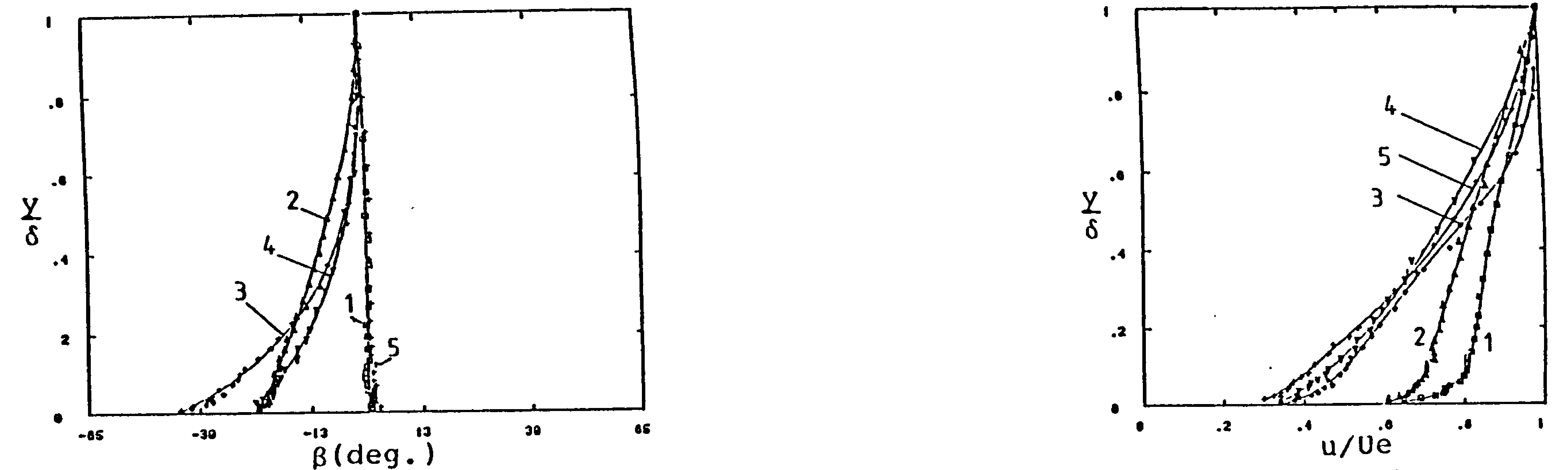

.a) Skew angle profiles

b) Streamwise velocity profiles

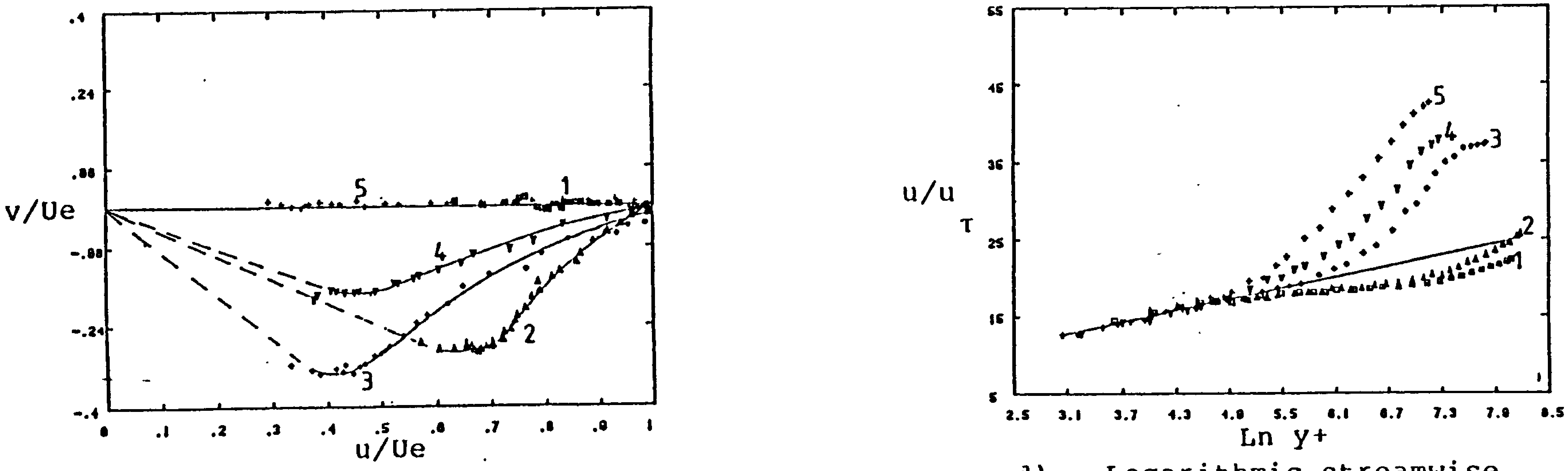

c) Polar profiles

d) Logarithmic streamwise velocity profiles

M_{inlet} =0.15, X=555mm

——— Law of the wall

FIG. 4-42 ENGINE FACE BOUNDARY LAYER (DUCT N)

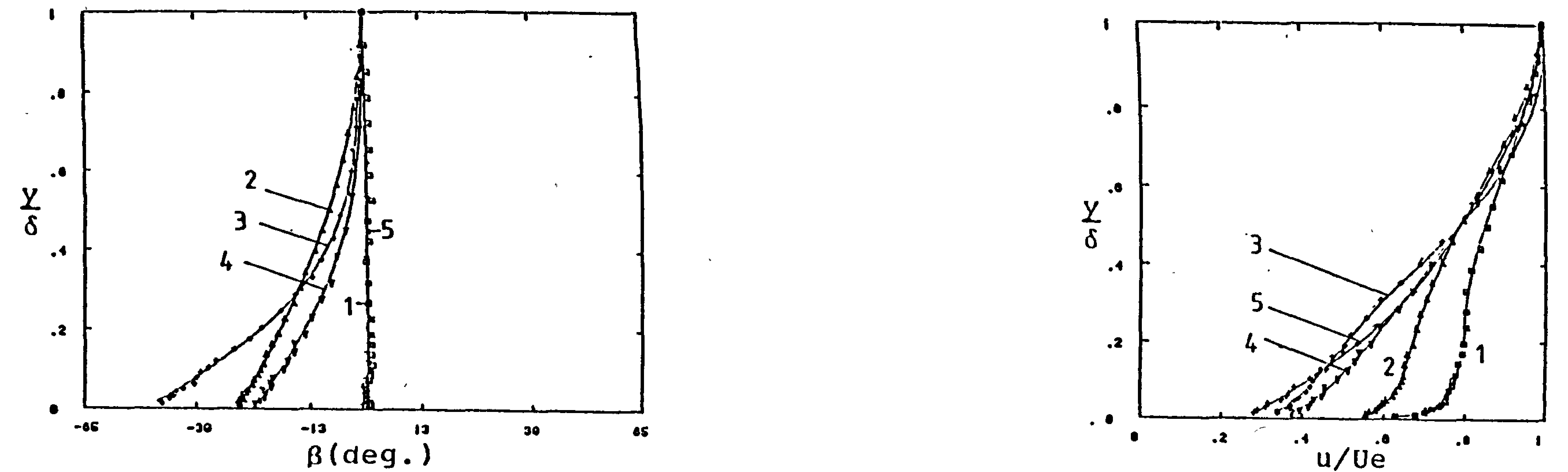

a) Skew angle profiles

b) Streamwise velocity profiles

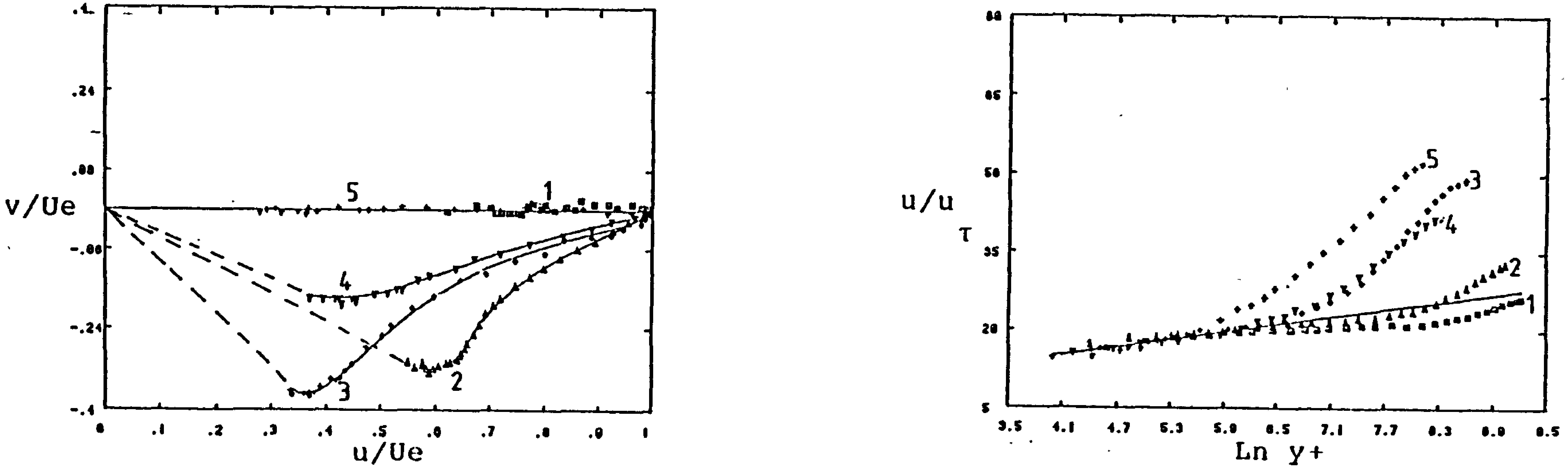

c) Polar profiles

d) Logarithmic streamwise velocity profiles

M_{inlet} =0.61, X=555mm

——— Law of the wall

FIG. 4-43 ENGINE FACE BOUNDARY LAYER (DUCT N)

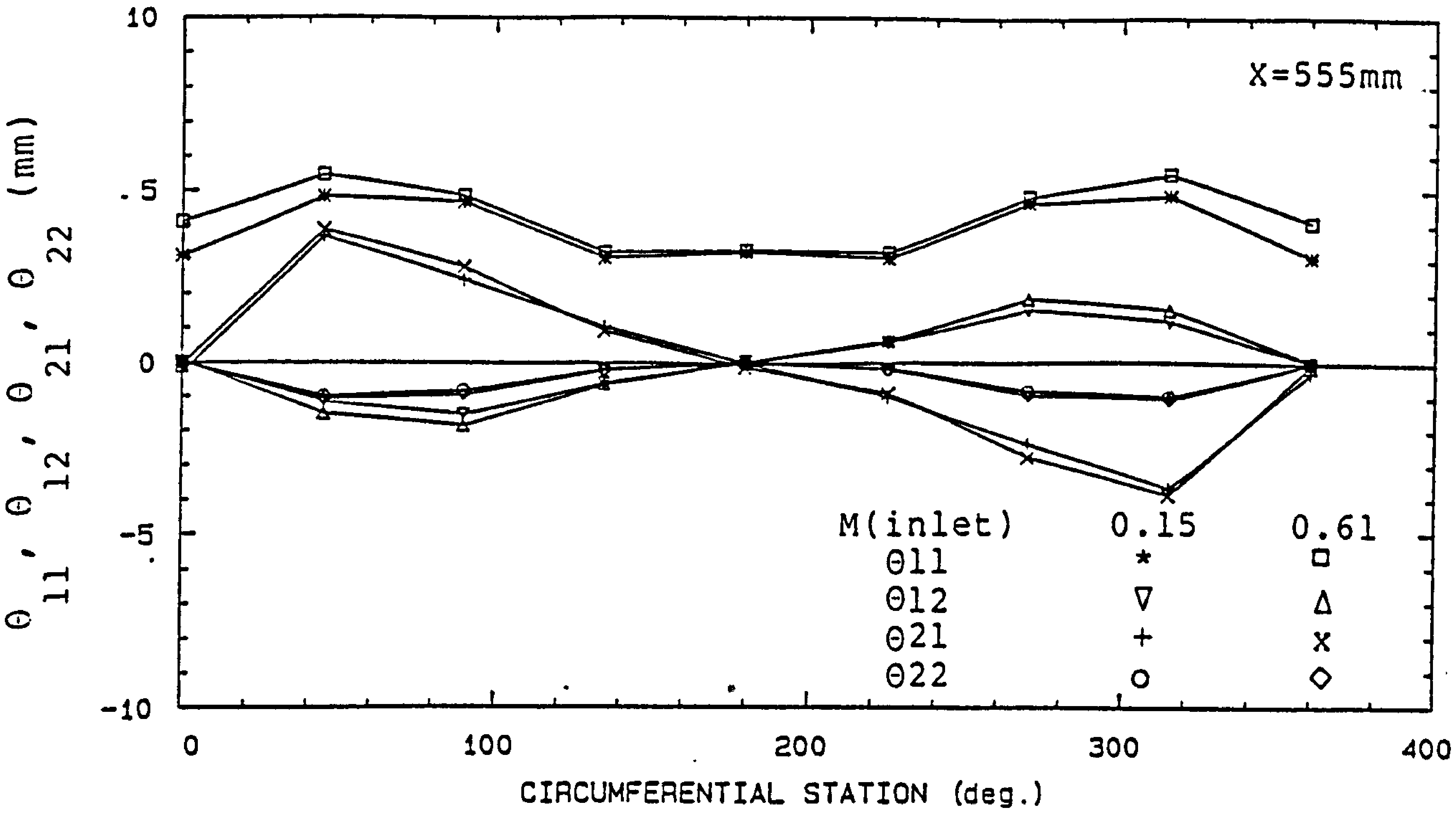

FIG. 4-44 MOMENTUM THICKNESSES DISTRIBUTIONS (DUCT N)

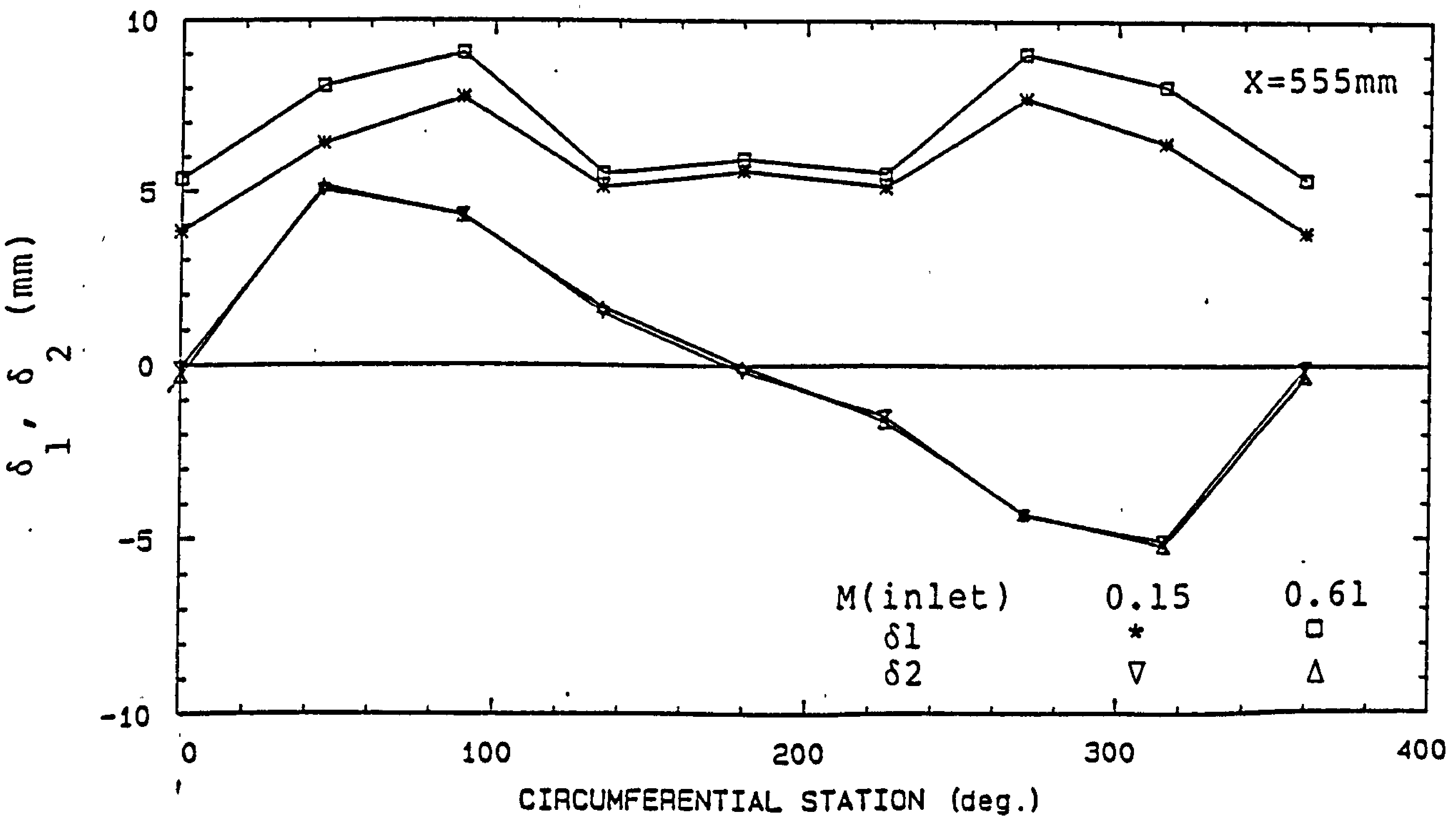

FIG. 4-45 DISPLACEMENT THICKNESSES DISTRIBUTIONS (DUCT N)

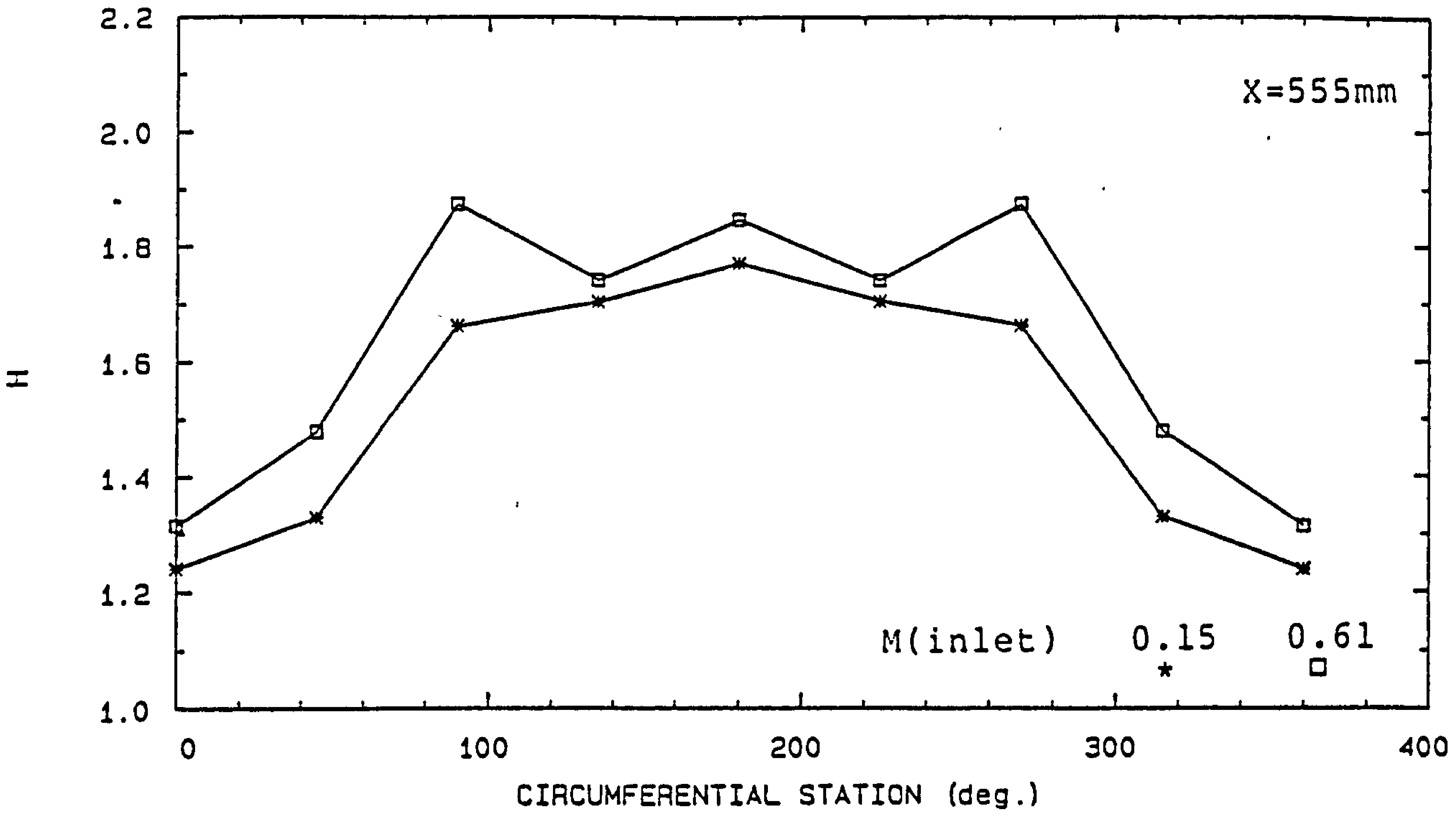

FIG. 4-46 SHAPE PARAMETER DISTRIBUTIONS (DUCT N)

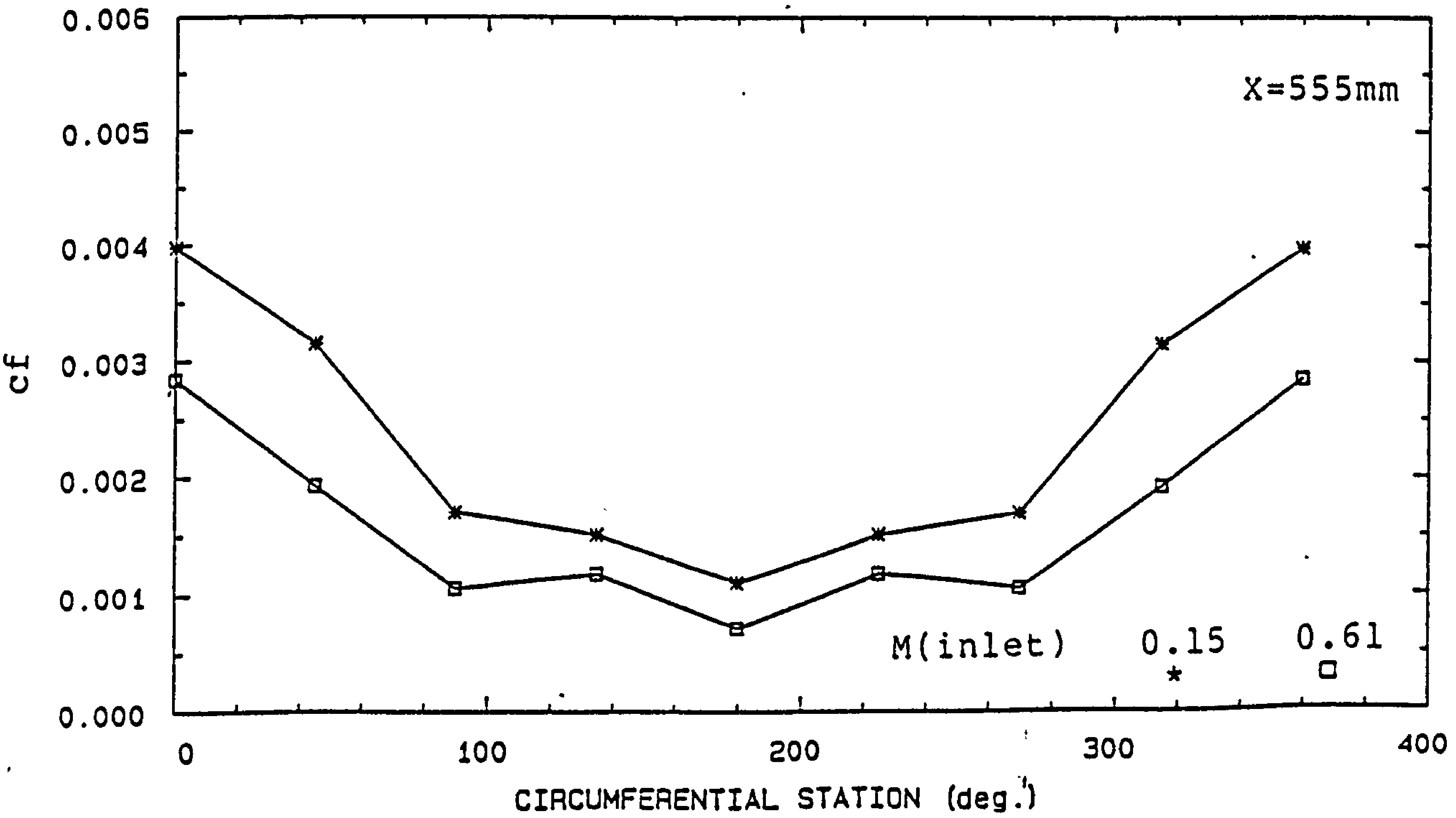

FIG. 4-47 SKIN FRICTION DISTRIBUTIONS (DUCT N)

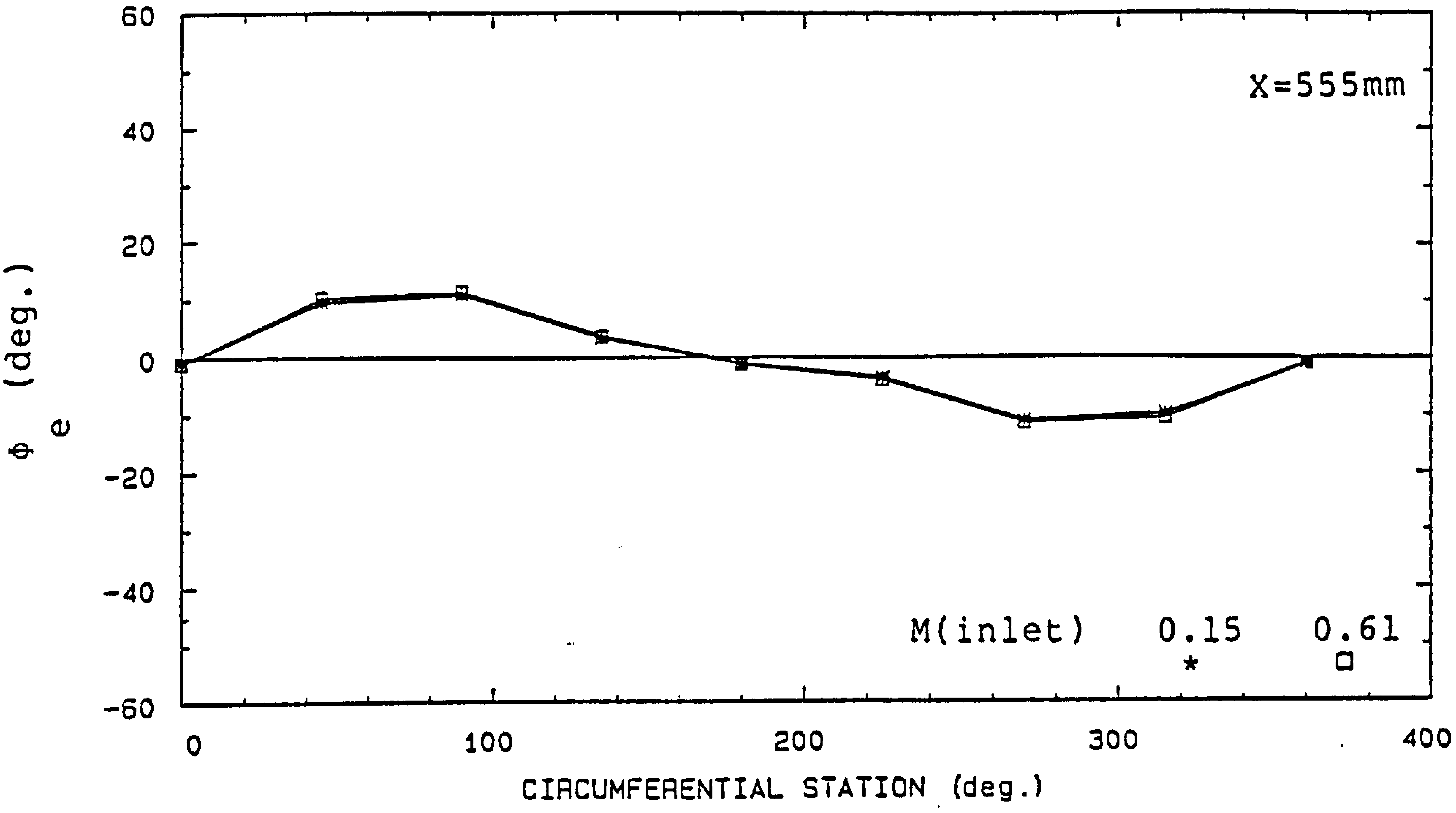

FIG. 4-48 BOUNDARY LAYER EDGE FLOW DIRECTIONS RELATIVE TO DUCT OUTLET AXIS (DUCT N)

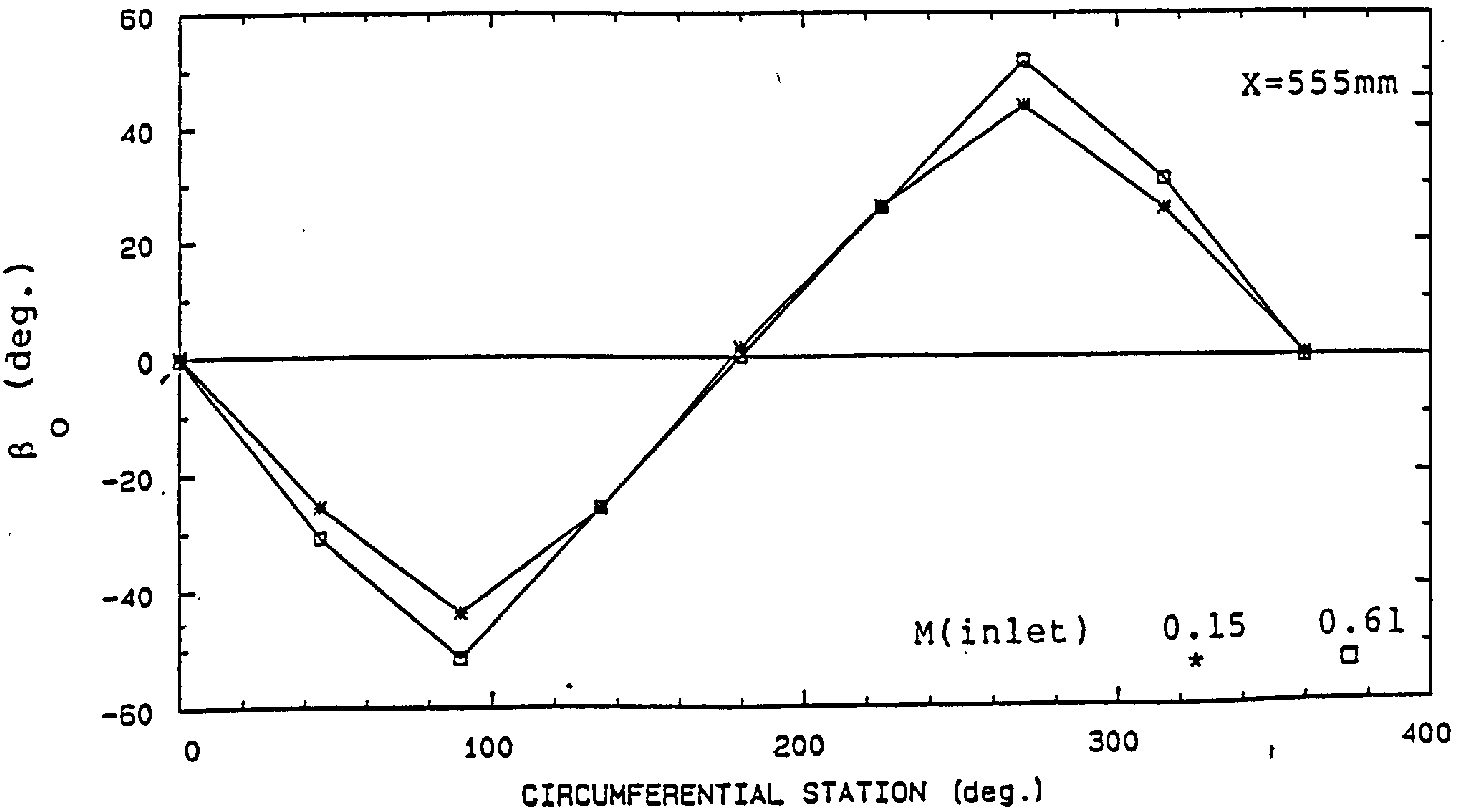

FIG. 4-49 LIMITING STREAMLINE ANGLE DISTRIBUTIONS (DUCT N)

a) $M_{inlet} = 0.15$

b) $M_{inlet} = 0.61$

FIG. 4-50 ENGINE FACE CROSSFLOW AND TOTAL PRESSURE DISTRIBUTIONS (DUCT N)

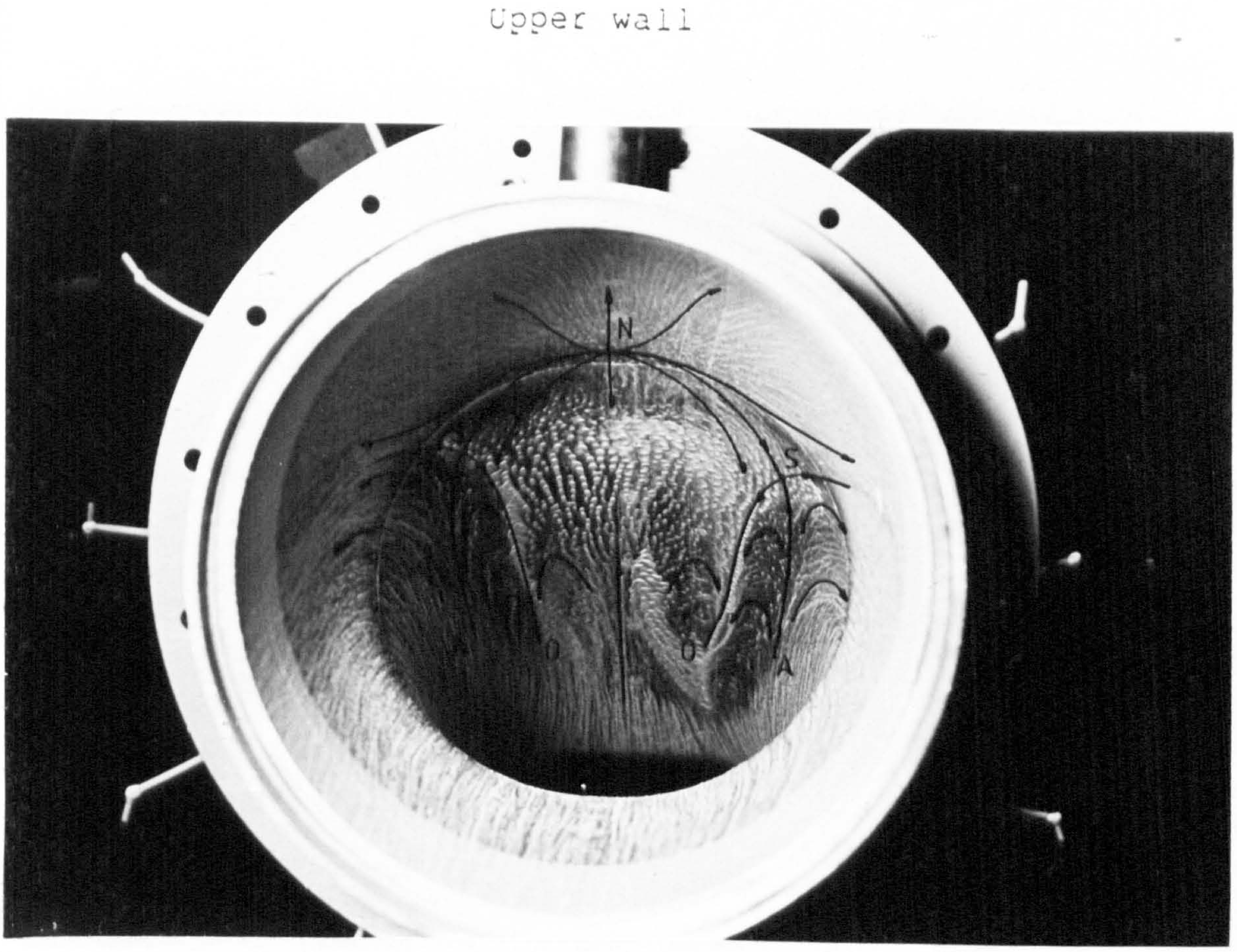

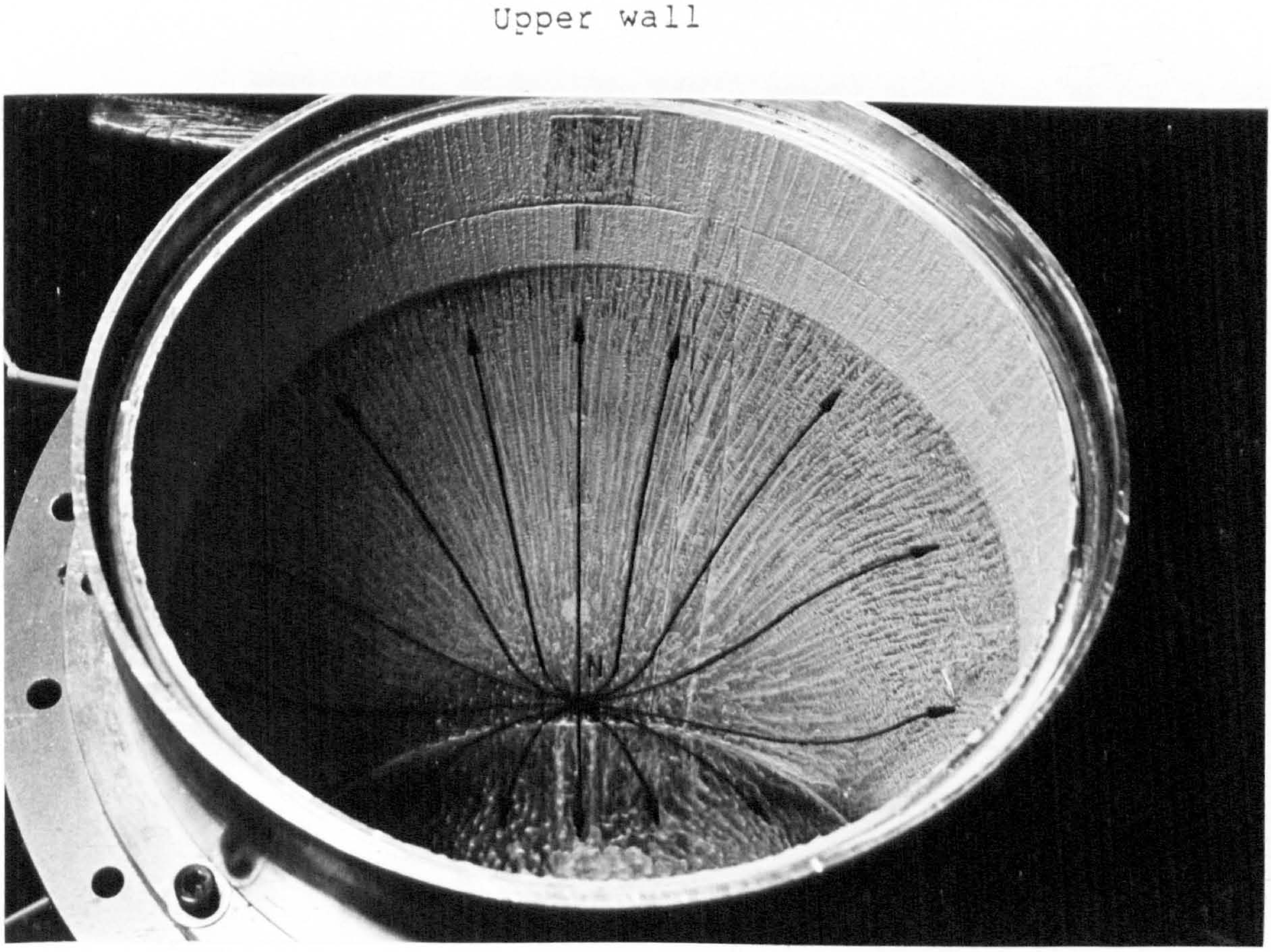

FIG. 4-51 SURFACE OIL FLOW VISUALIZATION AND TOPOLOGICAL STRUCTURE (DUCT N)

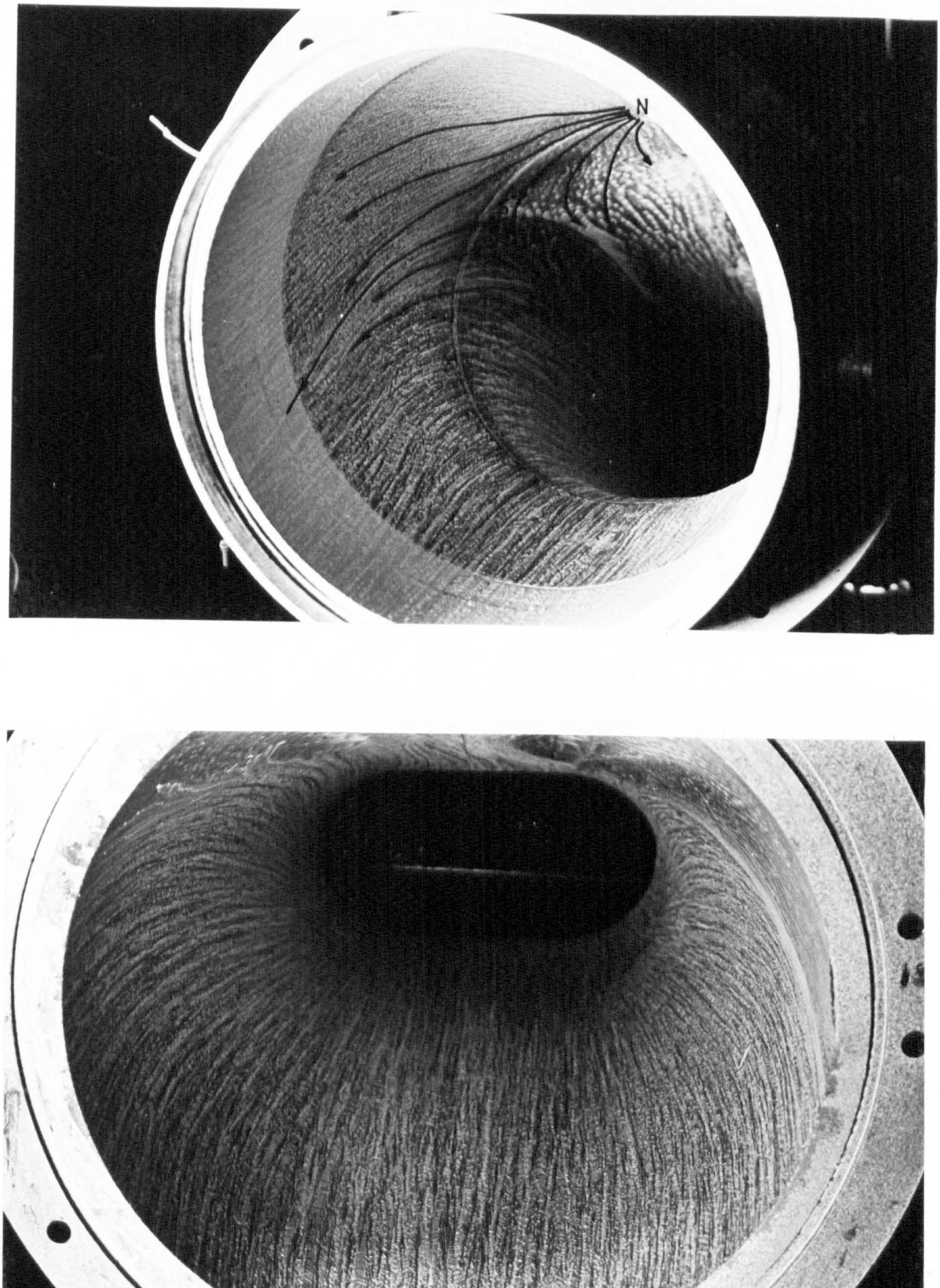

Upper wall

Lower wall (second bend detached)

FIG. 4-52 SURFACE OIL FLOW VISUALIZATION AND TOPOLOGICAL STRUCTURE (DUCT N)

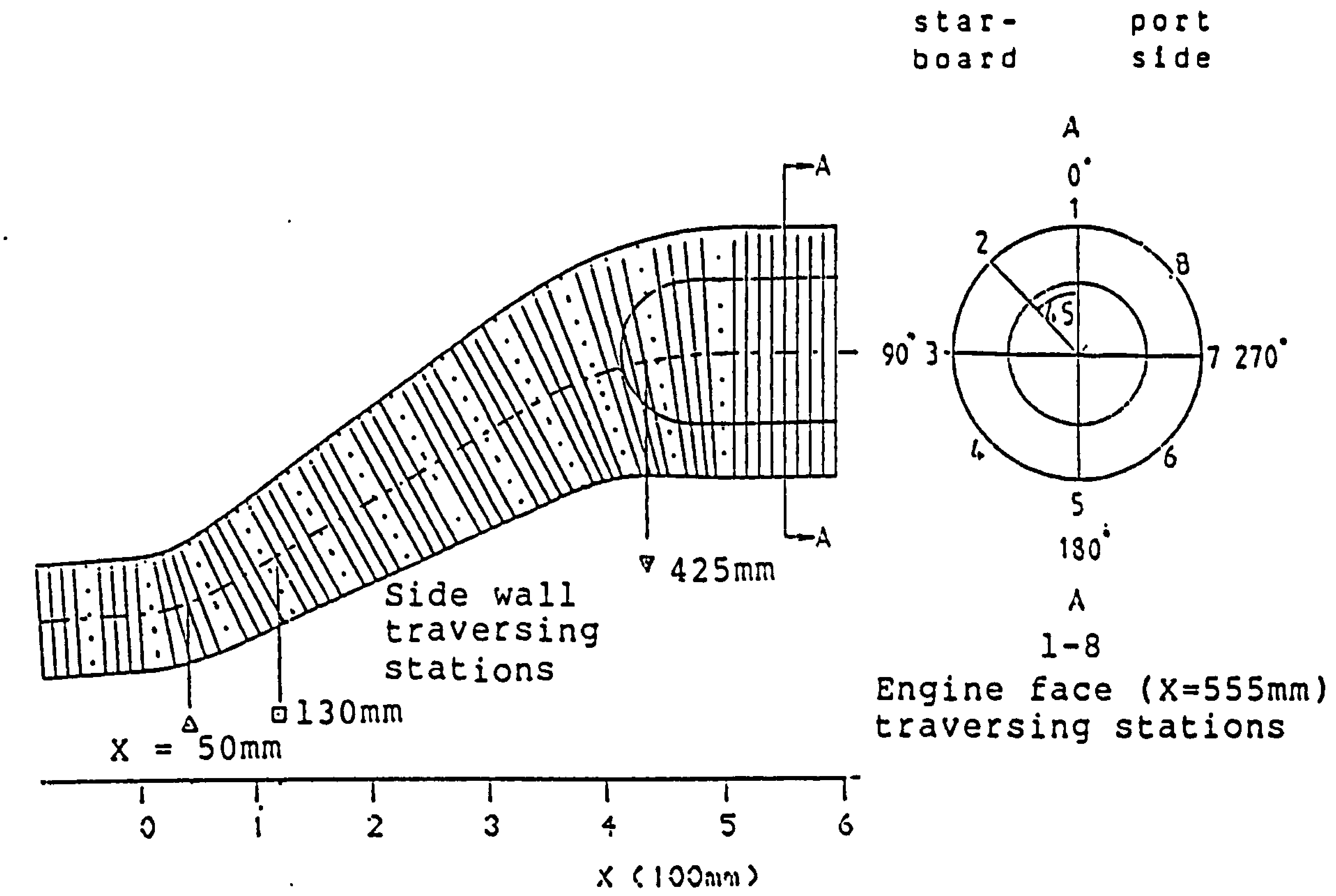

FIG. 4-53 DUCT J PROFILE

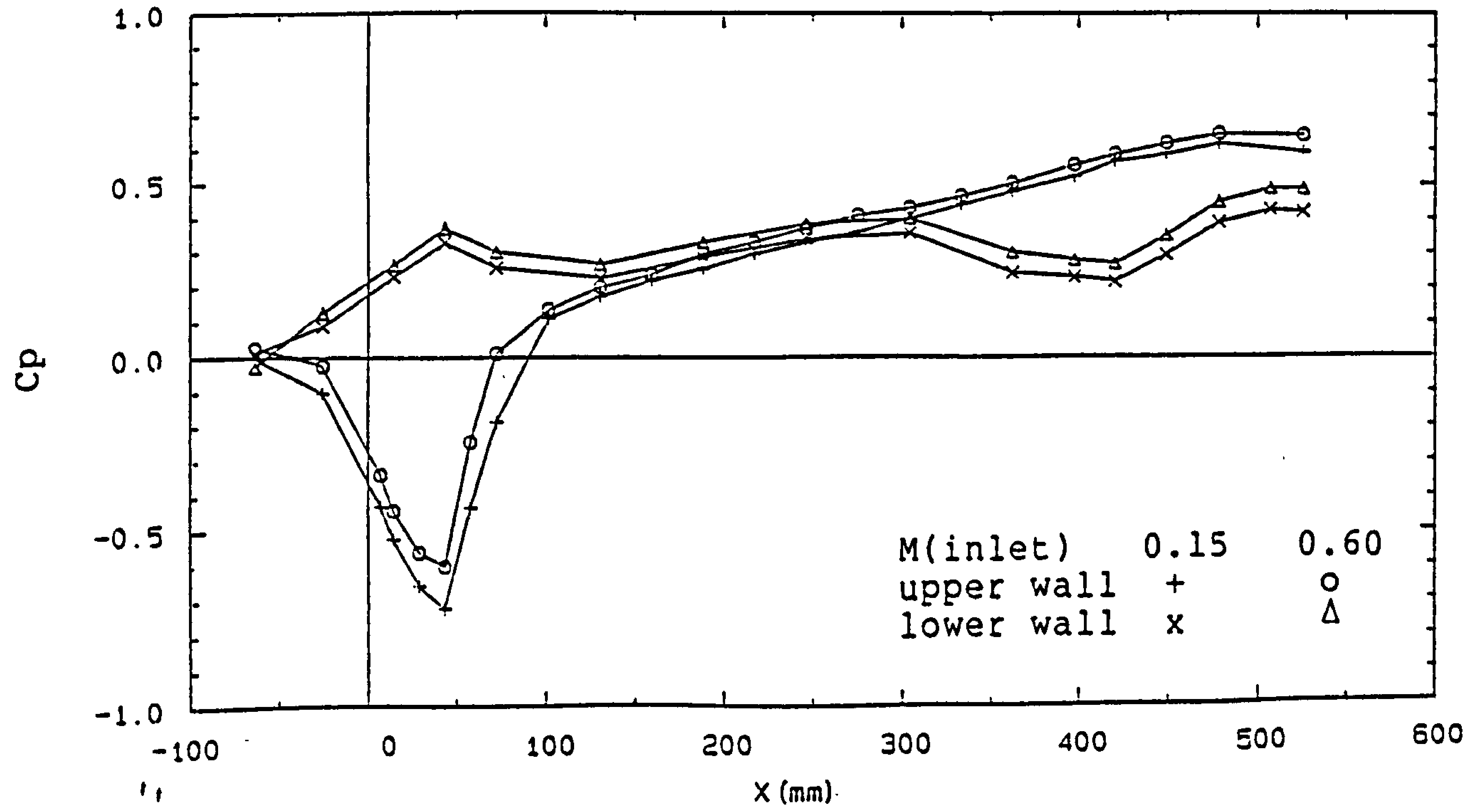

FIG. 4-54 PRESSURE DISTRIBUTIONS (DUCT J)

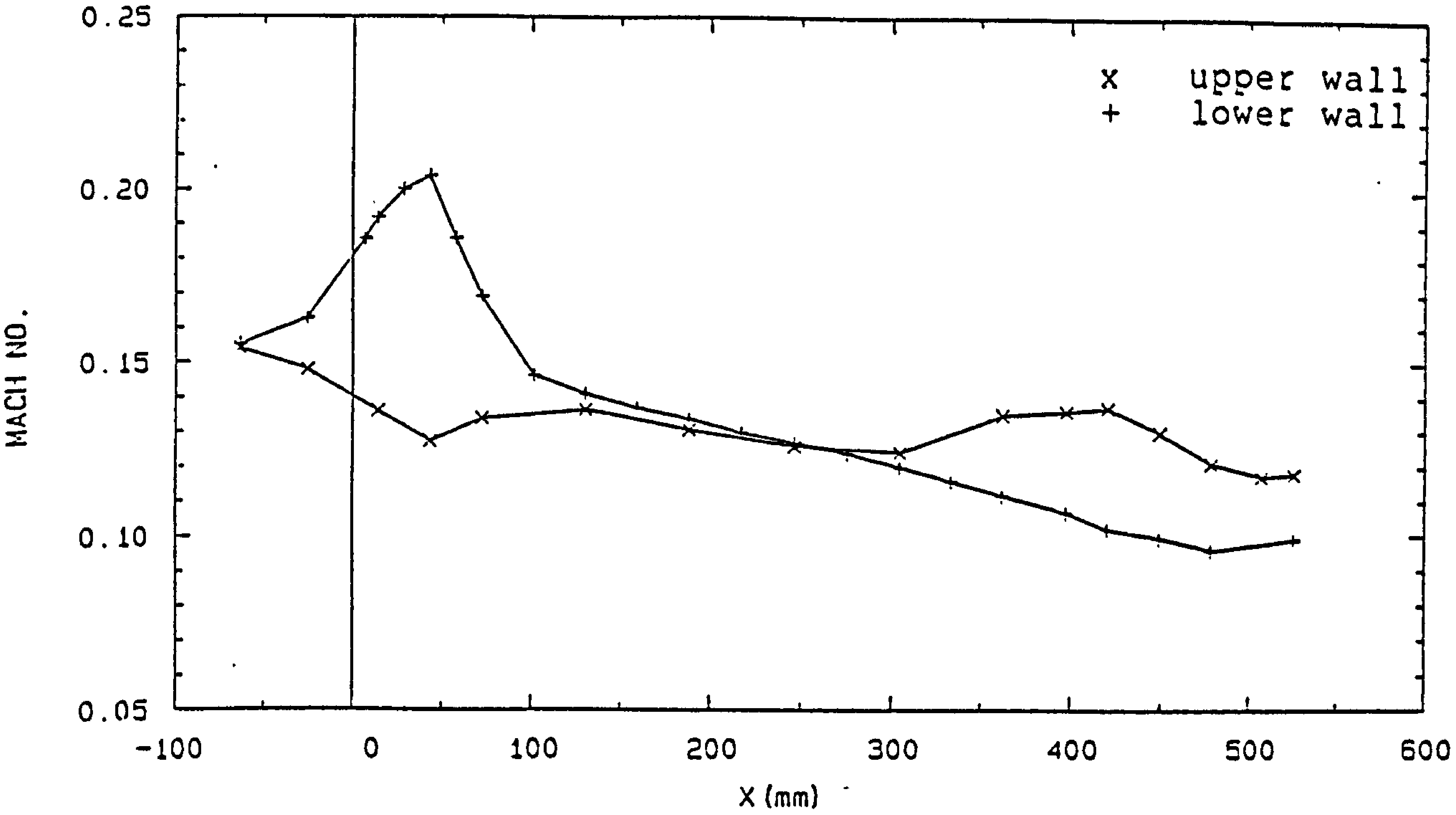

a) $M_{inlet} = 0.15$

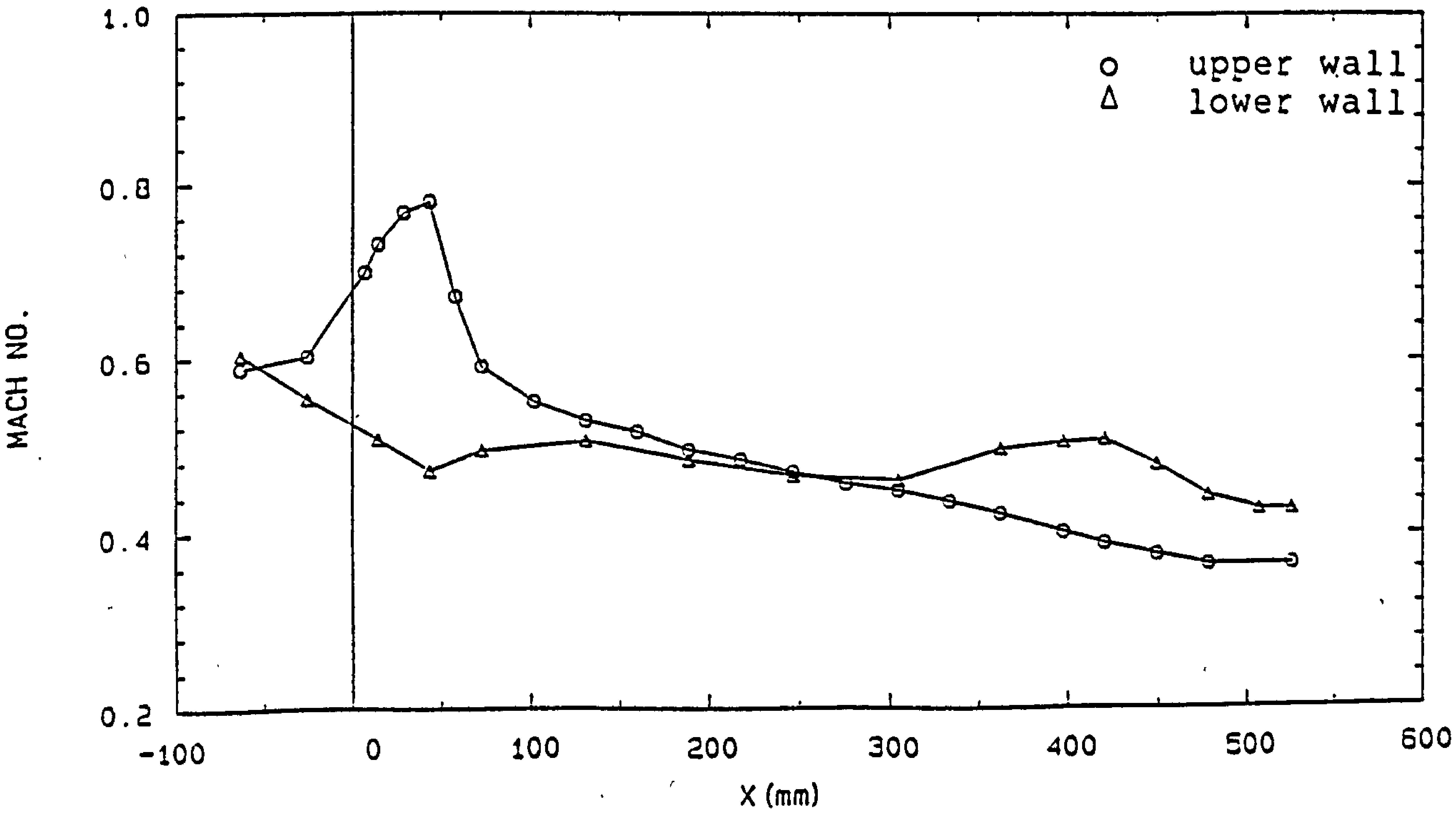

b) $M_{inlet} = 0.60$

FIG. 4-55 MACH NUMBER DISTRIBUTIONS (DUCT J)

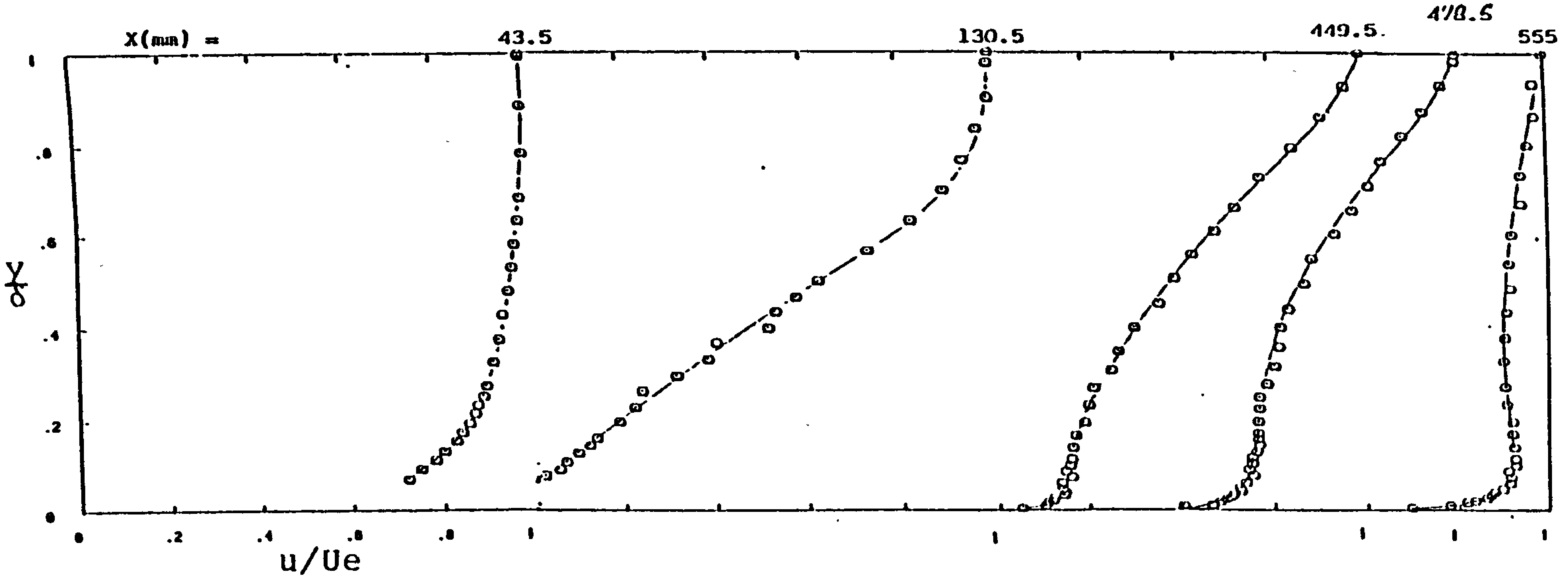

a) Upper wall

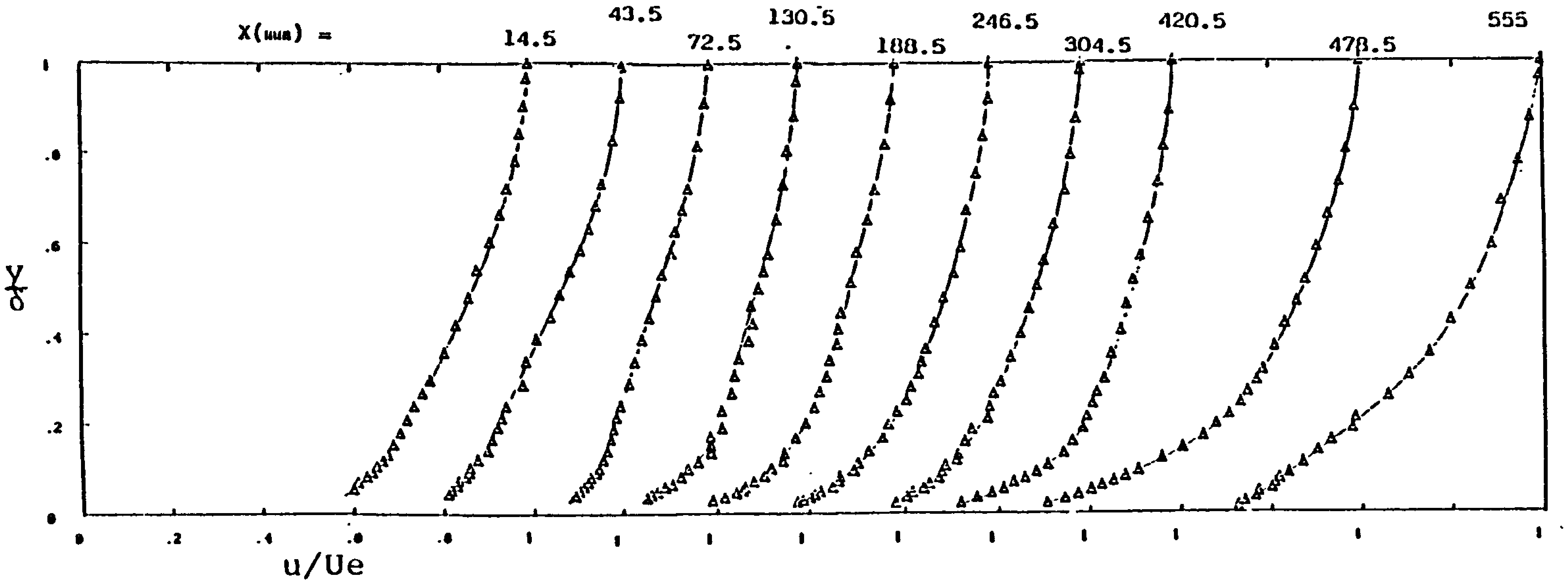

b) Lower wall

$M_{inlet} = 0.15$

FIG. 4-56 VELOCITY PROFILES (DUCT J)

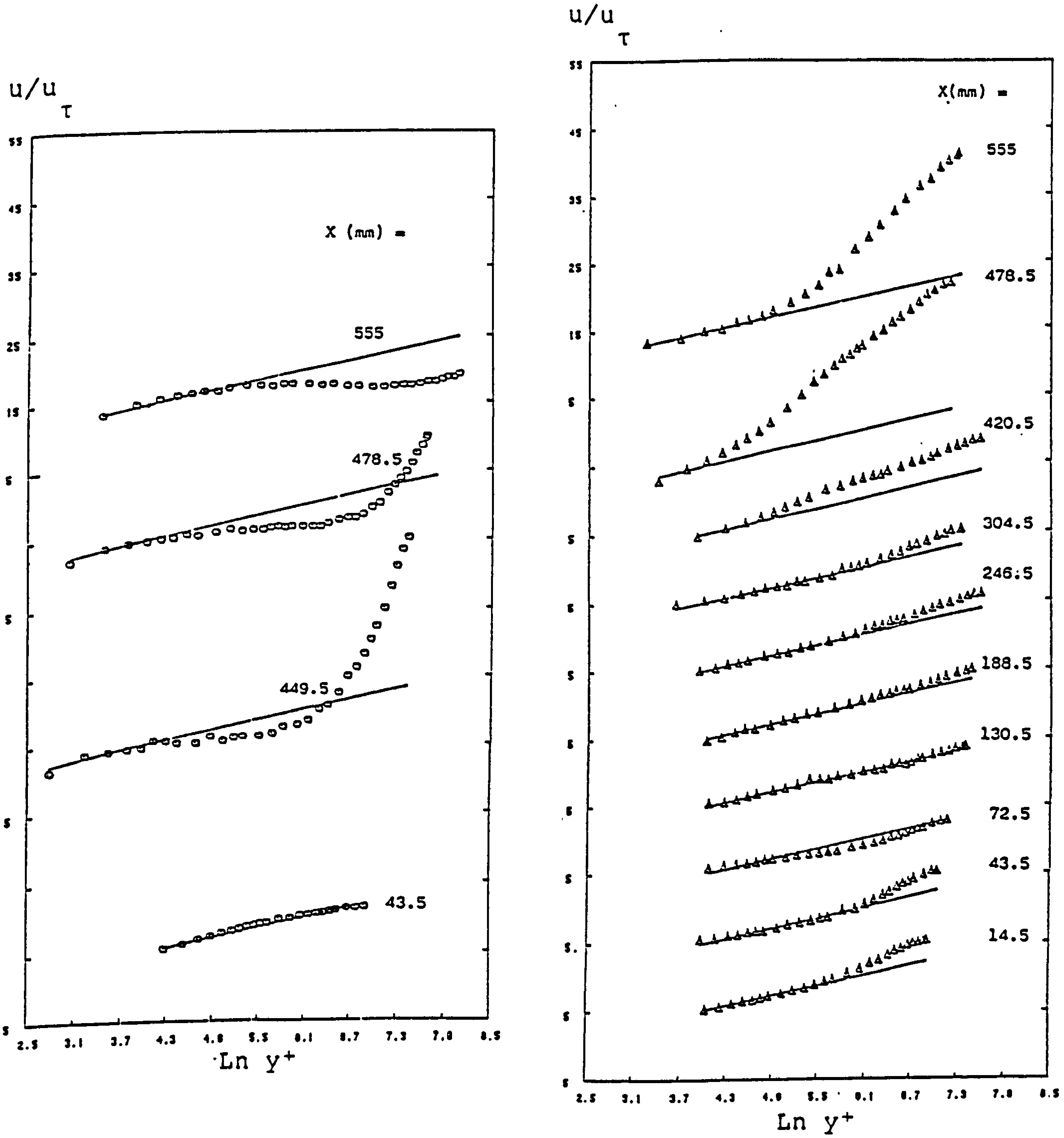

a) Upper wall

b) Lower wall

M_{inlet} = 0.15 ——— Law of the wall

FIG. 4-57 LOGARITHMIC VELOCITY PROFILES (DUCT J)

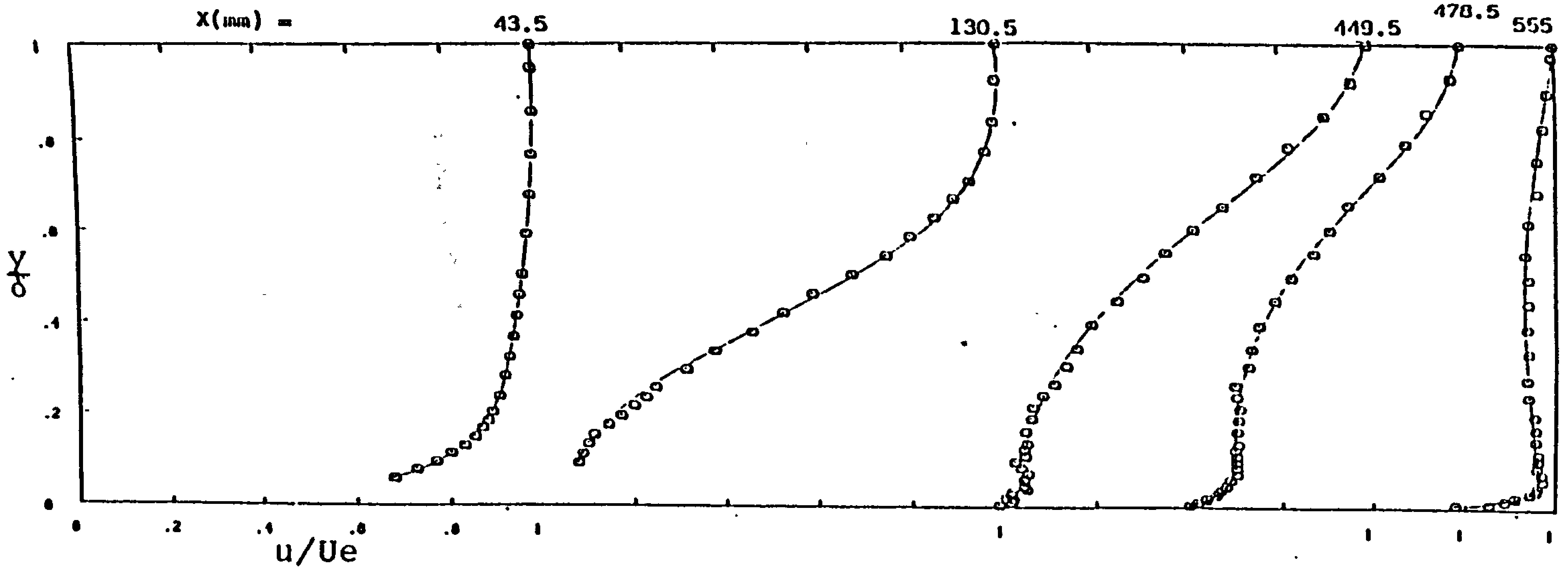

a) Upper wall

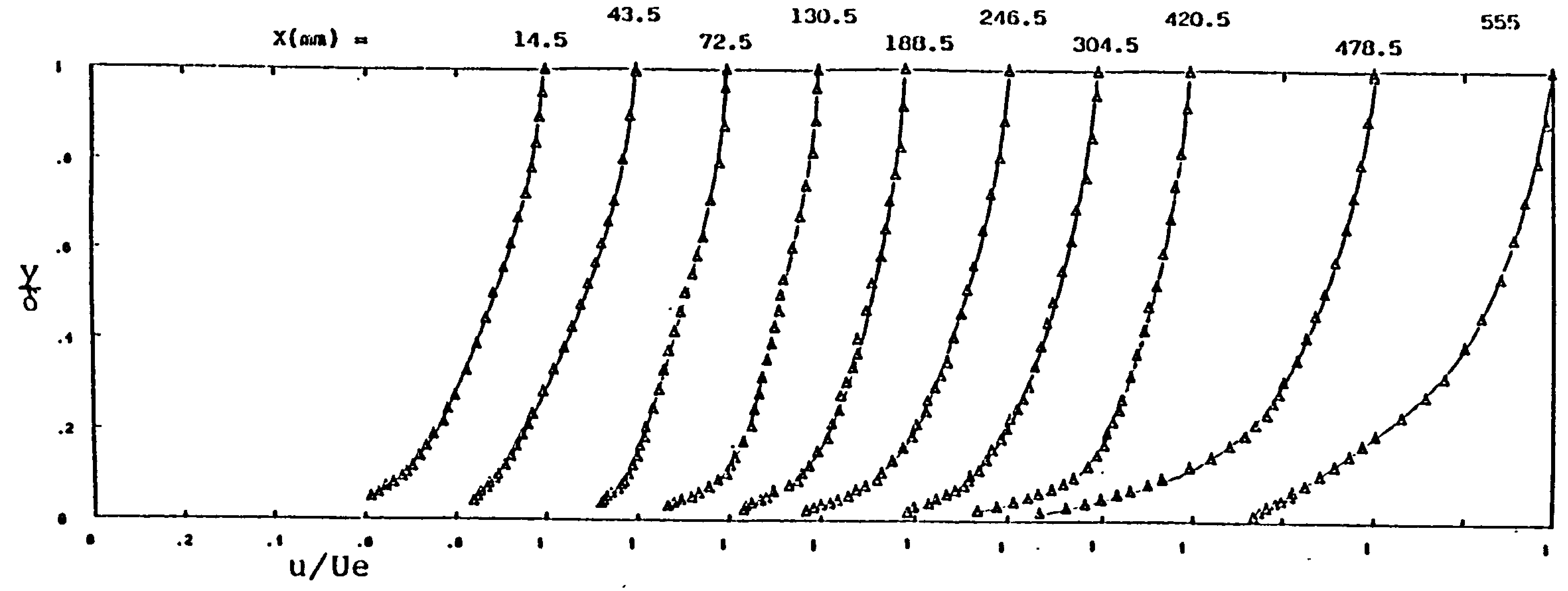

b) Lower wall

$M_{inlet} = 0.60$

FIG. 4-58 VELOCITY PROFILES (DUCT J)

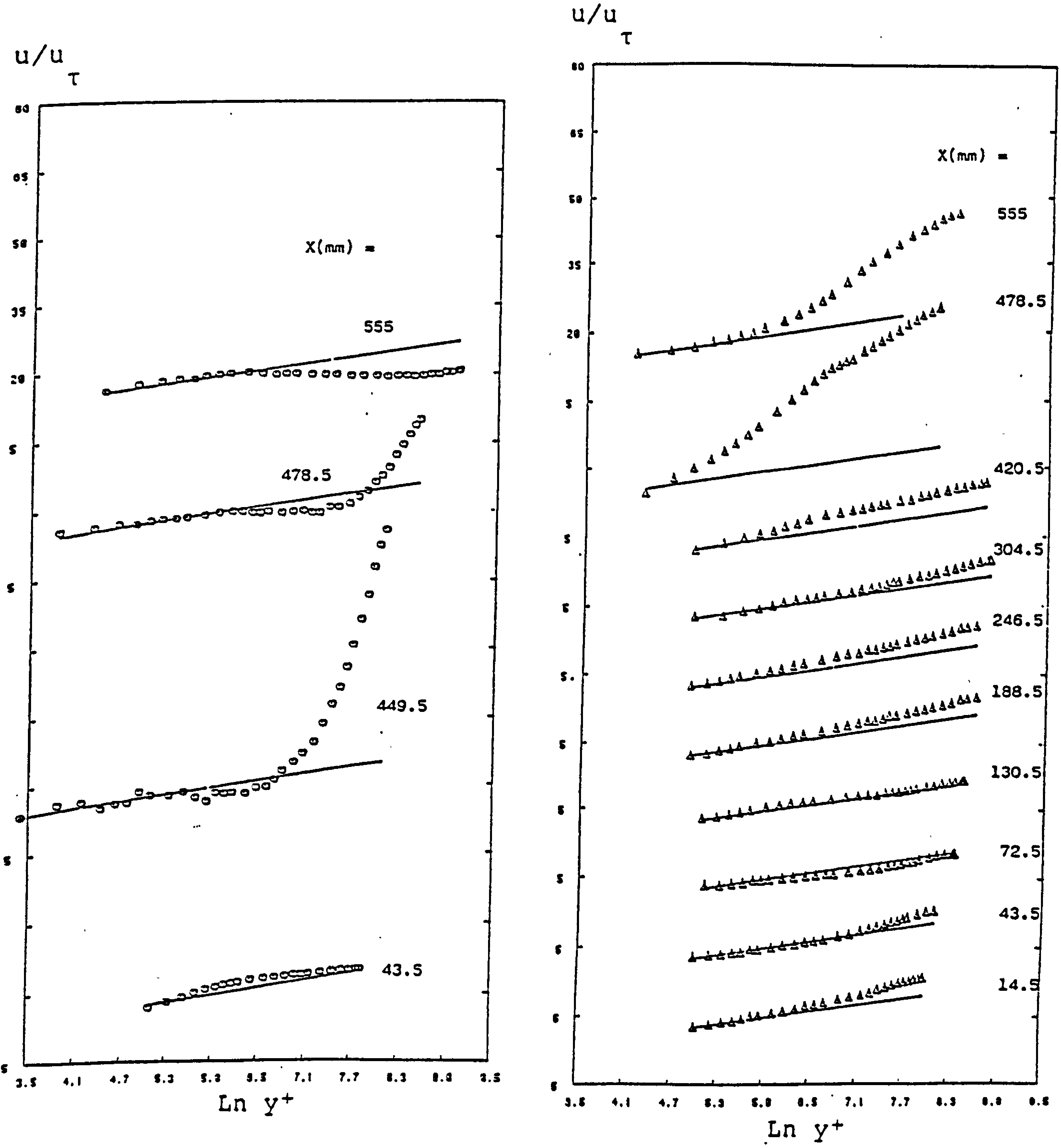

a) Upper wall

b) Lower wall

$M_{inlet} = 0.60$

—— Law of the wall

FIG. 4-59 LOGARITHMIC VELOCITY PROFILES (DUCT J)

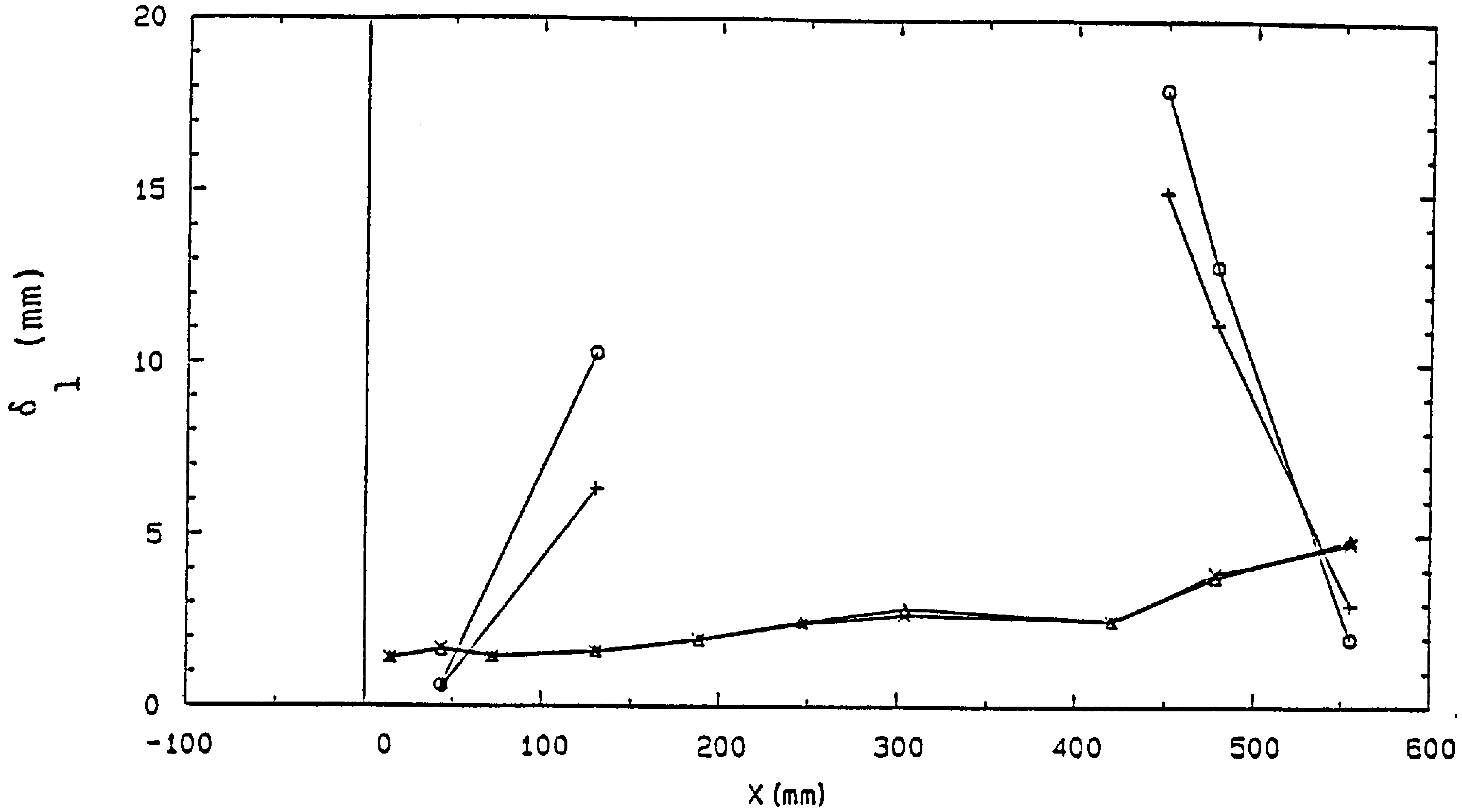

FIG. 4-60 DISPLACEMENT THICKNESSES DISTRIBUTIONS (DUCT J)

M(inlet)	0.15	0.60
upper wall	+	o
lower wall	x	Δ

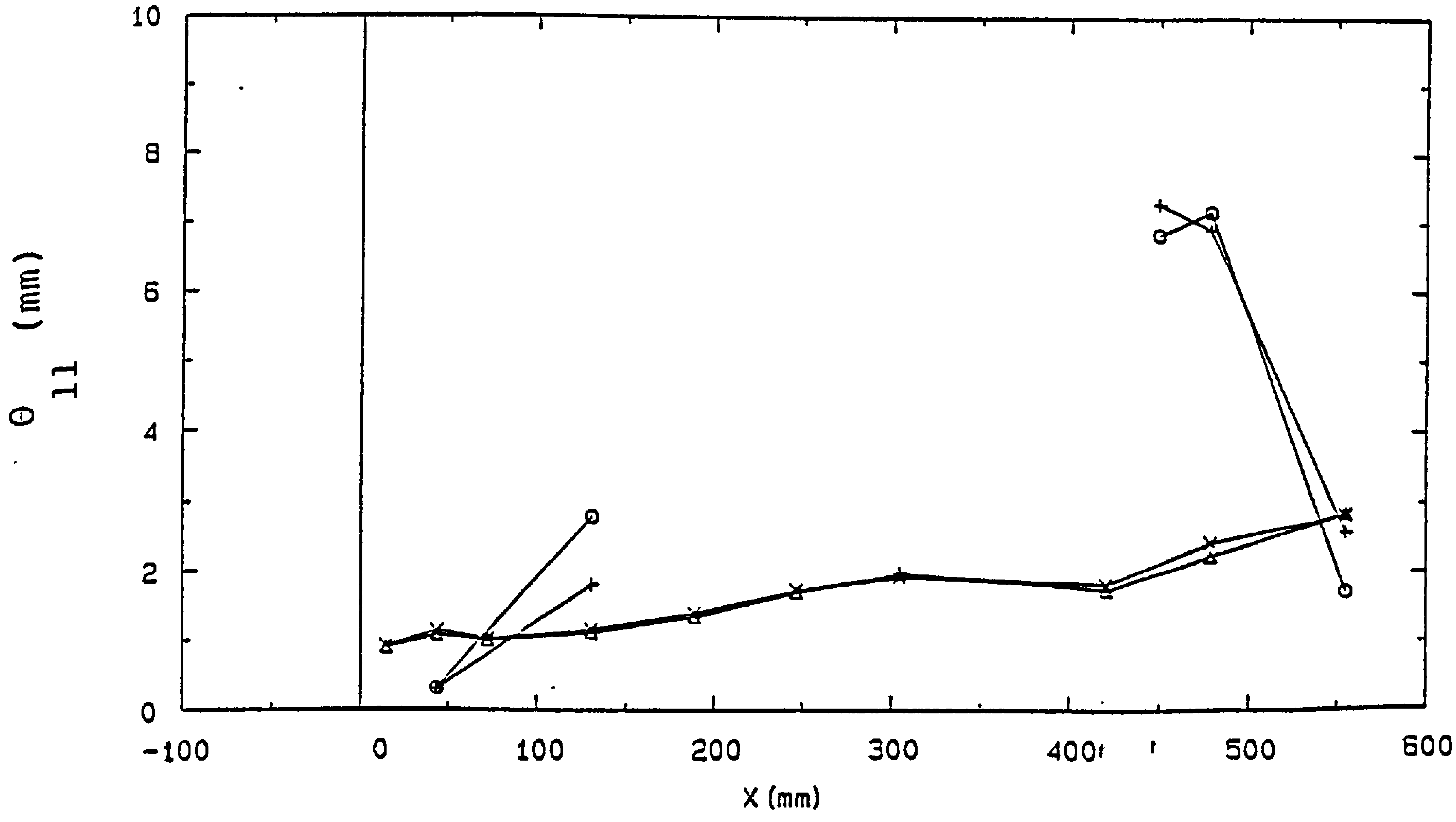

FIG. 4-61 MOMENTUM THICKNESSES DISTRIBUTIONS (DUCT J)

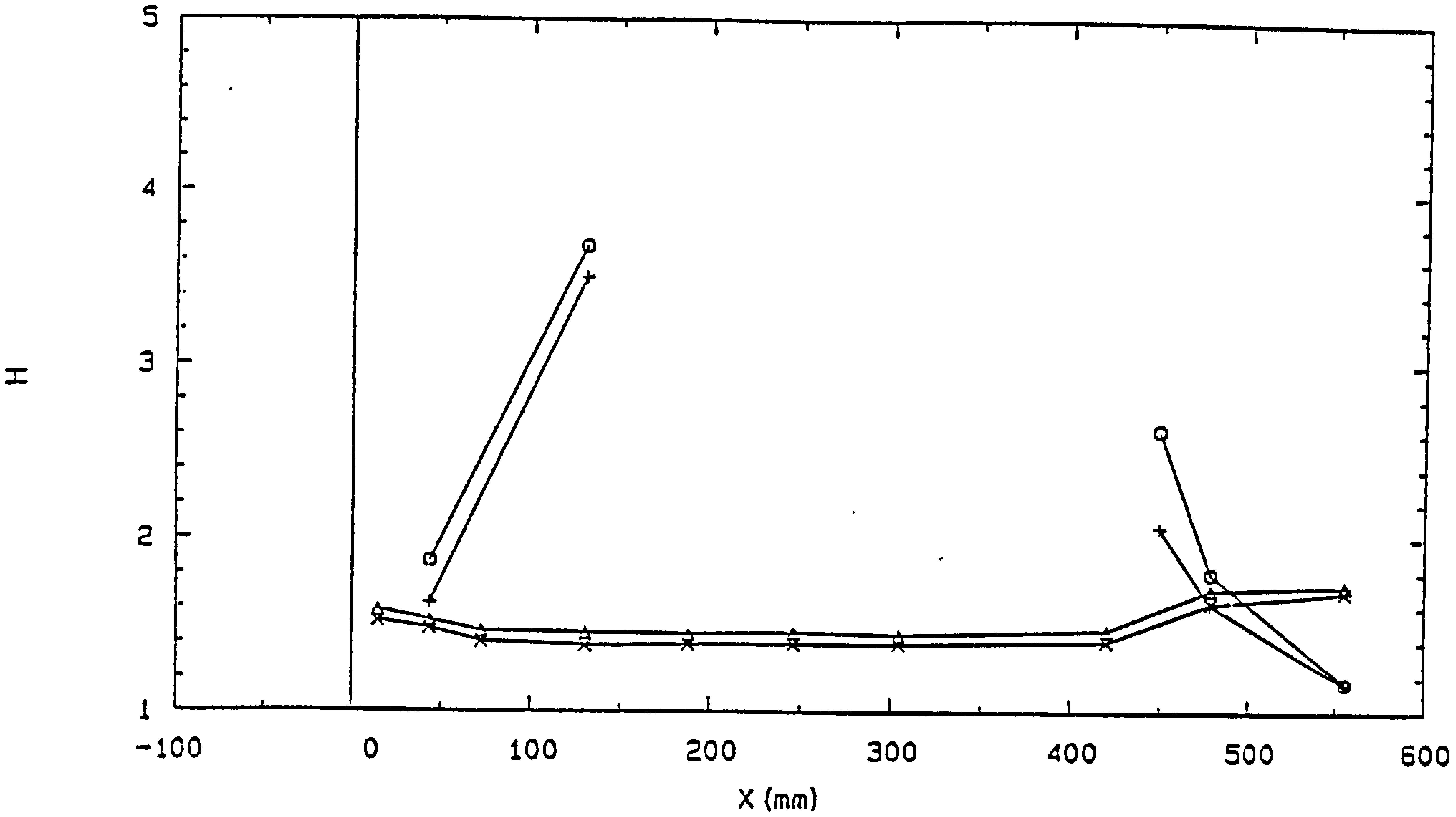

FIG. 4-62 SHAPE PARAMETER DISTRIBUTIONS (DUCT J)

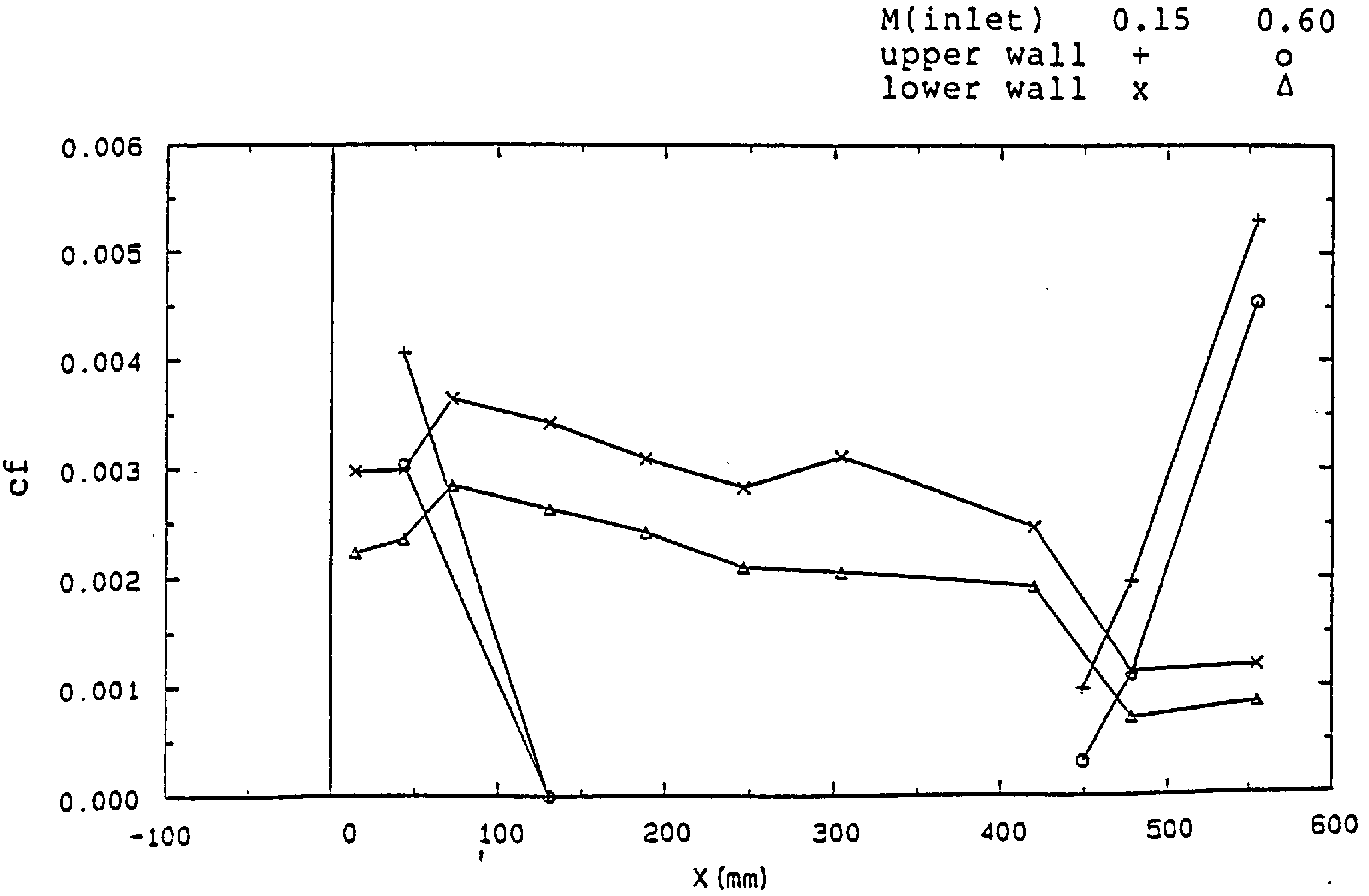

FIG. 4-63 SKIN FRICTION DISTRIBUTIONS (DUCT J)

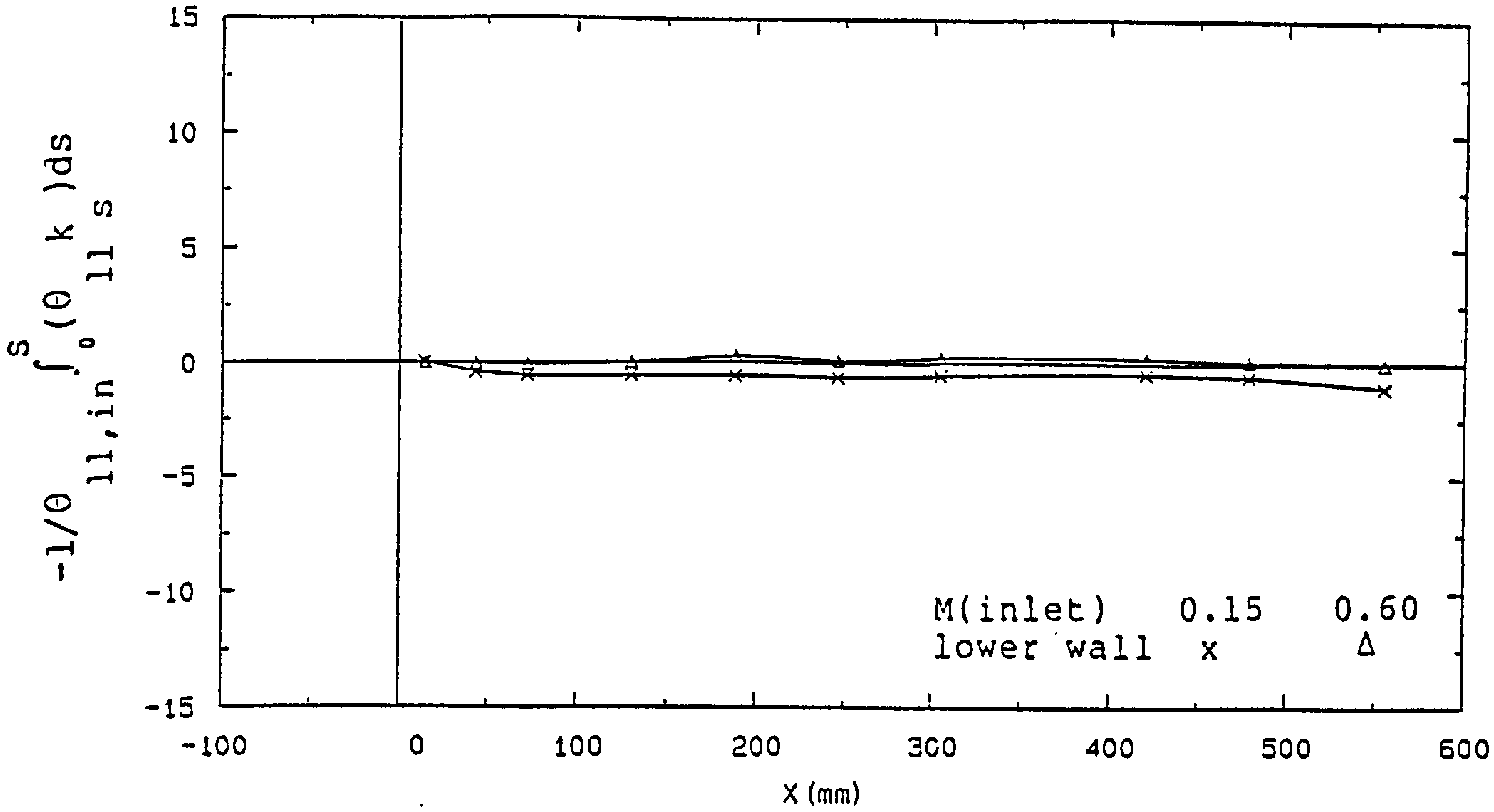

FIG. 4-64 MOMENTUM BALANCE (DUCT J)

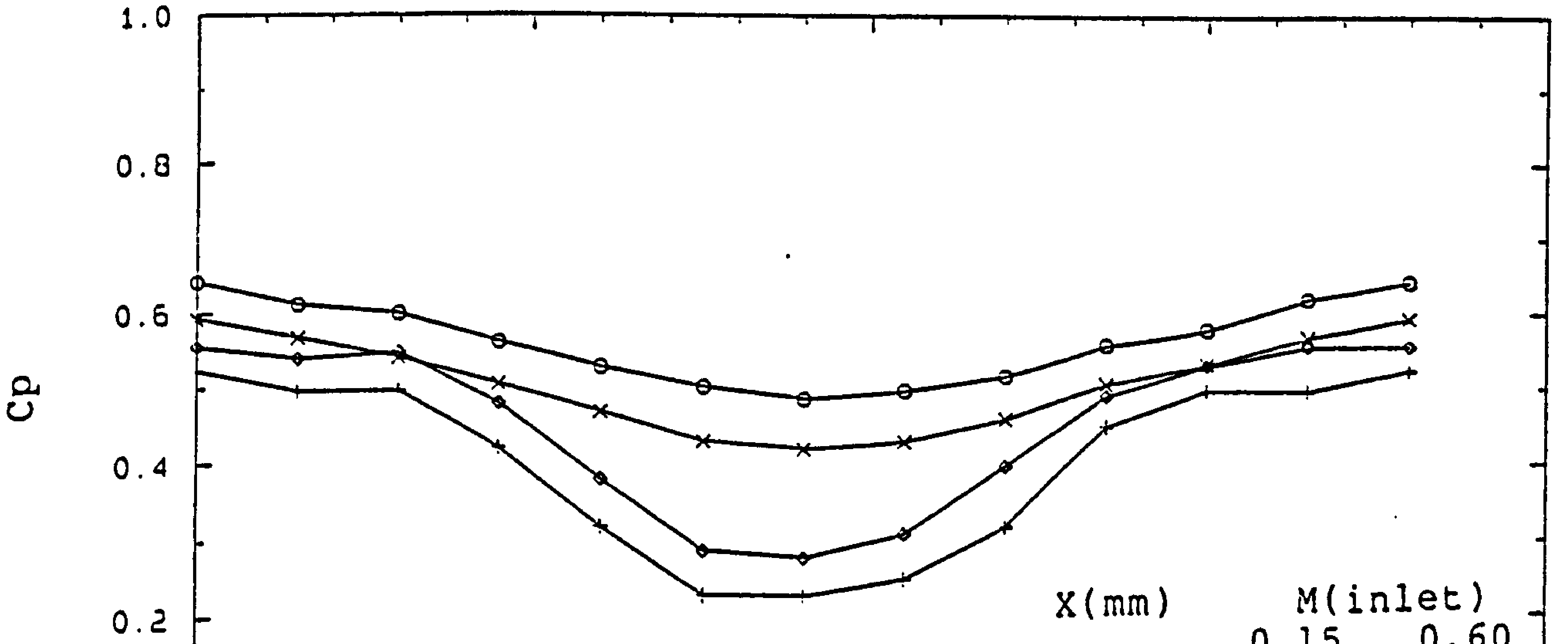

FIG. 4-65 PRESSURE DISTRIBUTIONS (DUCT J)

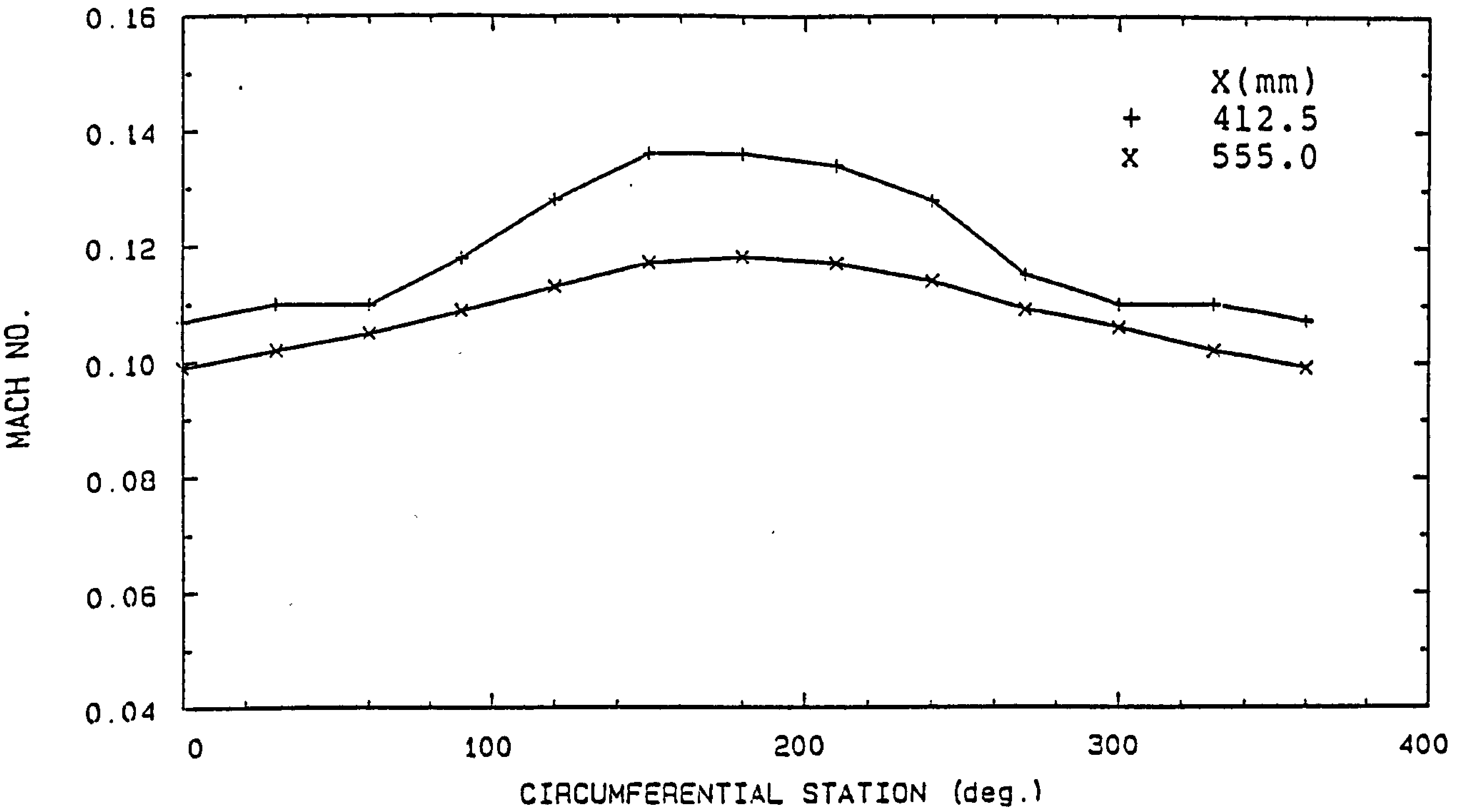

a) $M_{inlet} = 0.15$

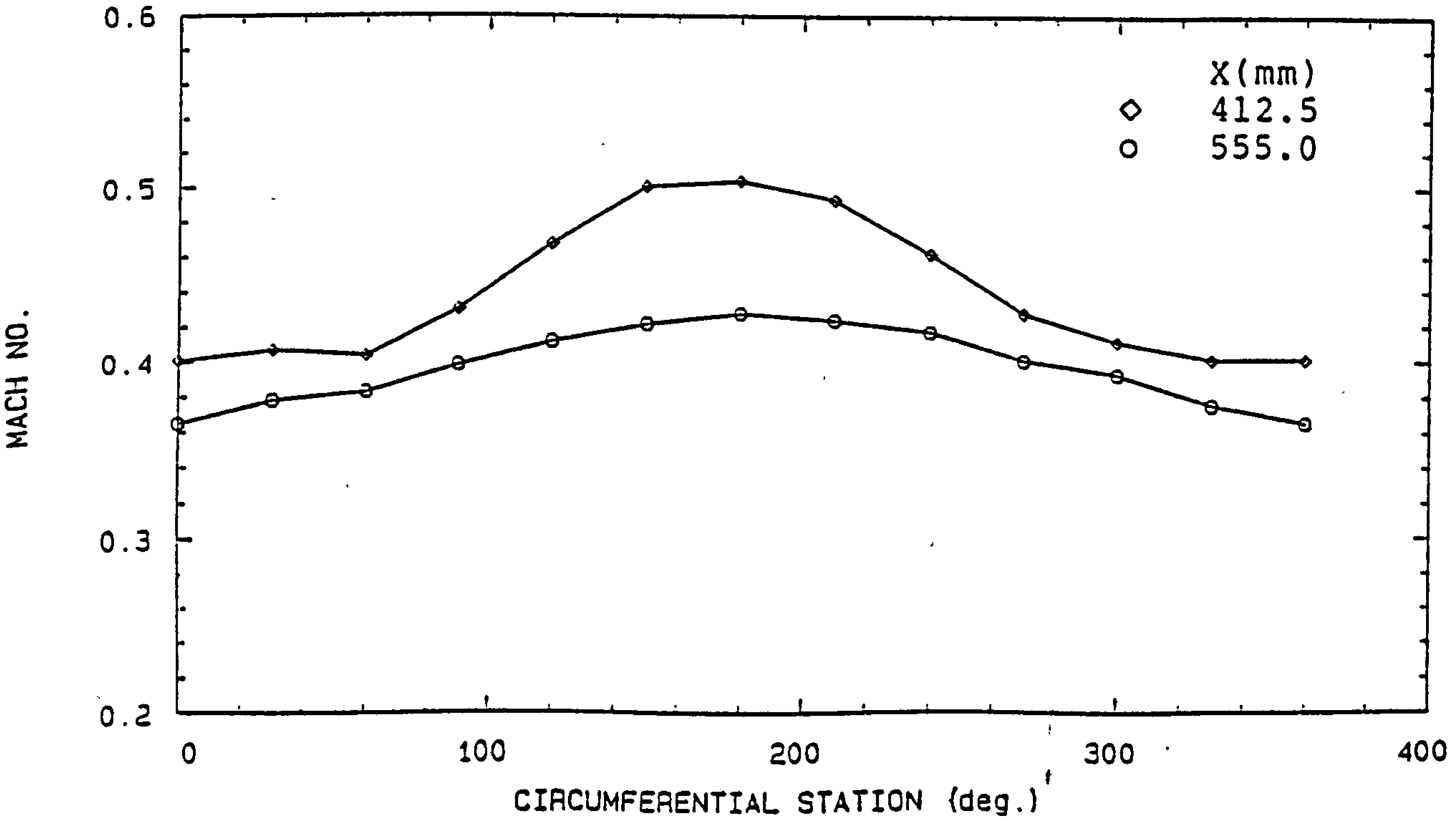

b) $M_{inlet} = 0.60$

FIG. 4-66 MACH NUMBER DISTRIBUTIONS (DUCT J)

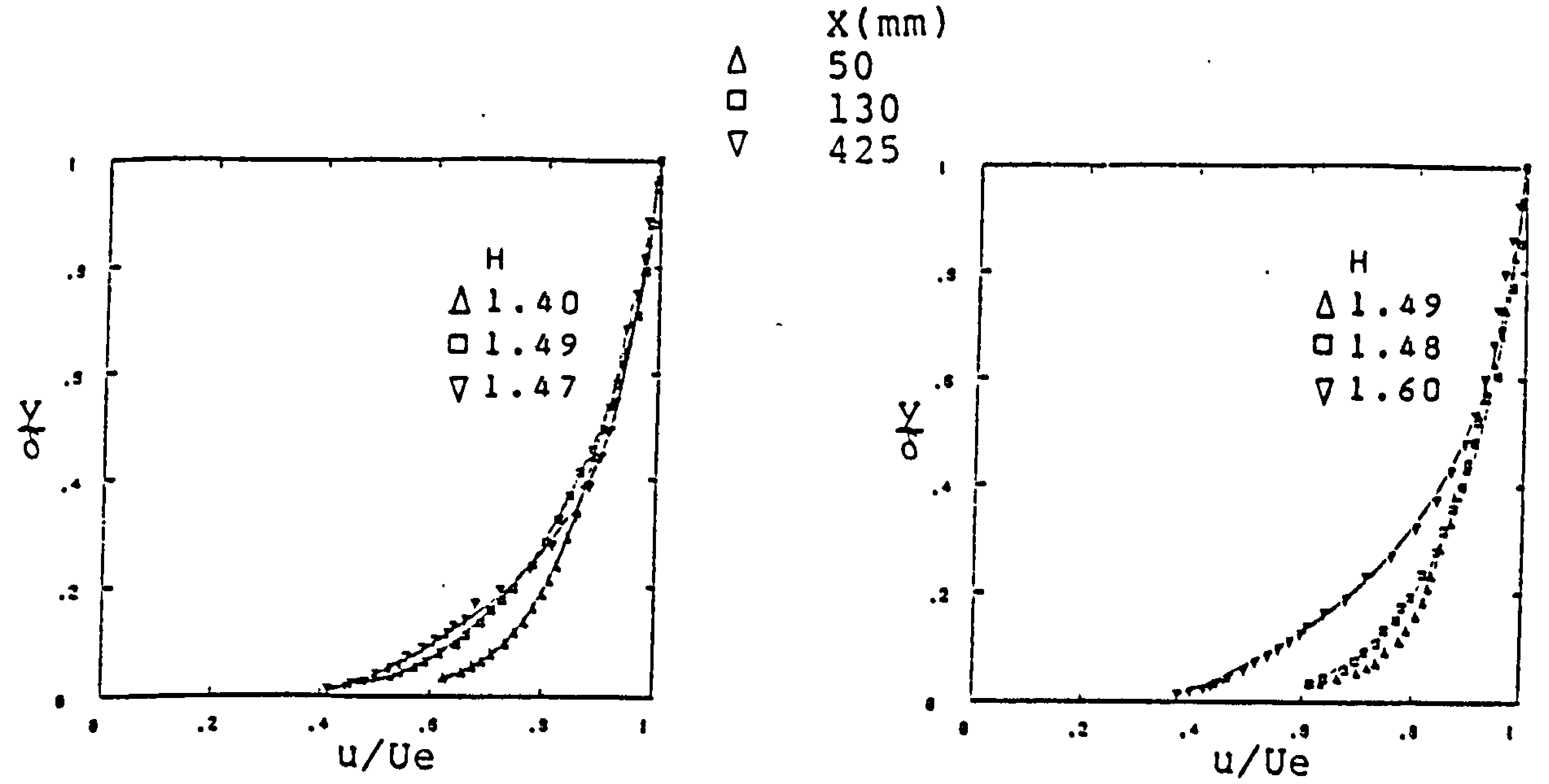

a1, a2) Streamwise velocity profiles

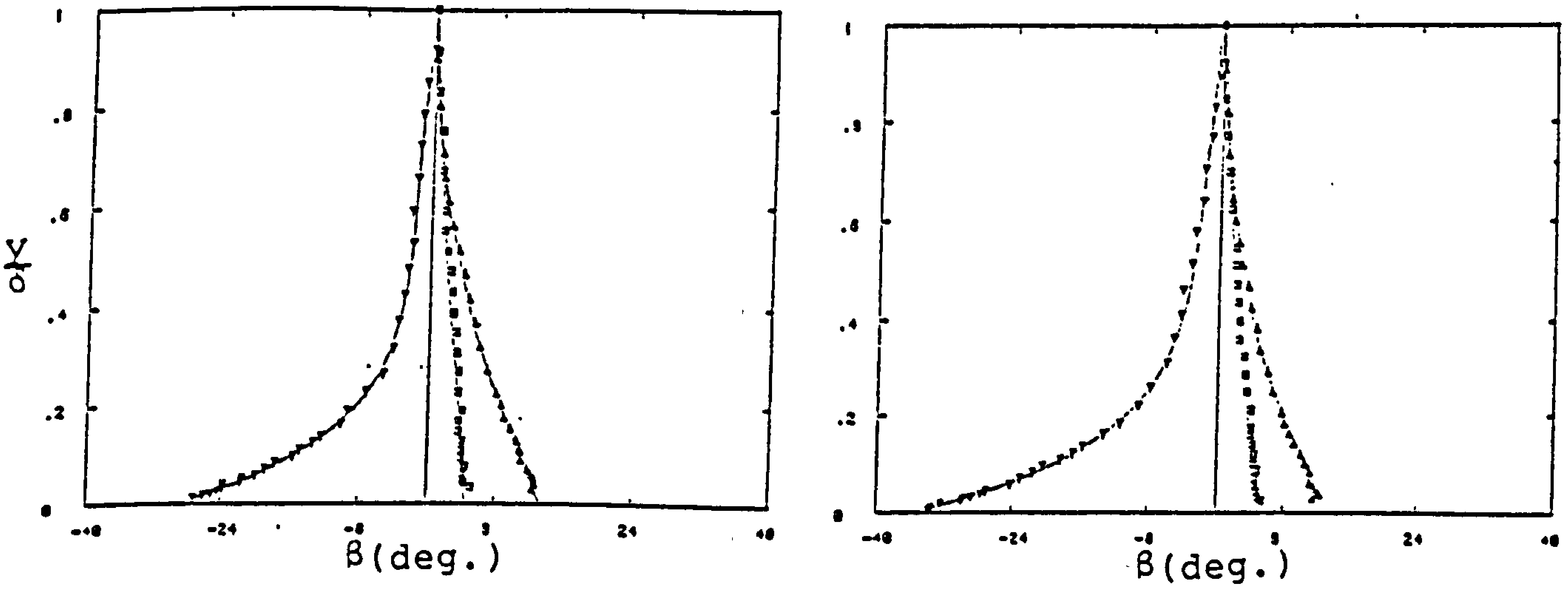

b1, b2) Skew angle profiles

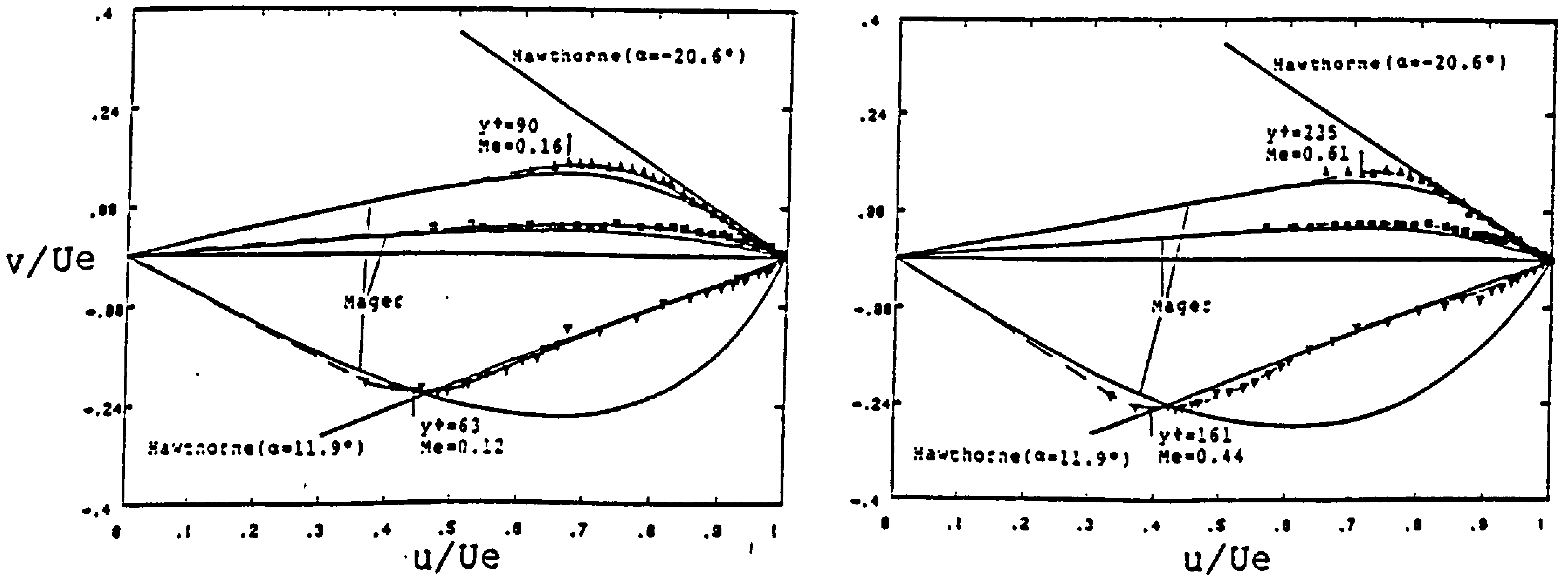

c1, c2) Polar plots

$M_{inlet} = 0.15$

$M_{inlet} = 0.60$

FIG. 4-67 SIDE WALL BOUNDARY LAYER (DUCT J)

a) Skew angle profiles

b1, b2) Streamwise velocity profiles

c) Polar profiles

d1, d2) Logarithmic streamwise velocity profiles

M_{inlet} =0.15, X=555mm

——— Law of the wall

FIG. 4-68 ENGINE FACE BOUNDARY LAYER (DUCT J)

a) Skew angle profiles

b1, b2) Streamwise velocity profiles

c) Polar profiles

d1, d2) Logarithmic streamwise velocity profiles

M_{inlet} =0.60, X=555mm

—— Law of the wall

FIG. 4-69 ENGINE FACE BOUNDARY LAYER (DUCT J)

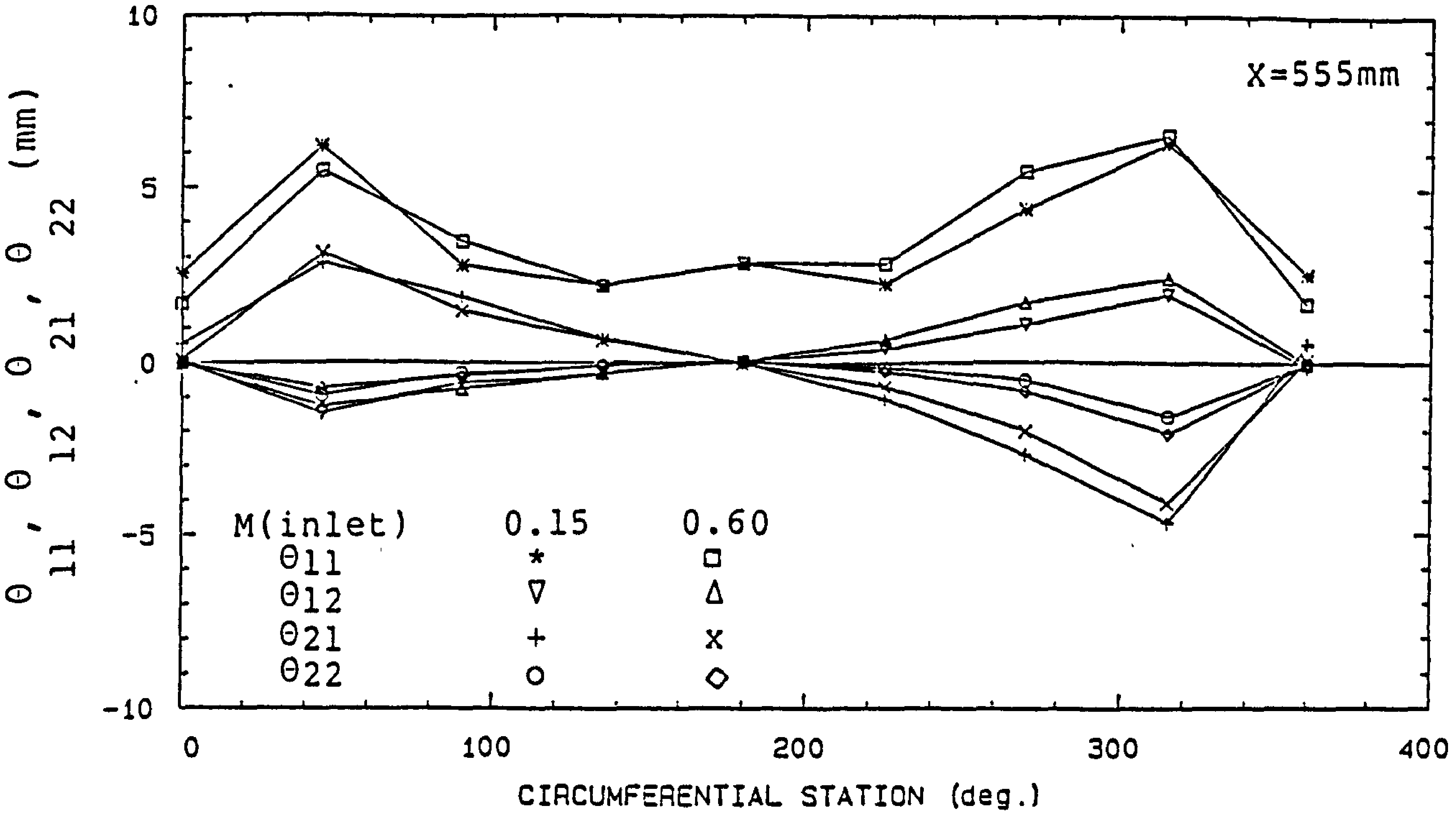

FIG. 4-70 MOMENTUM THICKNESSES DISTRIBUTIONS (DUCT J)

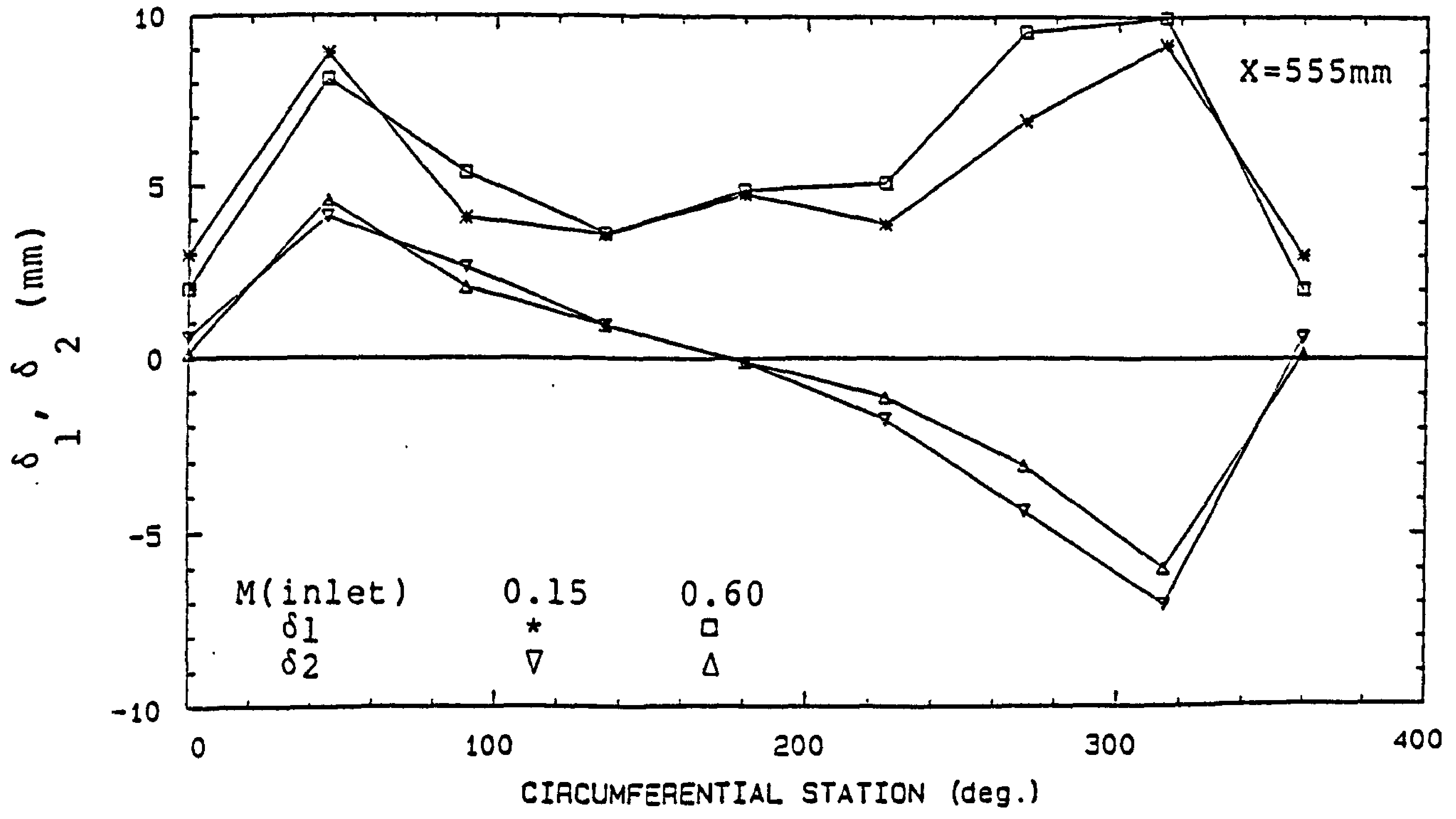

FIG. 4-71 DISPLACEMENT THICKNESSES DISTRIBUTIONS (DUCT J)

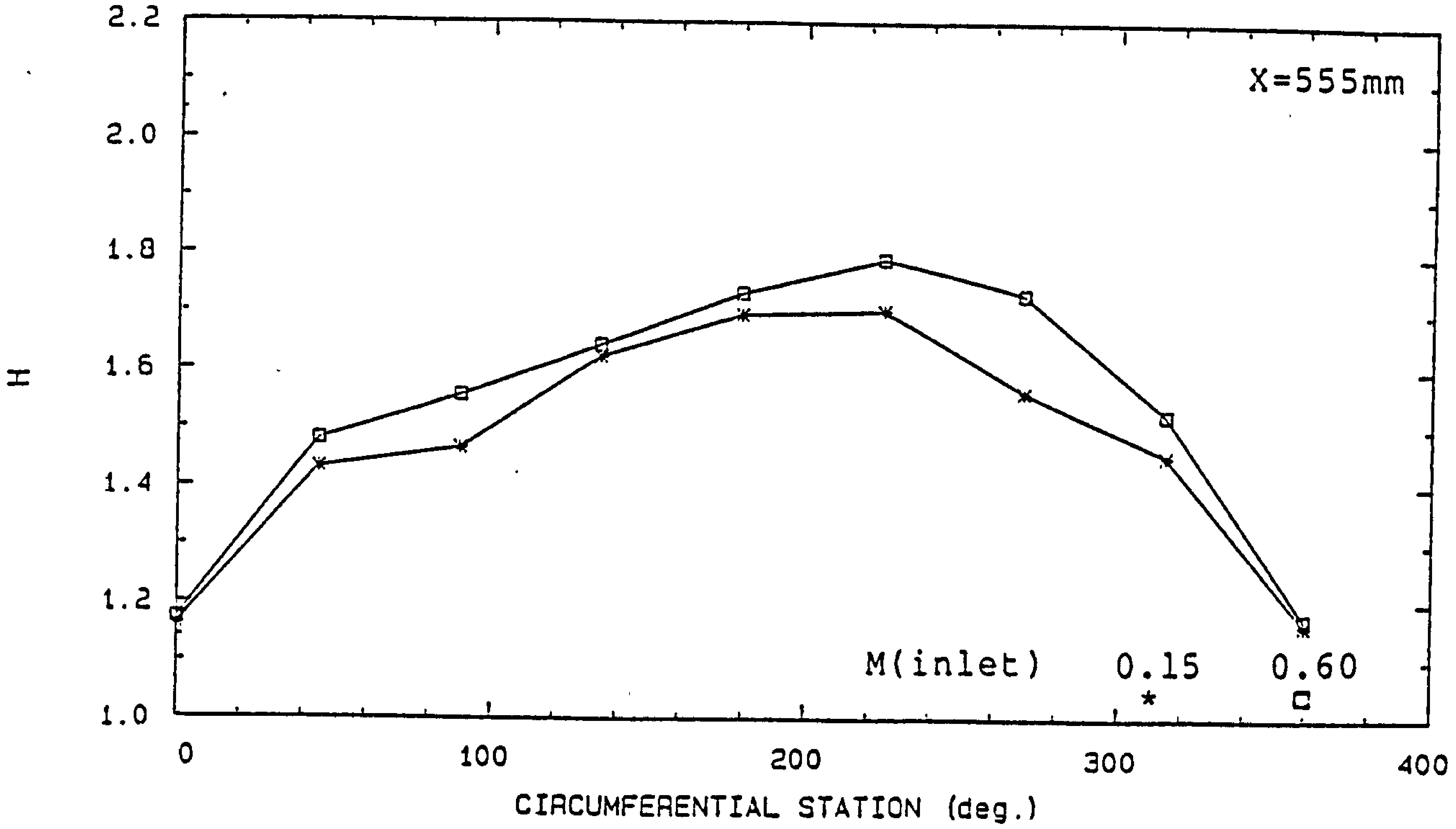

FIG. 4-72 SHAPE PARAMETER DISTRIBUTIONS (DUCT J)

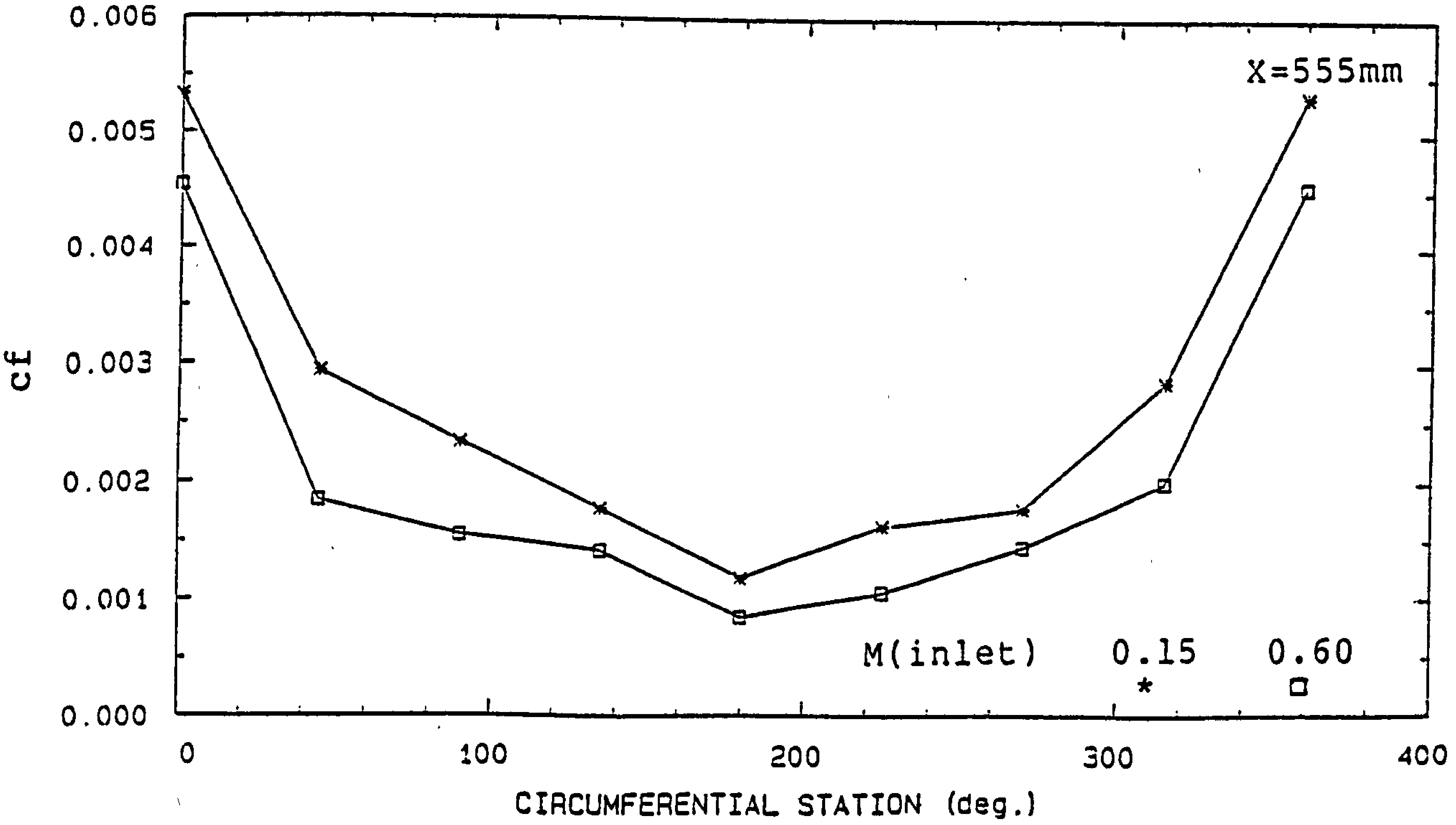

FIG. 4-73 SKIN FRICTION DISTRIBUTIONS (DUCT J)

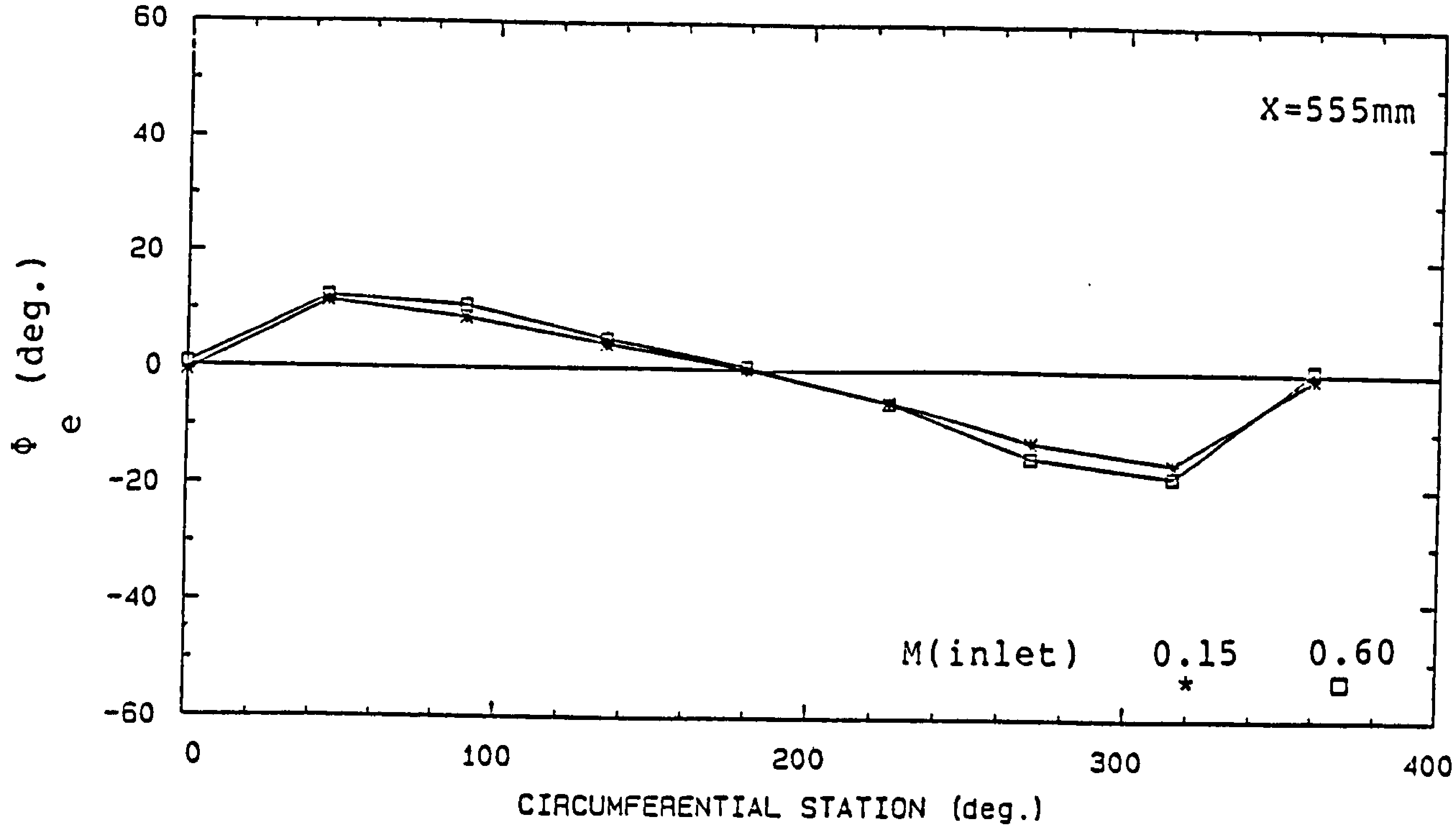

FIG. 4-74 BOUNDARY LAYER EDGE FLOW DIRECTIONS RELATIVE TO DUCT OUTLET AXIS (DUCT J)

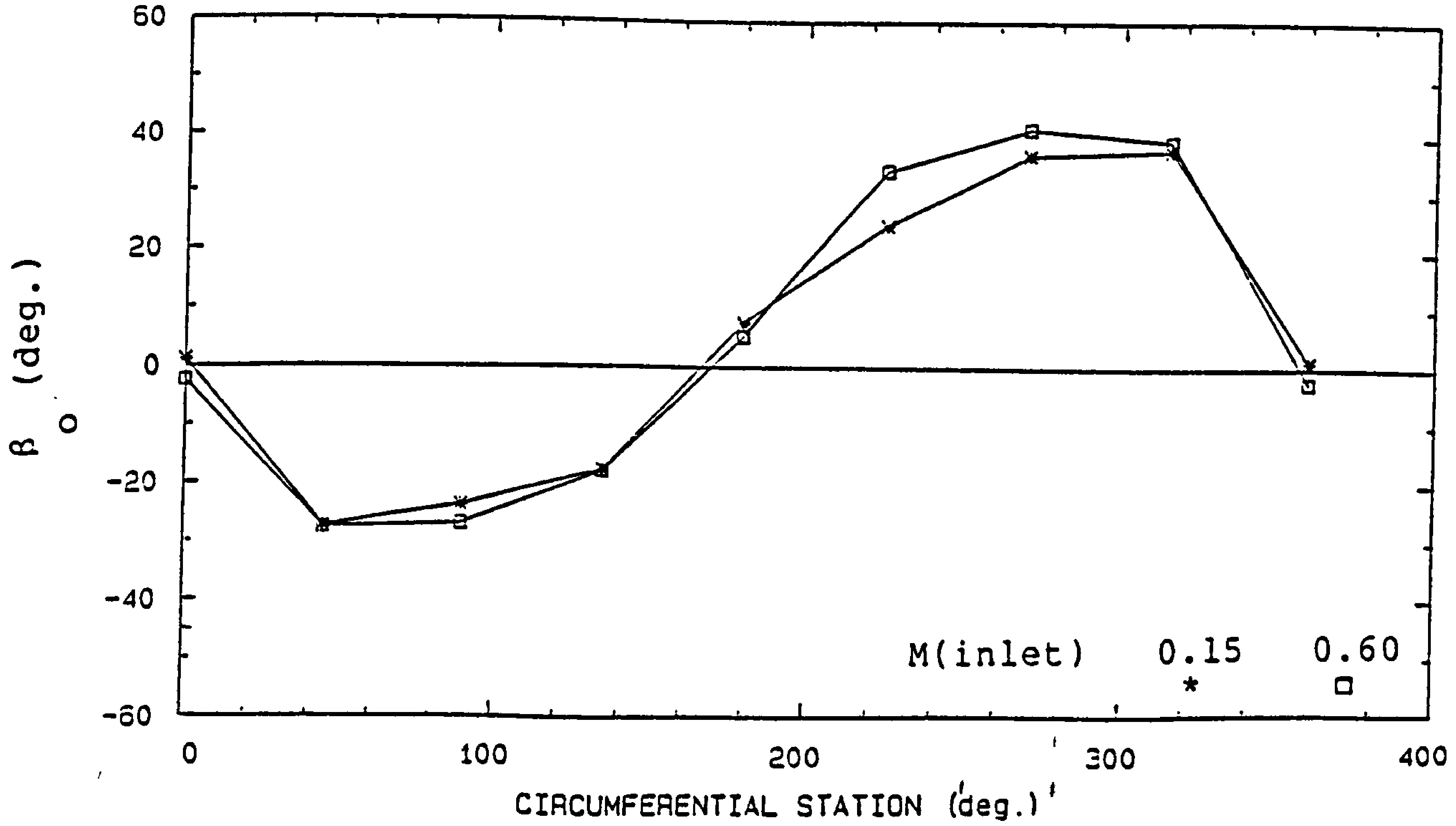

FIG. 4-75 LIMITING STREAMLINE ANGLE DISTRIBUTIONS (DUCT J)

a) $M_{inlet} = 0.15$

b) $M_{inlet} = 0.60$

FIG. 4-76 ENGINE FACE CROSSFLOW AND TOTAL PRESSURE DISTRIBUTIONS (DUCT J)

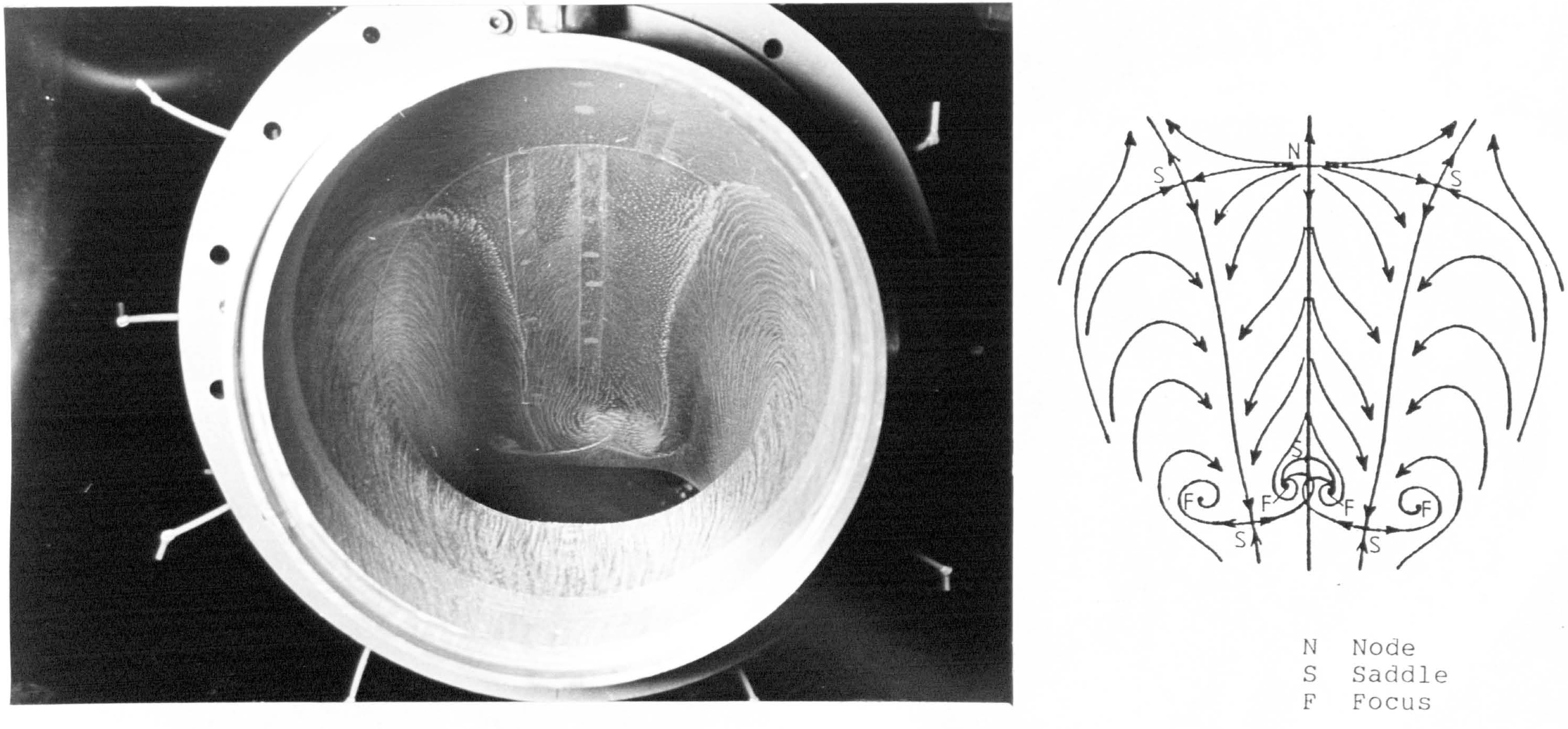

FIG. 4-77 SURFACE OIL FLOW VISUALIZATION AND TOPOLOGICAL STRUCTURE (DUCT J)

Upper wall

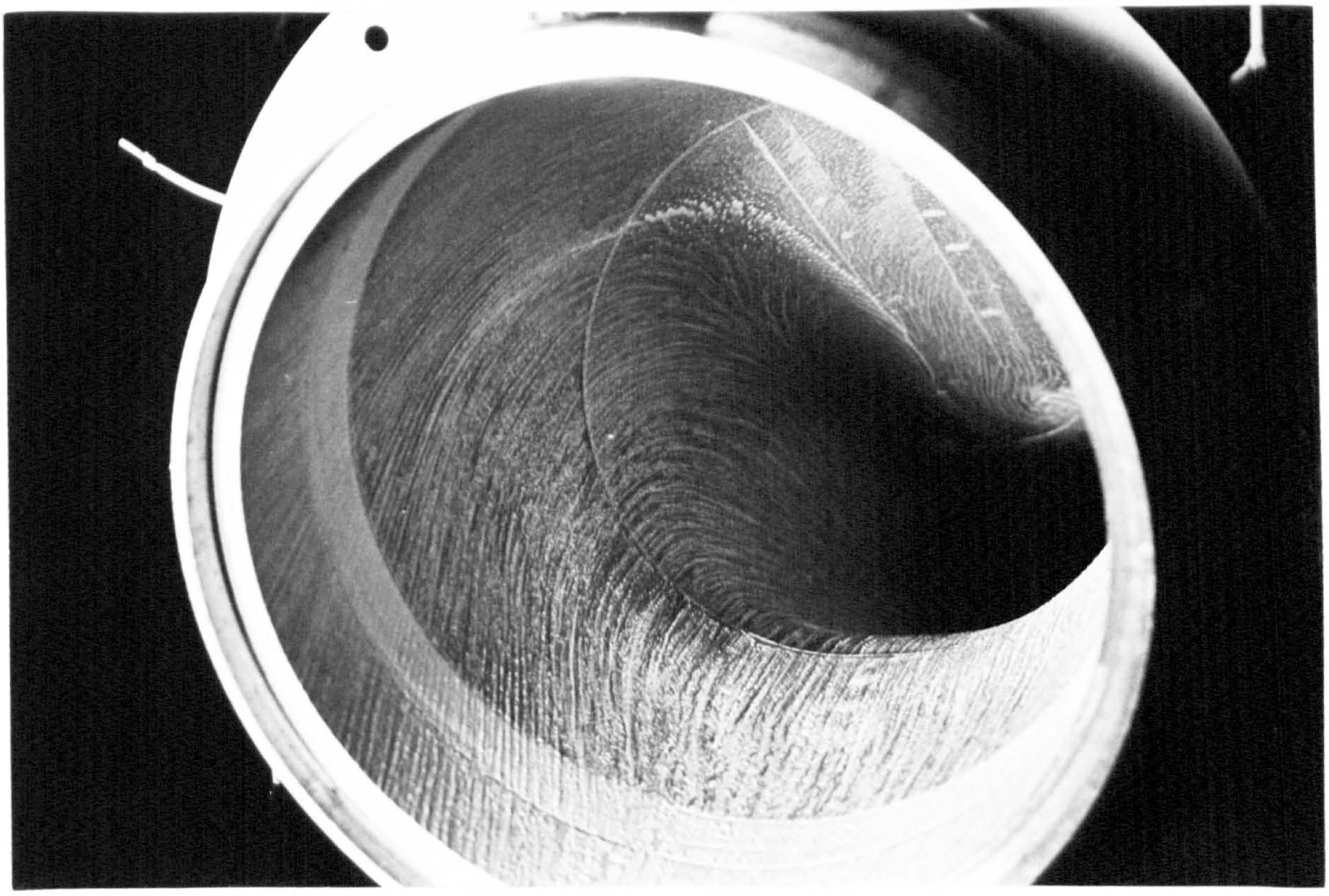

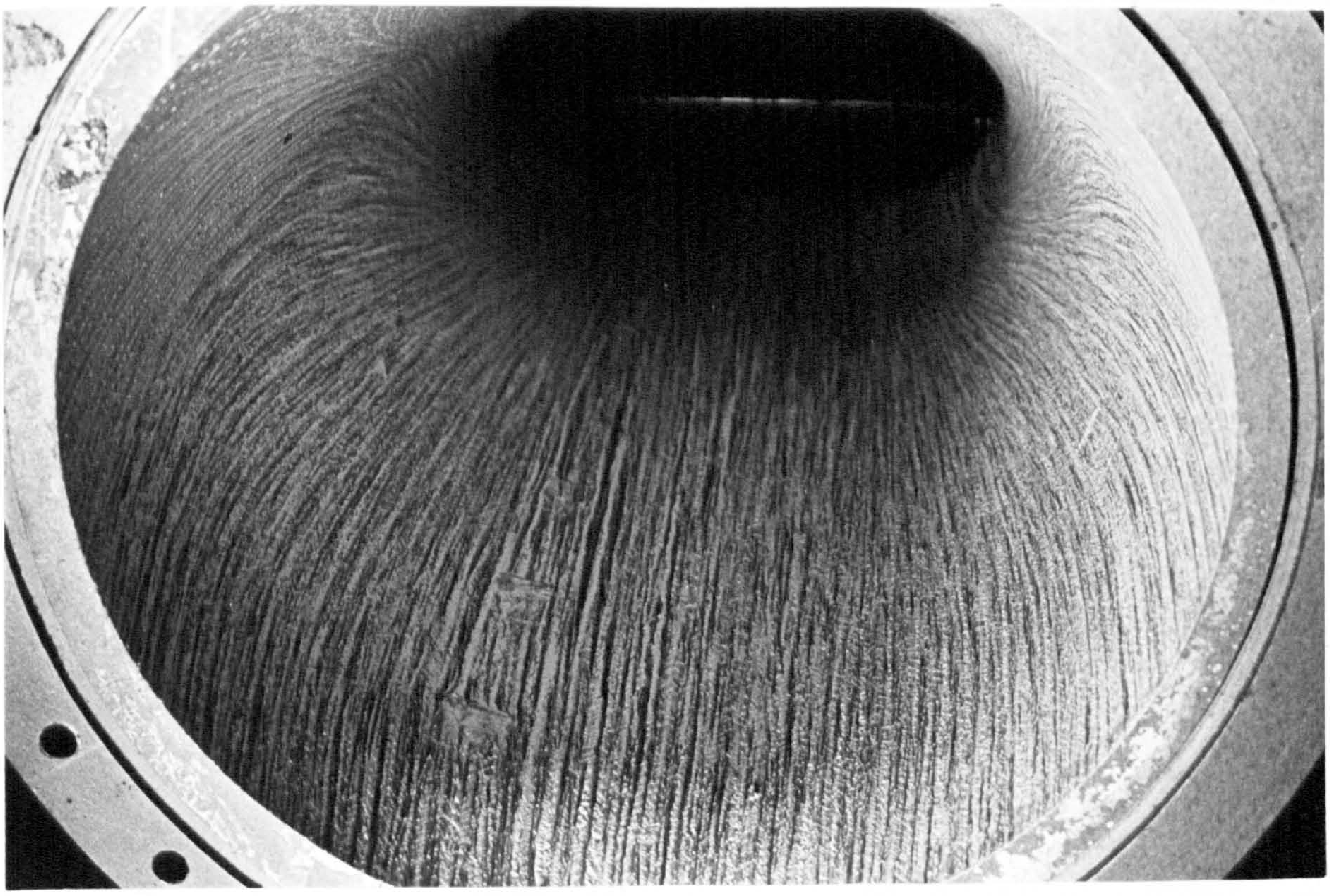

Lower wall (second bend detached)

FIG. 4-78 SURFACE OIL FLOW VISUALIZATION (DUCT J)

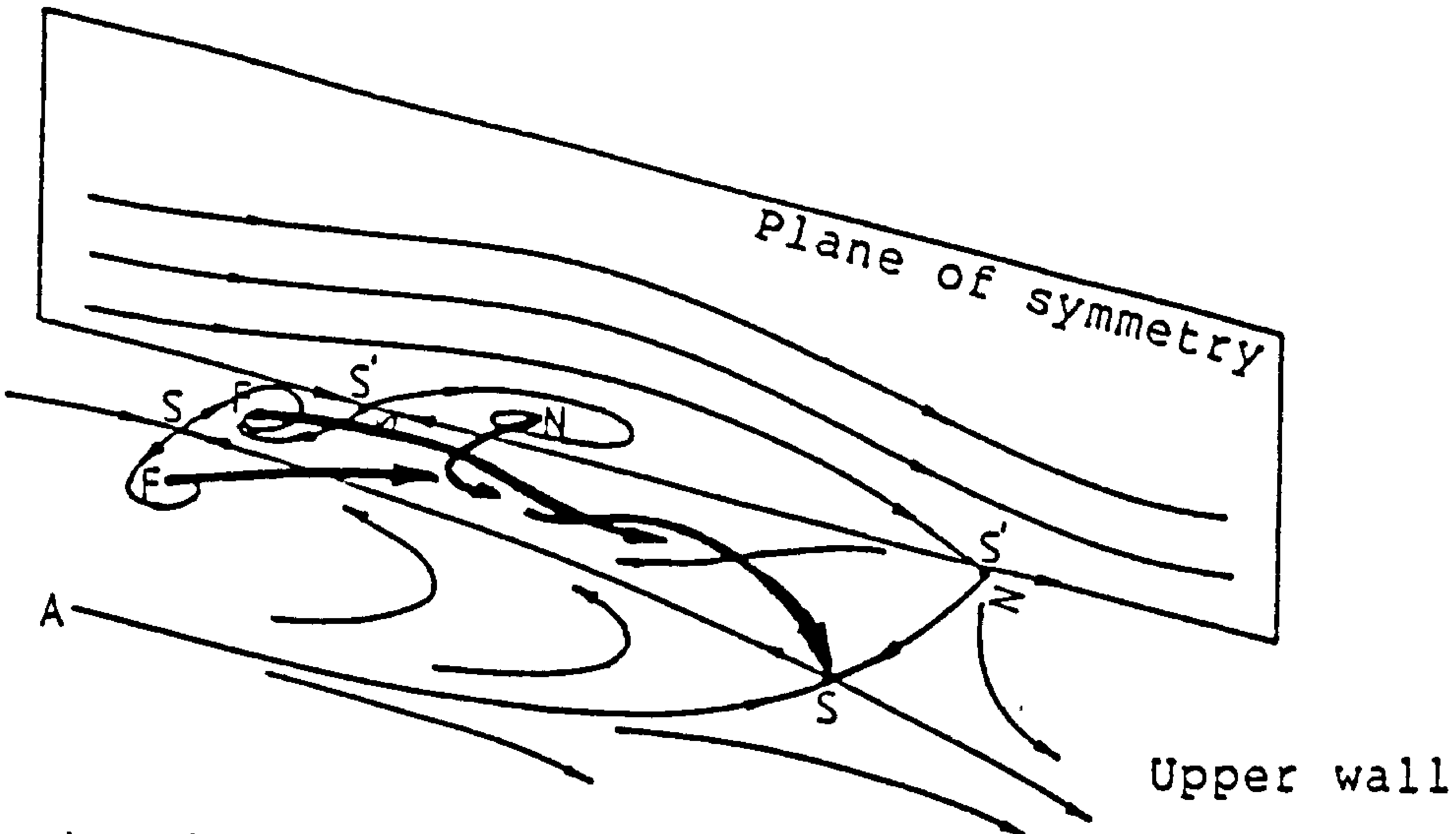

a) Separated flow terminates at the downstream saddle point

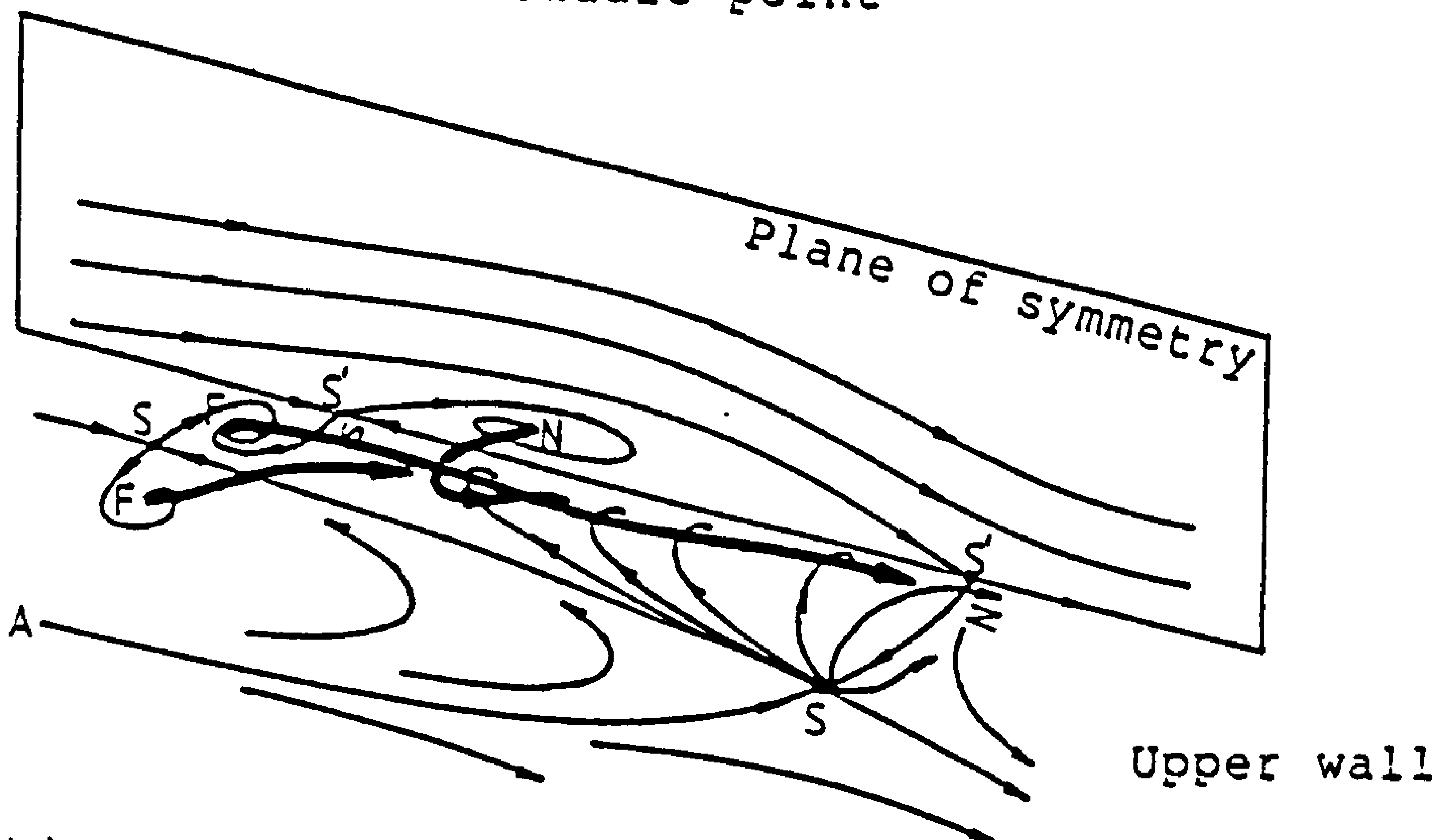

b) Separated flow continues beyond the downstream saddle point

FIG. 4-79 CONJECTURED TIME-MEAN THREE-DIMENSIONAL FLOWFIELD STRUCTURES BASED ON FIGS. 4-77 & 4-80

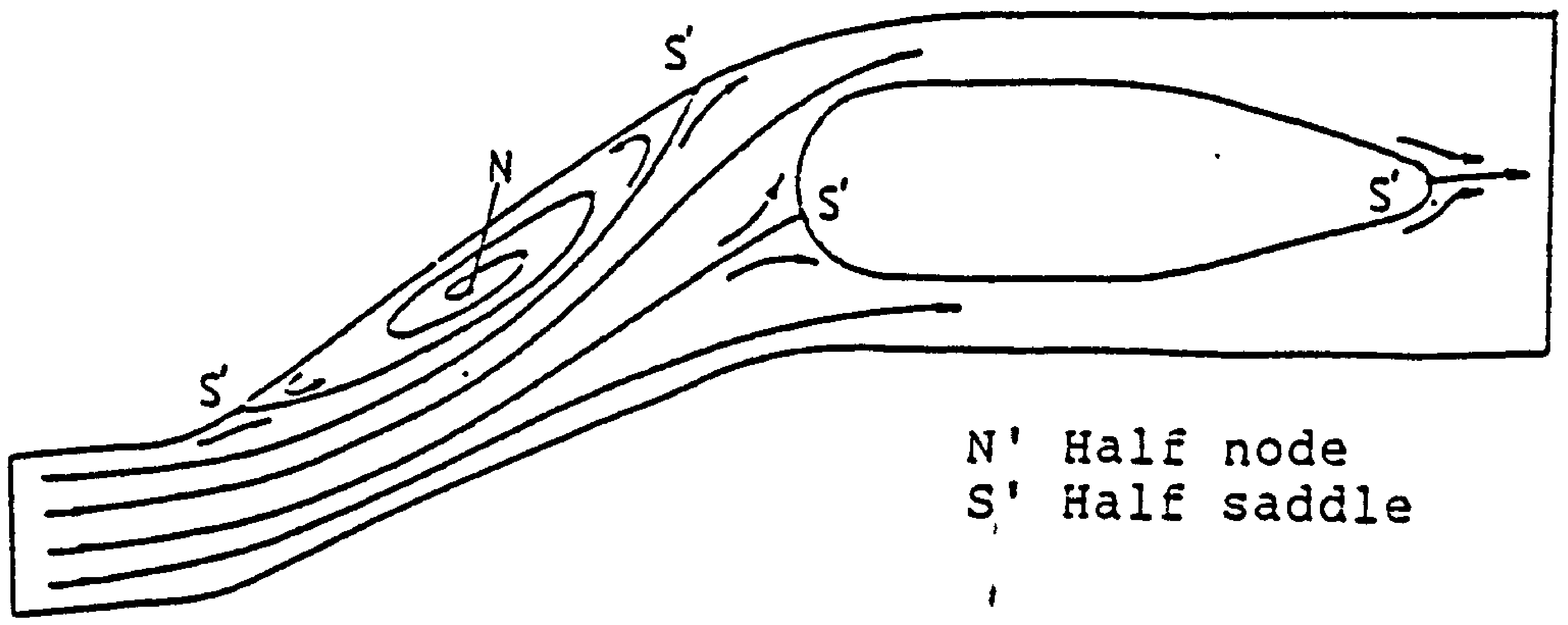

$$(\sum N + \tfrac{1}{2}\sum N') - (\sum S + \tfrac{1}{2}\sum S') = -1 \quad \text{(Hunt et al, 1978)}$$

FIG. 4-80 CONJECTURED FLOW PATTERN IN PLANE OF SYMMETRY BASED ON SURFACE CRITICAL POINTS AND HUNT'S TOPOLOGICAL RULE (ref.A3)

CHAPTER 5

NUMERICAL COMPUTATIONS

CHAPTER 5 NUMERICAL COMPUTATIONS

5.1 Introduction

In order to design efficient jet engine intakes it is an advantages to predict flows numerically in order to reduce development cost and time. Measurements are often carried out with scale models which may lead to boundary layer Reynolds numbers considerably smaller than that of full scale flow. Construction of full scale models and use of the large test facilities required can be prohibitively expensive. Recent high performance jet aircraft and/or jet engine propelled missiles have ducts with rather complicated three-dimensional shapes. It is therefore necessary to develop a three-dimensional flow calculation program, because flow three-dimensionality plays a crucial role in setting duct performance. Flow compressibility must also be built into the prediction program in order to calculate flows at high subsonic and supersonic speeds.

As yet the full Navier-Stokes equations cannot be solved with any confidence owing to deficiencies in numerical techniques and computer power, but fortunately many aspects of internal flows can be well predicted using approximate schemes, provided they retain the essential physics of the problem and are sufficiently economical in terms of computational effort.

There are a number of inviscid methods for solving three-dimensional duct flow problems. The most notable ones are those of Hawthorne's secondary flow analysis (1967), Stuart &

Hetherington's rotational Euler solving scheme (1970) ana Hamed & Abdullah's streamlike function approach (1978). However, these methods can only serve to provide an insight into the real flow problem rather then act as design tools owing to the underlying inviscid assumptions.

Earlier methods, mainly incompressible, which included the formulations of viscous effects for solving three-dimensional duct flow problems are typified by the parabolic schemes of Patankar & Spalding (1972), Briley (1974) and Robert & Forester (1978). Their schemes usually provided a forward marching solution in the main flow direction by assuming that the viscous diffusion with respect to the main flow direction, that is second derivatives, were negligible. As these methods neglect some features of elliptic effects they often lead to unreliable results in predicting flow in geometries other than those which are long in the streamwise sense as compared to the transverse size.

Levy et al (1980-83) later presented a method (PEPISG) to compute three-dimensional subsonic duct flow. The method is based on Briley's original parabolic procedure with the introduction of elliptic effects through a known three-dimensional pressure field obtained from an incompressible potential flow analysis; subsequent one-dimensional corrections are applied to the pressure field to account for the boundary layer blockage effect during the forward marching process. It is, however, doubtful whether such a technique could reflect the true elliptic and compressible nature of the subsonic flow. In particular, the simple one-dimensional correction to account for the viscous blockage effect oversimplifies the three-dimensional nature of the flow especially when the displacement effect of the boundary layer could significantly alter the effective duct flow geometry. These deficiencies are revealed by Vakili et al (1984) when the method was used in validation against subsonic flow data obtained from circular S-ducts.

Similarly, after noting the shortcomings of parabolic methods, Pratap & Spalding (1975) adopted a partially-parabolic approach to compute incompressible flow in square curved ducts. In their method, the elliptic influence of the pressure field is introduced by an iterative, marching-integration procedure where several sweeps of the flow domain are made; in each sweep a better estimate of the pressure field is used, and correction is applied to the pressure field at each streamwise station such that the mass-continuity equation is satisfied locally again retaining one-dimensional corrections which render the elliptic influences only in an approximate manner. Lin & Guo (1986) further developed this method for compressible duct flow and reported good agreement with the experimental data when the method is used to compute subsonic flow in an S-shaped square duct. Pratap et al demonstrated that the partially parabolic approach is a plausible method for tackling three-dimensional duct flow problems. However, their schemes required considerable re-formulations and further development in the grid generation area before it can be used for flow in arbitrary duct shapes.

In the present work, the viscous/inviscid interaction scheme developed by Ahmed et al (1984) is used. The scheme is developed for general three-dimensional duct flows based on high Reynolds number boundary layer models and rotational inviscid core flow with no approximation in the elliptic influences. This scheme is believed to be most appropriate for flows in jet engine intakes which often consists of a large proportion of core flow and a well defined boundary layer region.

The core flow method used here is based on the solution of the Euler equations by iterative space matching techniques in general curvilinear co-ordinates. The present method derives from the Stuart & Hetherington (1970) scheme which has been improved considerably by successive research workers at the University of Salford. The flow concerned is three-dimensional, compressible, inviscid and may contain major regions of vorticity in the core flow.

The wall, or boundary layer region, is calculated by an integral method which affords a very efficient use of computing time when compared to differential methods. The method is based on the work by Myring (1970). The flow considered is turbulent, fully three-dimensional and compressible.

Individual validations for the core flow and the boundary layer methods have been carried out by Ahmed (1984). However, in order to use this viscous/inviscid interaction method in practical cases, comparison between calculated and measured results is necessary. The validation of the overall viscous/inviscid scheme for design purposes is one objective of the current work.

Details of the methods introduced above are outlined in the following sections. The addition of centre body treatment, which is required in the present work, and the calculation procedure are also described.

Finally, the viscous/inviscid scheme is used to calculated flows in Duct M and N. Comparisons between the calculated and measured results are presented and discussed.

5.2 Theory

5.2.1 Grid generation

The need for grid generation of boundary-fitted curvilinear coordinates arises in the numerical solution of fluid flow problems influenced by complex surface geometries. In order to maintain accuracy at the boundaries it is important that the discretised boundaries are coincident with the mesh points used in the numerical solutions, thus avoiding interpolation of the boundary conditions.

The method used here is based on the work of Thompson et al (1982) and involves the solution of Laplace's equation in the transformed plane, yielding a quasilinear system of the equations in the physical plane, given by

$$g_{22}x_{\xi\xi} - 2g_{12}x_{\xi\eta} + g_{11}x_{\eta\eta} = -g(Px_{\xi} + Qx_{\eta}) \qquad (5\text{-}1a)$$

and

$$g_{22}y_{\xi\xi} - 2g_{12}y_{\xi\eta} + g_{11}y_{\eta\eta} = -g(Py_{\xi} + Qy_{\eta}) \qquad (5\text{-}1b)$$

where P and Q are control terms used to adjust the shapes of the mesh lines.

5.2.2 Core flow calculation

The inviscid rotational method is based on the work of Stuart & Hetherington (1970) and is derived from the continuity, momentum and energy equations for inviscid, compressible and rotational steady flow in general curvilinear coordinates. The analysis and presentation of these equations are achieved effectively by using standard tensor notation.

The basic steady flow equations written in general curvilinear coordinates are as follows:

$$\text{Continuity:} \quad (\rho u^i)_{,i} = 0 \qquad (5\text{-}2)$$

$$\text{Momentum:} \quad u^j u^i_{,j} = -\frac{1}{\rho} g^{ij} p_{,j} \qquad (5\text{-}3)$$

and

$$\text{Energy:} \quad u^i H_{o,i} = 0 \qquad (5\text{-}4)$$

The curvilinear velocities u^i are replaced by new variables λ^i, defined by

$$V\lambda^i = u^i$$

where $\lambda^3=1$, and λ^1 and λ^2 are the transverse velocity ratios; V is the through flow component along the x^3 axis in the general direction of the main flow. After much manipulation involving the equation of state and the second law of thermodynamics, the flow equations may be written in the form:

$$\text{Continuity:} \quad \frac{\partial}{\partial x^i}(\sqrt{g}\rho V\lambda^i) = 0 \qquad (5\text{-}5)$$

Momentum:
$$(1-M^2)\left[V^2\lambda^i \left\{ \frac{\partial}{\partial x^i}(g_{jk}\lambda^j) - \frac{\partial}{\partial x^k}(g_{ij}\lambda^j) \right\} + H_{o,k} + \frac{1}{\gamma}(H_o - \tfrac{1}{2}fV^2)(LnA)_{,k} - \tfrac{1}{2}f(V^2)_{,k} \right] - V^2 g_{lk}\lambda^l \left[\frac{1}{\sqrt{g}} \frac{\partial}{\partial x^i}(\sqrt{g}\lambda^i) - \tfrac{1}{2}\frac{V^2}{C^2}\lambda^i f_{,i} \right] = 0$$

$$(k=1,2,3) \qquad (5\text{-}6)$$

where

$$M^2 = \frac{V^2}{C^2} f, \quad f = g_{mn}\lambda^m\lambda^n \text{ and } A = \exp(-S/c_v)$$

and

Energy:
$$\lambda^i H_{o,i} = 0 \qquad (5\text{-}7)$$

The momentum equation in the x^3 direction $(k=3)$ is then replaced by the entropy conservation equation:

$$\lambda^i A_{,i} = 0 \qquad (5\text{-}8)$$

The through flow velocity in the two transverse momentum equations $(k=1,2)$ is replaced by V^η and V^ζ respectively. The x^1 and x^2 momentum equations become

$$(V^\eta)^2 a_1 - b_1 \frac{\partial (V^\eta)^2}{\partial x^1} + C_1 = 0 \qquad (5\text{-}9)$$

and

$$(V^\zeta)^2 a_2 - b_2 \frac{\partial (V^\zeta)^2}{\partial x^2} + C_2 = 0 \qquad (5\text{-}10)$$

where

$$a_k = \lambda^i \left\{ \frac{\partial}{\partial x^i}(g_{jk}\lambda^j) - \frac{\partial}{\partial x^k}(g_{ij}\lambda^j) \right\} - \frac{1}{2\gamma} f \frac{\partial}{\partial x^k}(\mathrm{LnA})$$

$$- \frac{\lambda^l}{(1-M^2)} g_{lk} \left\{ \frac{1}{\sqrt{g}} \frac{\partial}{\partial x^i}(\sqrt{g}\lambda^i) - \frac{\frac{1}{2}\overline{V}^2}{C^2}\lambda^i \frac{\partial f}{\partial x^i} \right\},$$

$$b_k = \tfrac{1}{2} f,$$

$$C_k = H_o \frac{1}{\gamma} \frac{\partial(\mathrm{LnA})}{\partial x^k} + \frac{\partial}{\partial x^k} H_o$$

and

$$\overline{V} = V^\eta \quad \text{when } k = 1$$

$$= V^\zeta \quad \text{when } k = 2$$

By replacing V by V^η and V^ζ, an extra unknown has been introduced. The additional equation required to complete the set may be obtained by writing the continuity equation in the following two forms:

$$\frac{\partial}{\partial x^1}(\overline{V}^\eta \lambda^1) + \frac{\partial}{\partial x^2}(\overline{V}^\zeta \lambda^2) + \frac{\partial}{\partial x^3}(\overline{V}^\eta) = 0 \qquad (5\text{-}11)$$

and

$$\frac{\partial}{\partial x^1}(\overline{V}^\eta \lambda^1) + \frac{\partial}{\partial x^2}(\overline{V}^\zeta \lambda^2) + \frac{\partial}{\partial x^3}(\overline{V}^\zeta) = 0 \qquad (5\text{-}12)$$

where

$$\overline{V}^\eta = \sqrt{g}\,\rho\,V^\eta, \quad \overline{V}^\zeta = \sqrt{g}\,\rho\,V^\zeta$$

and

$$\rho = H_o \frac{(\gamma-1)A}{1 + \frac{1}{2}(\gamma-1)M^2} \frac{1}{\gamma-1}$$

There are now six equations (5-7 to 5-12) for the six dependent variables H_o, A, V^η, V^ζ, λ^1 and λ^2.

The distributions of inlet total pressure, total temperature, transverse velocity ratios λ^1 and λ^2 and the through flow velocity or static pressure are required as inlet boundary conditions. The description of transverse velocities must be compatible with other boundary conditions and must satisfy the continuity equation at the inlet plane and the no through flow conditions at the passage wall.

At outlet the boundary conditions must be chosen so that downstream features are anticipated. The only general case in which simple outlet conditions can be specified involves a parallel passage of constant area in which the outlet flow settles into a pattern of similarity. Streamline gradients of the through flow velocity may for example be taken as zero at outlet. Thus

$$\frac{\partial V_3^\eta}{\partial x} = \frac{\partial V_3^\zeta}{\partial x} = 0 \qquad (5\text{-}13)$$

5.2.3 Boundary layer calculation

The integral boundary layer method used here has been developed for the calculation of three-dimensional compressible boundary layers with rotational outer flows. The method is based on the work of Myring (1970) and

Pilatis (1986), who derived the three-dimensional integral boundary layer equations in curvilinear coordinates.

Equations used in the present work are summarized below. The terms underlined account for variations in total pressure in the core flow.

The streamwise momentum equation is

$$\frac{\partial}{\partial s}\theta_{11} + \theta_{11}\left[(2-M_e^2)U_s + k_s\right] +$$

$$\frac{\partial}{\partial n}\theta_{12} + \theta_{12}\left[(1-M_e^2)U_n + 2k_n\right] -$$

$$\theta_{22}k_s + \delta_1 U_s + \delta_2 (U_n + k_n) = \tfrac{1}{2}cf_1 + \underline{Fk_u\delta} \qquad (5\text{-}14a)$$

The crossflow momentum equation is

$$\frac{\partial}{\partial s}\theta_{21} + \theta_{21}\left[(2-M_e^2)U_s + 2k_s\right] + \frac{\partial}{\partial n}\theta_{22} +$$

$$\theta_{22}(2-M_e^2)U_n + k_n(\theta_{22} - \theta_{11} - \delta_1) = \tfrac{1}{2}cf_2 - \underline{FAk_u\delta} \qquad (5\text{-}14b)$$

Continuity gives:

$$\frac{\partial}{\partial s}(\delta-\delta_1) + (\delta-\delta_1)\left[(1-M_e^2)U_s + k_s\right] -$$

$$\frac{\partial}{\partial n}\delta_2 - \delta_2\left[(1-M_e^2)U_n + k_n\right] = F \qquad (5\text{-}15)$$

where U_s and U_n are defined by

$$U_s = \frac{1}{U_e}\frac{\partial}{\partial s}U_e, \quad U_n = \frac{1}{U_e}\frac{\partial}{\partial n}U_e \quad \& \quad A = -\left(\frac{\partial v}{\partial u}\right)_e \qquad (5\text{-}16)$$

and

$$U_e = [1 + k_u(\delta - \delta^*)] \sqrt{[u_*^2 + v_*^2 + 2u_* v_* g_{12}/h_1 h_2]} \qquad (5\text{-}17)$$

where the subscript * denotes the displacement surface. The curvature terms k_s and k_n are derived from continuity and vorticity considerations in the streamline and curvilinear coordinate system. Thus

$$k_s = \frac{1}{h_{2s}} \frac{\partial}{\partial s} h_{2s}$$

$$= \frac{1}{q} \left\{ \frac{\partial}{\partial \xi}(q u_e/h_1 U_e) + \frac{\partial}{\partial \eta}(q v_e/h_2 U_e) \right\} \qquad (5\text{-}18)$$

and

$$k_n = \frac{1}{h_{1s}} \frac{\partial}{\partial n} h_{1s}$$

$$= \frac{1}{q} \left\{ \frac{\partial}{\partial \eta}(h_1 u_e/U_e + g_{12} v_e/h_2 U_e) - \right.$$

$$\left. \frac{\partial}{\partial \xi}(g_{12} u_e/h_1 U_e + h_2 v_e/U_e) \right\} \qquad (5\text{-}19)$$

The rotationality term k_u is related to the total pressure gradient normal to the boundary layer surface, and

$$k_u = \frac{1}{U_e} \frac{\partial}{\partial \zeta} U_e$$

$$= \frac{1}{\gamma M_e^2} \frac{1}{P_o} \frac{\partial}{\partial \zeta} P_o \qquad (5\text{-}20)$$

Several empirical assumptions are used in solving these equations; these include forms of velocity profiles in order to derive relationships between the boundary layer integral parameters:

a) The streamwise profile which is taken to be

$$u/U_e = (z/z_\delta)^n$$

where $z = \int_0^\zeta (\rho/\rho_e)d\zeta$ and $n = (\bar{H}-1)/2$

This assumption produces the following relationship

$$H_1 = (\delta-\delta_1)/\Theta_{11}$$

$$= 2\bar{H}/(\bar{H}-1)$$

where $\bar{H} = (H-0.2M_e^2)/(1+0.2M_e^2)$ and $H = \delta_1/\Theta_{11}$

b) The Mager crossflow velocity profile is chosen for the present work

$$v/U_e = u/U_e(1-z/z_\delta)^2\tan\beta_o$$

Together with a), the crossflow thicknesses Θ_{12}, Θ_{21}, Θ_{22} and δ_2 can be related to the streamwise momentum thickness Θ_{11}, $\bar{H}$ and β_o by the equations of the form

$$\Theta_{ij} = \Theta_{11}(\tan\beta_o)^{(i+j-2)} M_{ij}(\bar{H})$$

and

$$\delta_2 = \Theta_{11}(\tan\beta_o)M_2(\bar{H})$$

where $M_{ij}(\overline{H})$ and $M_2(\overline{H})$ are defined in [D14] and $\tan\beta_o$ is defined by

$$\tan\beta_o = \frac{\partial v}{\partial u}\Big|_{\zeta=0}$$

c) The streamwise component of the skin friction is based on the Ludwieg-Tillman relationship and is given by

$$cf_1 = 0.246\exp(-1.561\overline{H})Re_\theta^{-0.268}(T_e/T_m)^{0.762}$$

The crossflow value is

$$cf_2 = cf_1 \tan\beta_o$$

where

$$Re_\theta = U_e\theta_{11}/\nu_e$$

and

$$T_m/T_e = 0.72(1+0.18M_e^2) + 0.28$$

d) The entrainment function in Green's form of Head's original relation is expressed as

$$F = 0.025\overline{H} - 0.022$$

Figures 5-1 and 5-2 show these empirical assumptions against measured data for the present test cases. The comparisons are good, except in the vicinity of the flow separation (in Duct N), where poor correlation is found; this is inferred to be caused primarily by a breakdown of the usual boundary layer assumptions.

5.2.4 Centre body treatment

The calculation scheme in its present form cannot be applied to a duct with centre body nor can it handle bifurcations. The main reason is because of the formulation in Stuart & Hetherington method which assumes a finite flow magnitude with Mach number greater than 0.1 in the streamwise direction. The inclusion of a centre body would incorporate a stagnation point on the nose and introduce some form of flow bifurcation. Therefore, a correction scheme is introduced to include the centre body effect.

The existence of the centre body is treated axisymmetrically. The Hess & Smith (1967) ring source panel method (App. C) is used to calculate the flow in a circular duct with a centre body, having the same area distributions as the duct tested. The duct wall and the centre body profile are represented by ring source panels (Fig. 5-3a). The use of this special panel method eliminated the need of circumferential discretisation thus significantly reducing the error due to 'leakage', which is a typical deficiency in using panel method for internal flow problems.

The use of the panel method ensures the elliptic effect caused by the centre body is accounted for, as against the non-elliptic (or formally one-dimensional) area ratio approach (Fig. 5-3b).

In adopting the axisymmetric panel method approach the blockage effect caused by the centre body is assumed to be uniform around the duct wall. The shortcomings of the this assumption in applications to non-axisymmetric ducts will be discussed later.

The calculations are carried out with and without the centre body. Then the effects of the centre body, including both Mach number (using Prandtl-Glauert rule [A20]) and upstream effects, on the pressure field at the wall are generalized and used to correct the streamwise velocity in the core flow.

5.2.5 Calculation procedures

In the present test cases, a computational grid size of 9x9x36 (9x9 crosswise & 36 streamwise) is used for the core flow calculations; grid size of this order has been demonstrated by Ahmed to be sufficient to produce accurate solutions. The streamwise grid is further subdivided in order to obtain accurate boundary layer solutions; the inviscid flow variables at the new grid points are obtained by the cubic spline interpolation in the forward direction.

The first calculation plane is taken to be the inlet plane of the transition duct, which is 1.0 times the equivalent inlet diameter upstream of the duct throat. The inlet condition in this plane can safely be assumed to be uniform with negligible cross flow components.

Starting conditions required to perform the core flow calculation are inlet Mach number, inlet total temperature and inlet static pressure for the core flow calculation. Here, the measured values of static pressure, total pressure and total temperature are used; the inlet Mach number is calculated from isentropic flow relationships.

The boundary layer starting conditions required are the momentum thickness θ_{11} and shape factor H. These data are unavailable at the calculation inlet plane, hence are determined by an iterative process using a two-dimensional integral boundary layer analysis; the required data at the inlet are decided by matching calculated values to the measured values at the throat.

In order to avoid the outlet boundary conditions affecting the calculations, a constant cross-section extension of twice the the duct outlet diameter is added to the duct outlet. At the calculation outlet plane the flow is assumed to have settled into a pattern of similarity; the streamline gradients of the through flow velocity are taken as zero. The displacement surface method is used to match core flow and boundary layer development; this involves modifying the wall shape using the displacement thickness δ^* to give a new effective boundary for the core flow calculation. Using a core flow solution, the boundary-layer calculation is carried out. Then using the calculated displacement surface, the core grid is re-generated and another core flow calculation is carried out. This represents one cycle of the calculation; up to 250 cycles are required to obtain a converged solution. Typical cycle time is 45 sec using the CDC7600.

When pressure gradients which drive the boundary layer equations are applied in full, the calculation may fail, before proper matching of core and boundary layer solutions has taken place. Therefore a relaxed portion of pressure gradient is applied first, and slowly increased until the full pressure gradient is applied.

Convergence of the viscous/inviscid interaction calculations is assumed when the maximum successive change in the displacement surface thickness δ^* is less than 0.01% of the value of δ^* at the inlet; in the case of core flow calculations, convergence is assumed when the error between the two transverse through flow velocities V^η and V^ζ is less than 1%.

5.3 Results and discussions

5.3.1 Pressure coefficient and Mach number distributions

Flow quality in an intake duct may be assessed to some extent by surface pressure distributions along the duct at various circumferential stations. This shows the regions with strong pressure gradients in both circumferential and longitudinal directions. Hence problem regions may then be broadly identified, especially if viewed together with boundary layer parameters which will be discussed later.

The present intake ducts have no centreline shift in the Y (spanwise) direction so that the plane of symmetry contains the Z (pitchwise) axis. The flow at the outside of the bend near the engine face encounters difficult conditions upstream of the bend owing to continuous pressure rises. On the other hand the flow along the inside of the bend encounters some problems downstream of the bend owing to the flow expansion. Therefore, the measured pressures on both the upper and lower walls along the duct are compared with those calculated.

Figures 5-4 and 5-5 show the pressure coefficient Cp and Mach number developments of Duct M at low inlet Mach number.

The predicted pressures in upstream stages of the duct on the upper and lower walls coincide with each other, showing very little circumferential pressure gradient. However, the results for the upper and lower walls start diverging at about X=50mm indicating that the effects of the duct bend and the centre body reach even further upstream than predictions suggest. The prediction shown in the figure agrees very well with the measurement for the lower wall. There is disagreement around the upstream end of the centre body which starts at X=412mm. The calculation seems to have over estimated the effect of the centre body in the region of the centre body nose and consequently produces a rapid pressure rise especially on the inside wall just downstream of the bend. However, the overall correction to the streamwise velocity, due to the centre body seems to have produced reasonable results.

Figures 5-6 and 5-7 show the Cp and Mach number developments of Duct M at a higher inlet Mach number. The predicted results in the upstream region fall between the measured data along the upper and the bottom walls. In the region of the centre body nose the prediction again slightly over estimates the centre body effect. The general trend for the developments along the duct are very similar to those of the low inlet Mach number case. It is clear from these two cases of different inlet Mach numbers that even with the effects of flow compressibility starting to play an important role, the calculation procedure is capable of predicting the duct surface pressures with acceptable accuracy.

Duct N has two bends and even more severe turning angles than Duct M. Measurement has revealed a region of flow separation on the upper wall approaching the second bend. The aim of the exercise was to test the method in coping with such complex geometries and the associated difficult flow conditions. As a result, the strong viscous/inviscid interaction was encountered in the flow separation region which gave rise to serious difficulties of numerical stability in the computation. Hence, substantial initial relaxation in pressure gradient had to be used before a final converged solution with full pressure gradient was obtained.

The Cp and Mach number developments for Duct N at an inlet Mach number of 0.61 are shown in Figs. 5-8 and 5-9. The prediction falls short in capturing the peak Mach number and the maximum pressure drop on the inside wall of the first bend. This is likely to be caused by the lack of streamwise grid points in defining the high curvature convex surface. Consequently, the prediction appears to have missed the separation region on the upper wall, but overall it produced reasonable results for a very difficult flow involving compressibility effects.

5.3.2 Boundary layer parameters

The development of the boundary layer thickness influences the core flow solutions. An accurate prediction of duct flows is possible only if reasonably accurate prediction of the boundary layer parameters is available, and from these parameters the true duct performance parameters such as pressure loss and distortion levels can be evaluated.

Figures 5-10 and 5-11 show the displacement thickness δ_1 and momentum thickness parameter Θ_{11} developments for Duct M at low inlet Mach number. A rapid growth of the boundary layer upstream of the centre body is clearly seen. The general trends of the predicted results agree with those of the measurements. On the upper wall, the boundary layer grows and the shape parameter H increases. The growth rate on the upper wall is higher than that on the lower wall because of the bend. A rapid decrease in the thickness downstream of the bend is caused by the presence of the centre body. The flow accelerates in the streamwise direction giving favourable pressure gradients effectively produced by the centre body blockage. This is also seen in Figs. 5-12 and 5-13 where the shape parameter H and the skin friction coefficient cf_1 are presented. However, on the inside of the bend, fluid migration due to circumferential pressure gradients and exaggerated adverse pressure gradients from the calculation cause the boundary layer to grow much more rapidly than is indicated by the measurements, from approximately X=450mm: this is due to the special combination of the excessive streamwise adverse pressure gradient (see Fig. 5-4) and the boundary layer flow convergence in the region; this combination is possible only in fully three-dimensional flow.

Figure 5-14 shows the boundary layer parameters and the limiting streamline angle β_o at the engine face. Similarly, the agreements appear to be influenced by the limitations of the centre body treatment adopted. Discrepancies appear mainly on the lower wall, due to the reasons discussed above. However, the method predicted successfully the main features and the trend of the boundary layer growth up to this location.

In Duct N the growth of the boundary layer is more complex than that of Duct M owing to the combined effects of the two bends. Figs. 5-15 and 5-16 shows the developments of δ_1 and θ_{11} for Duct N at a high inlet Mach number. The developments of H and cf_1 for the same case are shown in Figs. 5-17 and 5-18. The comparison between prediction and measurement shows reasonable agreement in the upstream region of the duct. In the area of flow separation, the prediction shows only signs of near separation; the calculation did not break down numerically as might be expected for separating conditions. The failure to predict the maximum pressure drop near the throat is probably the result of both a deficiency in centre body correction and inlet conditions for the calculation which are idealized versions of the real inlet conditions. Small non-uniformities in the core flow and boundary layer may be amplified and cause more severe three-dimensional effects. This could lead to separation in the experiment but not in the calculation.

Figure 5-19 offers some insight into the direction of the fluid transport in the boundary layer of the idealized (predicted) flow in Duct N. In the diagram, the solid lines represent the direction of the external flow streamlines while the dotted lines represent the direction of the skin friction lines on the duct surface. Since the duct surface is non-developable, the streamline patterns are drawn in a rectangular cartesian system corresponding to the computational domain of the curvilinear grid. The choice of grid lines coincide very closely with calculated streamlines shapes, which consequently appear almost straight. The divergence and convergence of the skin friction lines is readily detectable; strong convergence of the skin friction lines indicate the build-up of boundary layer fluid, signalling the possibility of an approach to boundary layer separation. In the case of Duct N, the effect of the centre body can seen to have inhibited further build-up of boundary layer fluid on the upper wall of the duct thus preventing boundary layer separation. The boundary layer flow convergence problem is, however, shifted to the lower wall region and is further strengthened by the circumferential pressure gradient set up by the second bend.

5.4 Concluding remarks

A method of calculating jet engine air intake duct flows is presented; the flow concerned is three-dimensional and compressible. The overall solution is obtained using viscous/inviscid interaction. Measured and predicted results are compared for both a moderately curved and a more severely curved duct for both low and high inlet Mach numbers.

The developments of the surface pressure along the ducts obtained from prediction and measurement agree well. The general trends of the boundary layer development are also well predicted. Except in region where there is flow separation, the main disagreement can seen to be in the centre body region. This indicates that the limitation of applying the axisymmetric centre body correction to non-axisymmetric ducts, hence it suggests that further improvement is necessary in order to obtain better agreement.

It should be pointed out that the intake ducts investigated in this work are shorter than conventional ducts and are to be used on jet engines with exceptionally large compressor face centre bullets. Hence the effect of the centre bullet on the intake duct flow is significant and must therefore be accounted for in the flow calculation. On the other hand, for a more conventional aircraft intake where the length is normally less restricted, thus allowing an elongated S-duct with a small engine face centre bullet, the influence of the centre bullet is less pronounced and therefore much more amenable to the methods used here. Thus the method is likely to perform better in this circumstance.

The method is clearly shown to be capable of flow prediction in ducts with very difficult conditions. Although it is limited to the prediction of attached flow, the comparisons made have highlighted the diagnostic benefits of the method's capability in locating problem areas in flow passages. Hence, the onset of flow separation can be used in setting design limits such that flows remain attached, and where possible the optimization of the duct geometry in the interests of low losses and good profiles of total pressure. As described earlier, the prediction scheme offers a quick, effective means of assessing three-dimensional effects in intake ducts, especially where comparisons between ducts or changes in surface shape are considered.

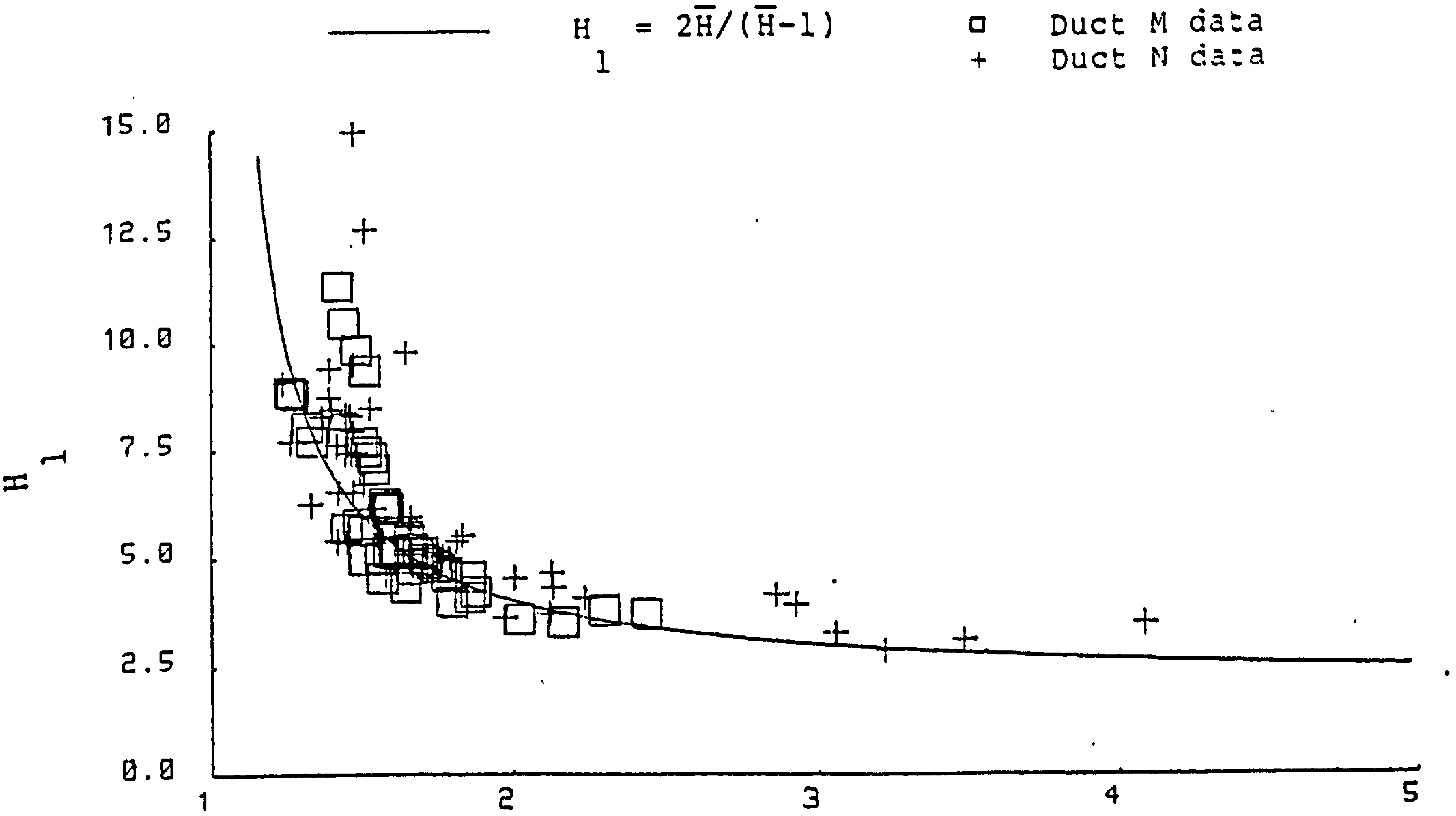

a) $H_1 - \bar{H}$ RELATIONSHIP

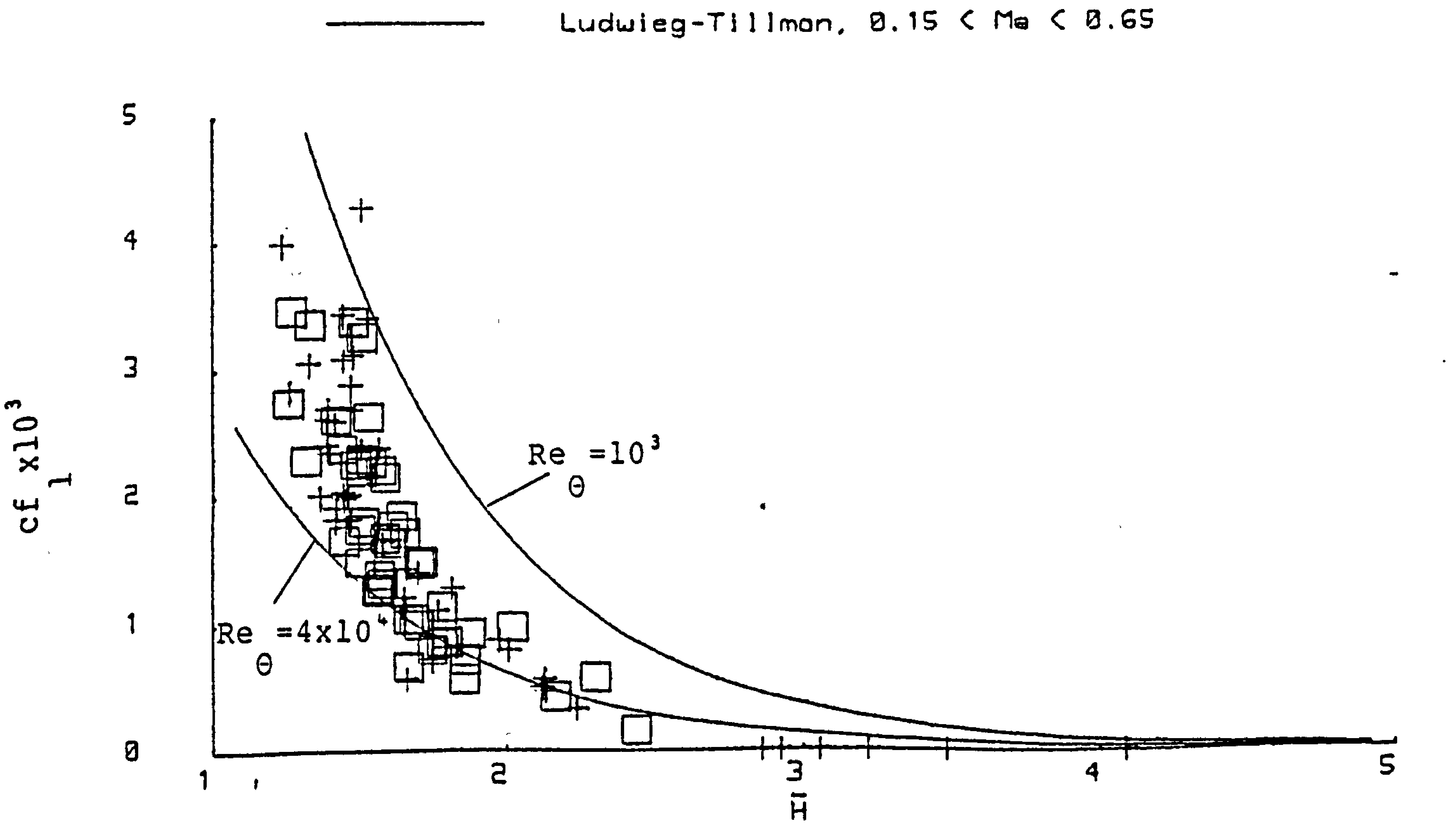

b) LUDWIEG-TILLMAN RELATIONSHIPS AT EXPERIMENTAL Re_Θ RANGE

FIG. 5-1 COMPARISONS OF EMPIRICAL ASSUMPTIONS WITH EXPERIMENTAL DATA

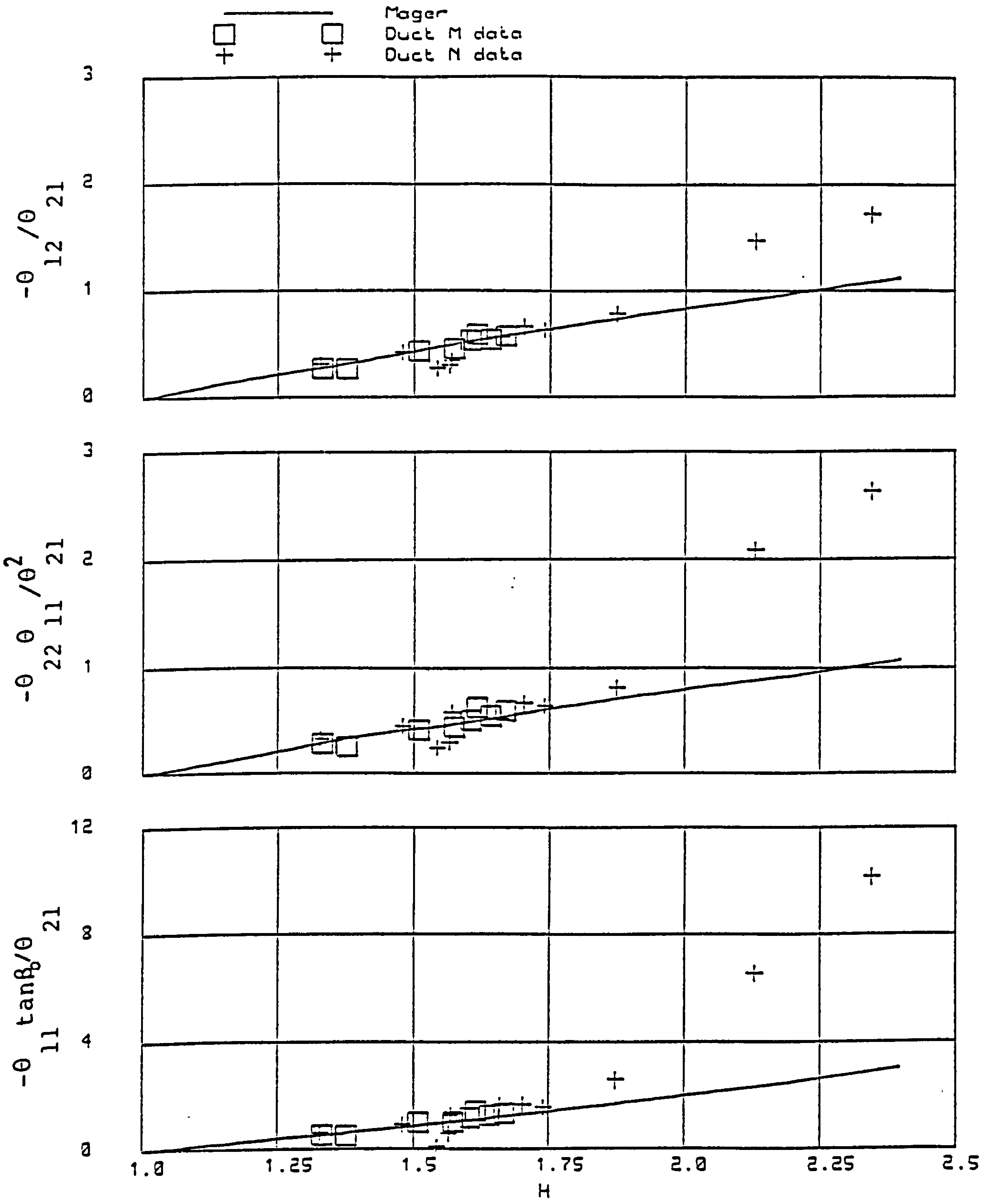

FIGS. 5-2

SECONDARY FLOW THICKNESS & SURFACE FLOW ANGLE PARAMETERS VERSUS STREAMWISE SHAPE PARAMETER H

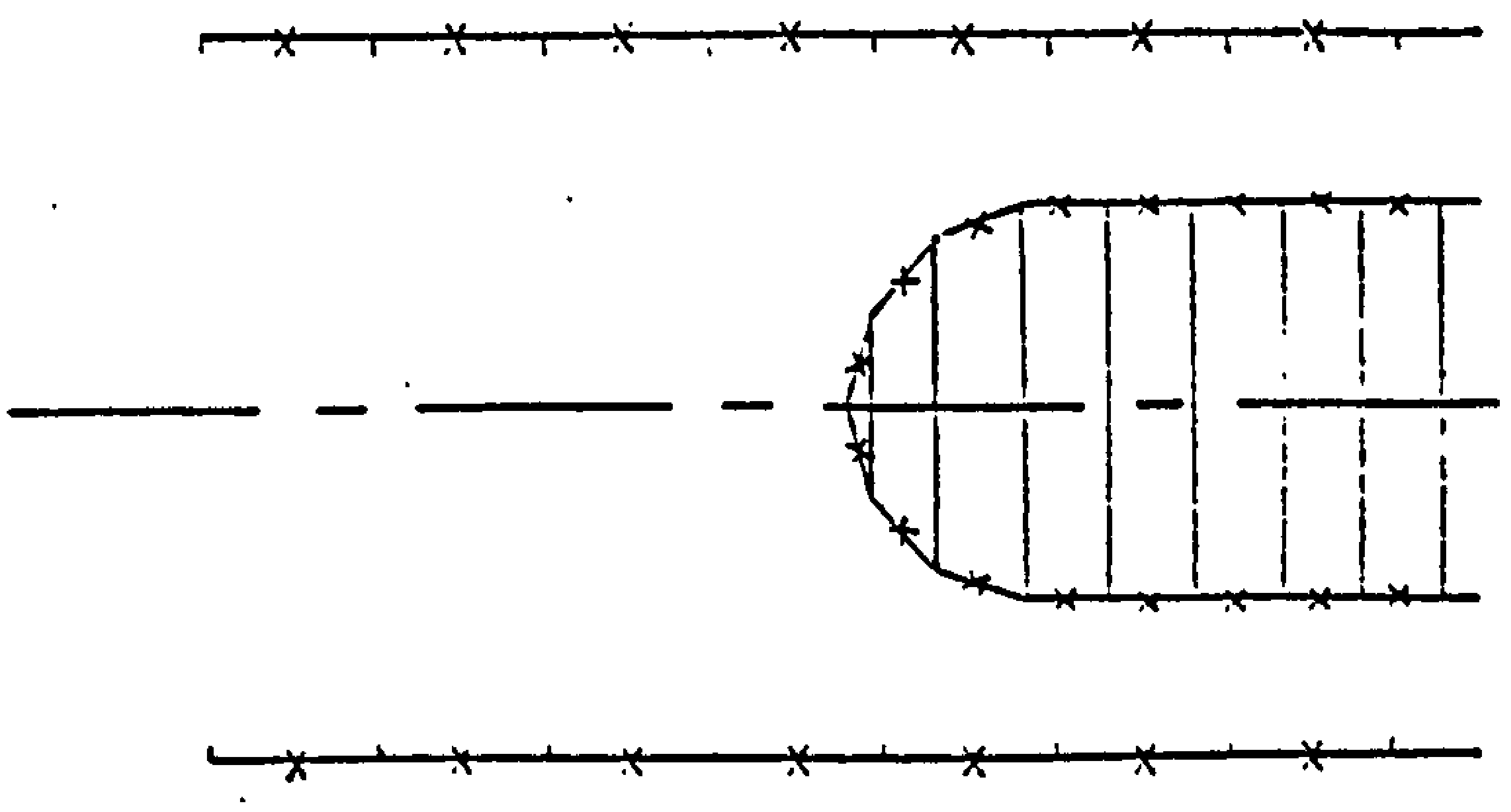

FIG. 5-3a RING SOURCE PANELS REPRESENTATION OF THE DUCT WALL AND THE CENTRE BODY

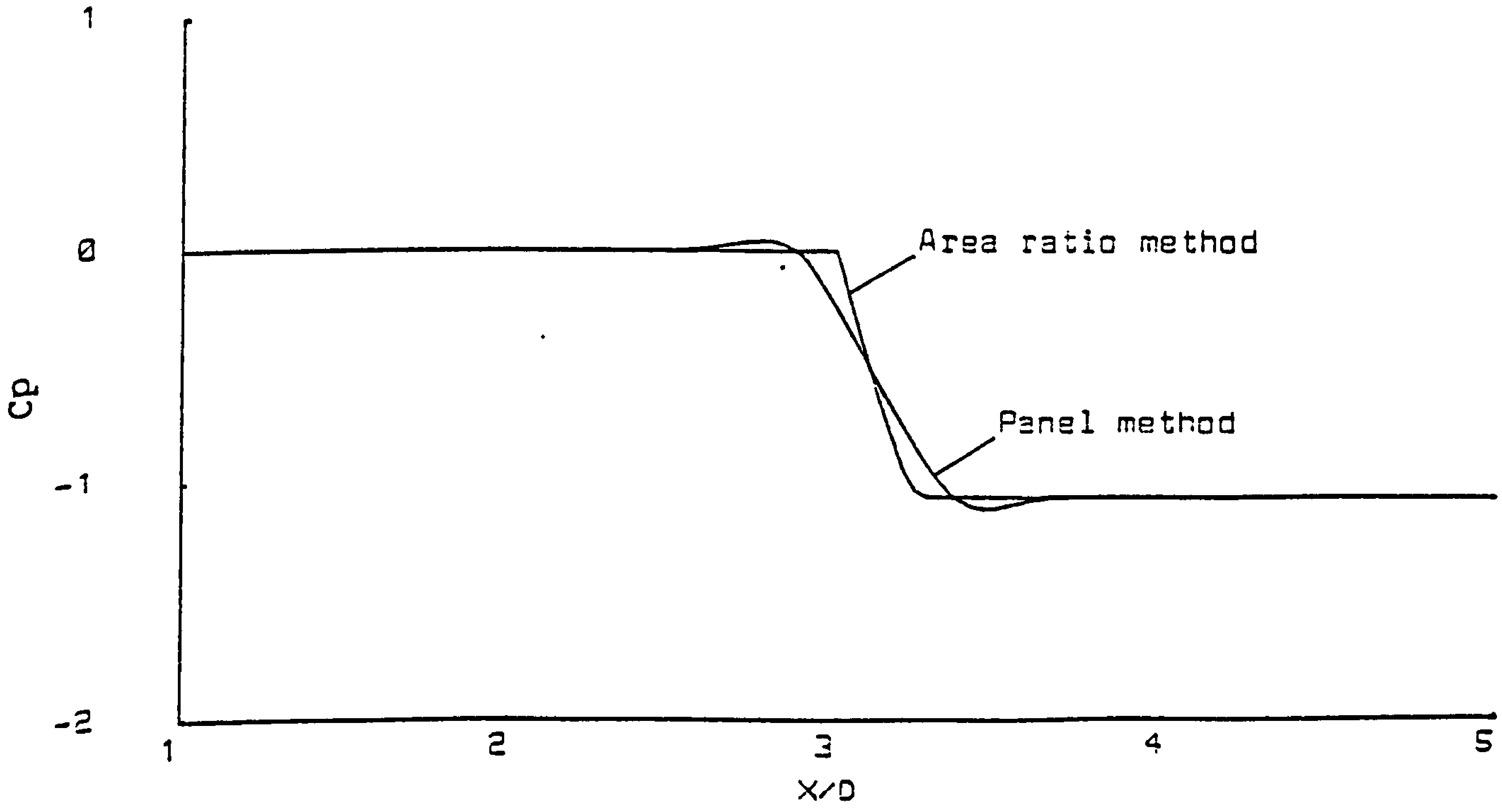

FIG. 5-3b THE INTRODUCTION OF THE ELLIPTIC EFFECT OF THE CENTRE BODY IN USING POTENTIAL FLOW METHOD

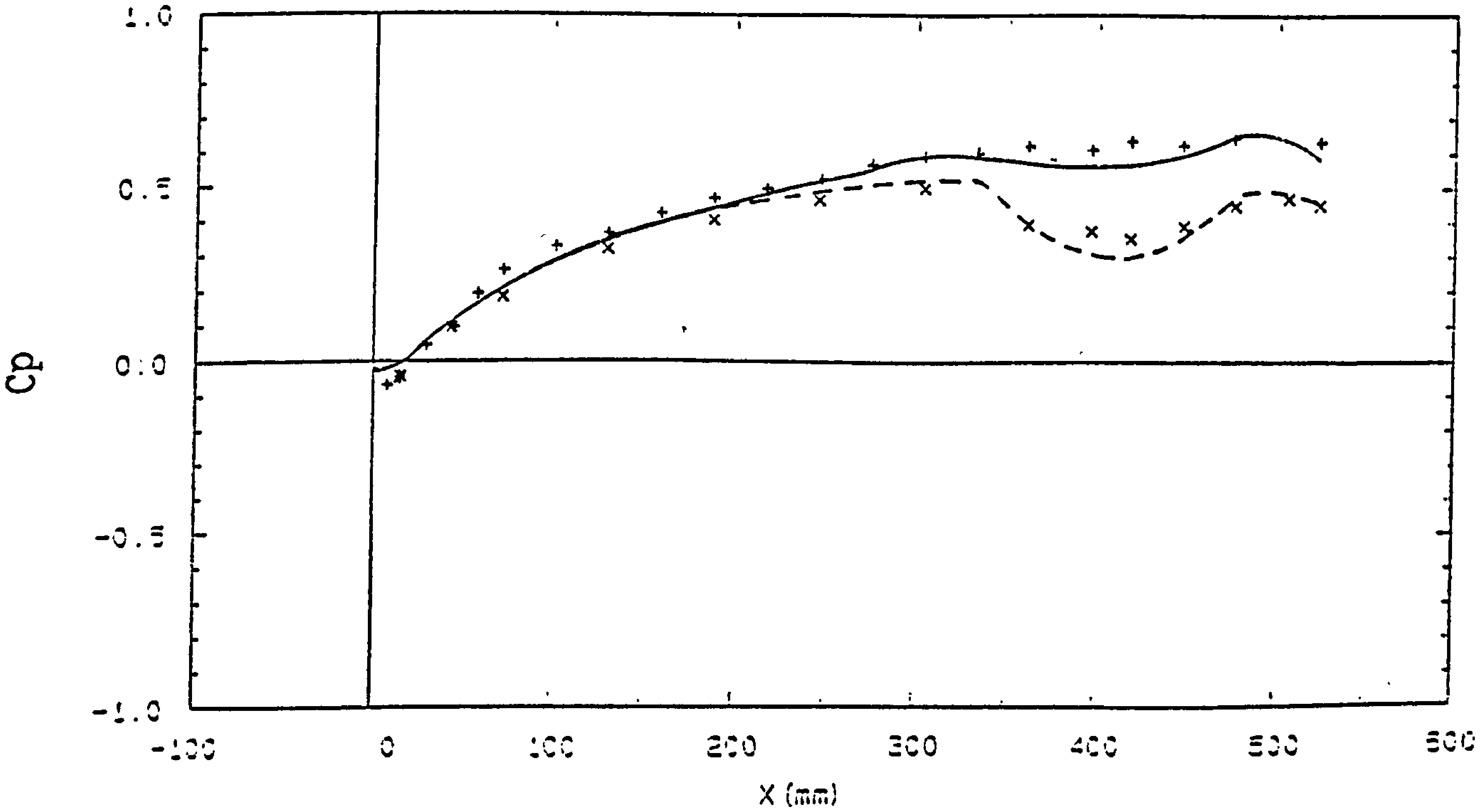

FIG. 5-4 PRESSURE DISTRIBUTIONS (DUCT M)

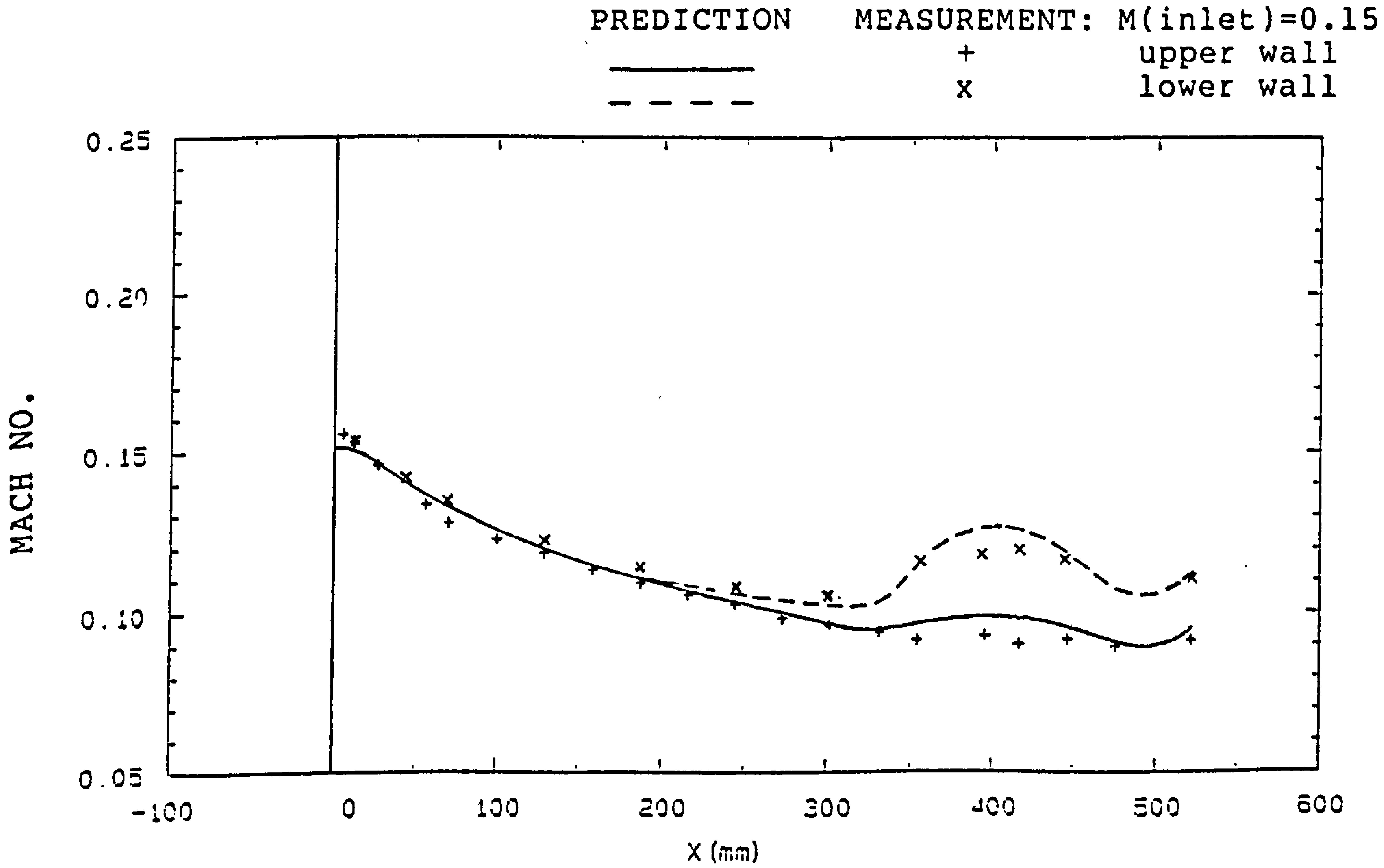

FIG. 5-5 MACH NUMBER DISTRIBUTIONS (DUCT M)

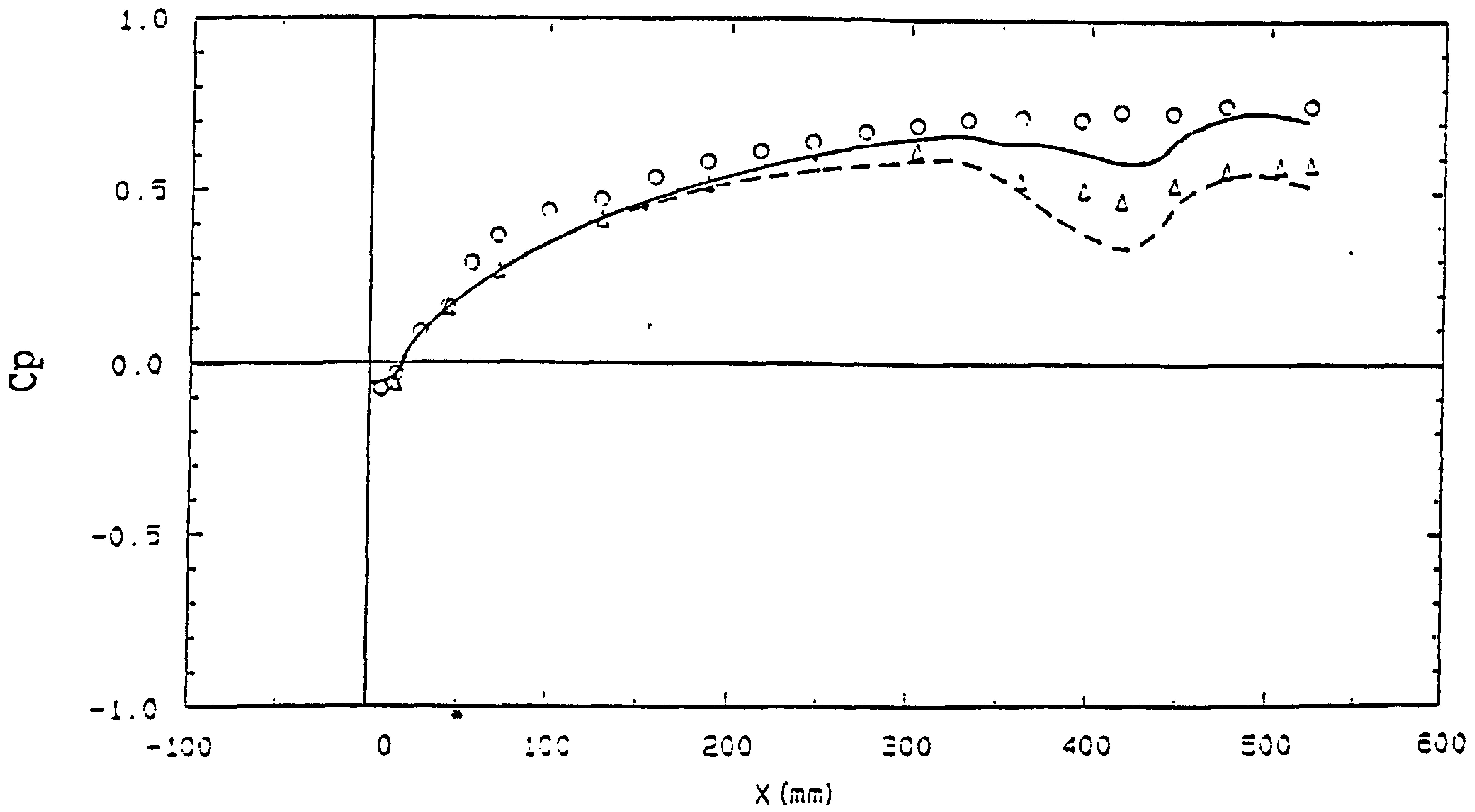

FIG. 5-6 PRESSURE DISTRIBUTIONS (DUCT M)

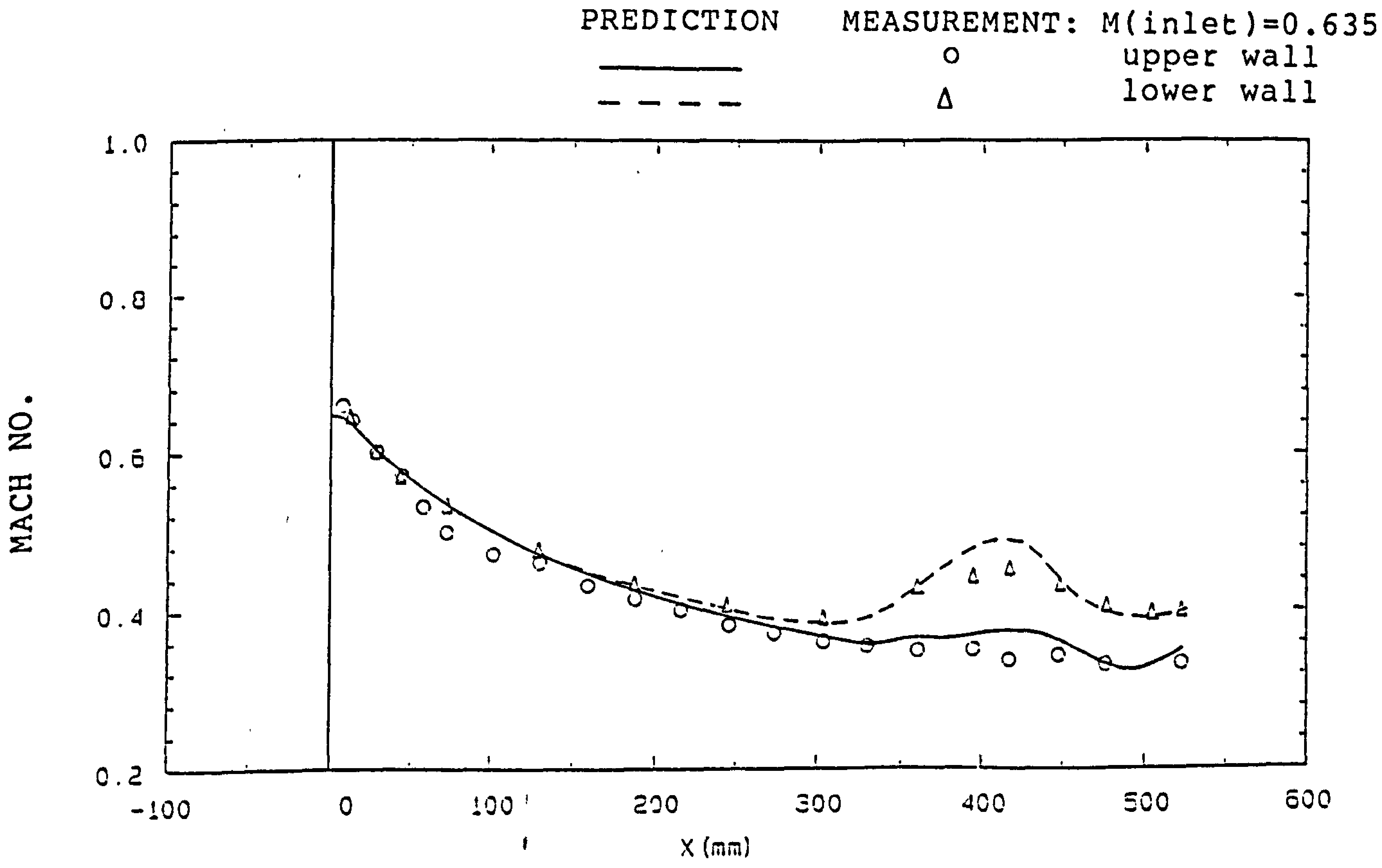

FIG. 5-7 MACH NUMBER DISTRIBUTIONS (DUCT M)

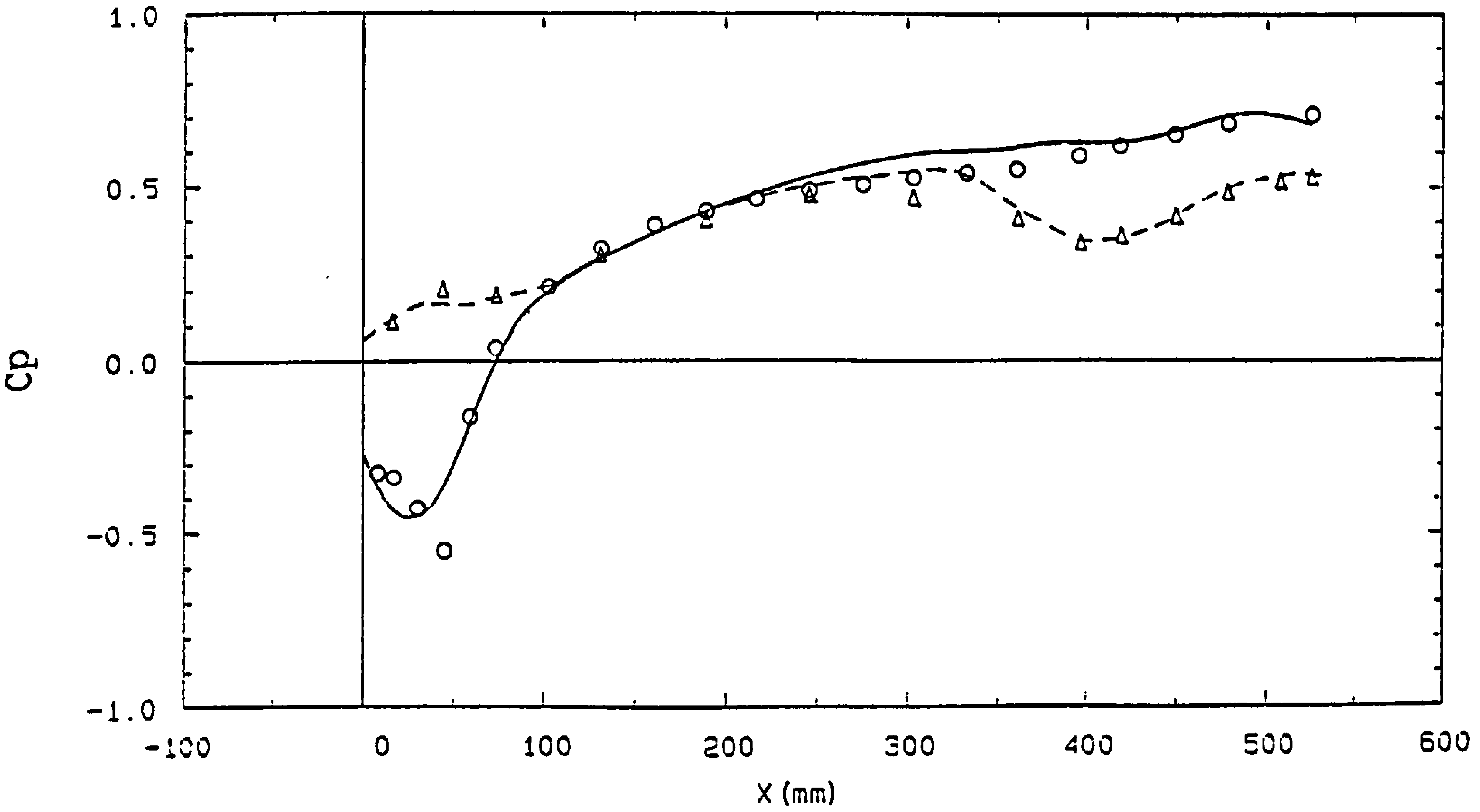

FIG. 5-8 PRESSURE DISTRIBUTIONS (DUCT N)

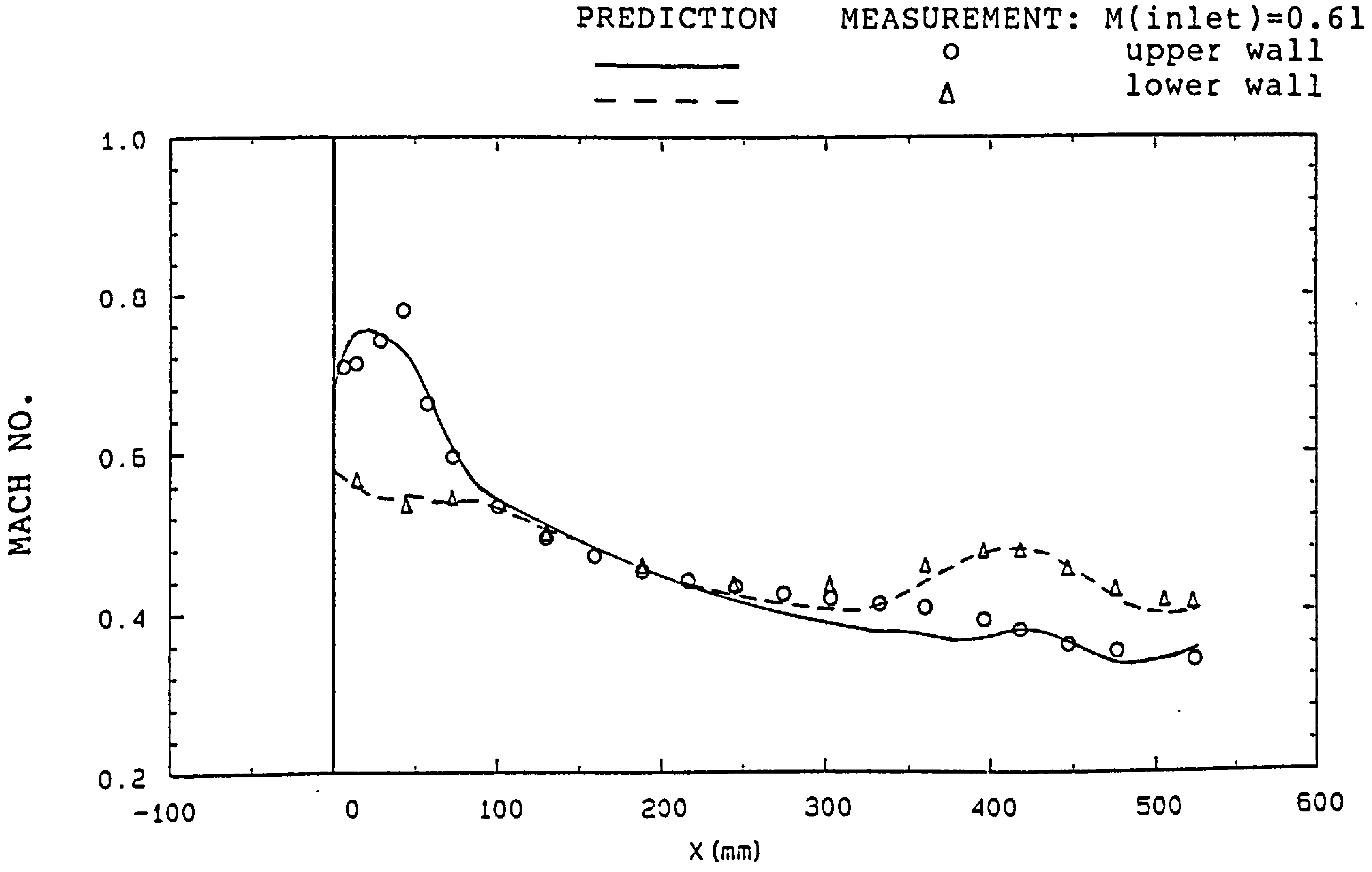

FIG. 5-9 MACH NUMBER DISTRIBUTIONS (DUCT N)

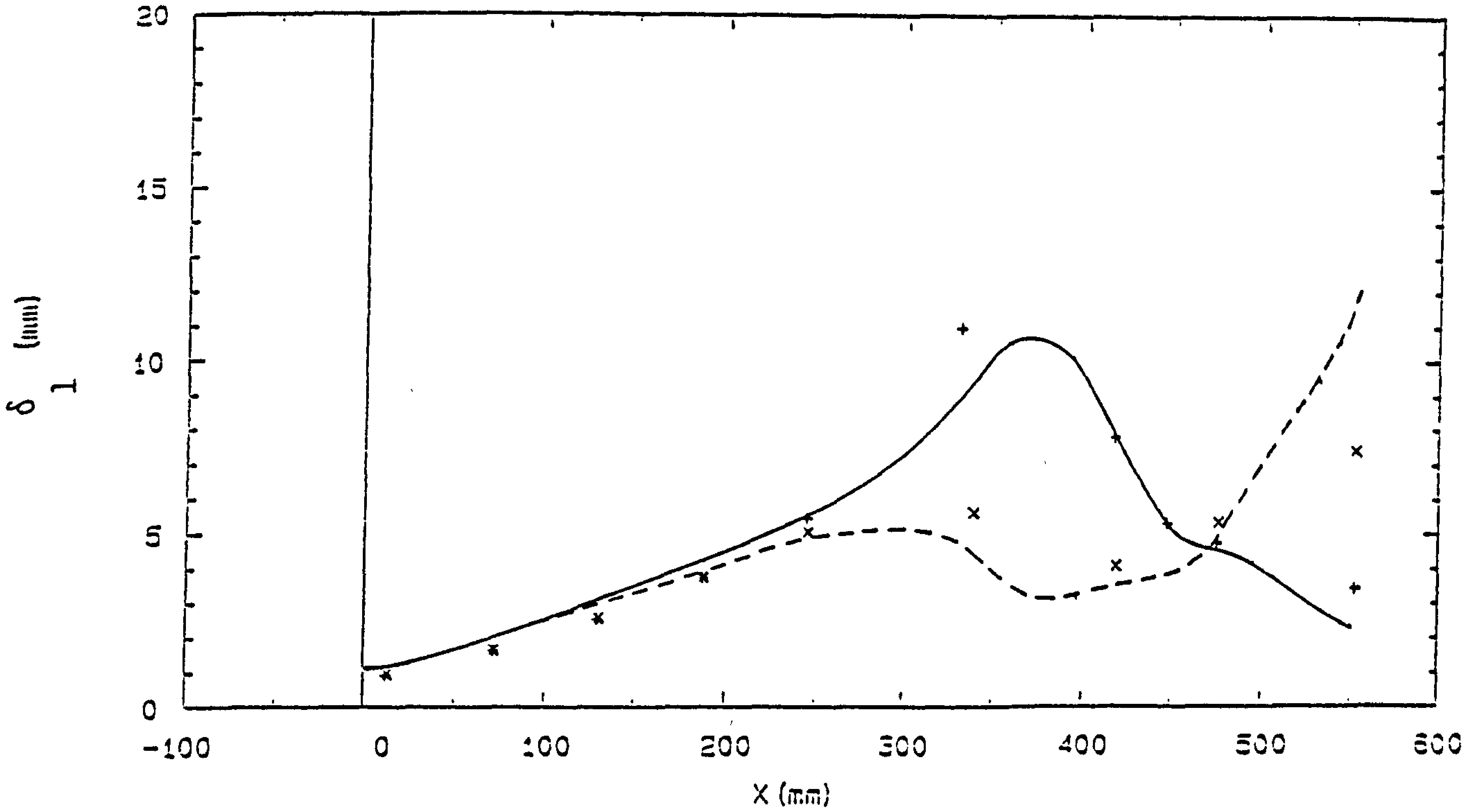

FIG. 5-10 DISPLACEMENT THICKNESS DISTRIBUTIONS (DUCT M)

PREDICTION	MEASUREMENT: M(inlet)=0.15	
———	+	upper wall
– – – –	x	lower wall

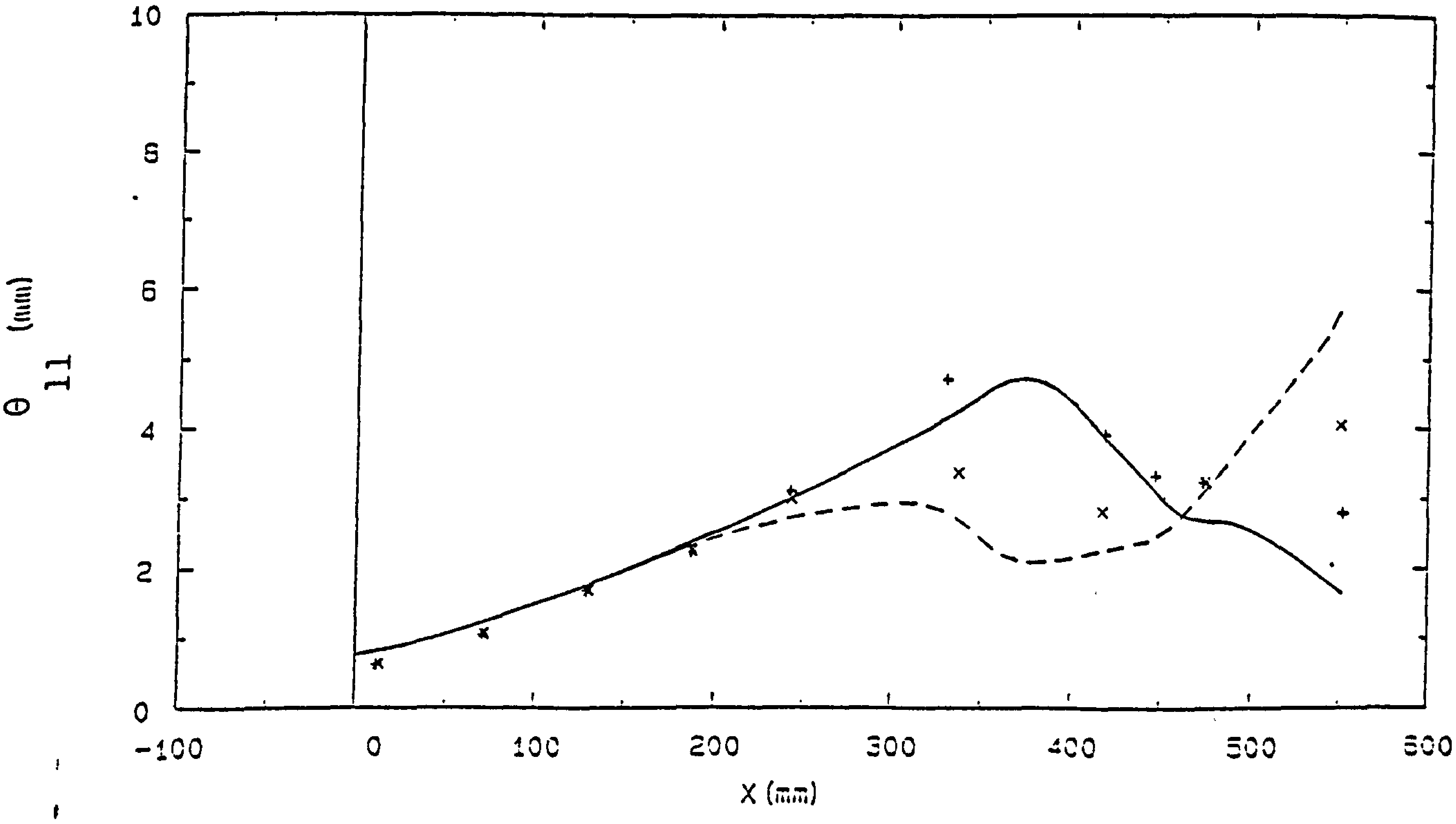

FIG. 5-11 MOMENTUM THICKNESS DISTRIBUTIONS (DUCT M)

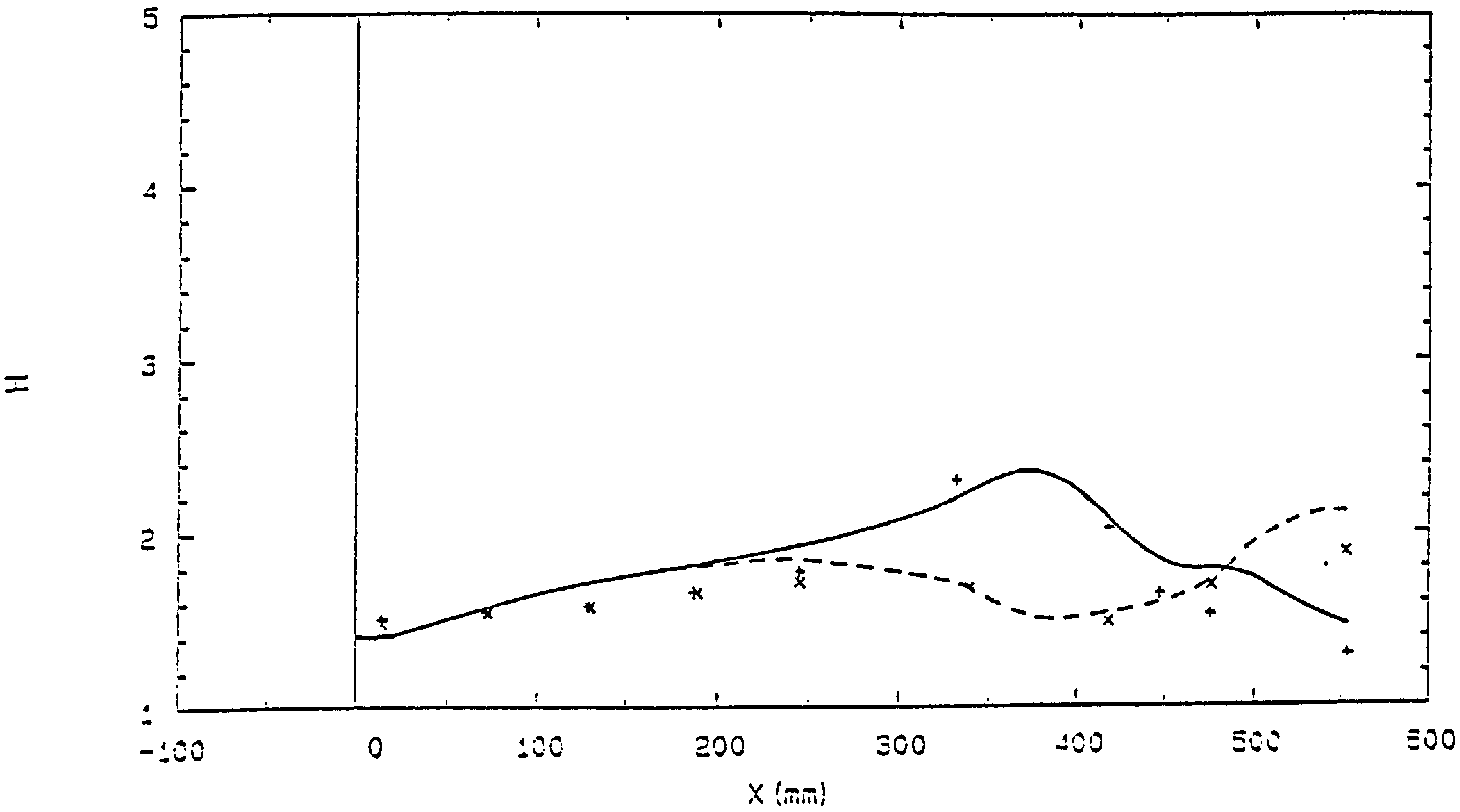

FIG. 5-12 SHAPE PARAMETER DISTRIBUTIONS (DUCT M)

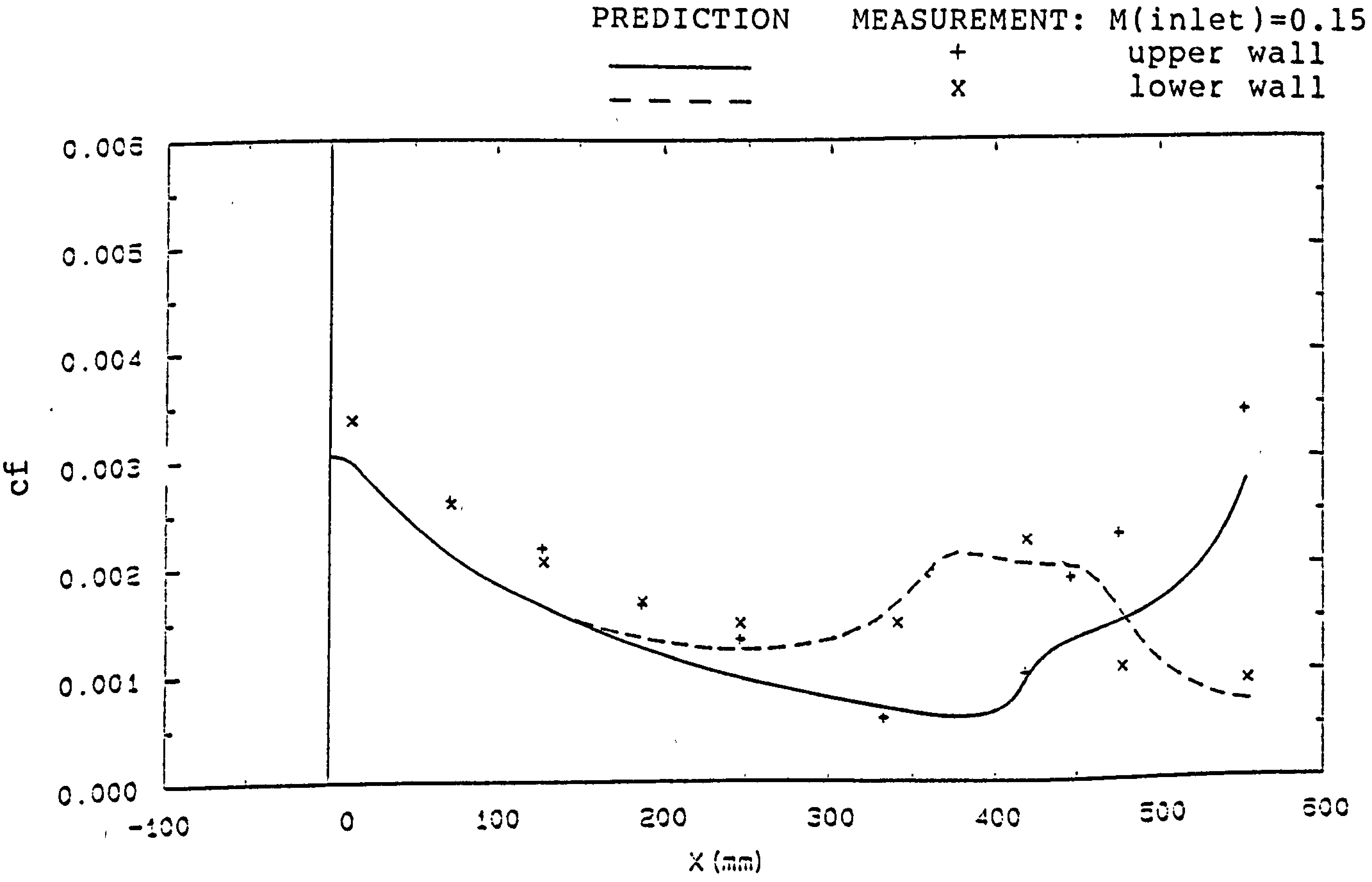

FIG. 5-13 SKIN FRICTION COEFFICIENT DISTRIBUTIONS (DUCT M)

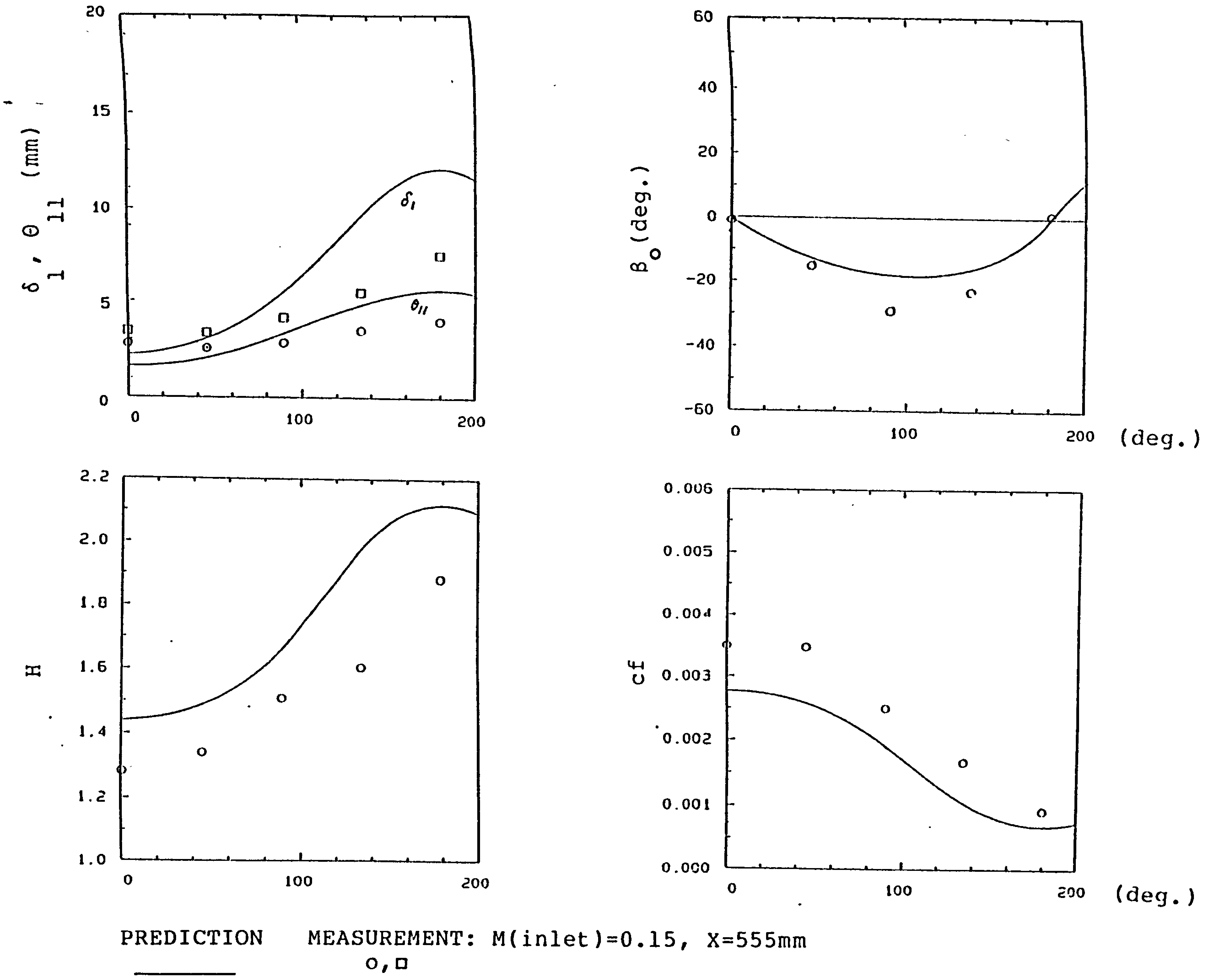

FIG. 5-14 CIRCUMFERENTIAL DISTRIBUTIONS OF BOUNDARY LAYER PARAMETERS AT THE ENGINE FACE (DUCT M)

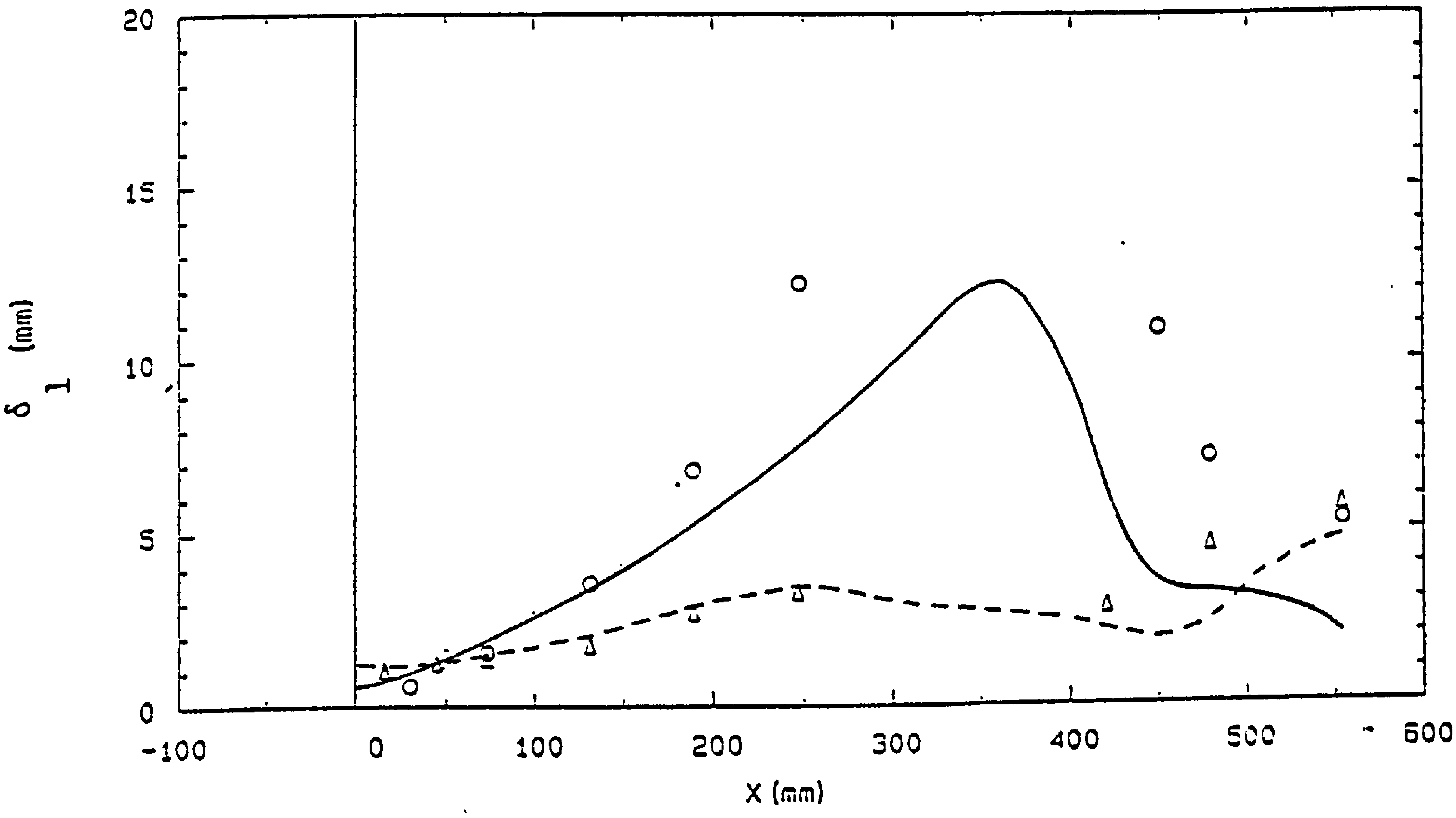

FIG. 5-15 DISPLACEMENT THICKNESS DISTRIBUTIONS (DUCT N)

PREDICTION	MEASUREMENT: M(inlet)=0.61	
———	○	upper wall
– – –	△	lower wall

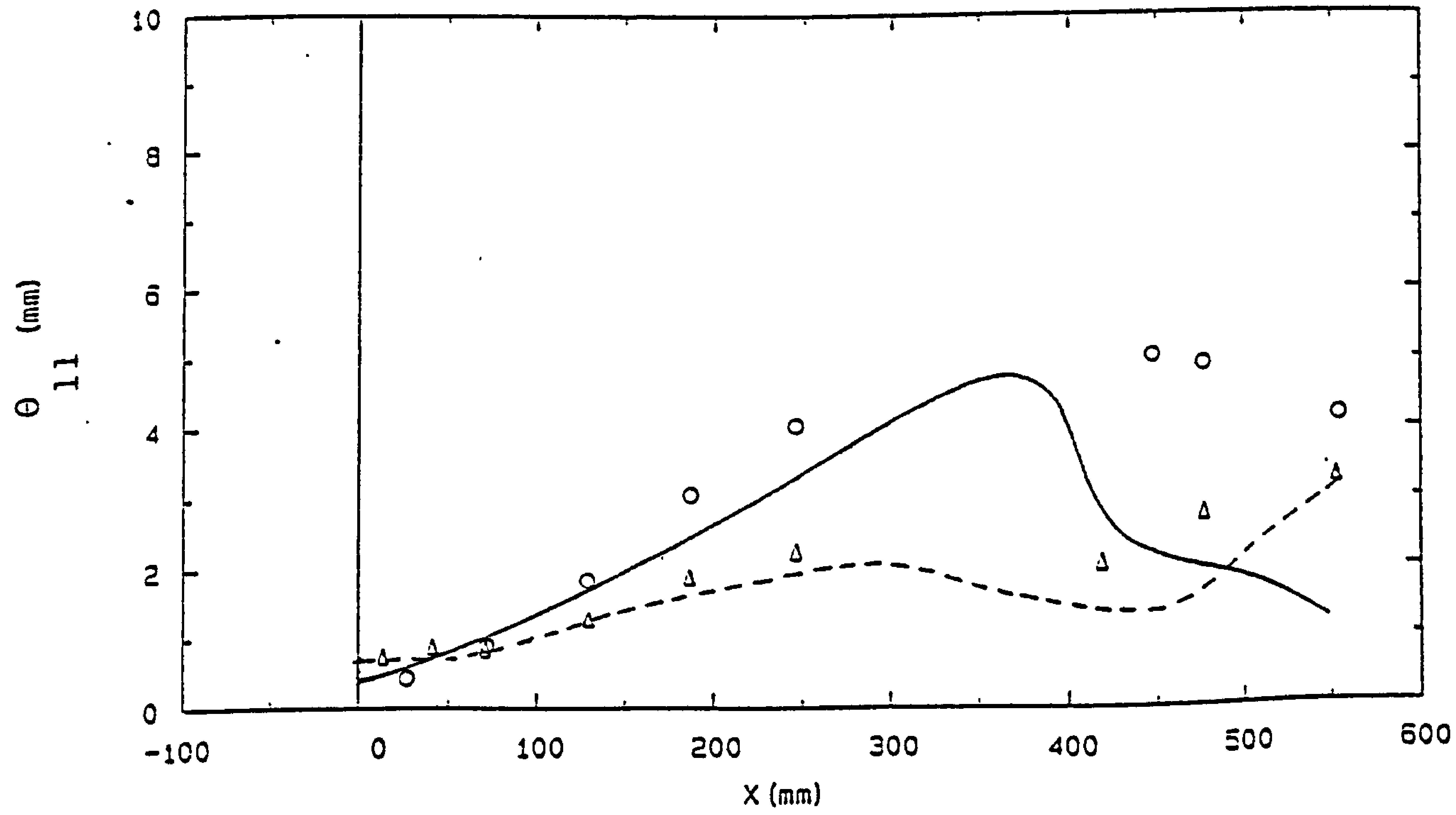

FIG. 5-16 MOMENTUM THICKNESS DISTRIBUTIONS (DUCT N)

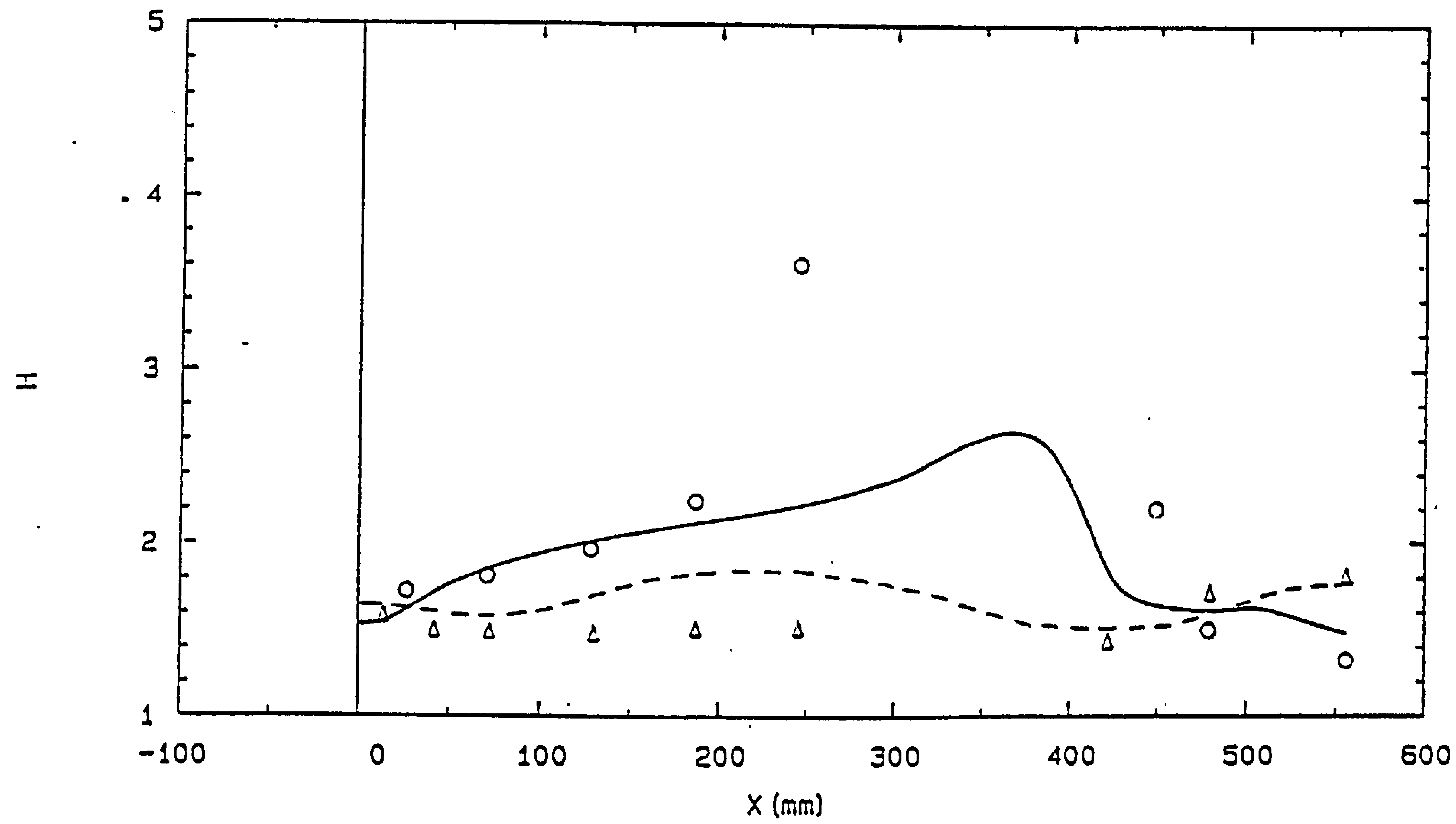

FIG. 5-17 SHAPE PARAMETER DISTRIBUTIONS (DUCT N)

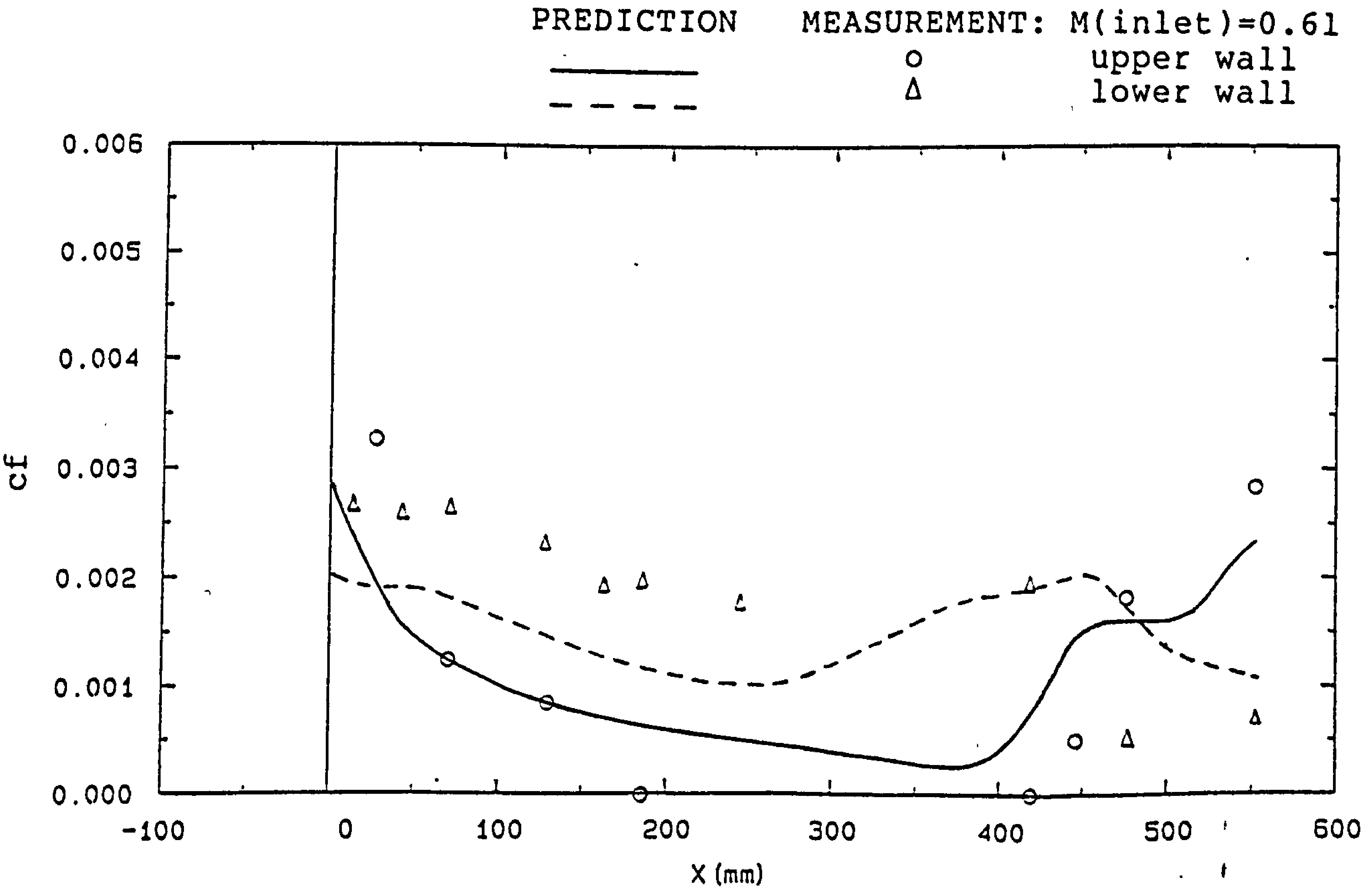

FIG. 5-18 SKIN FRICTION COEFFICIENT DISTRIBUTIONS (DUCT N)

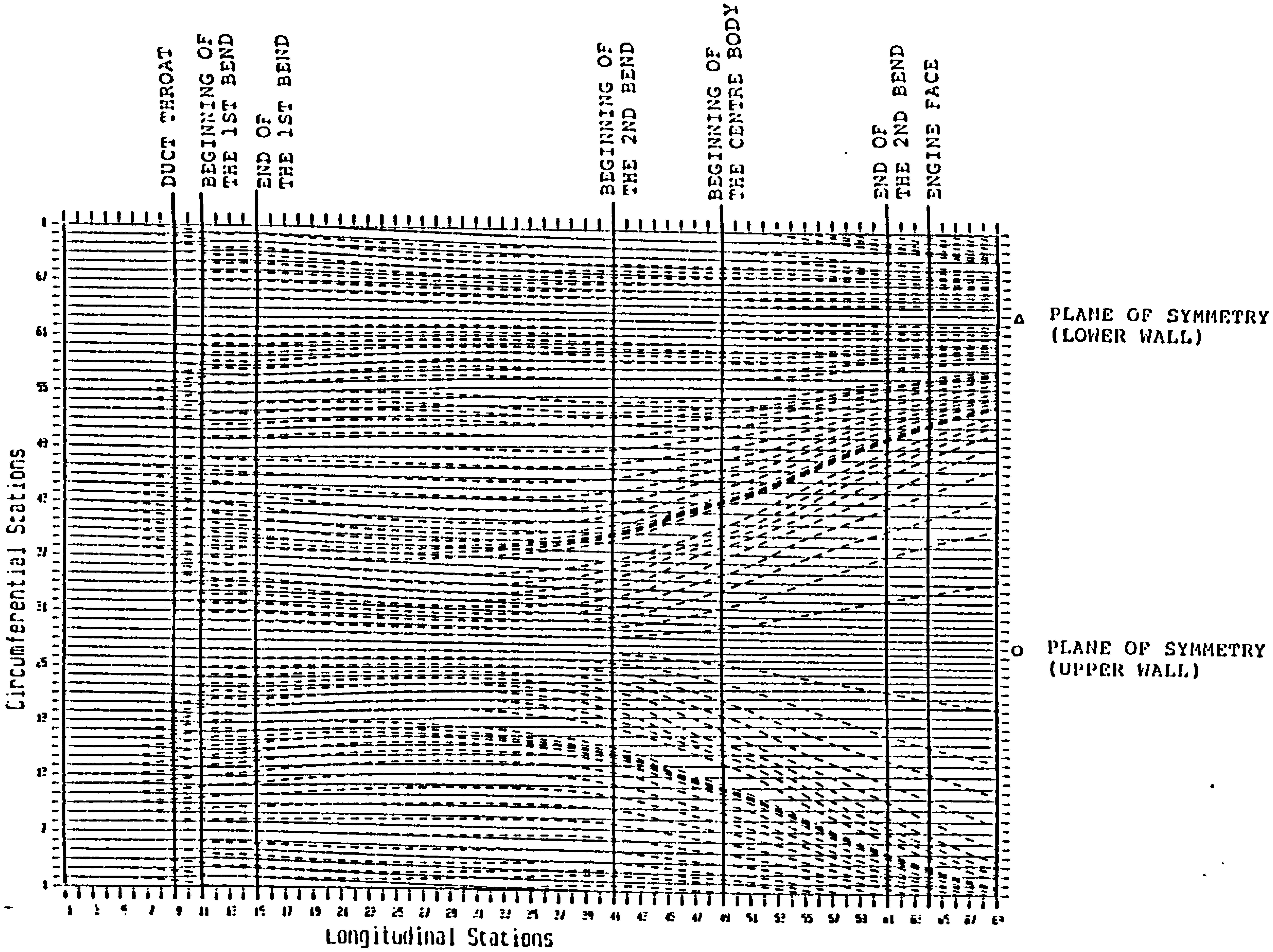

DUCT N, M_{inlet} =0.61 : ——— EXTERNAL STREAMLINES, _ _ _ SKIN FRICTION LINES

FIG. 5-19 STREAMLINE PATTERNS (DUCT N)

CHAPTER 6

CONCLUSIONS AND RECOMMENDATIONS FOR FURTHER WORK

CHAPTER 6 CONCLUSIONS AND RECOMMENDATIONS FOR FURTHER WORK

6.1 Conclusions

An open circuit static test rig and instrumentation system have been established in the aerodynamic laboratory of the University of Salford for the study of three-dimensional subsonic duct flow for both missile and aircraft applications. The rig is capable of mass flow rates and unit Reynolds numbers up to 5 kg/s and $2x10^7$/m respectively. Severe flow unsteadiness was initially experienced with this open circuit test facility. The problem was found to be caused by the inhalation of the ground vortex as a result of the proximity of the inlet to the ground. This problem was eventually solved by the use of a filter box which enclosed the inlet region of the rig.

Detailed flow measurements have been made in three different ducts designed as offset intakes to rear mounted gas turbine engines in missile applications. The duct offset is confined to a single plane, which is also the missile pitchwise plane and the plane of symmetry of the duct. Three ducts have been tested, each having different upstream bend geometries but identical downstream bend geometries, similar offsets and area distributions. The measurements were carried out at duct throat Mach numbers of nominally 0.15 and 0.6.

Care has been taken to ensure that a fully turbulent but thin boundary layer was established in the test duct inlet throughout the test speed range. This was necessary to avoid the uncertainty in the duct inlet boundary layer conditions which result from the natural transition.

Flow symmetry about the symmetry planes of the intake ducts was observed except in the case of Duct J where there was large scale flow separation.

Streamwise surface pressure distributions have clearly shown the effects of the duct bend, and the centre body which simulates the engine compressor face bullet. The surface pressure field offers an insight into the likely areas of difficulty within the flow passage. It is, however, unable to reveal clearly the region of flow separation in the complex three-dimensional internal flows.

Although boundary layer development in the plane of symmetry of each duct exhibits similarity to a two-dimensional boundary layer development, the plane of symmetry boundary layer flow contains strong flow convergence and divergence in the bend regions as a result of the transverse pressure gradients; this is clearly shown by the momentum balance and the surface oil flow patterns. The stabilizing and destabilising effects of the convex and concave surface of the bend, respectively, can be observed from the logarithmic velocity profiles.

From three-dimensional boundary layer measurements, various kinds of crossflow profiles including those similar to the Johnston and Mager types, and near separation and re-developing types were obtained. No bi-directional profiles were however encountered because of the long straight diffusing section which exists between the upstream and downstream bends in each duct. The effects of the re-direction of the flow by the upstream and downstream bends (i.e. sign reversal of the transverse pressure gradient) can be seen to have changed the direction of crossflow within the side wall boundary layers in the cases of Duct J and N. Significant crossflow within the boundary layer measured at the engine compressor face plane of each duct indicates the persistent effects of the transverse pressure gradient; the crossflow at the engine face contributed significantly to the swirl and distortion coefficients.

The duct flow features remain similar at low and high inlet speeds. The effects of compressibility at high inlet speed can be seen to have amplified the adverse conditions on the upper wall of each duct; the main cause could be attributed to the increase in streamwise pressure gradient immediately downstream of the first bend which results in the considerable thickening of the boundary layer thereafter. Owing to the small to moderate adverse pressure gradients on the lower wall of each duct, the boundary layer development remained largely unchanged with the increase in inlet speed, with the exception of the increase in shape factor and the decrease in local skin friction coefficient as a result of the compressibility effects. From the engine compressor point of view the viscous region becomes dominant at high speed, causing considerable total pressure loss and distortion.

The upstream bend geometry of the ducts is by far the most influential feature affecting the duct flow processes. Detailed evidence is presented in the forms of surface flow visualization and its interpretation indicating a firm trend towards three-dimensional separation as the upstream bend is increased in severity. The separation region embodies complex features which characterize three-dimensional boundary layer separation. These features are the critical points formed as the shear stress components of the boundary layer vanish at the surface. Critical points in the form of spiral focii, saddle points and attachment nodes were readily identifiable from the surface flow visualization. The most notable type is the spiral focus, which generally results in vortical flow springing from the surface. The effect of the centre body on ducts with flow separations can be seen to have imposed a re-attachment node point downstream of the separation region, which concludes the separation process. However, the re-developing boundary layer flow thereby introduced is most likely to be of high energy dissipation [D9] and the streamwise vortical flows induced as a result of the vortex type separation would certainly be continued further into the engine compressor. Topological analysis was carried out on the surface flow visualization thus enabling the spatial separation flow structure to be conjectured.

The method of Ahmed et al for the prediction of subsonic compressible flows in ducts of arbitrary three-dimensional geometry has been evaluated. The method is most appropriate to the treatment of high Reynolds number flows in which a significant inviscid core flow region may exist. The viscous flow in the wall region is assumed to be of the boundary layer type, and is represented by the three-dimensional integral method of Myring. The boundary layer and core flow regions are matched using the displacement surface method in which the boundary for the inviscid core calculation is taken to be the solid wall displaced inwards according to the local value of the displacement thickness.

The use of a general coordinate system based on the body surface, together with the method for obtaining the metric coefficients of the coordinate system from the Cartesian coordinates of the body surface, results in an extremely flexible computer program which enabled all the results contained herein, pertaining to various duct geometries, to be obtained with no changes to the program.

The prediction method is restricted to the treatment of attached flows. Comparisons of the calculated results with experimental data indicated that if separation is not imminent, the flow is most likely to be predicted with a high degree of accuracy. In regions where the flow is approaching separation, however, the predictions can be considerably in error. In addition, the prediction method does not support flow bifurcations or the presence of a body in the duct flow passages. Hence, the strong influence of the centre body on the duct flows in the present test cases had to be treated independently. The axisymmetric ring source panel method of Hess & Smith was used. Although this method produced reasonable correction factors including elliptic effects of the centre body, the results of the comparisons have shown that the axisymmetric treatment appeared to be too idealized for the complex three-dimensional flow. In addition, the favourable effect of the centre body on the diffusing duct flows can be seen to have introduced relaxing (non-equilibrium) type boundary layer flow in the engine face region which is likely to present a problem for the integral boundary layer prediction method.

Despite the aforementioned limitations, the prediction method has demonstrated the capabilities of predicting flows in ducts with severe geometries and of locating problem areas in flow passages. It is also believed that the method is most likely to perform better on conventional aircraft intakes with ducts usually of moderate offsets and geometries.

6.2 Recommendations for further work

Although the present instrumentation and data acquisition systems are well established for future research work, the dependency of the system on main frame computing facilities could in many circumstances lead to situations beyond the researcher's control. Hence, experimental progress could be hindered. An independent micro-computer system devoted to the test rig alone should be considered. Once such a system is established, the automation of the boundary layer traversing process should then become easy. It may take some time to develop such a system and the software. However in order to collect and process much more data than has been obtained in the present measurements, it will eventually save a considerable amount of time.

In the present work, intake ducts with only single plane offset were studied. Ducts with multiplane offsets are also common in aircraft intake systems as well as in other industrial installations; therefore these should also be studied. Results of the present investigation should be used to provide guide lines on the order of duct offset, the type of bend geometry and the appropriate area distribution such that large scale separation could be avoided in future ducts to be designed for investigation. Three-dimensional boundary layers with bi-directional cross-flow profiles could be obtained by minimizing the transition distance between opposite bends, therefore enabling bi-directional cross-flow models to be tested.

The present work considered only intake ducts subjected to uniform inlet conditions. The effects of non-uniform inlet conditions such as those produced by aircraft at high angles of incidence, side-slip, gust, etc. on the internal flow should be investigated. The experimental results could be used to check the effectiveness of the rotational core flow formulations in the prediction method.

Turbulence measurements should be carried out at some stage to obtain the Reynolds stress fields, in particular the $-\overline{u'v'}$ and the $-\overline{w'v'}$ shear stress vector components within boundary layers. The results should offer confirmation of the type of turbulence models to be adopted if a differential boundary layer method is to replace the integral method in the prediction method.

The prediction method excludes the treatment of ducts having cross-sections with sharp corners. The lack of this treatment accounts for some of the disagreements with experiment which were apparent when the code was used to predict flow in a military aircraft intake duct with square to circular cross-section transition [C12]. Ducts with square cross-section are also common in industrial installations and air-conditioning systems owing to their simplicity in construction. Therefore, corner flow treatment should be included at some stage and a differential boundary layer method with appropriate turbulent modeling is certainly required to produce good results.

Further, in order to increase the versatility of the prediction method, ways should be explored of extending the method to flow prediction in bifurcating ducts and flow passages with bodies such as the centre body and other flow conditioning devices.

Separation in three-dimensional flows presents major difficulties in prediction methods. Major efforts are certainly required to extend the present method to be able to calculate the type of complex three-dimensional separations encountered in this work. Although the problem provides an interesting challenge, it was of secondary importance here as the prime objective was to design intake ducts in which such separation is avoided. In the present method, the onset of separation can be used as a design boundary to be avoided where possible in the interests of low losses and good profiles of total pressure. For near separation regions where boundary layers have high values of H, the accuracy of the predictions in some cases will most probably be improved by using Coles law of the wall plus wake for the streamwise velocity profiles and the extension of Green's lag-entrainment relationship for calculating the entrainment coefficient [A26]. In small confined separations, boundary layer flows can be treated by the use of inverse methods such as the FLARE approximation of Williams [A1]. This would involve neglecting the $U_e \partial U_e/\partial s$ term and the specification of displacement thickness followed by an inverse solution of the other boundary layer parameters.

APPENDICES

Appendix A

Crossflow models

a) Linear inviscid model

Inviscid analysis of Squire, Winter & Hawthorne (1950-51) states that if velocity u is constant along the streamline, the change in streamwise vorticity between two stations is given by

$$\omega_{s2} - \omega_{s1} = -2\alpha\partial u/\partial\zeta \tag{A-1}$$

where α is the flow turning and ω_s is the streamwise vorticity. For flow with initially zero streamwise vorticity, negligible normal velocity w and spanwise gradient $\partial w/\partial n$ (see Fig. A-1), Equation (A-1) reduces to

$$\partial v/\partial\zeta = 2\alpha\partial u/\partial\zeta \tag{A-2}$$

If a boundary condition v=0 at $u=U_e$ is imposed then integration of Equation (A-2) gives an alternative crossflow model

$$v/U_e = -2\alpha(1-u/U_e) \tag{A-3}$$

b) Johnston's triangular model

Johnston (1960) obtained a result similar to Equation (A-3) for the outer portion of the boundary layer. For the inner portion he suggested the collateral (constant angle) flow condition, which also includes the allowance for finite velocity defect. Hence a triangular representation resulted (Fig. A-2)

$$v/U_e = \begin{cases} u/U_e \tan\beta_o & \text{Region I} \\ A(1-u/U_e) & \text{Region II} \end{cases}$$

where β_o is the limiting streamline angle and

$$A = -2u^2 \int_0^\alpha d\alpha/u^2$$

if u equals a constant along the streamline,

$$A = -2\alpha$$

c) Mager's model

Mager (1952) adopted a parabolic type crossflow representation (Fig. A-2),

$$v/U_e = u/U_e (1-\zeta/\delta)^2 \tan\beta_o$$

For compressible flow it is assumed that this representation may be generalized as

$$v/U_e = u/U_e (1-z/z_\delta)^2 \tan\beta_o$$

where $z = \int_0^\zeta (\rho/\rho_e)\, d\zeta$

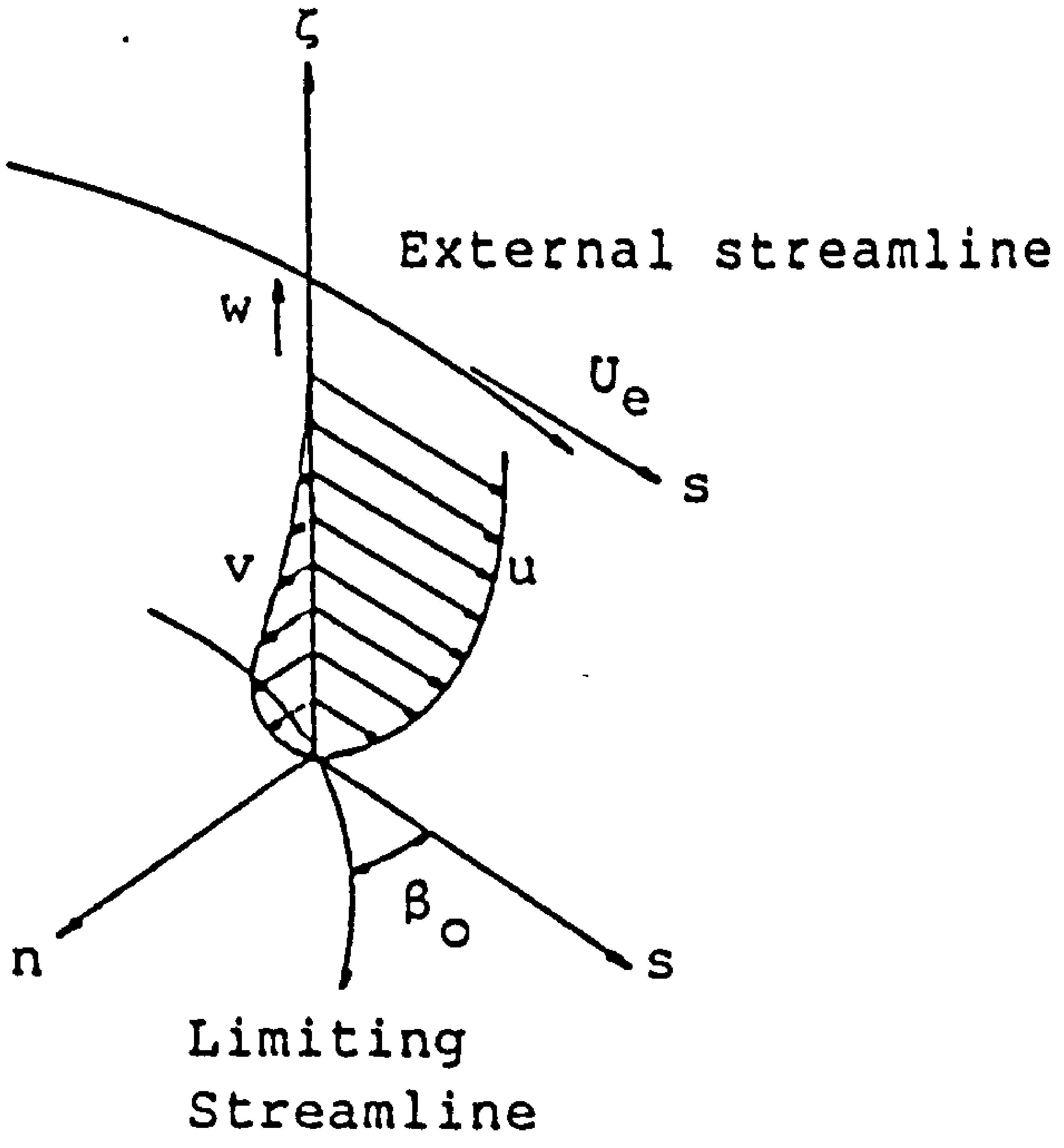

FIG. A-1 STREAMLINE COORDINATES AND UNI-DIRECTIONAL CROSSFLOW

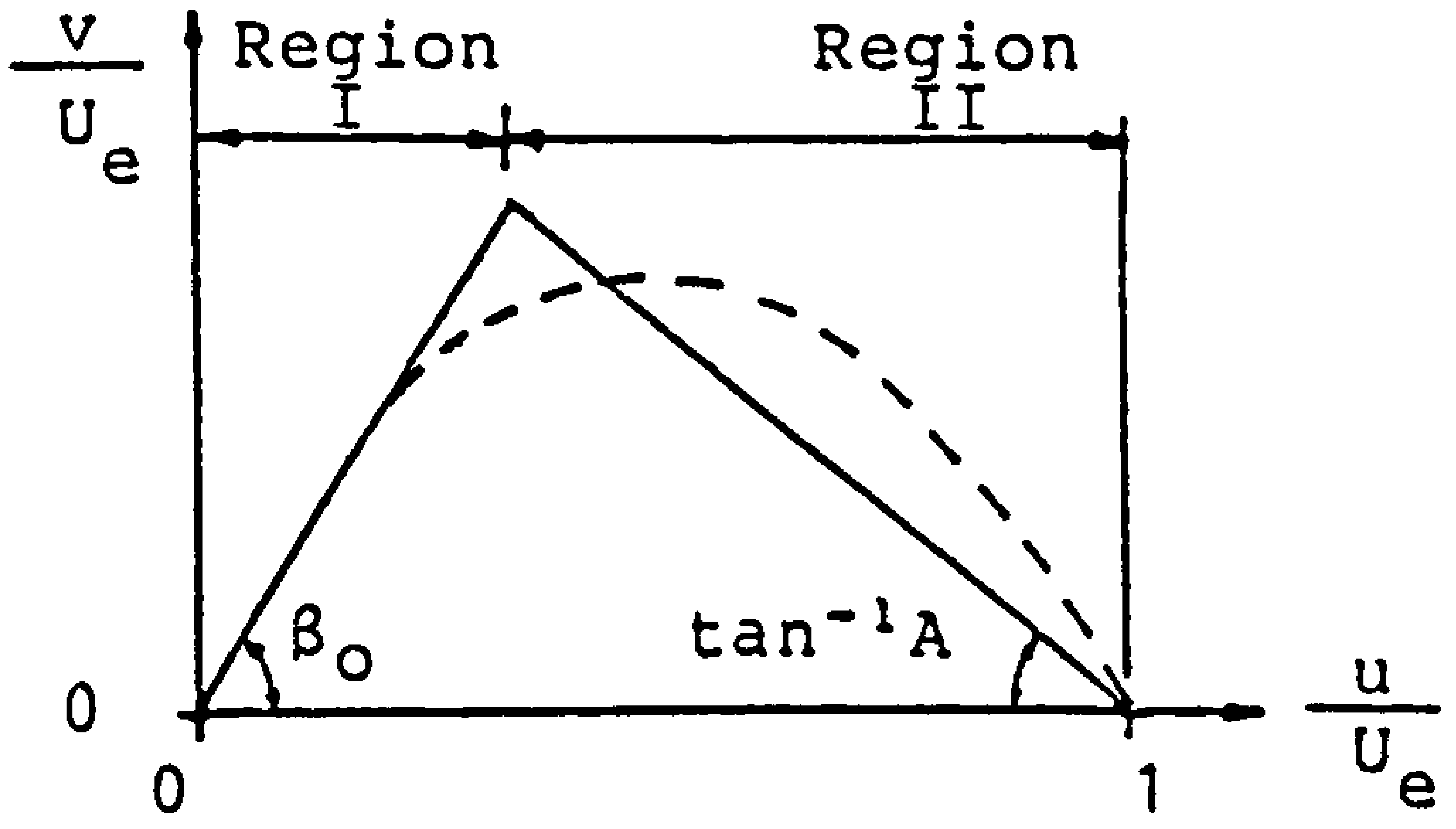

FIG. A-2 CROSSFLOW POLAR PLOT
——— JOHNSTON
- - - MAGER

Appendix B

Critical points in three-dimensional flow separations and various kind of vortex type flow separations

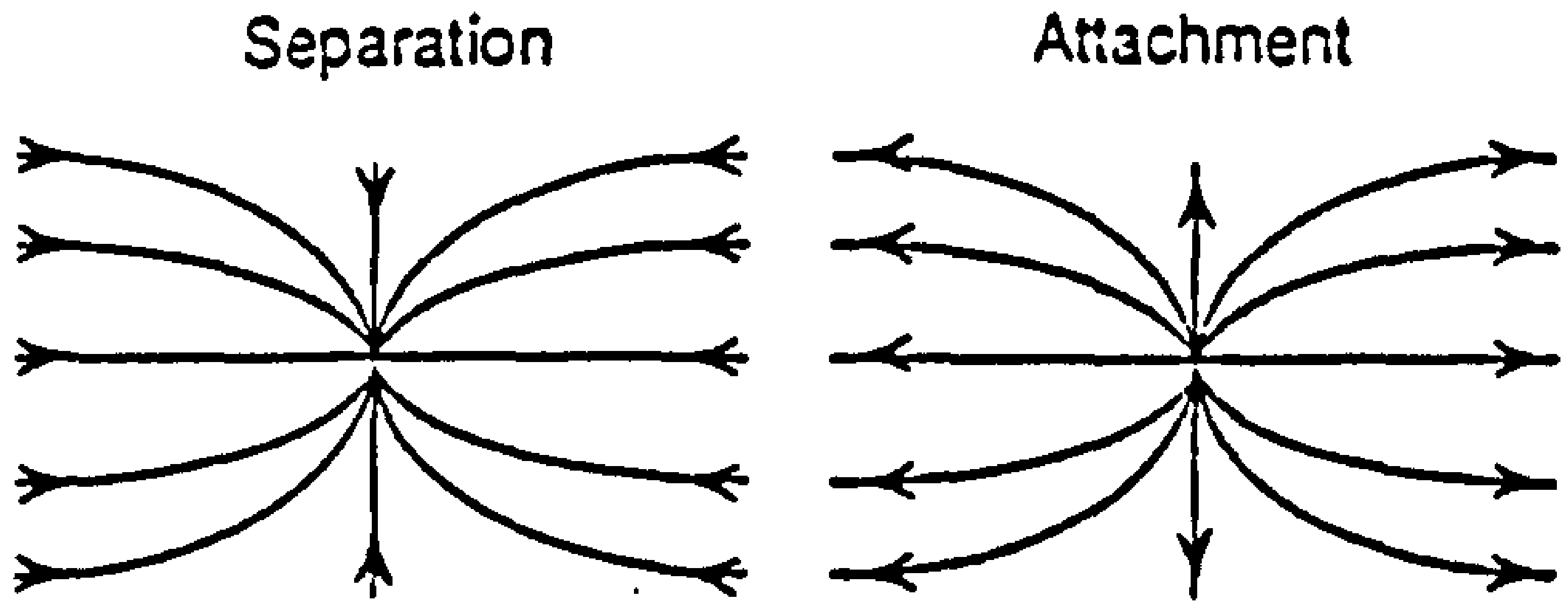

a) Nodal points

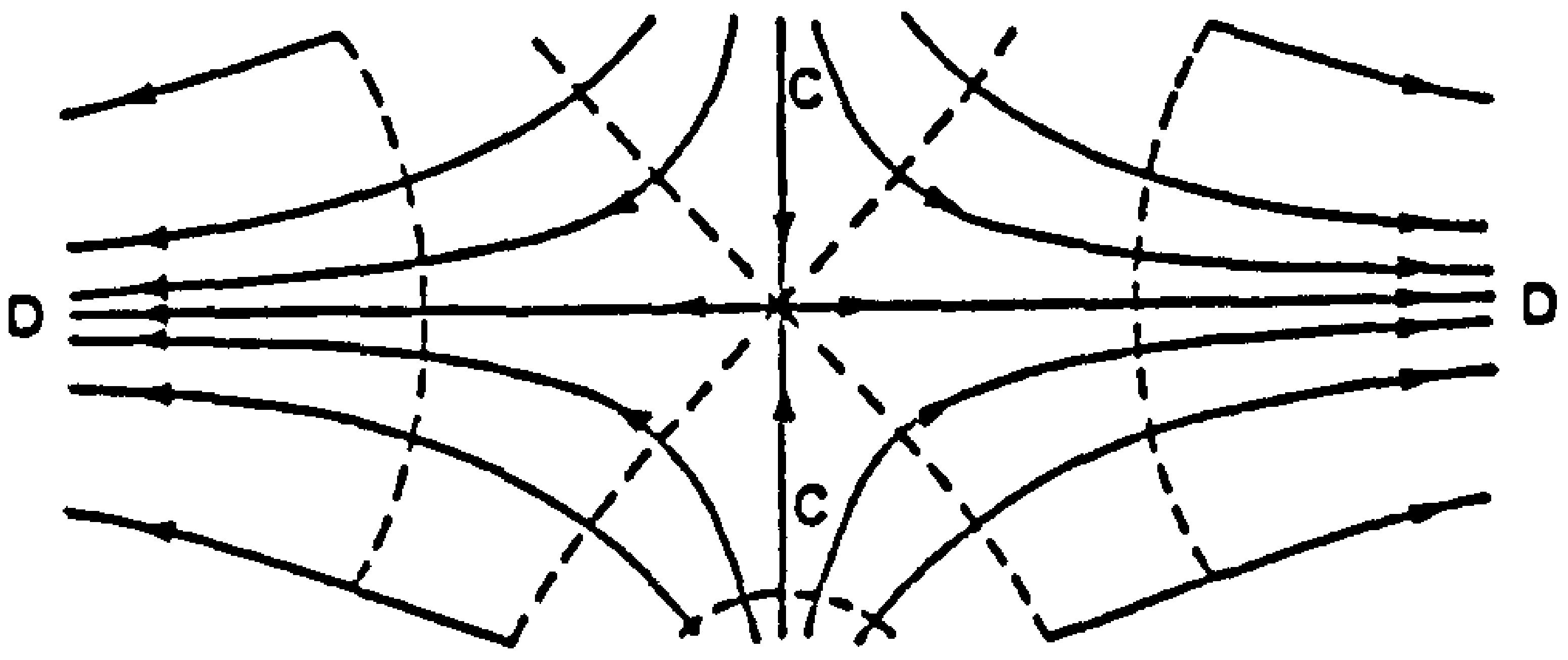

b) Saddle point

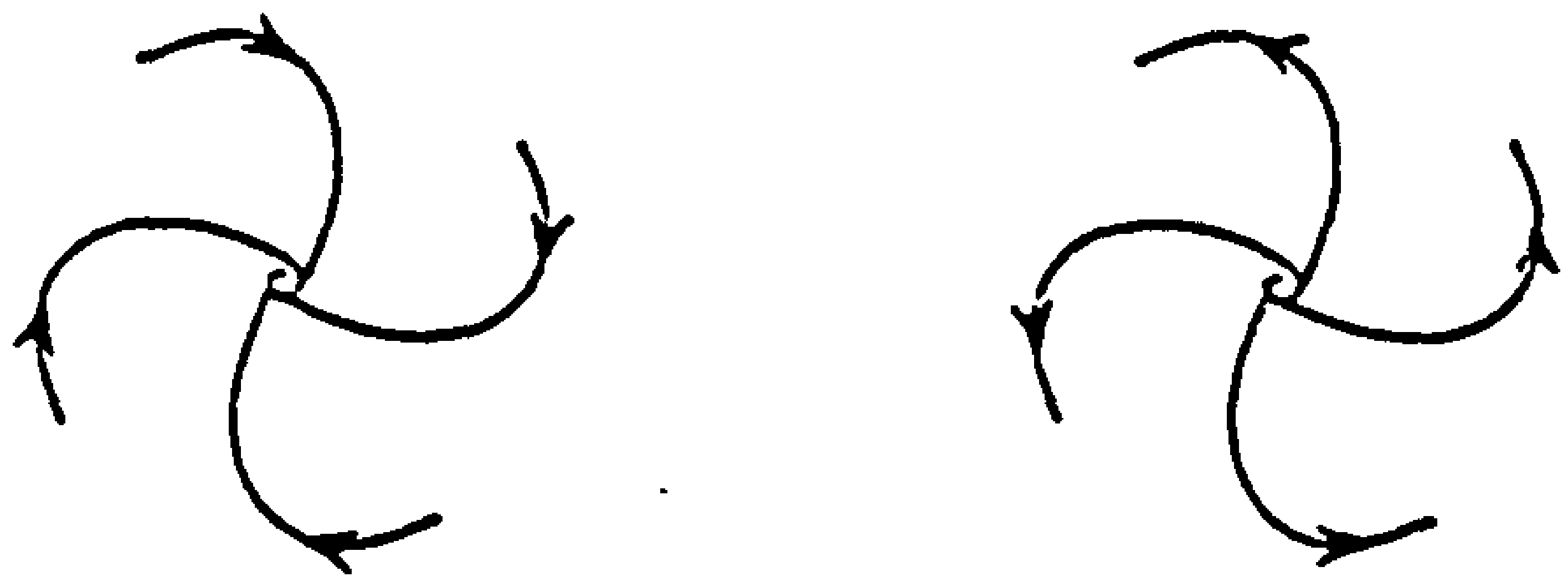

c) Spiral foci

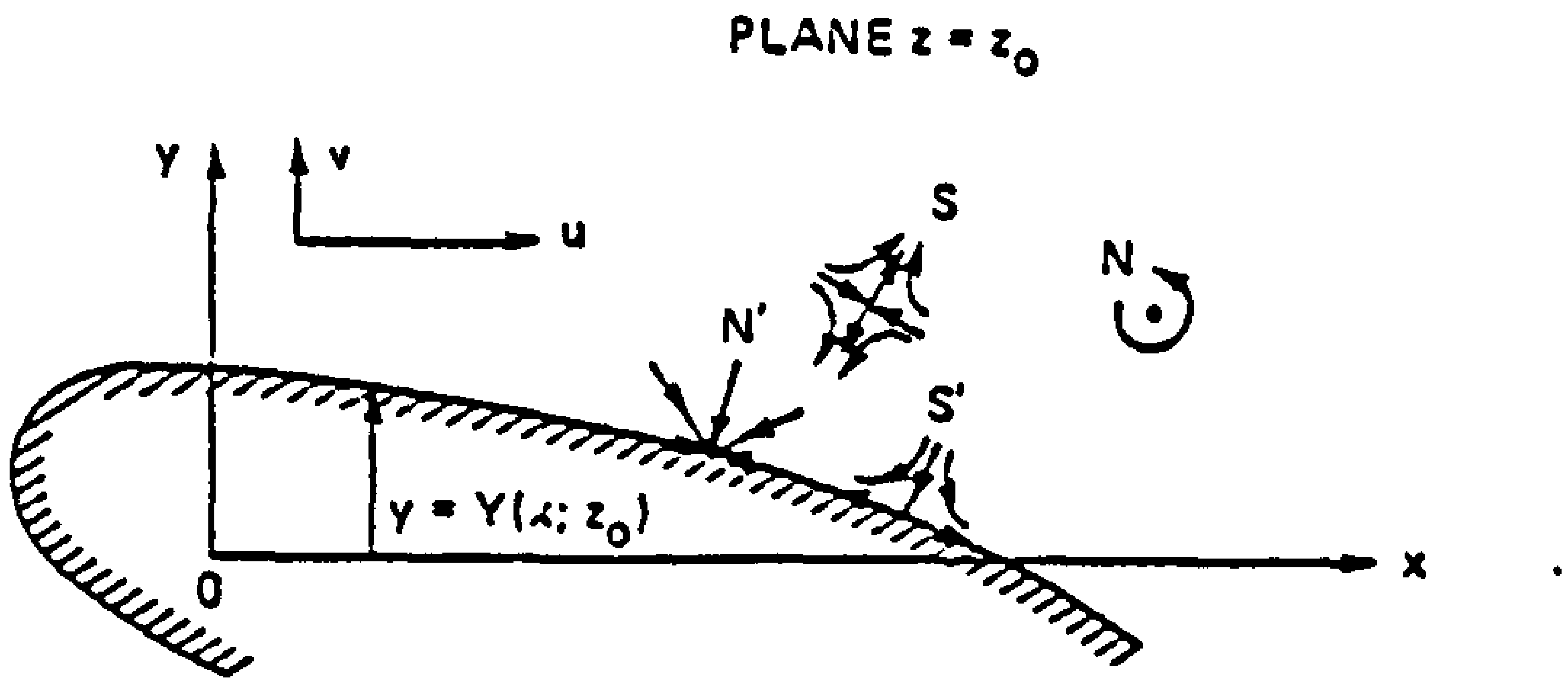

d) Critical points in cross section of flow [ref.F3]
N-node, N'-half node
S-saddle, S'-half saddle

FIG. B-1 CRITICAL POINTS [ref.F7]

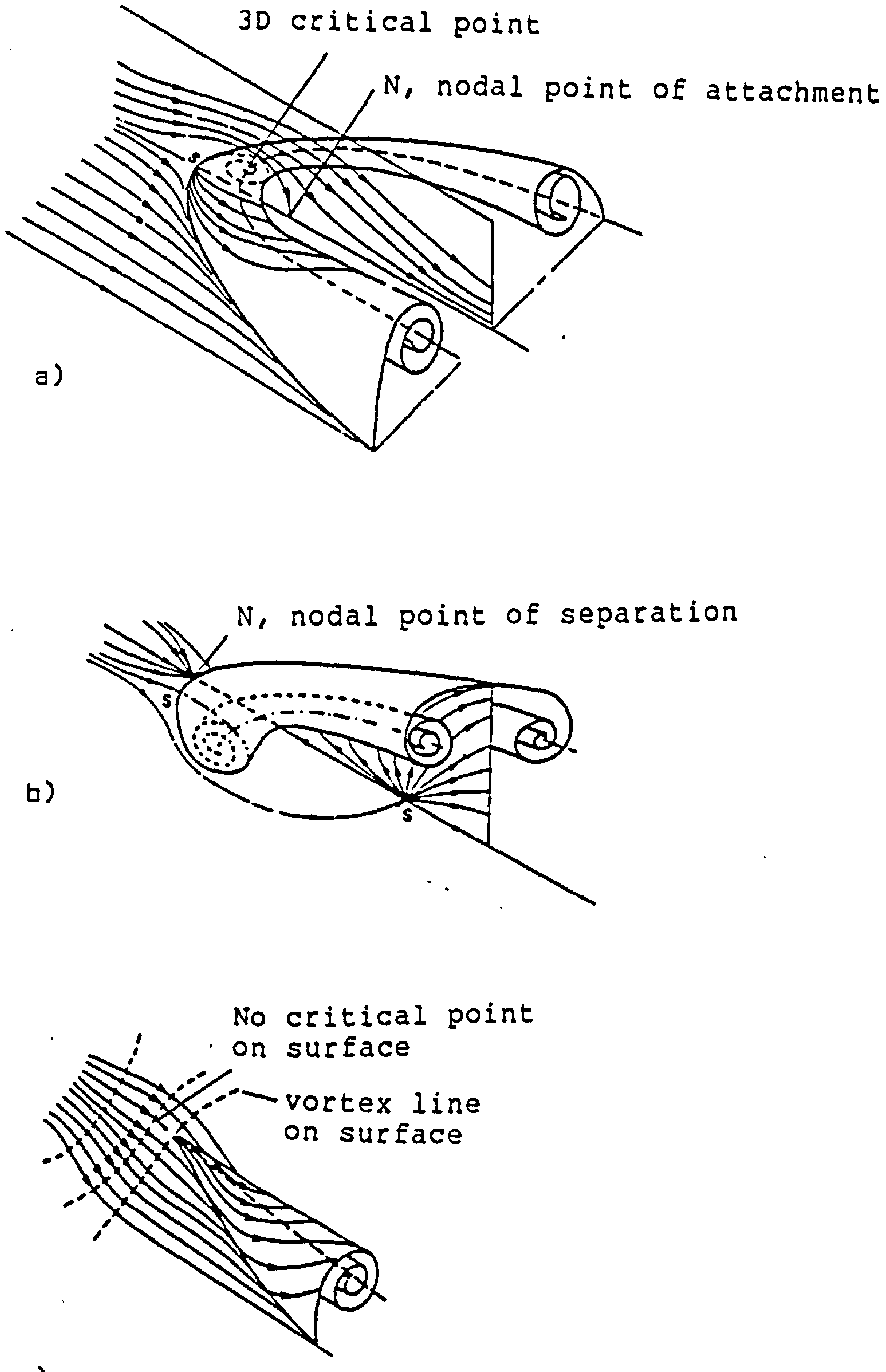

FIG. B-2 VORTEX TYPE FLOW SEPARATIONS [ref.F11]
a) & b) global types
c) local or open type
N-node, S-saddle

Appendix C

Axisymmetric ring source panel method of Hess & Smith

Consider Fig. C-1a. The potential φ_{ij} and the corresponding axial and radial velocity components at the control point i due to the thin ring source j of radius a and unit strength located at x=b are

$$\varphi_{ij} = - \int_{-\pi}^{\pi} (a/r_{ij})\, d\psi \qquad \text{(C-1)}$$

$$Vx_{ij} = -\partial\varphi/\partial x = 2a \int_{0}^{\pi} [\ (x-b)/r_{ij}^{3/2}\ ]\ d\psi \qquad \text{(C-2)}$$

$$Vy_{ij} = -\partial\varphi/\partial y = 2a \int_{0}^{\pi} [\ (y-a*\cos\psi)/r_{ij}^{3/2}\ ]\ d\psi \qquad \text{(C-3)}$$

where $r_{ij}^2 = (x-b)^2 + y^2 + a^2 - 2a*y*\cos\psi$

Integrals of Equations (C-2) and (C-3) can be written in terms of complete elliptic integrals thus enabling the velocity components to be represented by power series in terms of a, x and y [C6].

Equations (C-2) and (C-3) are to be integrated numerically for a ring source panel of finite length and special treatments are required for the case when i=j which are detailed in [C7].

The required source strengths (σ_j) in order to satisfy the prescribed boundary conditions are obtained by solving the system of linear equations:

$$\sum_{j=1}^{N} A_{ij}\,\sigma_j = -\underline{n}_i \cdot \underline{V}_\infty + F_i \qquad i=1,\ldots N$$

where

$A_{ij} = \underline{n}_i \cdot \underline{V}_{ij}$

$\underline{n}_i = -\sin\vartheta\underline{i} + \cos\vartheta\underline{j}$ (unit normal to panel)

$\underline{V}_{ij} = Vx_{ij}\underline{i} + Vy_{ij}\underline{j}$

N is the number of ring source panels

ϑ is the slope angle of the panel

$\underline{V}_{\infty}$ is the onset flow

F_i is the prescribed normal velocity

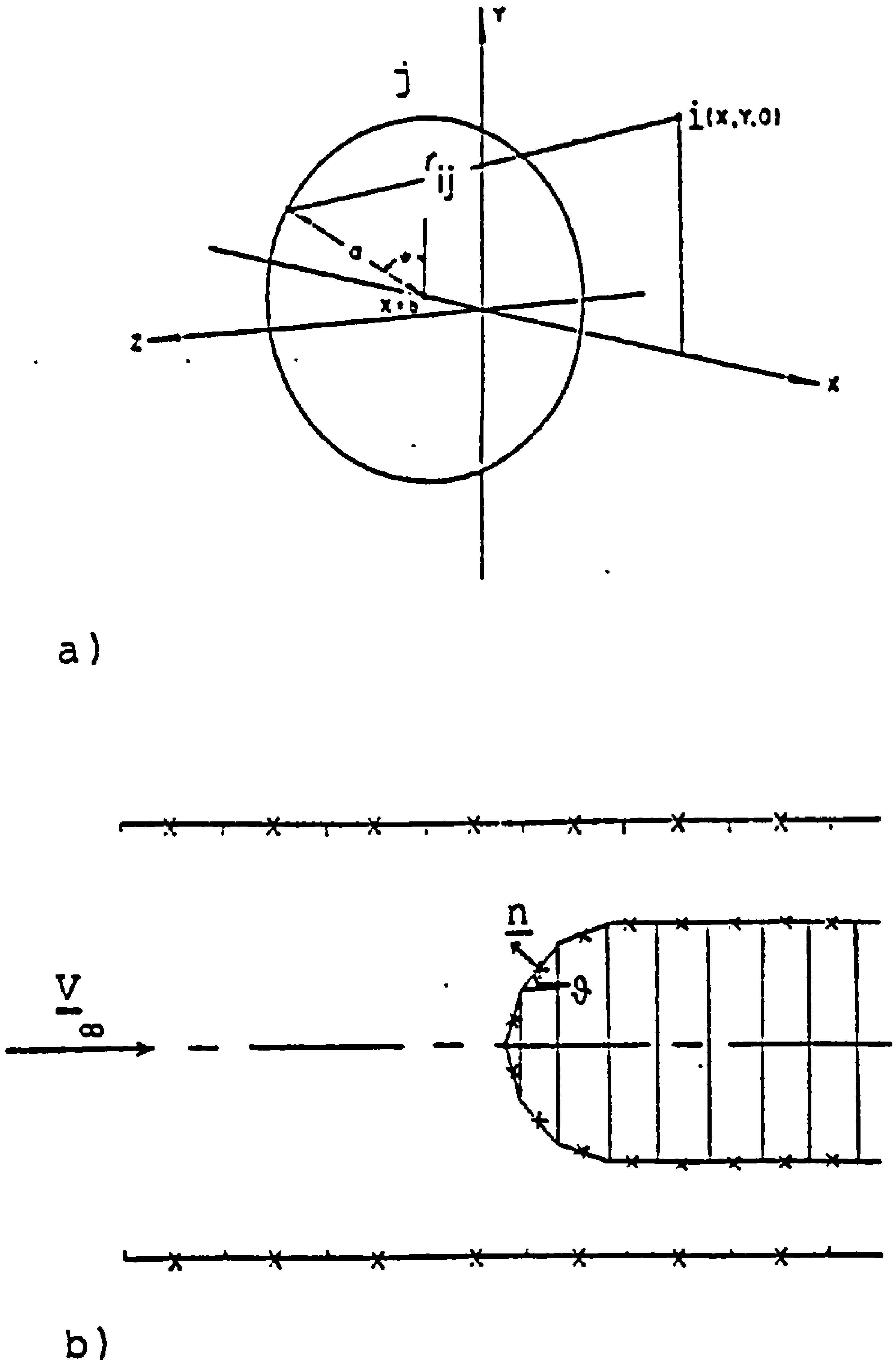

FIG. C-1 RING SOURCE PANEL METHOD

REFERENCES

References

A. General

1. Bradshaw, P., Cebeci, T. & Whitelaw, J.H.
   Engineering calculation methods for turbulent flow.
   Academic Press, 1981.

2. Bryer, D.W. & Pankhurst, R.C.
   Pressure-probe methods for determining wind speed and flow directions.
   NPL, Dept. of Trade & Industry,
   HM stationary office, 1971.

3. Dolan, F.X. & Runstadler, P.W.
   Pressure recovery performance of conical diffuser at high subsonic Mach numbers.
   NASA CR-2299, 1973.

4. Dudzinski, T.J. & Krause, L.N.
   Flow direction measurement with fixed position probes.
   NASA TM X-1904, 1969.

5. Fraser, C.J.
   The assessment of boundary layer two-dimensionality.
   Aero. J., vol.90, p.41, 1986.

6. Gibbings, J.C., Goksel, O.T. & Hall, D.J.
   The influence of roughness trips upon boundary layer transition, Part 1: Characteristics of wire trips.
   Aero. J., vol.44, p.289, 1986.

7. Goldstein, R.J.
   Fluid mechanics measurements.
   Hemisphere, 1983.

8. Hawthorne, W.R.
   Secondary circulation in fluid flow.
   Proc. Roy. Soc., A206, p.374, 1951.

9. Howatson, A.W., Lund, P.G. & Todd, J.D.
   Engineering tables and data.
   Chapman & Hall, 1972.

10. Kuchemann, D.
    The aerodynamics design of aircraft.
    Pergamon Press, 1978.

11. Laws, E.M. & Livesey J.L.
    Flow through screens.
    Ann. Rev. Fluid Mech., vol.10, p.247, 1978.

12. Ma, S.
A study of ground vortex.
Acta Aero. et Astro. Sinica, vol.10, p.a293, 1989.

13. MacMillan, F.A.
Experiments on pitot-tubes in shear flow.
ARC R&M 3038, 1956.

14. Milne-Thomson, L.M.
Theoretical aerodynamics.
4th ed., Dover, 1973.

15. Motycka, D.L. & Walter, W.A.
An Experimental investigation of ground vortex formation during reverser engine operation.
AIAA/SAE 11th Propulsion Conference, 1975.

16. Perkins, H.J.
The formation of streamwise vorticity in turbulent flow.
J. Fluid Mech., vol.44, p.721, 1970.

17. Poole, D.J.
Cartesian tensors in fluid mechanics.
Series in computational methods and fluid mechanics,
Maths., Aero. & Mech. Engg. Dept.,
Salford Univ., 1974.

18. Prandtl, L.
Essentials of fluid dynamics.
Blackie, 1952.

19. Rowe, M.
Measurements and computations of flow in pipe bends.
J. Fluid Mech., vol.43, p.771, 1970.

20. Sawyer, R.A.
Aerofoil design methods.
Series in computational methods and fluid mechanics,
Maths., Aero. & Mech. Engg. Dept.,
Salford Univ., 1973.

21. Schlichting, H.
Boundary layer theory.
6th, McGraw-Hill, 1968.

22. Scorer, R.S.
Environmental aerodynamics.
Ellis Horwood, 1978.

23. Squire, H.B. & Winter K.G.
The secondary flow in a cascade of aerofoil in a nonuniform stream.
J. Aero. Sci., vol.18, p.271, 1951.

24. Thompson, J.F., Warsi, Z.U.A. & Mastin, C.W.
Numerical grid generation:
Foundations & applications.
North-Holland, Elsevier, 1985.

25. Ward-Smith, A.J.
The flow and pressure losses in smooth pipe bends of constant cross-section.
Aero. J., vol.67, p.437, 1963.

26. Weir, J.
Incompressible turbulent boundary layer.
Series in computational methods and fluid mechanics,
Maths., Aero. & Mech. Engg. Dept.,
Salford Univ., 1975.

B. High Reynolds number duct flows & intake aerodynamics

1. Anderson, B.H.
Three-dimensional viscous design methodology for advanced technology aircraft supersonic inlet systems.
NASA TM-83558, 1984.

2. Anderson, B.H.
CFD application to subsonic inlet airframe integration.
VKI lecture series (88-04) on intake aerodynamics, 1988.

3. Bansod, P. & Bradshaw, P.
The flow in S-shaped ducts.
Aero. Quarterly, vol.23, p.131, 1972.

4. Guo, R.W. & Seddon, J.
An investigation of the swirl in an S-duct.
Aero. Quarterly, p.25, Feb., 1982.

5. Guo, R.W. & Seddon, J.
The swirl in an S-duct of typical air intake proportions.
Aero. Quarterly, p.99, May, 1983.

6. Guo, R.W. & Seddon, J.
Swirl characteristics of an S-shaped air intake with both horizontal and vertical offsets.
Aero. Quarterly, p.130, May, 1983.

7. Guo, R.W.
Monitoring parameters of swirling flow in S-shaped diffuser.
Acta Aero. et Astro. Sinica, vol.6, p.489, 1985.

8. Ho, S.S.H.
Wall pressure measurements in S-shaped intake ducts.
Internal Report FM/33/85,
Aero. & Mech. Engg. Dept., Salford Univ., 1985.

9. Ho, S.S.H., Myring, D.F. & Livesey, J.L.
Flow development in S-shaped intake ducts.
Cong. proc., vol.2, p.C228,
4th Asian Cong. of Fluid Mech., Hong Kong, 1989.

10. Ho, S.S.H., Noguchi, Y., Myring, D.F. & Livesey, J.L.
Three-dimensional flows in jet engine air intake ducts.
(in preparation)
Aero. J., 1990.

11. Leamer, P.C., Kennon, I.G.
Investigation of a 0.15 scale model of an
underfuselage normal-shock inlet.
NASA CR-3049, 1978.

12. Lin, Q. & Guo, R.W.
Vortex control investigation of swirl in
S-shaped diffuser.
Acta Aero. et Astro. Sinica, vol.10, p.A35, 1989.

13. Neumann, H.E., Povinelli, L.A. & Coltrin, R.E.
An analytical and experimental study of a short
S-shaped subsonic diffuser of a supersonic inlet.
AIAA paper 80-0386, 1980.

14. Seddon, J.
Understanding and countering swirl in S-ducts:
tests on the sensitivity of swirl to fences.
Aero. J. p.117, April, 1984.

15. Seddon, J. & Goldsmith, E.L.
Intake aerodynamics.
Collins, 1985.

16. Stocks, C.P. & Bissinger, N.C.
The design and development of
the Tornado engine air intake.
AGARD FD Panel Symposium, paper 10, 1981.

17. Stumpf, R., Neumann, H.E. & Giamati, C.C.
Dynamic distortion in a short S-shaped
subsonic diffuser with flow separation.
NASA TM-83412, 1984.

18. Tayler, A.M.K.P., Whitelaw, J.H. & Yianneskis, M.
Developing flow in S-shaped ducts,
1 - Square cross-section duct.
NASA CR-3550, 1982.

19. Tayler, A.M.K.P., Whitelaw, J.H. & Yianneskis, M.
Developing flow in S-shaped ducts,
2 - Circular cross-section duct.
NASA CR-3759, 1984.

20. Vakili, A.D., Wu, J.M., Bhat, M.K. & Liver, P.
Compressible flow in a diffusing S-duct with flow separation.
1st International Symposium on Transport Phenomena, Hemisphere, U.S.A., p.201, 1985.

21. Vakili, A.D., Wu, J.M., Liver, P., & Bhat, M.K.
Flow control in a diffusing S-duct.
AIAA paper 85-0524, 1985.

22. Warsop, M.D.
Research into S-bend diffusers for air breathing missile applications.
British Aerospace Rpt. TRGW 83/075, 1983.

C. Prediction methods for duct flows

1. Ahmed, N.M.A.
The prediction of three-dimensional flows in ducts of arbitrary geometries.
PhD thesis, Aero. & Mech. Engg. Dept., Salford Univ., 1984.

2. Ahmed, N.M.A., Konarski, S.E., Myring, D.F. & Livesey, J.L.
The prediction of flows in general three-dimensional passages using viscous/inviscid interaction.
IMechE paper C72/84, 1984.

3. Briley, W.R.
Numerical method for predicting three-dimensional steady viscous flows in ducts.
J. Comp. Physics, vol.14, p.8, 1974.

4. Hamed, A. & Abdullah, S.
Three-dimensional rotational flow in highly curved ducts due to inlet vorticity.
AIAA paper 78-146, 1978.

5. Hawthorne, W.R.
The applicability of secondary flow analysis to the solution of internal flow problems.
Fluid mechanics of internal flow, p.236, Sovran ed., Elsevier, 1967.

6. Hess, J.L.
Calculation of potential flow about bodies of revolution having axes perpendicular to the freestream direction.
J. of Aero. Sci., vol.29, p.726, 1962.

7. Hess, J.L. & Smith, A.M.O.
Calculation of potential flow about arbitrary bodies.
Progress in Aero. Sci., vol.8, p.1, Pergamon Press, 1967.

8. Konarski, S.E., Myring, D.F. & Livesey, J.L.
Viscous/inviscid interaction in general three-dimensional internal passages.
Conf. on numerical methods in laminar & turbulent flow, Canada, 1987.

9. Levy, R., McDonald, H., Briley, W.R. & Kreskovsky, J.P.
A three-dimensional turbulent compressible flow analysis for use with constructed coordinate systems.
AIAA paper 80-1398, 1980.

10. Levy, R., McDonald, H., Briley, W.R. & Kreskovsky, J.P.
Viscous primary/secondary flow analysis for use with nonorthogonal coordinate systems.
AIAA paper 83-16785, 1983.

11. Lin, Q. & Guo, R.W.
Governing equations and numerical analysis of compressible turbulent flow in an S-duct.
Acta Aero. et Astro. Sinica, vol.7, p.157, 1986.

12. Livesey, J.L., Myring, D.F., Noguchi, Y. & Ho, S.S.H.
Military aircraft intake computation: CC12 duct flow calculations.
British Aerospace Contract Order No. SG0552421, ref. 6750-AD1110,
Aero. & Mech. Engg. Dept., Salford Univ., 1987.

13. Pilatis, N.
Turbulent boundary layer prediction in three-dimensional ducts with core vorticity.
PhD thesis, Aero. & Mech. Engg. Dept., Salford Univ., 1986.

14. Patankar, S.V. & Spalding, D.B.
A calculation procedure for heat, mass and momentum transfer in three-dimensional parabolic flows.
Int. J. Heat and Mass Transfer, vol.19, p.1787, 1972.

15. Pratap, V.S. & Spalding, D.B.
Numerical computations of the flow in curved ducts.
Aero. Quarterly, vol.26, p.219, 1975.

16. Roberts, D.W. & Forester, C.K.
A parabolic computational procedure for three-dimensional flows in ducts with arbitrary cross-sections.
AIAA paper 78-143, 1978.

17. Stuart, A.R. & Hetherington, R.
The solution of the three-variable duct flow equations.
Conf. of Fluid Mech. of Turbomachinery, Penn. State Univ., 1970.

18. Vakili, A. & Wu, J.M.
Comparison of experimental and
computational compressible flow in a S-duct.
AIAA paper 84-0033, 1984.

D. Three-dimensional boundary layers

1. Ahmed, N.M.A., Konarski, S.E., Myring, D.F. &
Livesey, J.L.
Differential and integral predictions of
three-dimensional boundary layers:
a critical comparison.
Proc. BAIL III Conf., Dublin, 1984.

2. Bradshaw, P. & Pontikos, N.S.
Measurements in the turbulent boundary layer on
an 'infinite' swept wing.
J. Fluid Mech., vol.159, p.105, 1985.

3. Cooke, J.C. & Hall, M.G.
Boundary layers in three dimensions.
Progress in Aero. Sci., vol.2, p.221,
Pergamon Press, 1962.

4. East, L.F. & Hoxey, R.P.
Low-speed three-dimensional turbulent boundary data.
Part 1 & 2, ARC R&M No. 3653, 1969.

5. Fishcher, M.C. & Weinstein, L.M.
Turbulent compressible three-dimensional
mean flow profiles.
AIAA J., vol.12, no.2, p.131, 1974.

6. Ho, S.S.H.
Plane of symmetry boundary layer measurements in
S-shaped intake ducts.
Internal Report FM/40/87,
Aero. & Mech. Engg. Dept., Salford Univ., 1987.

7. Ho, S.S.H.
Three-dimensional boundary layer measurements in
S-shaped intake ducts.
Internal Report FM/42/87,
Aero. & Mech. Engg. Dept., Salford Univ., 1987.

8. Hornung, H.G. & Joubert, P.N.
The mean velocity profile in three-dimensional
turbulent boundary layers.
J. Fluid Mech., vol.15, p.368, 1963.

9. Horton, H.P.
Re-developing turbulent boundary layers behind
yawed separation bubbles.
Aero. Quarterly, vol.23, p.211, 1972.

10. Johnston, J.P.
On the three-dimensional turbulent boundary layer generated by secondary flow.
J. Basis Engg., Trans. ASME, vol.82, p.233, 1960.

11. Johnston, J.P.
Experimental studies in three-dimensional turbulent boundary layers.
Thermosci. Div. Rpt. MD-34
Mech. Engg. Dept.,
Stanford Univ., 1976.

12. Joubert, P.M., Perry, A.E. & Brown, K.C.
Critical review and current developments in three-dimensional turbulent boundary layers.
Fluid mech. of internal flow, p.210,
Sovran ed., Elsevier, 1967.

13. Mager, A.
Generalization of boundary layer momentum equation to three-dimension flows, including those of rotating systems.
NACA Rpt. 1067, 1952.

14. Myring, D.F.
An integral prediction method for three-dimensional turbulent boundary-layer in incompressible flow.
RAE Tech. Rpt. 707147, 1970.

15. Patel, V.C. & Baek, J.H.
Boundary layers in planes of symmetry,
Part I: Experiments in turbulent flows.
AIAA J., vol.25, p.550, 1987.

16. Patel, V.C. & Baek, J.H.
Boundary layers in planes of symmetry,
Part II: Calculations for laminar and turbulent flows.
AIAA J., vol.25, p.812, 1987.

17. Pierce, F.J.
The turbulent flow at the plane of symmetry of a three-dimensional turbulent boundary layer.
J. Basis Engg., Trans. ASME, vol.86, p.227, 1964.

18. Pierce, F.J. & Zimmerman, B.B.
Wall shear stress inference from two- and three-dimensional turbulent boundary layer velocity profiles.
J. Fluids Engg., Trans. ASME, vol.95, p.61, 1973.

19. Power, J.L.
Wall shear stress and mean-velocity measurements in a three-dimensional turbulent boundary layer.
Rpt. 4056, Naval ship R&D center, 1973.

20. Prahlad, T.S.
Wall similarity in three-dimensional
turbulent boundary layers.
AIAA J., vol.6, p.1772, 1968.

21. Prahlad, T.S.
Mean velocity profiles in three-dimensional
incompressible turbulent boundary layers.
AIAA J., vol.3, p.359, 1973.

22. Rogers, B.K. & Head, M.R.
Measurements in three-dimensional
turbulent boundary layers.
Aero. J., vol.73, p.796, 1969.

23. Sarohia, S. & Young, A.D.
Wind tunnel investigations of some three-dimensional
separated turbulent boundary layers.
Three-dimensional turbulent boundary layers, p.126,
ed. by Fernholz & Krause, Springer-Verlag, 1982.

24. Sutton, E.P.
Experiments on a flow with swept separation and
reattachment of a boundary layer.
Three-dimensional turbulent boundary layers, p.138,
ed. by Fernholz & Krause, Springer-Verlag, 1982.

25. Taylor, E.S.
The skewed boundary layer.
J. Basic Engg., Trans. ASME, vol.81, p.297, 1959.

26. Vagt, J.D.
Experimental techniques in three-dimensional
turbulent boundary layers.
Three-dimensional turbulent boundary layers, p.19,
ed. by Fernholz & Krause, Springer-Verlag, 1982.

27. Xin, D., Deng, X., Chen, Y. & Wang, C.
Experimental study on the behaviour of three-dimensional turbulent boundary layer induced by
a straight wing erected on a flat plate.
Acta Aero. et Astro. Sinica, vol.5, p.366, 1984.

28. Young, J.W.S., Howard, J.H.G. & Jerie, J.
A zero-streamwise-pressure-gradient,
three-dimensional turbulent boundary layer in
a 90° curved rectangular duct.
Trans. Can. Soc. Mech. Engg., vol.1, p.87, 1972.

E. Turbulent boundary layers on curved surfaces

1. Hoffmann, P.H., Muck, K.C., & Bradshaw, P.
The effect of convex surface curvature on
turbulent boundary layers.
J. Fluid Mech., vol.161, p.347, 1985.

2. Hoffmann, P.H., Muck, K.C., & Bradshaw, P.
The effect of concave surface curvature on turbulent boundary layers.
J. Fluid Mech., vol.161, p.371, 1985.

3. Hunt, I.A. & Joubert, P.N.
Effects of small streamline curvature on turbulent duct flow.
J. Fluid Mech., vol.91, p.633, 1979.

4. Meroney, R.N., & Bradshaw, P.
Turbulent boundary layer growth over a longitudinally curved surface.
AIAA J., vol.13, p.1448, 1975.

5. Smits, A.J., Young, S.T.B. & Bradshaw, P.
The effect of short regions of high surface curvature on turbulent boundary layers.
J. Fluid Mech., vol.94, p.209, 1979.

6. So, R.M.C. & Mellor, G.L.
Experiment on convex curvature effects in turbulent boundary layers.
J. Fluid Mech., vol.60, p.43, 1973.

7. So, R.M.C.
Experiment on turbulent boundary layers on a concave wall.
Aero. Quarterly, vol.16, p.25, 1975.

F. Three-dimensional flow separations

1. Dallmann, U.
Topological structures of three-dimensional vortex flow separation.
AIAA paper 83-1735, 1983.

2. Doerffer, P. & Dallmann, U.
Reynolds number effect on separation structures at normal shock/wave turbulent boundary-layer interaction.
AIAA J., vol.27, 1989.

3. Hunt, J.C.R., Abell, C.J., Peterka, J.A. & Woo, H.
Kinematical studies of the flows around free or surface-mounted obstacles; applying topology to flow visualization.
J. Fluid Mech., vol.86, p.179, 1978.

4. Lu Z., Deng, X. & Liu, M.
Study of the separation criterion for three-dimensional viscous flows.
Acta Aero. et Astro. Sinica, vol.7, p.332, 1986.

5. Maskell, E.C.
Flow separation in three-dimensions.
RAE Rpt. 2565, 1955.

6. Peake, D.J., Rainbird, W.J. & Atraghji, E.G.
Three-dimensional flow separations on aircraft and missiles.
AIAA J., vol.10, p.567, 1972.

7. Peake, D.J. & Tobak, M.
Three-dimensional separation and reattachment.
AGARD-LS-121, paper 2, 1982.

8. Smith, J.H.B.
A review of separation in steady, three-dimensional flows.
AGARD CP-168, 1975.

9. Tobak, M. & Peake, D.J.
Topology of two-dimensional and three-dimensional separated flows.
AIAA paper 79-1480, 1979.

10. Tobak, M., & Peake, D.J.
Topological structures of three-dimensional separated flows.
AIAA paper 81-1260, 1981.

11. Tobak, M. & Peake, D.J.
Topology of three-dimensional separated flows.
Ann. Rev. Fluid Mech., vol.14, p.61, 1982.

12. Wang, K.C.
New developments about open separation.
Three-dimensional turbulent boundary layers,
ed. by Fernholz & Krause, Springer-Verlag, 1982.

13. Wang, K.C.
On the disputes about open separation.
AIAA paper 83-0296, 1983.

14. Wolfgang, S., Ahmad, A. & Mahmood, M.
Experimental investigations of the flow past a square plate at large incidence.
Cong. proc., supp. vol., p.C244,
4th Asian Cong. of Fluid Mech., Hong Kong, 1989.